FLOW CHARACTERIZATION OF LIFTED FLAMES IN SWIRLING, REACTING FLOWS

A Dissertation
Presented to
The Academic Faculty

by

Ianko Chterev

In Partial Fulfillment
of the Requirements for the Degree
Doctor of Philosophy in the
School of Aerospace Engineering

Georgia Institute of Technology
August, 2017

FLOW CHARACTERIZATION OF LIFTED FLAMES IN SWIRLING, REACTING FLOWS

Approved by:

Dr. Timothy Lieuwen, Advisor
School of Aerospace Engineering
Georgia Institute of Technology

Dr. Jerry Seitzman
School of Aerospace Engineering
Georgia Institute of Technology

Dr. Suresh Menon
School of Aerospace Engineering
Georgia Institute of Technology

Dr. Caroline Genzale
School of Mechanical Engineering
Georgia Institute of Technology

Dr. Devesh Ranjan
School of Mechanical Engineering
Georgia Institute of Technology

Date Approved: April 17, 2017

To mom and dad:

I am forever grateful for your unfailing love and support

To my beautiful girlfriend, Katya:

Through your patience, love and dedication I found strength

ACKNOWLEDGEMENTS

I would not be completing my PhD without the professional support of many individuals as well as the emotional support through these and many other people's friendship. First off, I acknowledge my academic advisor Professor Tim Lieuwen for taking me under his wing in the summer of 2010, and being a most excellent mentor all these years. Throughout this trying but fruitful journey, he has provided security, and invaluable guidance, while pushing me hard to reach my fullest potential. He kept me focused on my combustion research, while supporting my specialty in laser diagnostics. I knew him from my undergraduate classes, through which he inspired me to pursue a PhD. I am forever grateful for him believing in me and for his model of academic excellence. Outside of work, many joyful, serene, and exciting memories come to mind from hanging out with Professor Lieuwen's family, dog and the rest of the research group. I fondly recall kayaking, white water rafting, driving a car spiritedly, star gazing, discussing broadband flame noise while watching a camp fire, mountain biking, hiking, playing volleyball, even wiffle ball, wonderful feasts, and getting pranked.

I am deeply thankful to Professor Jerry Seitzman for effectively being my co-advisor and also offering excellent mentorship. He is been with Professor Lieuwen and I every step of the way, always encouraging my scientific curiosity and urging me to search for answers. He has always treated me as one of his own students. I particularly owe my formal training in laser diagnostics to him: I have had countless "aha" moments as the theory he taught me suddenly consolidated the bits and pieces of my partial understanding of a subject. Professors Lieuwen and Seitzman have maintained a wonderfully complementing and effective partnership for many years, and I am very fortunate to have received their joint direction.

I acknowledge the rest of my great committee who I am honored to have, consisting of Professors Suresh Menon, Caroline Genzale and Devesh Menon. I am thankful to them for bringing their knowledge, expertise and valuable feedback to my dissertation, despite their hectic schedules.

I have received exceptional hands-on mentorship from several top-notch laser diagnostics experts, some from the combustion lab, and some from outside. I acknowledge the excellent applied physicist Sasha Bibik for investing so much of his valuable time in teaching me his secrets. We have spent many hours together perched over dozens of different lasers or having engaging discussions about solid state physics and often the meaning of life. He looked out for me in the lab as I slowly matured scientifically and professionally.

I was fortunate to meet Sukesh Roy, who graciously invited me to intern for him and his team at Spectral Energies, LLC, Wright-Patterson Air Force Base, for a summer semester, where I was taught to be a better laser diagnostician. I am grateful to Sukesh for the wonderful, exciting, and highly instructive experience, as well as the lasting relationships I formed with him and his team. Drew Caswell was my immediate boss there, challenging me with fun tasks, and sharing his expertise. I am grateful to Drew for the extensive hands-on instruction and fun memories. While there, I met another exceptional diagnostician Naibo Jiang, who has also been an excellent mentor to me. Naibo has also spent many sleepless, back-breaking nights of experiments alongside me at Georgia Tech. I thank him for teaching me to work smarter, not harder. I was fortunate to work with some of the rest of the Spectral Energies great team, including Joe Miller, Waruna Kulatilaka, Ben Halls and Amy Lynch.

I am very thankful to Professor Adam Steinberg of University of Toronto Institute for Aerospace Studies for working with me on experiments, and for sharing precious tricks of the trade and words of wisdom. I also acknowledge Professor Tonghun Lee from University of Illinois, Urbana for his valuable partnership on my liquid fuel work. And I was fortunate to work with two of Professor Lee's students, Steve Hammack and Eric Mayhew, whose expertise and sense of humor certainly lightened the load. Last, but not least I acknowledge the early mentorship of a now graduated student of Professor Seitzman, Karthik Periagaram, who through his passion for and extensive knowledge of optics and lasers only intensified my love for them.

I have also been blessed with the vital support from excellent research engineers with whom I have had the honor to work extensively throughout the years: Bobby Noble, Ben Emerson, Vishal Acharya, Brad Ochs, and Professor David Scarborough. I further acknowledge the irreplaceable help and support from Eugene Lubarsky, Dmitriy Shcherbik, David Wu, Kristopher Manion, Chris Balance, Shane Getchell, and Seth Hutchins.

Of course, none of my research would be possible without my sponsors: United Technologies Corporation (UTC), Air Force Research Lab (AFRL) and Office of Scientific Research (AFOSR), and Federal Aviation Administration (FAA). I acknowledge the following people for their hard work behind the scenes, which made the partnerships and support possible, as well as for their stimulating and insightful interactions, and academic contributions: Randy McKinney, Bill Proscia, Jeff Lovett, Baris Sen, and Saadat Syed from UTC; Jim Gord from AFRL; Chiping Li from AFOSR; and Mohan Gupta from the FAA.

My experimental rigs would have not existed without the expertise of the AE machine shop’ Scott Elliot, Scott Moseley, and Red Russell, who have always made me feel welcome in their shop and have offered advice on a broad range of topics from coon hunting to real estate business ownership.

I would have also been lost without Professor Jechiel Jagoda and Daurette Joseph looking out for me from the Aerospace Department over the years, offering much needed administrative help. I also thank Glenda Duncan for her support and help in making events happen on time every time. I am also honored to have worked in a lab bearing Professor Ben Zinn’s name – I am grateful for his hard work and dedication.

I am grateful to have received early, influential mentorship from older graduate students such as: Jack Crawford, Dong-Hyuk Shin, Prabhakar Venkanteswaran, Vishal Acharya, Ben Emerson, Brad Ochs, Jackie O’Connor, Alberto Amato, Sai Thumuluru, Shreekrishna, Yash Kochar, Nishant Jain. Chris Foley had a special role as my project partner for many years – he showed me how to manage the many aspects of sponsored research effectively, while balancing my life.

I have also worked with many other supportive and intellectually stimulating colleagues over the years to whom I am thankful: Brandon Sforzo, Sampath Adusumilli, Nishant Jain, Aimee Williams, Travis Smith, Anna Hotle, Gautham Sundararajan, Michael Aguilar, Michael Malanoski, Dan Fries, Julia Lundrigan, Matt Quinlan, Andrew Marshall, Danny Foti, Nick Magina, Luke Humphrey, Ryan Sullivan, Benjamin Knox, Gina Magnotti, Arun Radhakrishnan, Andrew Irby, Danny Bloomer, Alex Demaeo,

Debolina Dasgupta, Vedanth Nair, Matt Sirignano. I would like to acknowledge every member of the Combustion Lab for their help and support through my time here.

I also thank Professor Mitchell Walker from the electric propulsion lab, who has always cheered me up, and pushed me to succeed. Early on, I met Adrienne Little from Professor Garimella's group, to whom I am thankful for providing advice and moral support, as well as exchanging research ideas with me.

I am very thankful to my successors Nick Rock and Hanna Ek for their dedication, hard work and respect. I have spent thousands of hours alongside these two troubleshooting electronics and combustor rigs, writing computer code, and acquiring and analyzing data. I leave knowing that my data is in very good hands, and I am excited to see what they do with it.

Most of all I am grateful to mom and dad for their sacrifices to ensure I receive an excellent education and a good chance of a bright future. Everything I have done in my life has been founded on their unconditional love and support. Everything they have done, they in some way selflessly intended to better me. I am also thankful to my extended family back in Bulgaria, every member of which has had a role in helping me get to where I am.

Last, but certainly not least, my beautiful girlfriend Katya and her family have been exceptionally kind and supportive over the past four years. Katya has had to carry heavy emotional weight in persevering with me through this journey. Her love and dedication never seize to amaze me.

TABLE OF CONTENTS

CHAPTER

LIST OF TABLES

Page

LIST OF FIGURES

Page

NOMENCLATURE

Acronyms

CB	Centerbody
CDF	Cumulative density function
DACRS	Dual annular counter-rotating swirl
DPSS	Diode-pumped solid state (laser)
FOV	Field of view
FWHM	Full-width at half-maximum
HSS	High shear swirler
IRZ	Inner recirculation zone
ISL	Inner shear layer
OPO	Optical parametric oscillator
ORZ	Outer recirculation zone
OSL	Outer shear layer
PAH	Polycyclic aromatic hydrocarbons
PDF	Probability density function
PIV	Particle image velocimetry
PLIF	Planar laser-induced fluorescence
PVC	Precessing vortex core
RFP	Reverse flow probability
RMS	Root mean square
SE	Standard error (uncertainty in the estimate of the mean of a variable)

SNR	Signal-to-noise ratio, mean/RMS
sPIV	Stereo particle image velocimetry
VBB	Vortex breakdown bubble

Latin Symbols

$A_{\mathrm{pert,z}}$	Axial perturbation amplitude in simple precession model [m]
D_0	Centerbody or nozzle inner diameter [m]
f	Lens focal length [mm]
$f(r)$	Two-point normalized correlation over coordinate r
f_{N}	Nyquist frequency [Hz]
$f_{\mathrm{pert,z}}$	Axial position perturbation function [m]
f_s	Sampling frequency [Hz]
$f_{x_i}(x_i)$	Probability density function of measured quantity “x_{i}”
$F_{x_i}(x_i)$	Cumulative density function of measured quantity “x_{i}”
f/D	Lens aperture or f-number
$f''(r)$	Second spatial derivative of two-point normalized correlation
l_{G}	Gibson flame length scale [m]
l_0	Length scales of the largest eddies [m]
l_{11}	Longitudinal integral length scale of turbulence [m]
L	Characteristic combustor length, taken here as D_0 [m]
M	Number of sets
N	Population size

$\dot{m}$	Mass flow rate [kg/s]
n	Sample size
$n_{1/2,\mathrm{e}}$	Half number of elements in ensemble for autocorrelation calculation
$\hat{n}$	Normal unit vector
$\overline{p}_1$	Probability field of any detectable fuel spray
$\overline{p}_2$	Probability field of fuel spray only
$\overline{p}_{OH,elev}$	Progress variable (probability) field of elevated OH
$r(\tau)$	Autocorrelation function
$r,\ \theta,\ z$	Cylindrical polar coordinate system
ρ	Dimensionless precession radius, R_p/R_0
R_center	Cross-section center radial coordinate [m]
R_cs	Cross-section radius [m]
Re	Reynolds number, UL/ν
$R_\mathrm{le}(\mathrm{t})$	Radial coordinate of the flame leading edge [mm]
R_p	Radius of precession [m]
R_0	Cross-section parabolic profile characteristic length [m]
S_G	Geometric swirl number
S_L	Laminar (displacement) flame speed [cm/s]
S_m	Momentum based swirl number
S_t	Strouhal number, fL/u
T_ph	Preheat temperature of reactants [K]
$T_{1/2,\mathrm{e}}$	Half-time duration of ensemble for ensemble-averaged calculation [s]

u'	RMS velocity [m/s]
U	Characteristic flow velocity [m/s]
U_b	Backflow velocity [m/s]
U_f	Forward velocity [m/s]
U_r(r,z,t)	Radial flow velocity component [m/s]
$U_{r,le}$(t)	U_r at flame leading edge [m/s]
U_z(r,z,t)	Axial flow velocity component [m/s]
$U_{z,le}$(t)	Axial velocity component at flame leading edge [m/s]
$U_{z,ref}$	Reference axial velocity used to binarize velocity field for RFP maps [m/s]
$U_{z,0}$	Mean axial nozzle exit velocity [m/s]
U_θ(r,z,t)	Azimuthal flow velocity component [m/s]
$U_{\theta,le}$(t)	U_θ at the flame leading edge [m/s]
$x_1(x_2)\vert x_3$	Variable x_1 is a function of variable x_2, and is conditioned on additional variable x_3
$\tilde{x}$	Variable x normalized by its maximum value, i.e. $x/\max(x)$
Y_{le}(t)	Vertical coordinate of the flame leading edge [mm]
Z_f(t)	Instantaneous axial coordinate of the unconditioned flame leading edge from OH-PLIF [mm]
$Z_{f,mean}$	Axial coordinate of most upstream point of $\bar{c} = 0.5$ isocontour of flame; i.e., “average” unconditioned flame leading edge from OH-PLIF [mm]
Z_s(t)	Axial coordinate of the leading edge of the instantaneous axial velocity stagnation (Uz=0) isocontour within the PIV/PLIF measurement plane (r-z) [mm]
$Z_{s,mean}$	Axial coordinate of the leading edge of the mean axial velocity stagnation ($\bar{U}_z = 0$) isocontour within the PIV/PLIF measurement plane (r-z) [mm]

$Z_{\mathrm{le}}(\mathrm{t})$	Axial coordinate of the flame leading edge [mm]
$Z_{\mathrm{b}}(t)$	In-plane instantaneous axial velocity at leading stagnation point [m/s]
$\overline{Z_b}$	In-plane average of instantaneous axial velocity at leading stagnation point [m/s]
$Z_{\mathrm{b,ave}}$	In-plane average axial velocity at leading stagnation point [m/s]
$Z_{\mathrm{b,g}}(t)$	Global instantaneous axial velocity at leading stagnation point [m/s]
$\overline{Z_{b,g}}$	Global average of instantaneous axial velocity leading stagnation point [m]
$Z_{\mathrm{b,g,ave}}$	Global average axial velocity at leading stagnation point [m]

Greek and Special Symbols

β	Backflow ratio, $U_{\mathrm{f}}/U_{\mathrm{b}}$
δ_{L}	Laminar flame thickness [m]
δ_{ls}	PIV laser sheet thickness [m]
Δ_{PIV}	PIV resolution [m]
Δ_{PLIF}	PLIF resolution [m]
ε	Turbulence dissipation rate [J/s/kg]
η	Kolmogorov length scale [m]
θ	Precession angle [rad]
θ_{t}	Axis of rotation tilt angle [deg]
$\theta_{\mathrm{r\text{-}z,le}}(\mathrm{t})$	Flow angle at the flame leading edge in the *r-z* plane [deg]
$\kappa(\mathrm{r,z,t})$	Flame stretch rate [1/s]
$\kappa_{\mathrm{curv}}(\mathrm{r,z,t})$	Curvature term of flame stretch [1/s]
κ_{ext}^{RZ}	Extinction stretch rate [1/s]

$\kappa_s(r,z,t)$	Hydrodynamic flame stretch rate [1/s]
$\kappa_{s,incomp}(z)$	Hydrodynamic strain for opposed jet flame assuming incompressibility [1/s]
$\kappa_{s,le}(t)$	Hydrodynamic flame stretch rate at the flame leading edge [1/s]
$\kappa_{s,norm}(r,z,t)$	Normal stress sub-terms of hydrodynamic strain term of flame stretch [1/s]
$\kappa_{s,shear}(r,z,t)$	Shear stress sub-terms of hydrodynamic strain term of flame stretch [1/s]
κ_s^{RZ}	Hydrodynamic strain [1/s] for opposed jet flame at the edge of the flame reaction zone, defined at $\partial U_z / \partial z = 0$
ν	Kinematic viscosity [m^2/s]
ρ	Mass density [kg/m^3]
σ	Standard deviation
σ^2	Variance
τ	Time delay used to define autocorrelation function [s]
τ_c	Integral time scale of turbulence, obtained by integrating the autocorrelation function $r(\tau)$ over all time delays τ [s]
χ_i	Mole fraction of specie "i"
ϕ	Fuel/air equivalence ratio
$\phi_{0,p}$	Precession initial phase [rad]
$\phi_{0,z}$	Axial disturbance initial phase [rad]
ω_p	Precession angular frequency [rad/s]
$\omega_{pert,z}$	Axial perturbation angular frequency [rad/s]
$\bar{\Omega}_{xy}$	Out-of-plane component of vorticity [1/s]
$\overline{(\ )}$	Time average of a quantity
$\langle\ \rangle$	Expected value of a quantity

SUMMARY

Swirl stabilized combustors are commonly used in gaseous fueled land-based gas turbines, as well as liquid fueled aerospace combustors to achieve simultaneously high efficiency, low emissions, wide operability limits and low thermal and mechanical (thermoacoustic) hardware loadings. Properties such as flame shape and location are critical to successful design, and therefore understanding them is the general focus of this work. This thesis considers swirl stabilized lifted flames in both gaseous premixed and spray fuel systems. High swirl flows with vortex breakdown are frequently used to create recirculating flow regions for flame stabilization. Lifted flames are common in swirling combustors, and are subject flow instabilities such as precession, which in turn can affect time-averaged quantities, and this effect is investigated. Furthermore, the conditions under which premixed aerodynamically stabilized flames exist or do not exist are not well understood, and experiments are needed to characterize the associated flame and flow properties. We perform such experiments here and discuss our findings on the flame stabilization physics. Considering specifically spray combustion at elevated pressure, there is a large gap in available experimental measurements needed to study internal combustion physics and to validate CFD due to the greatly increased difficulty in performing measurements under these conditions

The research questions and findings are summarized below for each topic.

Stagnation point dynamics

This work analyses how precession influences the relationship between the reacting flows' time-averaged and instantaneous features. Its objective is to provide

interpretive insights into high fidelity computations or experimental results. It shows how precession influences three significant topological features in the time-averaged flow: (1) centerline axial jets, (2) centerline stagnation points, and (3) symmetry of the flow about the centerline. It also discusses the extent to which these first two features provide insight into the actual instantaneous flow topology. A particularly significant result of this work is in regards to aerodynamically stabilized flames. Stabilization of such flames requires a low velocity interior stagnation point(s), presumably in the vortex breakdown region. We show how precession causes systematic differences between the location of the time-averaged position of the instantaneous stagnation point, and the stagnation point of the time-averaged velocity. An important implication of this point is that a perfect prediction of the time-averaged flow field could still lead to a completely erroneous time-averaged flame position prediction. Finally, we discuss the influence of precession and coherent motion on convergence of estimated averaged quantities. An additional contribution is the implementation of progress variable fields to flow velocity as a nonlinear averaging technique to reveal swirl flow dynamics.

Aerodynamically stabilized flames

Aerodynamically stabilized flames are substantially more difficult to experimentally characterize than shear layer stabilized flames, as the flame leading edge moves around significantly and may or may not coincide with a diagnostic laser sheet, in contrast to the near-fixed leading edge of shear layer stabilized flames. This work describes a novel approach to characterize the leading edge conditions, based upon simultaneous stereo Particle Image Velocimetry (sPIV), OH Planar Laser-Induced Fluorescence (PLIF) and OH* chemiluminescence data. Frames are conditionally analyzed when the flame's most upstream point was captured in the laser sheet. These conditioned frames were used to determine the coordinates, local flow velocity and full, three-dimensional, hydrodynamic strain component of flame stretch at the dynamically evolving flame leading edge. Results are taken at two conditions, 70 m/s and 45 m/s axial velocity, referred to as case 1 and 2, respectively. These data show that the leading edge of the flame precesses off-axis, with additional uncorrelated radial and axial motions. The conditioned mean flame stretch rate is positive in both cases, due to the bulk flow deceleration from the high velocity nozzle flow into the larger diameter combustor. Mean strain or velocity values conditioned on the leading flame edge are substantially different from mean values calculated at the same location. For example, the case 1 mean conditioned axial velocity at the flame leading edge is 9 m/s, while the mean axial velocity at the same location is 4 times higher, 36 m/s. In addition, the case 1 mean hydrodynamic strain rate is 3.6 times higher than the corresponding laminar flame extinction stretch rate, κ_{ext}, calculated from detailed kinetics for the high velocity case, while less than half of κ_{ext} in case 2. The mean strain rate predicted from bulk velocity scaling changes by a factor of 70/45 between the two cases, a value confirmed by measurements. However, the conditioned mean stretch values differ by a factor of 14. This result illustrates the significant difficulty in correlating flame stretch rates for understanding flame stability. A key takeaway from these results is that current correlations for flame stability do not capture much of the intermittency that is present in swirl flows with precessing flow features, and illustrates the need for continued work in very basic physics of how and when flames are stabilized aerodynamically.

Spray combustion physics through two-phase PIV and fuel/OH-PLIF

Simultaneous, high speed (5 kHz) stereo PIV, OH and fuel-PLIF in a pressurized, liquid fueled, swirl stabilized flame are implemented to characterize the flow field, qualitative heat release and fuel spray distributions, and flame dynamics. Acquiring high speed OH-PLIF in pressurized, liquid fuel systems is difficult due to the strong overlap of the fuel's absorption and emission spectra that of the OH fluorescence spectrum. The key contribution of this portion of the work is presenting the first known to this author simultaneous measurements of these quantities. To overcome difficulties associated with the overlap, the OH and fuel fluorescence signals were partially separated by using two cameras with differing spectral filters and data acquisition timing. Upon data reduction, regions containing fuel, OH and a mixture of fuel and OH are identified. Instantaneous and time-averaged results are discussed showing the flow field, flame position and dynamics, and spray distribution from the fuel signal for two multi-component liquid fuels, at two inlet temperatures and three pressures. These results are used to infer several important observations on coupled flow and flame physics. Specifically, the flame is "M-shaped" at higher preheat temperature and higher fuel/ air ratio, as opposed to no visible reaction on the inside of the annular fuel/air jet at low temperature and fuel/air ratio conditions. While such fundamentally different flame topologies in gaseous, premixed flames is well known, these results show that there is also different families of flame shapes and heat release distributions in spray flames. In addition, the flame position with respect to the flow is different for the spray flame than in gaseous, premixed flames – in premixed flames with this geometry, the flame lies in the low velocity shear layer separating the reactants and the recirculating products. In contrast, the flame location is controlled by the spray location in this spray flame, as opposed to the velocity shear layer. For example, reactions are observed near the nozzle outlet in the core of the high velocity annular jet, something which would not be observed in the premixed flame configuration. Also of interest is the near invariance of the key flow features – such as jet core trajectory or shear layer locations – to the operating condition changes for this study, even as the spray penetration and distribution, and flame position change appreciably.

CHAPTER 1

INTRODUCTION, BACKGROUND, MOTIVATION, AND SCOPE

Our work is generally concerned with swirl stabilized combustion and focuses on two more specific topics: (1) swirling aerodynamic flame stabilization and (2) experimental innovations in and physical characterization of spray flames. This chapter consists of two sections, accordingly.

1.1. Premixed Swirl Stabilized Combustion

We begin by introducing premixed swirl combustion and discuss some of its uses and advantages. Then we give background information, starting generally with non-swirling non-reacting jets and adding effects of swirl and heat release. Next, we discuss the topology of swirling flows with vortex breakdown, listing general flow features for a few geometric variations, and flame shapes observed with these flows. We continue by discussing hydrodynamic flow instabilities such as the precessing vortex core (PVC) and shear layer helical instabilities, and their role in flame stabilization by modifying the instantaneous flow field to create instantaneous features drastically different from the time-averaged ones. We then consider in more detail aerodynamically stabilized flames. We point out two specific topics needing further research which motivate our work and present our research scope.

1.1.1. Introduction to Premixed Swirl Combustion

Premixed swirl combustion is widely used in gaseous fuel land-based power generation gas turbine combustors. In response to high gaseous fuel prices and increasingly stringent emissions requirements, such as for NOx and CO, combined with practical design considerations, facility design demands premixed, high efficiency, high power-density, variable power, low hardware heat loading combustors. Turbine design considerations further require a uniform combustor outlet pattern factor. Moreover, combustion instabilities can cause destructive thermoacoustic oscillations. The associated mechanical and thermal stresses can reduce hardware longevity, and therefore, thermoacoustic stability limits are essential to combustor design. Combustion instability limits are controlled by the axial heat release distribution, so knowing the flame shape and location is critical. Unfortunately, some of these constraints involve trade-offs. For example, high power-density makes a combustion device more susceptible to combustion instabilities, exacerbating the concern for hardware longevity. Thus, understanding the internal combustor physics is critical to the design process.

High swirl, premixed, dump combustors are commonly used to meet these requirements due to their advantages over their bluff body stabilized counter-parts. Their premixed nature allows lean burning, which simultaneously lowers NOx and CO emissions, but makes them more susceptible to combustion instabilities. Flame stabilization relies on low velocity regions in the resulting flowfield from vortex breakdown of swirling flows to replace bluff flame holders. Advantages over bluff flame holder stabilization include lower pressure drop due to smaller wakes, and additional flame attachment regions associated with vortex breakdown. These additional flame stabilization regions satisfy the variable power requirement by allowing the flame to adjust its stabilization location and length, rather than blow-off or flash back at high or low power operation, respectively. Commonly swirl combustors can support lifted, aerodynamically stabilized flames inside the vortex breakdown bubble or in low velocity regions due to flow divergence. These lifted flames are interesting because of their potential to reduce heat transfer to the combustor walls and nozzle, and ability to shift within the combustor.

1.1.2. Topology of Swirl Flows

Annular jets without swirl

Annular swirling flows exhibit complex fluid mechanic features, and many fundamental aspects of the flow instability and topology are under active investigation. Annular jets in the absence of swirl have been extensively investigated by Ko and co-workers [1-5]. These studies demonstrated the strong dependence of the time-averaged flowfield upon the nature of the centerbody by considering both bluff and aerodynamically tapered centerbodies. Bluff centerbodies lead to a wake flow with reverse flow along the flow centerline. In addition, the two annular shear layers interact with each other and modify the shear layer stability characteristics. The centerbody wake is greatly reduced with an aerodynamic centerbody.

Vortex breakdown

Introducing sufficient swirl to the flow triggers a global hydrodynamic instability known as vortex breakdown (VBD). VBD can be seen in nature in a tornado, with its recirculating core flow. VBD arises from the conversion of radial and axial vorticity to azimuthal vorticity [6] and is associated with flow reversal and the appearance of an interior stagnation point. The first laboratory observations of vortex breakdown in swirling flows were of the flow over a “Gothic” wing [7] and of the leading edge vortices from swept delta wings [8, 9]. Interestingly, in the framework of wing design VBD was undesirable as it increased drag [10], and was later observed to cause buffeting, unsteadiness, and poor control [11]. Sixty years after the discovery of VBD, its physics are still only partly understood, and there is no generally accepted theory. Leading theories from numerical and theoretical studies explain VBD by considering hydrodynamic stability, flow stagnation/separation analogy, and wave phenomena such as wave propagation and transition between conjugate flow states [12].

A large literature exists on the mechanisms of vortex breakdown and swirling flow structure, with comprehensive reviews by Hall [13], Leibovich [14] , [15], Stuart [16], Escudier [12], Lucca-Negro and O'Doherty [17], and other works by Liang and

Maxworthy [18], Billant et al. [19], and many more, e.g., [20-22]. To emphasize the importance of stagnation points, consider the evolution of swirling flow inside pipes [23-25]. In calculations using the unsteady Euler equations, above a critical swirl level, starting with a Burgers vortex model initial state, the flow evolves from a swirling jet, to developing an axial velocity deficit near the centerline, to complete flow reversal, associated with a stagnation point where positive and negative axial flow meet.

Throughout this work we refer to swirling flows with VBD as critical flows. Several forms of axisymmetric and non-axisymmetric VBD have been observed depending on swirl and Reynolds (*Re*) numbers, and geometry. Note that the swirl number is commonly defined either as the ratio of azimuthal to axial momentum of the flow, or geometrically. In the framework of swirling combustors, the swirl number is typically moderate to high, and *Re* is high. Under combustion specific operating conditions, the only axisymmetric kind, the bubble type or B-type VBD is observed. A B-type VBD is visualized in Figure 1.1 (left) from Sarpkaya [26]. The non-axisymmetric kinds come in several varieties, but only the spiral type (S-type) VBD is observed at high *Re*, pictured in Figure 1.1 (right) from Leibovich [14]. Even then, S-type transitions to B-type with high swirl. This bubble creates a time-average “blockage” in the flow, forcing the fluid to flow around the bubble and converting even a circular jet into an annular jet downstream of the breakdown bubble stagnation point.

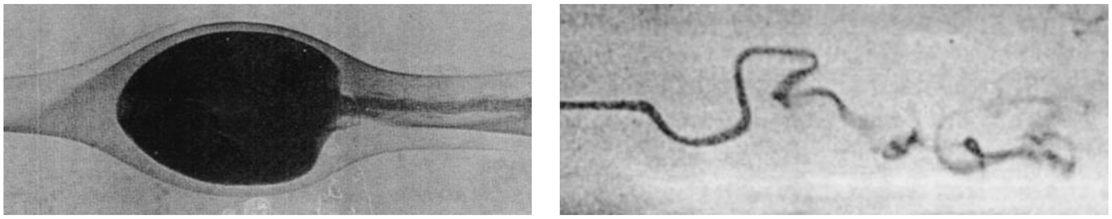

Figure 1.1: Left: Bubble type vortex breakdown [26]. Right: spiral type vortex breakdown [14]

Flow topology of practical swirl combustor geometry

Next the time-averaged topological features of the B-type VBD flowfield and its common variations are discussed. Figure 1.2 illustrates six general features of a practical dump swirl combustor with a centerbody [12, 27-31], numbered in the figure as:

(1) Outer recirculation zone (ORZ), a toroidal recirculating region generated by the rapid expansion of the nozzle into the combustor

(2) Centerbody wake and inner recirculation zone (IRZ), strongly associated with the vortex breakdown bubble (VBB)

(3) High velocity, annular fluid jet which divides (1) and (2)

(4) Two annular shear layers which divide the recirculation zones (1) and (2) and the annular jet (3), denoted here as the outer shear layer (OSL) and inner shear layer (ISL)

(5) Positive centerline jet

(6) Centerbody wake

Double-cell inner and outer recirculation zone structures are observed [32, 33] depending on geometry, and is coupled to heat release. The centerbody wake (6) and IRZ (2) can exist as a single merged recirculating structure or as distinct structures, depending on the swirl number and *Re* [30, 34]. Sheen et al. [30] observed that *Re* has a weak effect on the recirculation structure of swirling flows at sufficiently large value (*Re* > 500). Sheen et al. [30] and Vanierschot and Bulck [34] observed that for a small range of swirl numbers above the critical value, the centerbody wake structure and VBB exist as separate structures, while they merged into a single recirculating cell at higher swirl numbers, leading to the loss of a time-averaged stagnation point in the interior of the flow itself. Additionally, confinement by combustor walls and outlet boundary conditions such as exhaust contraction ratio strongly influence the vortex breakdown structure further [30, 31, 35]. Sheen et al. [30] observed that confining the flow lowered the swirl number at which the centerbody wake and VBB merge. Emara et al. [31] similarly observed the strong sensitivity of the centerline velocity features (e.g., negative flow, positive flow, presence of stagnation points) to the exhaust contraction ratio, exhaust and/or the combustor length.

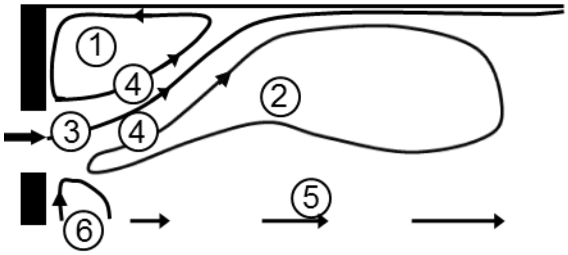

Figure 1.2: Notional flowfield for a bluff centerbody annular nozzle. 1: ORZ, 2: IRZ, 3: Annular jet, 4: Shear layers, 5: Central jet, 6: CB wake structure

Combustion effects

Combustion significantly alters swirling flow features [36, 37]. Gas expansion associated with heat release by combustion increases the average axial flow velocity but has little effect on the average azimuthal velocity, leading to a decrease in swirl number and an increase in axial velocity gradients and shear. As such, both the time-average (bubble length, width, backflow velocity) and dynamical features of the flow are affected by heat release, but in a manner which is a strong function of the configuration and operating conditions of the device, so that few general comments on heat release effects can be made.

1.1.3. Secondary Hydrodynamic Flow Instabilities

Swirl flows are influenced by three different types of hydrodynamic instabilities: the Kelvin-Helmholtz instability of the axial and azimuthal shear layers, the Rayleigh instability due to the radial gradient in azimuthal velocity, and an inertial instability associated with the Coriolis force. Several sources of flow disturbance can be identified. In addition to turbulent flow disturbances, multiple steady and unsteady flow structures, including axisymmetric and helical disturbances, are generally present in swirling flows and can perturb the VBB and stagnation point axially and transversely. During combustion instabilities, the VBB is often subjected to additional harmonic axial and/transverse acoustic forcing [38-41], as well as harmonic axisymmetric and helical vortical structures [42, 43]. For example, flame and flow dynamics can couple to acoustics via the swirler geometry causing axial and azimuthal disturbances [44, 45]. Meanwhile, incoming acoustic oscillations interact with the swirler to create a vorticity wave which induces swirl number fluctuations [44, 45]. The angular fluctuations perturb the flame, while the acoustic wave causes vortex shedding from the nozzle lip and flame rollup. Flame and flow dynamics can also couple to acoustics via flow precession and inner recirculation zone size variation in response to swirl number variations [46]. Furthermore, these flow structures create instantaneous stagnation points and local low velocity regions which would be important to flame stabilization as discussed later.

The precessing vortex core (PVC) is a commonly observed hydrodynamic helical instability, during which the instantaneous center of rotation of the flow precesses around the geometric center of rotation [27, 47-51]. For example, Figure 1.3 (following Syred [46]) shows the axial and azimuthal velocity characteristics. In reference to B-type VBD, the central region of recirculating flow is coupled to the PVC, and also precesses and spirals axially in a helical motion.

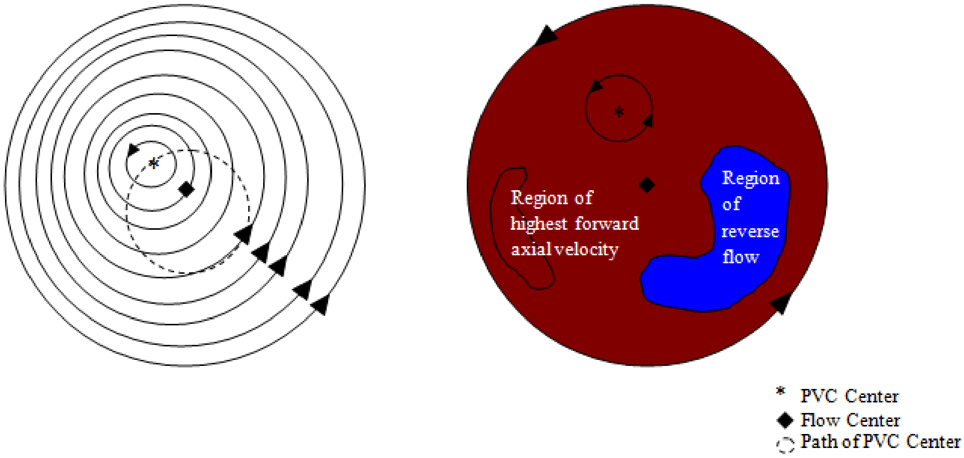

Figure 1.3: Azimuthal velocity isocontours (left) and axial velocity regions (right) showing PVC. Following Syred [46]

The PVC distorts the VBB into a spiral shape as shown in Figure 1.4 from Chanaud [50]. Double PVCs have also been observed [46, 48]. For non-reacting conditions, the onset of PVC is a function of swirl number, burner geometry, and exhaust contraction ratio [27, 48, 52, 53]. Under reacting conditions equivalence ratio and method of fuel injection enter the picture [27, 52-55]. PVC can often be suppressed by merely altering axial or azimuthal components of fuel injection. However, premixed flows are more susceptible to PVC [27, 48, 52].

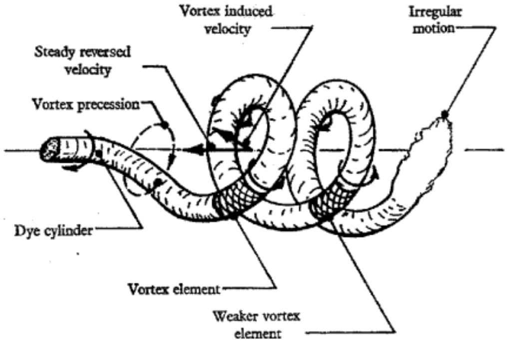

Figure 1.4: Distortion of vortex breakdown bubble by PVC [50]

The ISL and OSL illustrated in Figure 1.2, item (4), are subject to the Kelvin–Helmholtz instability, which can be convectively or absolutely unstable, depending on the reverse flow velocity and swirl number [56, 57]. For this reason, the nature of the reverse flow introduced by the centerbody wake is dynamically significant in terms of the shear layers as well. These shear layer hydrodynamic instabilities may trigger helical vortex shedding independent of a PVC, appearing in radial-axial cuts as staggered eddies. PVCs can coexist and couple with such secondary helical structures [46], as have been observed [58-61] in the ISL and OSL, referred to as inner helical vortices (IHV) and outer helical vortices (OHV), and can trigger thermoacoustic instabilities. No causality is implied as to the PVC inducing these structures.

Stagnation point dynamics

We proceed to the first research topic of this work by reviewing the mechanics of stagnation point motion. As the PVC distorts and causes the inner recirculation region to precess, this precession is imparted onto the stagnation point. If the flame leading edge is stabilized by the stagnation point of the breakdown bubble as will be discussed later, then the flame leading edge oscillates significantly as well. Figure 1.5 from Brücker [62] illustrates how the stagnation point follows the precessing asymmetric, S-type, VBD structure. Additionally the free VBD stagnation point [50] experiences axial motion as helical structures have been shown to undulate axially experimentally and numerically [63]. Although the stagnation point motion is already known to occur, what need investigation are its effects on the average flow field of high swirl number flows, and its sensitivities to operational conditions and geometry.

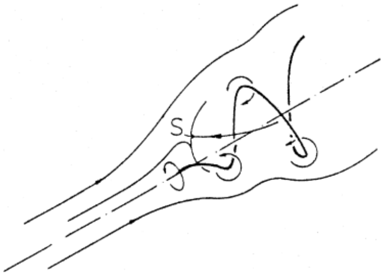

Figure 1.5: Stagnation point precession [62]

1.1.4. Flame Shapes and Geometric Effects

A key focus of this study is the types of flame shapes and flow fields which can occur in swirling aero engine geometry, and the conditions under which there are abrupt bifurcations between different flame shape or flow field families. As indicated by the different flame configurations in Figure 1.6, flames can stabilize in either the low velocity regions in the shear layer (b) and (c), or near interior stagnation points associated with the vortex breakdown bubble (a) [35, 64-66], or in the case of the aerodynamically tapered centerbody configuration, in instantaneous stagnation regions created by PVC and secondary helical vortices (a’), and OSL (d). There are many studies of these flame shapes in the literature with similar observations, for example, Santavicca’s [67, 68] and Ghoneim’s groups [69-71]. The latter analyzed these transitions using methane/hydrogen blends, and found similar flame shapes. As expected, the equivalence ratio at which the flame transitioned from one shape to another was a function of hydrogen fraction in the fuel. The relationship between equivalence ratio and hydrogen fraction at these transitions could be scaled with a normalized extinction stretch rate.

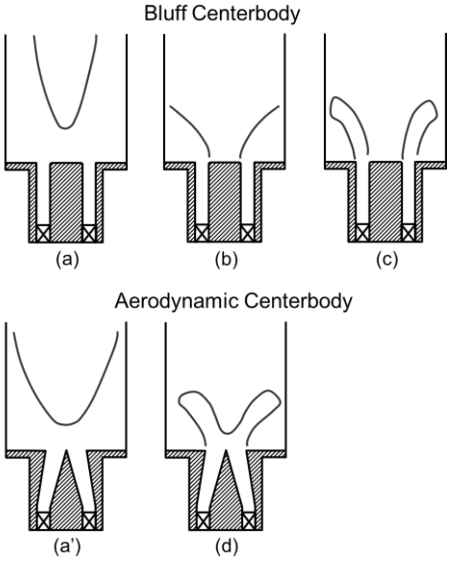

Figure 1.6: Illustration of a few common flame configurations for annular, swirl flows with bluff and tapered centerbodies

The location and spatial distribution of the flame in a combustion chamber are fundamental problems which have important ramifications on combustor operability, durability, and emissions. Flame stabilization location controls the flame shape, which, in turn influences heat loadings to combustor hardware (e.g., centerbody, combustor liner, dome plate). For example, the heat transfer to the centerbody is different in configurations (b) and (c) than in (a), (a') and (d). This, in turn, affects centerbody design and life. Similarly, the flame shape and length varies between, for example, configurations (b) and (c), resulting in significant differences in liner heat transfer distributions.

Next, flame location has an important influence on combustion instability boundaries [72]. As is well established, combustor stability limits are controlled by the time delay between when a fuel/air ratio disturbance or vortex is created and when it reaches the flame. This time delay is a function of parameters such as flame standoff location and flame length and, for example, varies between configurations (a’) and (d). This also illustrates that discontinuous changes in combustor thermoacoustic stability behavior may occur when the flame abruptly bifurcates from one stabilization location to another.

Additionally, potential stabilization locations (or lack thereof, such as if no inner shear layers are present) influence the blowoff limits of the system. In reality, shifts in flame location can be thought of as a sequence of local blowoff events. For example, flame configuration (c) bifurcates to configuration (b) due to local blowoff of the flame from the outer shear layer.

1.1.5. Aerodynamic Flame Stabilization

Next we will discuss aerodynamically stabilized flames in more detail as this work is motivated in part by a few key points made next. One might expect that aerodynamic flame stabilization is a straightforward problem, as expressed by the following three related hypotheses:

(a) The flame will stabilize at a location where the turbulent flame speed balances the time-averaged flow velocity.

(b) The flame will flash back if the turbulent flame speed is everywhere greater than the mean flow velocity.

(c) The flame will blowoff if it is everywhere else.

However, none of these hypotheses based upon time averaged flow concepts are true. Using time-averaged flow features to understand flame stabilization is complicated by the presence of precession in swirl flows, which causes the instantaneous flow to never resemble the time-averaged flow. For example, in Chapter 4.1 the effects of flow precession on time-averaged flow features are analyzed. In contrast to hypothesis (a) above, it is shown how precession causes systematic differences between the location of the time-averaged position of the instantaneous stagnation point and the stagnation point of the time-averaged velocity, which in turn causes the flame to stabilize at a very different location than would be anticipated based on the time-averaged flow velocity.

Another interesting observation is that VBD is not sufficient to ensure aerodynamically stabilized flames [35, 73]. For example, Zhang et al. [73] described fuel composition effects on the blowoff sequence of methane/hydrogen fuel blends. This study used a tapered bluff centerbody, a configuration which supported both shear layer and aerodynamically stabilized flames. They forced transitions in flame shapes, and ultimately blowoff, by decreasing fuel/air ratio, finding that high-H_2 flames blew off from a shear layer stabilized configuration and that no aerodynamically stabilized flames were observed. In contrast, the low H_2 flame transitioned from a shear layer stabilized flame to an aerodynamically stabilized one as blowoff was approached.

Aerodynamically stabilized flames have been observed in various swirling geometries to be stabilized via three main flow features:

(1) Low axial velocity regions in subcritical flows due to flow divergence

(2) Existence of an interior time-averaged stagnation point

(3) Existence of instantaneous stagnation points

An example of the first scenario is when in subcritical swirling flows divergence of the rotating jet causes a low velocity inner region where the flame speed can equal the axial flow speed. This is how the low swirl burner (LSB) [42, 74] stabilizes flames (see Figure 1.7 (a)), which is a practical combustor geometry also used in fundamental studies [75-77].

The second scenario occurs in swirling geometries with interior stagnation points and no predominant inner shear layers to preferentially stabilize flames, as in the annular geometry of Figure 1.6 (a), flames readily stabilize near the interior stagnation point [65, 67, 69-71, 78, 79].

Aerodynamically stabilized flames have also been described for swirl flows without centerbodies, which may be their only flame stabilization mode, if they are designed without separating flow features such as backward facing steps [41, 80-84].

The third scenario is in contrast to hypothesis (c): aerodynamic flames are also observed in many cases where there is reverse flow all the way back into the nozzle without flashing back [34, 35, 85, 86]. Example flame shapes are depicted in Figure 1.7 (b) and (c).Time-averaged considerations would suggest that the flame should propagate upstream into the nozzle, attaching to the separating shear layers along the centerbody. In these cases the flame stabilizes aerodynamically by relying on instantaneous stagnation points created by large scale structures. For example, near the blowout limit the flame can stabilize at the wake of the PVC in a cyclone combustor [87, 88]. Syred suggested that the PVC wake produces low velocity regions where the flame can stabilize, and the flame position is determined by the flame speed equaling the PVC positive velocity. Additionally, Stöhr et al. [58] have observed significant heat release near an instantaneous stagnation point – unseen in the average field – induced by a PVC in an annular swirler, for a flame mainly stabilized in the inner shear layer. This author has also observed flames stabilizing at instantaneous stagnation points in a flow with no average stagnation point for the annular swirler [35] depicted in Figure 1.7 (b,c) and also for the high shear swirler nozzle depicted in Figure 2.5, Chapter 2, Experimental Setup. In both of these cases helical structures were observed.

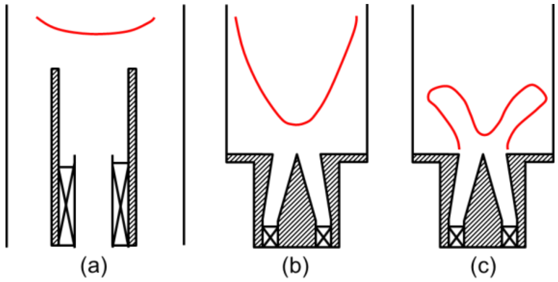

Figure 1.7: Illustration of three flame configurations for annular, swirl flows

Effects on flame speed

In reference to hypothesis (a), flame properties affecting local temperature and burning rate [89], and therefore flame speed, may be affected by aerodynamic flame stretch [90]. Flow shear, as induced by the shear layers and recirculating structures of swirling flows, introduces aerodynamic stretching on the flame [90]. If the shear strain rate and consequent flame stretch rate are too large, the flame will locally extinguish and either blow out of the combustor completely, or stabilize at another location, such as transitioning from configuration (c) to (b) in Figure 1.6 or from configuration (b) to (a). It is logical to ask if flame stretch is preventing the aerodynamically stabilized flames in our third scenario from flashing back – something to which this work alludes.

Furthermore, the high centrifugal accelerations associated with swirling flows [87, 91, 92], on the order of 1000's of g, and flame stretch caused by turbulent motion can modify flame speed. G-forces may affect flame speed by inducing a buoyancy force near the boundary of low density products and high density reactants.

1.1.6. Work Scope

Stagnation point dynamics

First, this work considers the stagnation point dynamics of swirling flowfields, as the stagnation point relates to flame stabilization. The general flowfield and stagnation point are subject to perturbation by turbulence, hydrodynamic instabilities and the resulting large scale flow structures. This implies that even if one is only interested in some time-averaged quantity, such as emissions, pattern factor, or average flame position, one often must understand the instantaneous flow features. In particular, precession of the stagnation point can cause a peculiar average flowfield relative to the instantaneous. Although the mechanisms of stagnation point precession have been studied in the literature, it is desirable to know how these dynamics affect the average flow field for various combustor geometries. The dynamic nature of the flowfields and associated flames has important implications to the interpretation and limitations of time-averaged experimental measurements or computations. Furthermore, this affects how time-resolved measurements and computations are analyzed and interpreted.

We study stagnation point dynamics in an atmospheric methane/air combustor with a counter rotating swirler without a centerbody. We use a non-linear averaging technique as an alternative to simple averaging, to extract the signature of precession from radial-axial cut planar velocity data. Next we use these data to study how precession of the instantaneous stagnation point affects the average flowfield:

(1) Location of time-averaged stagnation point

(2) Existence of instantaneous stagnation points in flows with no average stagnation points

(3) Symmetry of the time-averaged flow

(4) Effect on convergence of means

Aerodynamically stabilized flames

Motivated by the preceding discussion, this work focuses on the dynamics of the leading edge of an aerodynamically stabilized flame in a methane/air atmospheric combustor with an aero engine swirler. Its focus on this leading edge location stems from the fact that in the quasi-steady limit, this point controls its overall stability, as the rest of the flame necessarily spreads downstream from this point. In particular we examine:

(1) Where the flame leading edge is located

(2) What the local flow and flow gradients are there

(3) How these different quantities are correlated

Several prior studies have similarly analyzed the structure and flame stretch characteristics of shear layer stabilized flames, characterizing the factors leading to flame stretch, the magnitude of flame stretch relative to extinction values, and the orientation of the flame leading edge with respect to the flow [65, 93]. Similarly, the near-blowoff dynamics of bluff-body shear layer stabilized flames have been analyzed, such as the different stages encountered before blowoff, [94] and the intermittent nature of extinction and re-ignition events before final blowoff [95-98]. In shear layer stabilized flames, the leading edge remains relatively stationary. For instance, Foley et al. [93] observed the leading edge of the CH layer moving by only a few mm. The aerodynamically stabilized flame problem has significant additional challenges. First, the flame leading edge can move substantially in the axial and radial directions. Moreover, for planar imaging work needed for velocity field/flame stretch characterization, the flame leading edge in the image plane will generally not coincide with the global leading edge. Finally, determination of flame stretch generally requires characterization of flame curvature in both dimensions, and velocity gradients in all three directions. We present a technique for addressing these challenges and present conditioned measurements of the flame leading edge, describing the characteristics of its location, local velocity field and flame stretch rate, as well as the correlation among these quantities.

1.2. Spray Fuel Swirl Combustion

Next we introduce spray fuel swirl combustion and compare and contrast it with premixed swirl combustion in the present context. Then we give an overview of developments in particles image velocimetry (PIV) and planar laser-induced fluorescence (PLIF) to study internal combustion physics and validate computational fluid dynamics results for two-phase high pressure reacting flows. We explain the difficulties with these experiments and the resulting need for more data, and experimental development and associated data reduction and analysis.

1.2.1. Introduction to Spray Fuel Swirl Combustion

Combustion of liquid fuel is more advantageous than gaseous fuel in certain applications, such as aviation, where minimizing fuel storage volume is critical. Furthermore, liquid fuel in aircraft gas turbine engines is generally not premixed with air but sprayed into the combustor, for simplicity and to reduce risks of flashback. The physics of spray fuel combustion are different than of premixed combustion, and therefore, design for low emissions and increased operability conditions is subject to different constraints. Compared to premixed fuel combustion, emissions and operational limits for spray fuel combustion are further influenced by: liquid phase fuel distribution, including droplet velocity, size, and morphology; and gas phase fuel distribution and local fuel/air ratio. Moreover, unburned hydrocarbon and particulate emissions become important. Understanding the physics of high pressure liquid fueled combustion requires experimental characterization of two-phase flowfields, chemical composition and heat release distributions. Such experiments are especially difficult and new techniques are needed, as well as further development of existing ones.

1.2.2. Progress in Nonintrusive Laser Diagnostics for Reacting Flows

Before discussing flow/flame physics in these combustors we first consider basic issues and progress in the various diagnostics which can be employed. With innovations in laser systems, intensifiers, and cameras in recent years, high speed imaging for combustion research has seen a rapid increase using either short bursts of pulses [99, 100] or sustained high repetition pulse trains [101-103]. High speed (kHz), spatially resolved imaging techniques provide important insights into these dynamic processes. High speed particle image velocimetry (PIV) systems have enabled significant improvements in understanding the morphology of unsteady, premixed, three-dimensional swirling flows [101, 104], while high speed planar laser-induced fluorescence (PLIF) techniques, particularly systems imaging OH radical distribution, have enabled simultaneous visualizations of the flame zone with kHz rate temporal resolution to study the flow and flame physics [102, 103, 105-110].

Difficulties with optical measurements in multi-phase, high pressure, reacting flows

Significant challenges arise, however, when making measurements in multi-phase (liquid fueled), high pressure, reacting environments. First, the cost and complexity associated with operating high pressure, high power rigs pose challenges in optimizing the setup over multiple iterations. Also, the need to image through multiple optical windows introduces additional issues, such as scattering, window fouling from soot or PIV seed particles, and optical distortions. Viewing windows, which must be able to withstand the pressurized and high temperature conditions, must also have high transmittance when performing diagnostics in the UV range. In addition, the vibrations and noise of the combustor may require the laser system to be physically separated from the test cell, requiring a longer beam path which is more sensitive to vibrations. Finally, it is difficult to differentiate regions containing fuel from those containing OH when detecting fluorescence from complex fuels.

Prior PIV in multi-phase, high pressure, reacting flows

Many prior workers have reported results from high pressure, liquid fueled, reacting PIV. Examples of such low repetition rate work are from Hochgreb's group [111, 112] and researchers at DLR [113, 114], and high repetition rate from [115, 116]. OH-PLIF has been performed at low repetition rates in reacting flow systems with liquid fuel. Allen et al. [117] described OH-PLIF measurements on neat fuel sprays (heptane, methanol and ethanol) from 1 to 10 bar, and observed interference from polycyclic aromatic hydrocarbons (PAH) fluorescence. The PAH levels increased with pressure, similar to soot production, as also noted in other studies [118, 119]. Frank et al. [120] presented 10 Hz OH fields at varying global fuel/air ratios and pressures up to 20 bar with liquid fuel. Locke et al. performed 10 Hz OH-PLIF in a swirl-stabilized fuel tube combustor with JP-8 spray at pressures up to 18 bar [121, 122]. Interference from PAH was also observed in 10 Hz CH_2O-PLIF measurements with n-dodecane at 60 bar from Skeen [123].

PIV challenges in multi-phase, high pressure, reacting flows

The current work focuses on simultaneous high speed stereoscopic PIV (sPIV), OH-PLIF, and fuel-PLIF measurements in high pressure, liquid fueled, swirling, reacting flows. The main challenges identified by the above studies and others with obtaining these measurements are outlined as follow. First, PIV suffers from interference caused by liquid droplet scattering, as the droplets may be brighter than the seeding particles. This produces a measured velocity bias as large droplets do not follow the flow well. Two options are to mask out the region of spray from the PIV fields [113, 114] or attempt to separate the spray and seeding particles before PIV processing [115, 116]. In the present work we employ a new approach similar to the latter, by using simultaneous fuel-PLIF data to identify gaseous and liquid spray regions in the PIV images, thus, enabling calculation of conditioned gaseous velocity fields and liquid velocity fields.

Prior OH-PLIF in multi-phase, high pressure, reacting flows

Initial work on high-speed OH-PLIF imaging in a liquid fueled, swirl combustor employed multiple, low repetition rate lasers to create an eight shot burst at pressures up to 13 bar [124]. Similarly, in IC engines OH-PLIF has been obtained with short bursts of pulses [125] and sustained high repetition rate imaging [126, 127]. Continuous high speed, simultaneous PIV and OH-PLIF has been applied to liquid fueled combustors [115, 116] and IC engines [127].

LIF challenges in multi-phase, high pressure, reacting flows

Key challenges associated with OH-LIF in high pressure, liquid fuel combustion are [128-131]:

(1) Reduction of fluorescence yield due to increase in collisional quenching (mitigated somewhat by increase in number density)

(2) Collisional broadening (decay in strength of spectral lines) and overlap of the excitation lines

(3) Fluorescence trapping due to the increased optical density at high pressure

(4) Laser energy absorption by liquid fuel and higher gas concentration

(5) Interference from liquid fuel and unburnt hydrocarbon fluorescence resulting from fuel decomposition

High speed measurements add further complications, as the excitation energy (per pulse) is reduced substantially. A typical high speed dye laser system has pulse energies in the ~ 100μJ range, compared to ~ 10mJ for low speed Nd:YAG-pumped dye lasers and optical parametric oscillators (OPO's), and ~ 100mJ for tunable excimer lasers [117]. We note that pulse-burst laser systems are becoming increasingly useful for high energy, high to ultra-fast (MHz) repetition applications, despite suffering from low frame numbers (low hundreds). For PLIF applications pulse-burst lasers can be used to pump OPO's at ~ 10–50 kHz rates for pulse energies up to ~ 100mJ [132-134]. The high pulse energy of the lower repetition rate and pulse-burst systems produces better contrast in the fluorescence signal, compensating for the losses associated with fluorescence quenching (challenge 1 above), trapping (2), and laser energy depletion. In practice, the interference from fuel and other hydrocarbons (4) is the most critical issue, as shown in the earlier high speed imaging work in similar flames [124] and require specialized detection and post-processing schemes discussed in this work.

1.2.3. Insights into High Pressure Multi-Phase Reacting Flow Physics Using PIV/PLIF

Despite these difficulties, it is clear that the simultaneous deployment of these flow and scalar measurement enables significant insights into the structure of the coupled flow, spray, flame, and other scalars such as pollutants, which is not possible when these measurements are made in isolation. Furthermore, results can materially differ when data are taken at combustor relevant conditions vs. conditions more conducive to optical diagnostics (such as low pressure and combustor power).

Such measurements are now routinely used in the IC engine community to provide insight into flame-flow-spray interactions. For example, Peterson and Sick [127] utilized simultaneous PLIF, PIV, and spark energy measurements in an optical engine to show that spark energy observed linearly increased with shear strain rate. Skeen [123] presented simultaneous formaldehyde PLIF (requiring techniques to separate the fluorescence from polycyclic aromatic hydrocarbons, PAH, from the formaldehyde, as discussed above) and Mie scattering to show that low temperature reactions initiate on the radial edges of the spray and forms rapidly near the injector after the end of injection. Müller et al. [126] presented OH-PLIF measurements in an optical IC engine with variable valve timing, showing the pronounced slowing of flame kernel growth after ignition as exhaust gas recirculation levels increased.

Similarly, simultaneous PLIF and PIV measurements are now a standard measurement for understanding thermoacoustic instabilities in swirl burners. These measurements clearly demonstrate that the flow structure is strongly three-dimensional, being dominated by large scale helical flow structures and precession of flow/flame features. As such, application of, for example, line-of-sight chemiluminescence measurements alone is of limited value in understanding flame-flow interactions. For example, Steinberg et al. [103] presented simultaneous PIV, OH-PLIF, and OH* chemiluminescence in a thermoacoustically unstable swirl burner and was able to show how the interactions between a helical flow disturbance led to flame area distortions and heat release oscillations that led to the instability. They also showed how the regions of acoustic amplification and damping varied in space and time. Arndt et al. [102] presented results using the same diagnostics and showed clearly how the transition to instability was associated with a change in flame stabilization location – specifically, a liftoff of the flame from the burner nozzle.

Similar conclusions apply in spray combustors. For example, in a series of papers [111, 112, 135] Hochgreb’s group used simultaneous phase Doppler particle analyzer (PDPA), PIV, and chemiluminescence measurements in a gas turbine combustor to compare a biodiesel and Jet-A liquid fuel and showed, for instance, that changing the fuel composition had relatively little impact on the flow field (a similar observation as in this study), but could correlate changes in flame length with the different droplet evaporation characteristics. Lantz et al. [124] employed PLIF at multiple wavelengths (to visualize liquid and gas phases of the fuel, as well as OH) and Mie scattering in a high pressure gas turbine burner and showed how the OH-containing regions appeared both inside and outside of the fuel spray cone, consistent with the observations in this study at some conditions. Such inferences are highly significant for understanding the space-time structure of the heat release, as it influences thermal loadings on combustor hardware as well as thermoacoustic instabilities. Slabaugh et al. [115] used 5kHz simultaneous PIV and OH-PLIF to enable similar observations. For example, they quantified the spatial structure of the flame surface density with respect to key geometric details of the burner, such as the pilot or annular bluff body features, and flow field, such as regions of high shear. Specifically, they showed regions of high flame surface density in regions of high turbulence intensity where partially premixed and pre-vaporized reactants meet recirculating hot combustion products. Locke et al. [121] presented OH-PLIF measurements in a lean direct injection combustor at 10 atm and showed how a Multipoint Lean Direct Injection (MP-LDI) injector design influences flame location, for example, showing how one injector design led to poor mixing and localized hot spots along the combustor wall. Meier et al. [114] presented PIV, OH PLIF, chemiluminescence, and laser induced incandescence (LII) measurements in in a high pressure, triple nozzle combustor sector to analyze the coupled interactions of the flow, flame, and soot production. One observation particularly worth highlighting with respect to the results of the present study is the location of the flame with respect to the high velocity air jet. Their chemiluminescence measurements suggest that the reaction zone exists in a region of high axial velocities, an interpretation they deemed questionable. Our measurements are consistent with this observation and, as discussed later, demonstrate the fundamental difference between reaction zone location in a premixed flame and a spray flame.

On data reduction and analysis techniques

A significant portion of the present work focuses on data reduction to separate the OH and fuel signals, and analysis of the resulting images. Once the time-resolved detailed measurements are obtained, the next challenge is to reduce the resulting large amounts of instantaneous data into a form which can be used to study flame/flow physics and interactions, sensitivities to operating conditions, and compare with and validate CFD. A few examples from the above-reviewed studies and the broader literature for developing reduced basis descriptions of data sets include proper orthogonal decomposition (POD) analysis for flame-flow dynamic interactions [103, 136] and dynamic mode decomposition (DMD) for deconvolution of dynamic flow structures [137, 138].

1.2.4. Work Scope

The substantive progress that has been made in obtaining scalar and flow measurements in pressurized, liquid fueled systems implies that significant new insights can be obtained into internal reacting flow physics.

A key contribution of this work is to provide insights into the combustion physics of high pressure (2 – 5 bar) liquid fueled aero engine type combustor by applying simultaneous sPIV, OH-PLIF, and fuel-PLIF, with two different liquid fuels to show the simultaneous structures of the spray, flame position, and gas and liquid phase flow field.

Observations are presented on the effects of operating conditions and fuel type on spray distribution, flame shape, and flame anchoring characteristics. A secondary contribution is in developing data reduction techniques to allow instantaneously separating the OH and fuel-PLIF fields.

CHAPTER 2

EXPERIMENTAL SETUP

This chapter is divided into two sections. The first one details the different combustor facilities used and associated air and fuel metering methods. The second describes the optical diagnostic techniques used for vector and scalar quantity measurements, including standard data reduction for the case of PIV. Each section is organized by combustor facility, and the second section included uncertainty analysis sections.

2.1. Combustion Facilities

Three different combustor facilities are used in the presented work. Two are premixed methane/air atmospheric facilities, and the third is a high pressure liquid fuel spray combustor. Next we detail the three different facilities, geometric information, operating conditions, fuel type and metering details.

2.1.1. Atmospheric CH_4/Air Annular Counter-Swirling Nozzle

The following section describes the CH_4/air annular counter-swirling nozzle experimental facility. A schematic of the facility is shown in Figure 2.1. The test section is meant to be a laboratory “unwrapped” version of a section of an annular combustor. The internal dimensions are 1.14m × 0.10m × 0.34m, where the longest dimension is along the y-axis in Figure 2.1. The top of the combustor enables optical access through a rectangular quartz window 0.2 × 0.09m, while allowing exhaust gases to pass through 0.08m diameter ports on either side of the optical window. Two large quartz windows, referred to as the main windows, allow optical access to the flow field through a 0.27m × 0.27m viewing area. The combustor is fabricated from stainless steel and insulated with ceramic inserts from ZIRCAR Refractory Composites, using the refractory sheet type RSLE-57.

The air supply is regulated to 20psig and metered using a calibrated orifice plate in conjunction with a differential and static pressure transducers. The air is preheated to 400K using a WATLOW electric heater and enters the combustor through an insulated settling and conditioning chamber. The air enters the combustion chamber through a single dual-annular, counter-rotating swirler (DACRS) premixer [139-141] with a geometric swirl number of approximately $S = 0.62$. The injector seals into the bottom of the combustor as shown in the section view. It is fueled in the swirlers with natural gas, supplied at 25 psig and metered using a calibrated orifice plate and static and differential pressure transducers. The equivalence ratio, ϕ, is 0.95. The fuel has an approximate composition by volume of 97.5% CH_4, 0.9% higher hydrocarbons, 0.4% CO_2, and 1.1% N_2 (these were average values over the month of April, 2007). The nominal exit velocity, $U_{z,0}$, is 25m/s, corresponding to a $Re = 30{,}600$ based on the outer diameter of the premixer, $D_0 = 31.7$mm. The operating conditions are summarized in Table 2.1.

Figure 2.2 illustrates the time average, unforced flow field, where the colorized vector plot depicts the velocity field (colored by axial velocity) and the colorized contour plot illustrates the out-of-plane vorticity field. The spatial coordinates of both plots are normalized with the nozzle exit diameter, D_0. The magnitudes of axial velocity, $\bar{U}_z$, and vorticity, $\bar{\Omega}_{xy}$, plots are normalized by the bulk velocity, $U_{z,0} = 25$ m/s, and bulk inverse time scale, $U_{z,0}/D_0$, respectively. The PIV measurements used to obtain these data are detailed in the Optical Diagnostics Setup Section 2.2.

As the flow proceeds downstream, it expands around the time average leading edge of the central recirculation zone or VBB. The white line designates the points of zero axial velocity in the VBB region. The time averaged stagnation point of the VBB is located approximately 1.3 diameters downstream of the dump plane, indicated here by the black and white bull’s-eye. The time averaged flame leading edge, represented by the dashed white line, shows that the flame stabilizes upstream of the time average stagnation point, and in between the two shear layers associated with the development of the annular jet. The flame edge was extracted from the seeding density discontinuity in the Mie scattering PIV images. The dashed lines in the vorticity contour indicate linear fits to maxima in absolute values of the vorticity, where blue contours indicate clockwise rotation and red contours indicate counter-clockwise rotation. The vortices originate from the edge of the nozzle dump plane. The vorticity depicted inside the nozzle radius is a result of the annular jet diverging left and right around the VBB. The measurements are detailed in the Optical Diagnostics Setup Section 2.2 below.

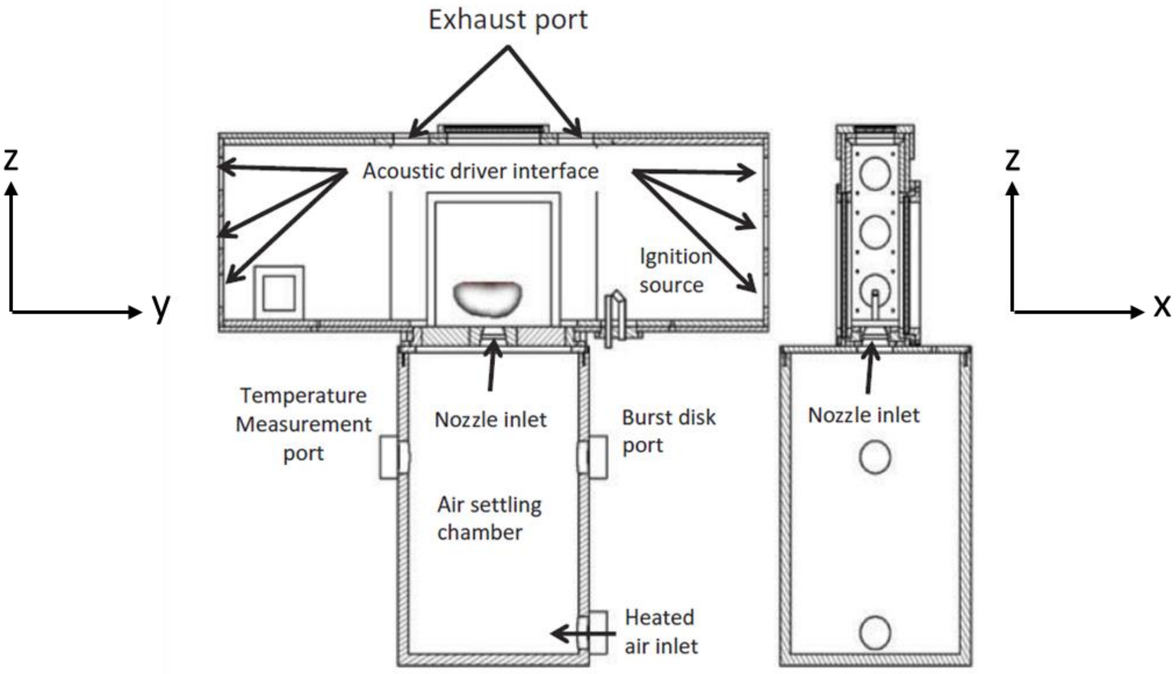

Figure 2.1: Experimental facility with DACRS nozzle. Coordinate system shown.

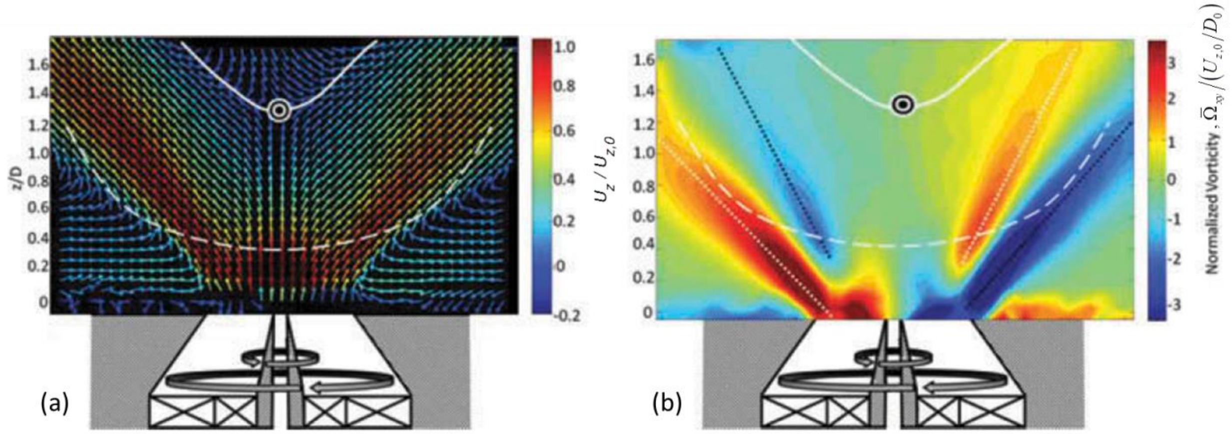

Figure 2.2: Time-averaged flowfield and flame location of DACRS nozzle facility. In-plane velocity vectors are plotted in (a), and out-of page vorticity in (b). Dashed white line is the flame time-averaged leading edge obtained from PIV Mie scattering images. Solid white line is the axial velocity stagnation contour, $\bar{U}_z = 0$, and bull's-eye represents centerline axial stagnation point. Dotted lines in (b) indicate the shear layers, as the loci of points of maximum vorticity.

Table 2.1. Operating conditions for atmospheric CH_4/air DACRS nozzle

Case	***p* [bar]**	**T_{ph} [K]**	**ϕ**	**Nozzle velocity [m/s]**	**Premixed Fuel**
1	1.0	400	0.95	25	CH_4

2.1.2. Atmospheric CH_4/Air High Shear Swirler

The experimental facility utilized here consists of a swirling, premixed combustor in a quartz cylinder for optical access. It is divided into a reactant supply system, flow preconditioning and fuel/air mixing, premixer, combustor, and exhaust sections as shown in Figure 2.3. The coordinate system used to indicate axial, radial, and azimuthal directions is also indicated Figure 2.3.

We now walk through these sections in detail by beginning with the air and fuel supply. The air and natural gas lines supplied are regulated to upstream supply pressures of 60psi and 25psi, respectively. The fuel and air mass flow rates are separately measured using sub-critical, calibrated orifice plates.

The error in the flow velocity in the premixer section, $U_{z,0}$, resulting from uncertainties in the measured static and differential pressure across the orifice plate, is calculated to be 0.40 and 0.25m/s for nominal premixer velocities, $U_{z,0}$, of 45 and 70 m/s at reactant temperatures of 533K. For these uncertainties, no uncertainty in cross-section area or mixture density was assumed. Next, the uncertainty in the reported equivalence ratio is calculated as a function of ϕ for both velocities. Uncertainty in ϕ, σ_ϕ, is dominated by uncertainty in the mass flow rate of fuel, $\dot{m}_f$. At $\phi = 0.60$, of $\sigma_\phi = 0.017$ for $U_{z,0}$ = 45m/s and 0.006 for $U_{z,0}$ = 70m/s. Note that uncertainties in ϕ are considerably less for the higher premixer velocity test case.

After flow rate measurement, the air supply then enters a 50kW WATLOW electric heater raising the air to a preheat temperature of 533K. The air enters the combustion facility as shown in Figure 2.3 from two sides of a pipe T-junction. The air passes through a perforated plate, see Figure 2.3 item (1), with a 50% blockage ratio to remove large structures from the flow, and into the preconditioning section. This blockage plate was created using a 4", schedule 40 blind pipe flange by drilling 32 0.50" holes.

Approximately 3.3" after the blockage plate fuel is injected into the flow through eight equally spaced radial fuel injectors, see Figure 2.3 item (2). Figure 2.4 provides a detail of the injector configuration and injector hole spacing. The injection holes increase in size in the radial direction such that the fuel concentration remains radially uniform. After fuel injection, the fuel and air mix over a ~ 39" settling section, after which they pass through a honeycomb flow straightener, Figure 2.3 item (3) and turbulence reducing wire mesh (4) [142]. The honeycomb straightener had 2" long cells, 0.020 in wall thickness, and cell width varying from 0.30x0.14 to 0.30x0.17 with increasing radius, for an area blockage ~ 14%. The wire mesh is installed ~ 1.75" downstream of the end of the honeycomb, made of 1/16" diameter wire in 0.3"x0.3" mesh sizes.

Non-reacting measurements show a maximum radial variation in fuel/air ratio of 7.5% at the combustor inlet. The fuel is the same as with the DACRS nozzle above. The flow then enters the nozzle, which is quite similar to the high shear swirler (HSS) design described by [143-145] as well as other studies [146, 147]. The combustor consists of a 13.5cm diameter, 20.2cm long quartz tube for optical access. Physical dimensions are non-dimensionalized using the nozzle inner diameter, D_0. The flow exits the combustor through a smoothly converging exhaust, with a sufficient area contraction ratio of 1.5 to ensure closeout of the time-averaged VBB with heat release within the combustor; i.e., it is designed so that no reverse flow occurs at the combustor exit at the reacting operating conditions [35].

Figure 2.5 also plots the 3-component time-averaged velocity field with the axial velocity stagnation contour overlaid in a black line. As indicated by the velocity field, this flowfield exhibits vortex breakdown, with reverse flow along the center line. The annular jet is surrounded by an inner and outer shear layers, ISL and OSL. On the inside of the annular jet is the inner recirculation zone, IRZ, and on the outside the outer recirculation zone, ORZ. Details on this data set can be in the Optical Diagnostics Setup section 2.2 below. The additional solid red contour is the mean flame position obtained from the $\bar{p}_{OH}(r,z)=0.5$ isocontour, obtained from time averaging the binarized OH-PLIF images (binarization is based on an intensity threshold from the inflection point of the histogram as detailed in the Data Reduction section). The open circle denotes the most upstream location of this isocontour, referred to here as the mean flame leading edge in the r-z plane, $Z_{\mathrm{f,mean}}$(r). Note that this point lies in a location of reverse flow. Time-averaged considerations would suggest that the flame should propagate upstream into the mixer. Stated alternatively, they would suggest that this mean stabilization location should occur at a point where the axial flow velocity balances the turbulent flame speed. The data clearly indicate that neither of these considerations is correct, a point explained later in this paper.

Data were taken at a preheat temperature of T_{ph} = 572K, and fuel-to-air equivalence ratio of ϕ = 0.60. Two data sets were taken with different nozzle velocities: case 1 was at

$U_{z,0}$ = 70m/s, and case 2 at 45m/s, with the objective of significantly influencing the stretch rate that the flame is subjected to. Typical nozzle exit velocities range from 45 to 70 m/s, corresponding to Reynolds numbers based on D_0 on the order of ~ 10^5. The operating conditions are summarized in Table 2.2. For both cases, the central part of the flame is aerodynamically stabilized, and wraps around into a lifted flame sitting in the outer shear layer, as shown in Figure 2.5. For case 1, at $U_{z,0}$ = 70 m/s, at $\phi < 0.55$ the outer shear layer stabilized flame starts to intermittently detach, and the entire flame blows out at $\phi \sim 0.45$. These blowoff values are slightly higher for case 2.

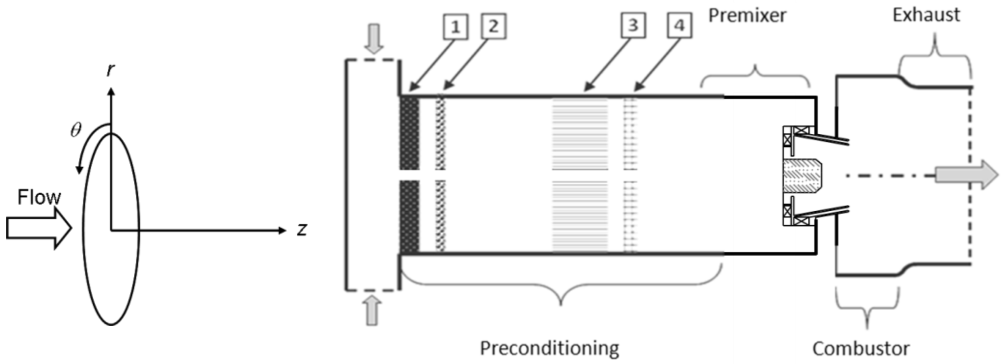

Figure 2.3. Schematic of test facility (right, not to scale) and coordinate system (left).

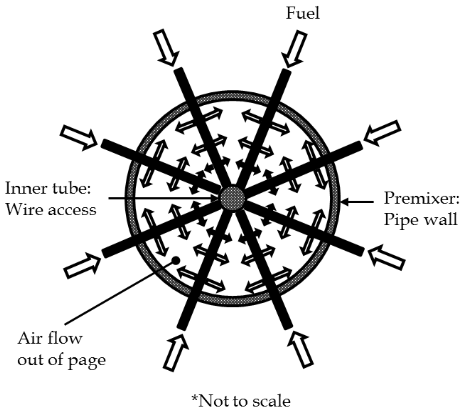

Figure 2.4: Detail of fuel injector configuration, location (2) in Figure 2.3.

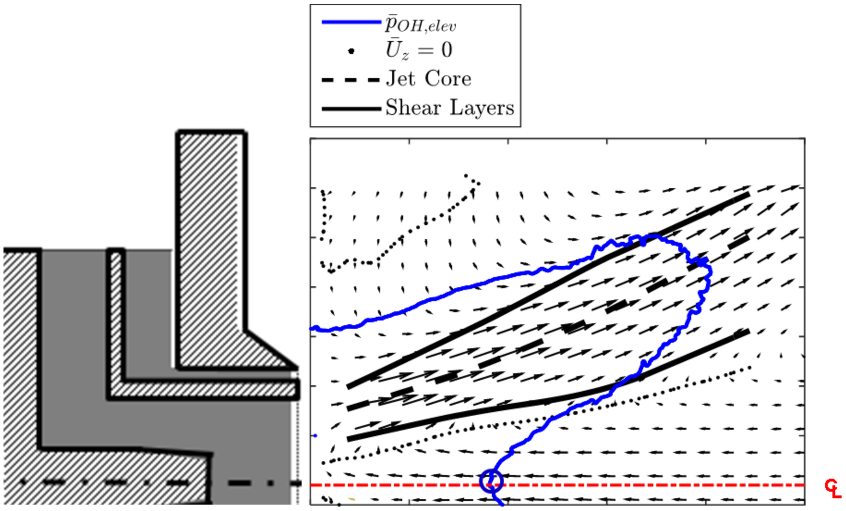

Figure 2.5: Mean flow field with mean flame edge (derived from the $\bar{c}(r,z)=0.5$ isoline of the progress variable field, obtained from mean of binarized OH-PLIF images) denoted by blue line. The location of the mean flame leading edge, $Z_{f,mean}(r)$, is denoted with a blue open circle. Thin black dotted line denotes mean the axial velocity stagnation isocontour ($\bar{U}_z(r,z)=0$). Black dashed line is the jet core (locus of maximum velocity magnitude for each z). Solid black lines are the inner and outer shear layer (computed as loci of out-of-page vorticity extrema).

Table 2.2. Operating conditions for atmospheric CH_4/air high shear swirler facility

Case	*p* [bar]	T_{ph} [K]	ϕ	Nozzle velocity [m/s]	Premixed Fuel
1	1.0	572	0.60	70	CH_4
2	1.0	572	0.60	45	CH_4

2.1.3. High Pressure Jet Fuel High Shear Swirler

The facility details are reproduced below. Key components include air supply and preconditioning, fuel supply, the optically accessible pressure vessel and liner, fuel injector, and exhaust section. Compressed air at pressures up to 20 bar is heated to temperatures from 350 to 750K. Following this heating process, a portion of the air is sent to the test section and the remainder is cooled to approximately 320K in a heat exchanger. This secondary air flows around the liner and keeps the pressure vessel structure and windows cool. Hot combustion products mix with the cooling air downstream of the test section and exit through a water cooled exhaust. A choked orifice plug of variable size is installed at the exhaust exit to maintain a prescribed pressure in the combustion chamber. Air mass flow rates are calculated using a Rosemount vortex flowmeter. The air temperature is measured with a K-type thermocouple 350mm upstream of the dump plane, and its value was continuously recorded during measurements. Its value typically remained within ±10K of the nominal value during a measurement. The uncertainty in the nozzle velocity calculation is estimated to be ~ 2%, calculated by standard uncertainty propagation approaches.

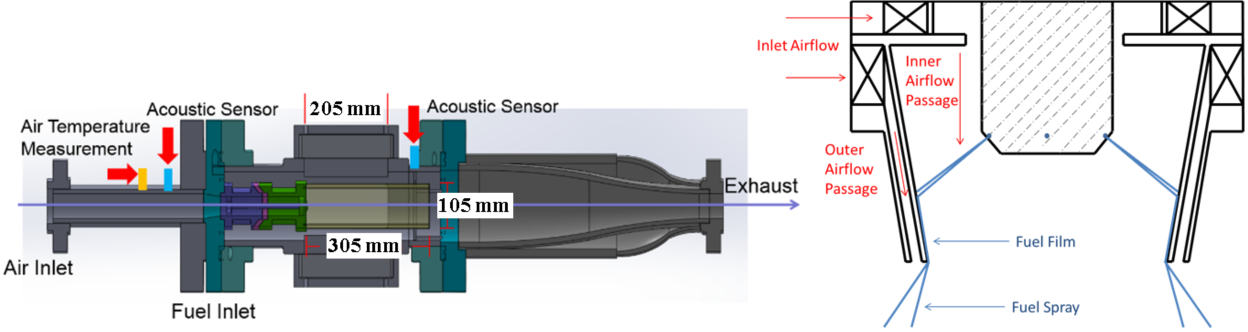

Figure 2.6: Schematic of combustor (left) and the swirler/fuel injector (right)

The combustor liner consists of a 305mm long, 105mm inside diameter quartz tube. The front end of the liner, or nozzle outlet, referred to as the “bulkhead” in this paper consists of a stainless steel wall without secondary cooling passages, and is shown in Figure 2.7. This bulkhead face contains four thermocouples situated flush with the surface for monitoring bulkhead temperature, a static pressure transducer, and an ignitor. Uncertainties in combustor pressure measurements are estimated to be ~ 1.0 %.

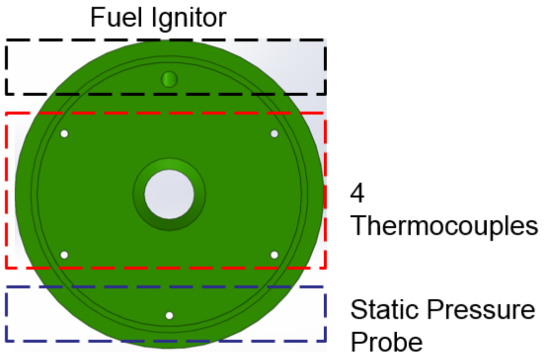

Figure 2.7: Bulkhead instrumentation placement schematic

The pressure vessel that the liner is mounted in has optical access on all four sides, with four quartz windows with dimensions 205 x 110 x 50mm, as shown in Figure 2.6. Prior to entering the test section, the pressurized, preheated air passes through the swirler depicted in Figure 2.6 (right), following a design from [144]. As shown in Figure 2.6 (right), air travels through two separate swirler passages. The air exits the nozzle with an average bulk velocity of 65–85m/s, depending on operating conditions (see Table 2.3). The airblast filming nozzle consists of 6 x 0.18mm diameter holes that spray radially into the flow.

The fuel of interest was pressurized using nitrogen, and the fuel flow was regulated by adjusting the fuel line pressure using a pressure regulator. Fuel flow rates were measured using an AW-Lake positive displacement gear meter. The estimated uncertainty in overall fuel/air ratio (ϕ) is ~ 3%. In between test conditions, when no liquid fuel was flowing but the combustor was hot, the fuel injector orifices were purged using nitrogen flow to prevent fuel coking. Fuel temperatures were measured at the fuel inlet depicted in Figure 2.6 and varied between 300 and 305K.

The data presented here are at various conditions and with two fuels indicated in Table 2.3 below. The C-5 fuel is a high aromatics content fuel (decane+trimethylbenzene), with a low boiling point and low viscosity compared to Jet-A [148].

The flow field for this high pressure reacting spray fuel implementation of the high shear swirler is similar to that of the gaseous version discussed above. However, we defer discussion of the flow features to the Results chapter, since this work is partially focused on developing experimental methods and data interpretation to reveal internal combustor physics.

Table 2.3: Operating conditions for the high pressure jet fuel high shear swirler.

Case	p [bar]	T_{ph} [K]	ϕ	Nozzle velocity [m/s]	Fuel
1	2.1	450	0.38	78	Jet-A
2	3.7	451	0.38	65	C-5
3	3.4	446	0.61	78	Jet-A
4	3.6	570	0.63	85	Jet-A
5	5.2	459	0.47	75	Jet-A
6	2.3	563	0.45	83	Jet-A
7	1.7	572	0.65	112	Jet-A
8	1.8	578	0.95	105	Jet-A
9	5.1	577	0.49	88	Jet-A

2.2. Optical Diagnostics Setup

In this section we detail the experimental setup of several optical diagnostic techniques employed in the present studies. We list the experimental techniques used on each experimental facility. The descriptions are meant to be stand-alone for convenience – this applies also for recurring techniques. Note that an uncertainty analysis subsection is added for the premixed and liquid fuel high shear swirler facilities.

2.2.1. Atmospheric CH_4/Air Annular Counter-Swirling Nozzle

We used particle image velocimetry (PIV) to obtain a two-component velocity field along the y-z plane (see Figure 2.1), aligned with the diameter of the nozzle.

High speed PIV

The laser sheet entered the experiment through the top window in a plane, termed the y-z plane, parallel to the axial flow direction. The field of view (FOV) was 1.8 D_0 tall by 3.0 D_0 wide. Seeded image pairs were obtained with a 10kHz PIV system, using a Litron Nd:YLF dual head laser with a wavelength of 527nm and a pulse energy of 1mJ. Aluminum oxide particles, 1 – 2μm in diameter, were introduced to the preheated air flow upstream of the settling chamber. The seeding air flowrate was about ~ 5% of the total air flow, a value that was optimized to produce sufficiently seeded reactant and product regions. A combination of spherical and cylindrical lenses was used to make a 1.0mm thick laser sheet. The illuminated particles were imaged with a Photron SA1.1 camera at 10,000 frames per second, with 704 by 400 pixel resolution resulting in 150μm per pixel. 10,000 PIV image pairs were acquired with a dual-pulse separation time of 18μs. The instantaneous velocity vector fields were calculated from the paired images in the DaVis 7.2 software, using multiple passes with decreasing interrogation window size. The final pass window size was 16 pixels by 16 pixels, yielding a spatial resolution of about 2.4mm.

2.2.2. Atmospheric CH4/Air High Shear Swirler

Simultaneous high speed stereoscopic PIV (sPIV), OH radical planar laser induced fluorescence (PLIF) and OH* chemiluminescence provide simultaneous, time-resolved 3-component velocity, OH qualitative concentrations, and line-of-sight qualitative heat release. The OH field marks the reaction zone as well as hot combustion products and is used for flame visualization in the measurement plane. The line-of-sight OH* chemiluminescence provides flame visualization integrated across the entire combustor volume. Table 2.4 lists the imaging optics specifications and settings, including cameras and intensifiers. As seen in the table, the two PIV cameras were run at 20kHz, while the PIV and PLIF lasers, chemiluminescence cameras and intensifiers were run at 10kHz. The camera memory limited the simultaneous number of processed frames (after creating

PIV image pairs) to 9701. The combined measurements are used to extract the hydrodynamic strain component of flame stretch at the leading edge of the aerodynamically stabilized flame (see Figure 2.5).

Table 2.4: Acquisition optics specifications

Function	Camera	Intensifier	Intensifier Gate	Lens	Frame Rate/ Resolution	f/D Setting	Spectral Filters
sPIV, C1	Photron SA5	N/A	N/A	Tokina AT-X M100 100mm, f/D=2.8	20kHz/512x512 pixels	4.0	Band-pass: 527/20nm FWHM, T=97%
sPIV, C2	Photron SA5	N/A	N/A	Tokina AT-X M100 100mm, f/D=2.8	20kHz/512x512 pixels	4.0	Band-pass: 527/20nm FWHM, T=97%
OH-PLIF, C3	NAC GX-3	Lambert HiCATT (25mm)	100ns	Cerco, 45mm, f/D=1.8	10kHz/416x416 pixels	1.8	Band-pass: 320nm/40nm FWHM (T=80%)
OH*, C4	Photron SA1	LaVision IRO (18mm)	5.0μs	Cerco, 45mm, f/D=1.8	10kHz/768x768 pixels	1.8	Band-pass: 320nm/40nm FWHM (T=80%)

Stereo PIV

For the stereo PIV, the combustor flow was seeded with aluminum oxide particles, which were illuminated by a laser sheet. The scattered light was imaged by two high speed cameras, arranged in a stereoscopic configuration, see Figure 2.8. The resolution of the camera system is approximately 100mm/pixel. A LaVision dual-plane dot pattern target was used to register the cameras, and LaVision's self-calibration was applied to compensate for slight misalignment between the laser sheet and the registration target facial plane. Lastly, the PIV images were processed using LaVision DaVis 8.1. Pre-processing included sliding minimum subtraction to reduce background interference and particle size normalization to enhance the PIV code sensitivity. Multiple passes with decreasing interrogation windows sizes starting at 96x96 pixels and ending at 24x24 pixels were used, and the final window size weighing function was an optimized non-uniform function. The final pass overlap was 50%, yielding a PIV vector spacing of 0.58 mm.

The PIV light source was a dual head, frequency doubled DPSS Nd:YLF 527nm laser, with measured pulse energy of approximately 2mJ. A dual pulse separation of 10μs was used. A laser sheet about 2.0 mm thick and 3.70 D_0 wide is formed using a combination of cylindrical lenses. The sheet enters through the top of the combustor and was aligned in the *r*-*z* direction to within 0.5mm to the combustor centerline as shown in

Figure 2.8. The field of view (FOV) was 1.5 D_0 tall by 1.6 D_0 wide. Data are acquired at 10kHz, 10,000 frames at a time. Imaging was performed with Photron SA5 cameras, at a resolution of 896 by 848 pixels, equipped with an f = 100mm AT-X M100 Tokina lens set to f/D = 4.0. Flame emission was cutoff with a laser band-pass filter centered at 527nm. The PIV cameras were configured for dual side scatter, angled at about 45 degrees relative to the laser sheet to provide equal displacement sensitivity in-plane and out-of-plane due to the high swirl number of the flow. Scheimpflug adaptors were used to tilt the camera lenses' focal planes. Note that there is some uncertainty of a few degrees in this angle due to the pivot center of the Scheimpflug adaptor not coinciding with the lens optical center for rotation in the horizontal plane.

The seeding system consisted of a passive agitation, swirling seeder, which operated with about 5% of total air flow. 1–2μm aluminum oxide particles were chosen to provide satisfactory run times before window clouding was a major issue. Effective particle size is expected to be somewhat larger due to agglomeration in the seeder and connecting lines, but great care was taken to minimize this by reloading the seeder with freshly dried seed every two hours of experiment time. The seed was dried in a 500K oven for 24 hours before use. The seeding particles were injected about 3.0m upstream of the nozzle exit plane, to ensure uniform seeding density. The quartz tube was cleaned after each run. A discussion of measurement uncertainties is presented in Uncertainty Analysis below.

OH-PLIF

For the OH PLIF, a DPSS Nd:YAG laser was run at 10 kHz, with a pulse energy of 4 mJ, to pump a tunable wavelength Sirah Credo dye laser, which was then frequency-doubled to yield a UV pulse energy of about 200μJ. The ~ 566nm output of the dye laser has a specified line width of 0.08cm^{-1}, and the doubled output linewidth is expected to be $\sqrt{2}$ broader or ~ 0.11cm^{-1}. The UV excitation was tuned to the OH $Q_1(6)$ transition of the (1,0) vibrational branch, corresponding to a wavelength of 282.93nm using a premixed stoichiometric methane/air test burner. The Q-branch provides the strongest fluorescence signals, and the $Q_1(6)$ line has weak temperature dependence. The PLIF sheet was aligned to the sPIV sheet, and had the same width, but was about 100μm thick.

A Photron SA-1 CMOS camera was coupled to a LaVision IRO high speed image intensifier, as listed in Table 2.4 and placed normal to the laser sheet as shown in Figure 2.8 (left). The intensifier allows for the collection of the UV light while also providing gating control to minimize interferences from flame emission. The intensifier gate was 100ns and was opened just before the rising edge of the excitation laser pulse. A 45mm, *f/D* = 1.8, UV camera lens was attached to the intensifier as shown in Figure 2.8 (left), and a 320nm band-pass filter with 40nm FWHM was placed in front of the lens. The approximate resolution of the camera system is 68μm/pixel.

OH Chemiluminescence*

For the OH* chemiluminescence measurements, a NAC GX-3 high speed CMOS camera was coupled to a Lambert HiCATT high speed image intensifier as listed in Table 2.4. Identical to the PLIF camera/intensifier assembly, a 45mm, *f/D* = 1.8, UV camera lens was attached to the intensifier as shown in Figure 2.8 (left), and a 320nm band-pass filter with 40nm FWHM was placed in front of the lens. The OH* chemiluminescence camera/intensifier assembly was also placed normal to the laser sheet as shown in Figure 2.8 (left). The OH* chemiluminescence intensifier gate was 5μs and placed as shown in Figure 2.8 (right). The approximate resolution of this camera system is 117μm/pixel.

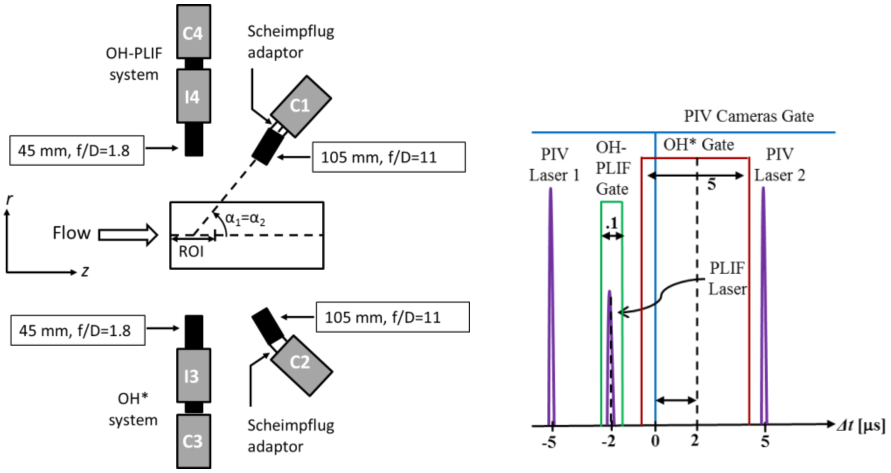

Figure 2.8: Left: sPIV/OH-PLIF/OH* camera configuration; Right: laser/cameras/intensifiers timing

Uncertainty Analysis

With a sheet thickness of 2.0mm, anticipated maximum momentum based swirl number S_m on the order of 1.0, nozzle velocity of 45m/s, and dual pulse separation of 10μs, the loss-of-pairs error due to out of plane motion is calculated to be less than about 22%, which is the worst case scenario, at the nozzle exit. This figure greatly improves away from the nozzle exit plane as the azimuthal velocity quickly decays.

Velocity resolution with LaVision's sub-pixel interpolation capability down to 0.1 of a pixel is 1.0m/s given by the camera magnification of 100μm/pixel and pulse separation of 10μs. Axial velocity loss-of-pairs error is minimized by using multiple passes with decreasing interrogation window size, allowing much longer axial displacements than a single pass algorithm of a typical interrogation window size.

Radial velocity bias due to centrifugal forces is reduced by the use of the small 0.5–1.0μm particles. Reference calculations for a simple annular swirler geometry can be found in [35].

We briefly discuss the frequency response of the particles next. Following equations 24b and 25 from Mei [149], the cutoff frequency, $f_{\text{cut-off}}$, defined based on 50% energy following, is given by eqn. (1):

$$f_{cut-off} \approx \frac{\nu}{\pi}\left(\frac{St_{cut-off}}{R}\right)^2 \tag{1}$$

where the cutoff Stokes number, $St_{\text{cut-off}}$, is given by eqn. (2):

$$St_{cut-off} \approx \left[\left(\frac{3}{2\rho^{1/2}}\right)^c + \left(\frac{0.932}{\rho - 1.621}\right)^c\right]^{1/c}, \quad c = 1.05, \quad \rho = \frac{\rho_p}{\rho_f} \tag{2}$$

where ρ_p refers to the seed particle density and ρ_f to the fluid density, showing that f_cutoff scales linearly with kinematic viscosity, and inversely with the square of the particle diameter. The cutoff frequency or 1.0–2.0μm particles, was calculated to be 4-17kHz for 450K preheat. These values increase by a factor of more than 10 in the products due to the much higher kinematic viscosity.

Lastly, we discuss uncertainties in the flame stretch rate computations from PIV gradients. The computation of derivatives in general amplifies noise. To calculate the axial velocity gradients, we use a central limit scheme, so that no bias is introduced and only random error. This error affects the uncertainty of the estimate of the mean flame stretch (the standard error of the measurement). The standard error for a Gaussian distribution is given by $SE_{\bar{\kappa}_{s,le}} = \sigma_{\kappa_{s,le}} \big/ \sqrt{N}$, and is 650 [1/s] for case 1 and 330 [1/s] for case 2.

2.2.3. High pressure Jet Fuel High Shear Swirler

Simultaneous high speed stereo PIV, OH-PLIF and fuel-PLIF were obtained to produce a three-component planar velocity field, along with flame location from the OH-PLIF and fuel droplet location and qualitative concentration from the fuel-PLIF. Post-processing is required (detailed in the Data reduction chapter) to separate the OH-PLIF and fuel-PLIF fields. Later in post-processing liquid and gaseous phase velocity fields are extracted using simultaneous information from the PIV and fuel-PLIF.

High Speed Stereo PIV Setup

The PIV light source is a dual head, frequency doubled, diode pumped, solid state, Nd:YLF 527nm laser, with 2mJ pulse energy, pulse duration of about 200ns, and dual pulse separation of 16μs. A 2.0mm thick and 3.70 D_0 wide laser sheet was formed using a combination of cylindrical lenses. It entered through the top of the combustor and was aligned in the *r*-*z* direction to within 0.5mm to the combustor centerline as shown in Figure 2.9. The field of view (FOV) was 2.8 D_0 tall by 1.7 D_0 wide. Data are acquired at 5kHz, 7500 frames at a time. Imaging was performed with a 12-bit Photron SA5 cameras at 10kHz, at a resolution of 896×848 pixels, equipped with an f = 100mm AT-X M100 Tokina lens set to f/D = 11, and a final resolution of approximately 70μm/pixel. A band-pass filter centered at 527nm was used to reject flame emission. The cameras were installed in a side-scatter configuration and were angled at about 45 degrees relative to the laser sheet to provide equal displacement sensitivity in-plane and out-of-plane due to the high swirl number of the flow (see Figure 2.9), and Scheimpflug adaptors were used. Table 2.5 lists the imaging optics settings and specifications.

The seeding system consisted of a passive agitation, swirling seeder, which operated with about 5% of total air flow. The 0.5–1.0μm TiO_2 particles were dried in a 500K oven for 24 hours before use. Seed particles were injected about 1.8m upstream of the nozzle exit plane, to ensure uniform seeding density. The windows were cleaned after each run by inserting a cleaning wand with a wet towel head up the exhaust.

A LaVision dual-plane dot pattern target was used to register the cameras, and LaVision’s self-calibration was applied to compensate for slight misalignment between the laser sheet and the registration target facial plane. The PIV images were processed using LaVision DaVis 8.1. Pre-processing included sliding minimum subtraction to reduce background interference and particle size normalization to enhance the PIV code sensitivity. Multiple passes with decreasing interrogation windows sizes starting at 96×96 pixels were used, and the final window size weighting function was an optimized non-uniform function. For cases 1 and 2, the final window size was 32x32 pixels with an overlap of 75%, yielding a vector spacing of 0.57mm. For case 3, 24 by 24 pixel final windows with 50% overlap were used, yielding a vector spacing of 0.86mm.

High Speed OH/fuel-PLIF Setup

A DPSS Nd:YAG laser was operated at 5kHz, with5 mJ pulse energy, to pump a Sirah Credo tunable dye laser, which was then frequency-doubled to yield a UV pulse energy of 300mJ. The ~ 566nm output of the dye laser has a specified line width of 0.08cm^{-1}, thus the frequency-doubled output linewidth is ~ 0.11cm^{-1}. The UV excitation was tuned to the OH $Q_1(6)$ transition of the (1,0) vibrational branch in the *A*-*X* system using a test burner, corresponding to a wavelength of 282.93nm. The Q-branch provides strong fluorescence signals, and the $Q_1(6)$ line has a weak temperature dependence. The PLIF sheet was aligned to the sPIV sheet, and had the same span, but was about 100μm thick. The laser sheets were coincident to better than ¼ of the PIV sheet thickness, or 0.5mm.

The imaging cameras (12-bit Photron SA1 and NAC GX-3) were coupled to a high speed image intensifier and placed normal to the laser sheet on either side of the rig, see Figure 2.9a for a schematic and Figure 2.9b for a photograph. Note the cylindrical polar coordinate system (r, θ, z) established in the figure. The intensifier allows for the collection of the UV light while also providing gating control to minimize interference from flame emission. An f = 45mm, f/D = 1.8, UV camera lens was attached to each intensifier, and spectral filters were placed in front of each lens to maximize signal separation, while rejecting the excitation wavelength.

The spectral separation of the fluorescence signals is illustrated in Figure 2.10. As shown, the laser excitation is narrow-band (~ 0.11cm^{-1}), most of the OH fluorescence is concentrated within a 15nm band, centered around 308nm, corresponding to the (0,0) vibrational band, and the fuel fluorescence is broad, coinciding with the OH and extending well into the visible range. A 40nm FWHM bandpass filter, centered at 320nm was used in conjunction with a 15nm FWFM bandpass filter, centered at 315nm to optimize OH imaging. The narrower filter had significant transmission into the visible spectrum (above 550nm) and, thus, required use of the broader filter in series. A 305nm Schott glass long-pass filter was used to reject only the excitation light and optimize for the fuel-emission. Since the fuel-emission was much brighter than the OH-PLIF, rejection of the OH-fluorescence band was not required. The fuel emission camera captured some emission from the quartz tube in the form of horizontal lines, which are easily subtracted in image pre-processing.

The OH- and fuel-PLIF cameras used different intensifier gate settings as illustrated in Figure 2.11, to achieve temporal separation by taking advantage of the longer lived fuel fluorescence relative to shorter lived OH fluorescence. As the excitation duration (~ 10ns) is on the same order of magnitude as the fluorescence lifetime, and there is overlap between the time of fluorescence and excitation, the intensifier gate opened shortly before the laser pulse. To maximize OH-PLIF, the intensifier gate closed as early as possible without cutting off the OH (~ 10ns after the laser pulse center) in order to avoid signal from the fuel-PLIF tail. On the fuel-PLIF intensifier, the gate was ended 30ns after the laser pulse center in order to capture all of the fuel fluorescence. Both gates were 40ns long. Note in Figure 2.10 that the significant portion of the intensifier gates ahead of the laser pulse has no effect on the fluorescence and was required due to the minimum gate duration limit of the intensifiers (~ 40ns).

The approximate resolution of the camera systems are 117μm/pixel for camera C3 and 68μm/pixel for C4. Table 2.5 lists the imaging optics specifications and settings.

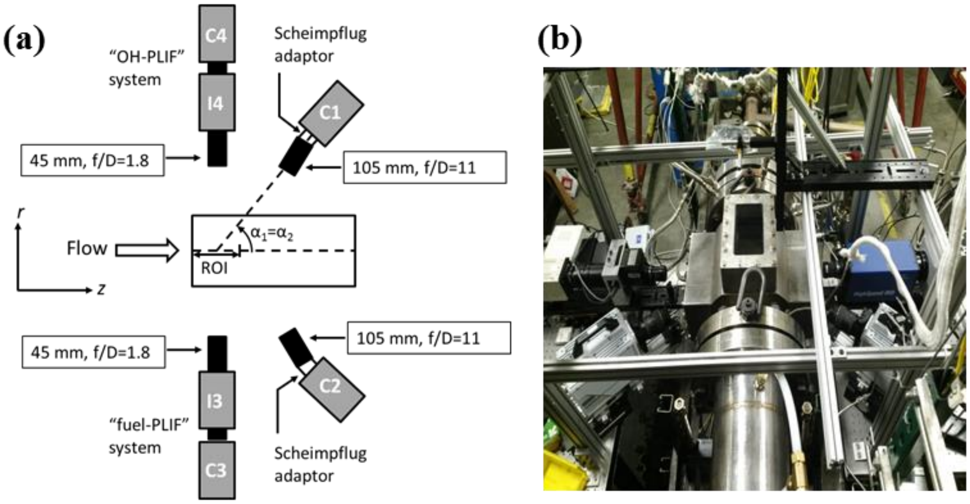

Figure 2.9: High speed sPIV and 2-Color OH-PLIF camera configuration. C1 and C2 are sPIV cameras, mounted at 45 degrees to laser sheet. C3 is the "fuel-PLIF" camera and C4 is the "OH-PLIF" camera, both coupled to image intensifiers.

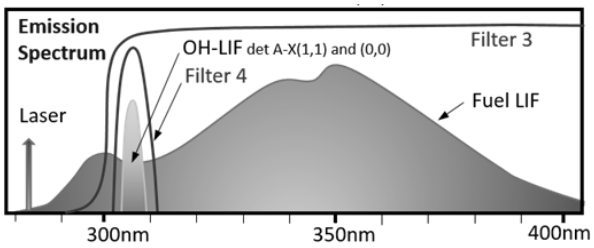

Figure 2.10: Use of spectral filters to partially separate OH and fuel-PLIF.

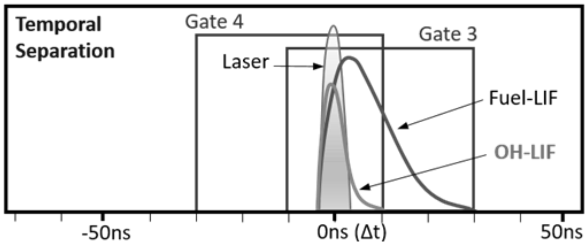

Figure 2.11: Use of intensifier gate timing to temporally separate fuel and OH-LIF signals.

Table 2.5: Imaging optics specifications and settings.

Function	Camera	Intensifier	Intensifier Gate	Lens	Frame Rate/ Resolution	f/D Setting	Spectral Filters
sPIV, C1	Photron SA5	N/A	N/A	Tokina AT-X M100 100mm, f/D=2.8	10kHz/896x848 pixels	4.0	Band-pass: 527/20nm FWHM, T=97%
sPIV, C2	Photron SA5	N/A	N/A	Tokina AT-X M100 100mm, f/D=2.8	10kHz/896x848 pixels	4.0	Band-pass: 527/2nm FWHM, T=97%
Fuel-PLIF, C3	NAC GX-3	Lambert HiCATT (25mm)	See Fig. 3	Cerco, 45mm, f/D=1.8	5kHz/512x720 pixels	1.8	Long-pass: 2mm Schott WG-305, T=92% above 370nm, O.D.>3.0 below 280nm
OH-PLIF, C4	Photron SA1	LaVision IRO (18mm)	See Fig. 3	Cerco, 45mm, f/D=1.8	5kHz/1024x1024 pixels	1.8	Band-pass: 320nm/40nm FWHM (T=80%) + 315/15nm FWHM (T=86%), range is up to 500nm

Uncertainty analysis

Loss-of-particle image pairs error can be problematic in swirling flows due their three dimensional nature. If the laser sheet is along the central plane of the combustor, as in the present study, the swirling component of velocity is out-of-plane. We use a thick laser sheet in order to control the loss-of-pairs error. With a sheet thickness of 2.0mm, anticipated S_m on the order of 1, and nozzle velocity of 65m/s, the loss-of-pairs due to out of plane motion is calculated to be less than about 50%, which is the worst case scenario, at the nozzle exit. This value greatly improves away from the nozzle exit plane as the azimuthal velocity quickly decays. The sheet was not made any thicker because increasing its thickness has the following effects: (1) reduction of the signal-to-background ratio for the scattered light from a given particle; (2) reduction of the correlation values computed by the PIV algorithm as the larger interrogation volume captures eddies which result in more complicated particle shift patterns; (3) the out-of-plane spatial resolution of the measurement decreases.

Note that in the raw PIV images most particles appear about 2-3 pixels in size, as a result of the optical system quality. It is important that particles are larger than 1 pixel to avoid pixel-locking error in the velocity computation, and to allow sub-pixel interpolation. Velocity resolution with LaVision's sub-pixel interpolation capability (0.1 of a pixel) is 0.45m/s given by the camera magnification of 72μm/pixel and pulse separation of 16μs. Axial velocity, U_z, loss-of-pairs error is minimized by using multiple passes with decreasing interrogation window size, allowing much longer axial displacements than a single pass algorithm of a typical interrogation window size.

Radial velocity, U_r, bias due to centrifugal forces is reduced by the relatively high preheat and further in the hot products, and by the use of the small 0.5–1.0μm particles. Reference calculations for a simple annular swirler geometry can be found in [35].

Following equations 24b and 25 from [149], see eqns. (1) and (2) above, the cutoff frequency based on 50% energy following for 0.5–1.0μm particles, was calculated to be about 17-67kHz for 450K preheat. The lower value provides a conservative estimate to allow for some seeding particle clumping in the seeder. These values increase by a factor of more than 10 in the products due to the much higher kinematic viscosity. The macro time scale corresponding to the nozzle diameter and average axial nozzle velocity, ranges from 180 to 310μs (5.5 to 3.2kHz), corresponding to the fastest and slowest nozzle velocity. The Nyquist frequency of the PIV acquisition is 2.5kHz.

CHAPTER 3

DATA REDUCTION AND SUPPORTING CALCULATIONS

This chapter is split into a section for each facility detailing corresponding data reduction and supporting calculations: Section 3.1 for the atmospheric gaseous fuel high shear swirler, and Section 3.2 for the high pressure jet fuel high shear swirler facilities. The gaseous fuel data used to study aerodynamically stabilized flames receive preprocessing of the flame images, flame edge extraction, flame leading edge conditioning, and conversion of statistics from Cartesian to polar coordinates, each discussed in a separate subsection. Furthermore, we consider flow, flame and measurement length and time scales; and calculate and measure flame stretch rate. The liquid fuel data needs special post-processing prior to analysis to extract internal combustion physics. We discuss in separate sections, the OH-PLIF/fuel-PLIF signal separation procedure, and the procedure check of robustness.

3.1. Atmospheric CH_4/Air High Shear Swirler

3.1.1. OH-PLIF and OH Images Preprocessing*

First, images from the OH-PLIF and OH* chemiluminescence cameras are pre-processed as follows:

Each flame image is corrected for the camera/intensifier/lens system response. We begin with a raw image from each camera, with a corresponding dark image, and flat field, described below:

I_{ij} = raw image array, where i is the index in x direction, and j is the index in y direction. i ranges from 1 to N, and j ranges from 1 to M

D_{ij} = dark image obtained with respective camera/intensifier/lens system.

F$_{ij}$ = raw flat field obtained for each camera/intensifier/lens system using a uniform (within 10%) light source. The flat fields are background subtracted and normalized using eqn. (3):

$$F_{ij,norm} = \left(F_{ij} - D_{ij}\right) \Big/ \max(F_{ij} - D_{ij}) \tag{3}$$

The background subtracted, normalized flat fields for the two cameras are plotted in Figure 3.1, with the region of interest (ROI) denoted by a dashed white line. The maximum variation within the ROI is about 25% for C3, the OH-PLIF camera, and 40% for C4, the OH* camera. Note that most of the variation is from the camera lens and intensifier relay optics, and C3 seems to have lower variation because the camera sensor is being centrally cropped.

Each data image is corrected for the camera/intensifier/lens system response given by eqn. (4):

$$I_{ij,\det.cor.} = \left(I_{ij} - D_{ij}\right) \Big/ F_{ij,norm} \tag{4}$$

Note that this is the final correction for OH* images.

The OH-PLIF camera is also corrected for the laser sheet profile obtained using a uniform concentration of acetone vapor, S$_{ij,raw}$. After background subtraction and flat field correction, the sheet profile is averaged along *y* (along *j*), to only capture variations normal to the direction of the laser sheet propagation, excluding laser depletion effects, using eqn. (5):

$$S_i = \frac{1}{N} \sum_{j=1}^{M} \frac{S_{ij,raw} - D_{ij}}{F_{ij,norm}} \tag{5}$$

Finally the 1-D laser sheet profile is normalized using eqn. (6):

$$S_{i,norm} = S_i \Big/ \max\left(S_i\right) \tag{6}$$

This is plotted in Figure 3.2. The final correction to the OH-PLIF images is given by eqn. (7):

$$I_{ij,cor.} = \left(I_{ij} - D_{ij}\right) / \left(F_{ij,norm} \cdot S_{i,norm}\right) \qquad (7)$$

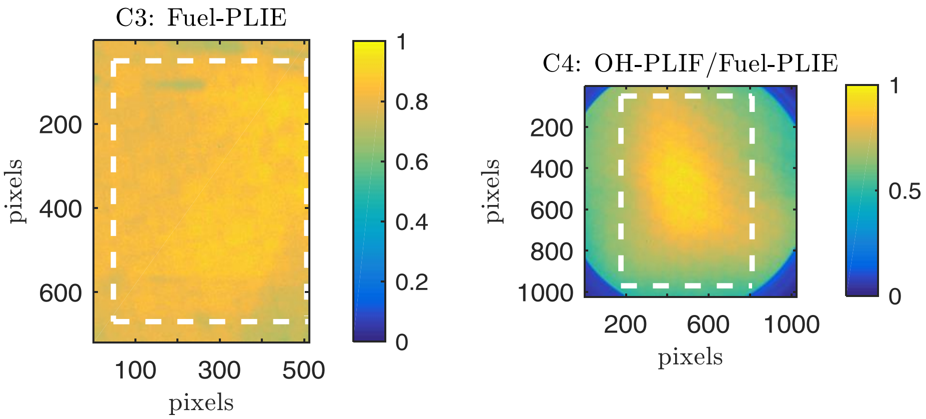

Figure 3.1: Flat field correction images with combustor dump plane drawn.

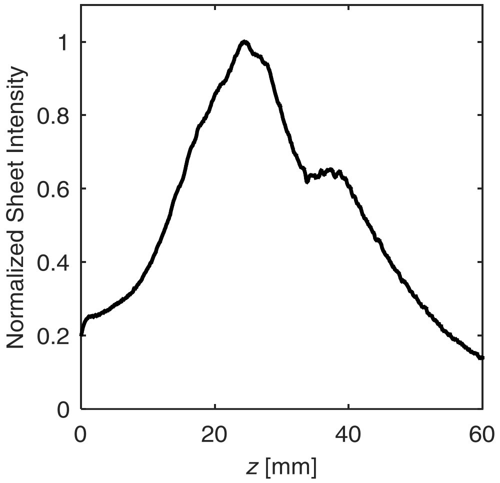

Figure 3.2: 1-Dimensional Sheet Correction profile obtained using acetone PLIF and averaged in the direction of laser sheet propagation. Includes flat field correction.

Lastly, image registration is performed on the PIV/OH-PLIF/OH* camera's and LaVision's self-calibration on PIV.

3.1.2. Flame Edge Extraction

Starting with the corrected OH-PLIF and OH* images as described above we apply the following:

1. *Edge preserving noise reduction:* 6x6 pixel median filter applied twice to OH-PLIF and OH* chemiluminescence images for noise reduction while preserving the edges.
2. *Edge sharpening:* Bilateral filter is applied to OH-PLIF and OH* chemiluminescence images for edge sharpening, while preserving the edges [150]. The filter spatial standard deviation is 3 pixels, and the normalized intensity standard deviation is 3.
3. *Edge extraction using intensity thresholds:* Planar and line of sight integrated edges must be extracted from the planar and chemiluminescence images. A large number of prior studies have described efforts for edge extraction of OH-PLIF images most commonly using intensity gradient-based methods [115, 151, 152], but also intensity-based [96] and Canny edge detection [153]. Next we describe the intensity-based thresholding approach used here.

Intensity histogram of the OH-PLIF and OH* images computed for all frames of a given run are shown in Figure 3.3 and Figure 3.4 respectively. Each histogram reveals two distinct populations, one corresponding to a weak background signal, and one corresponding to the OH-PLIF or OH* signal. These different populations can be seen more readily from the lower figure which plots the derivative. We will discuss this method in more detail, in the context of the three populations observed with the liquid fuel spray in section 3.2. In order to ensure that these different regions were not due to fundamentally different instantaneous images, histograms were also computed for smaller number of images which showed similar behaviors. The histograms of the OH-PLIF and OH* images from case 2 (45m/s) look qualitatively similar to histograms shown in Figure 3.3 and Figure 3.4 (case 1 at 70m/s). Two thresholds are defined which appear naturally from the inflection points of the histogram, as shown in Figure 3.3 and Figure 3.4. We call the first one the “background cut-off” and the second one the “signal cut-on”. We used the background cut-off for both OH-PLIF and OH* to denote detectable signal. The results are not very sensitive to this specific value; e.g., doubling the OH-PLIF signal cut-on threshold would move the edge by only about ~ 0.1mm, as the gradient is very sharp at the point of interest. While the OH* signal has a less sharp gradient, doubling the background cut-off threshold produces a shift in the OH* edge of ~ 0.3 mm. Using these thresholds flame edges are extracted from the OH-PLIF and OH* images as shown in Figure 3.6 and Figure 3.7.

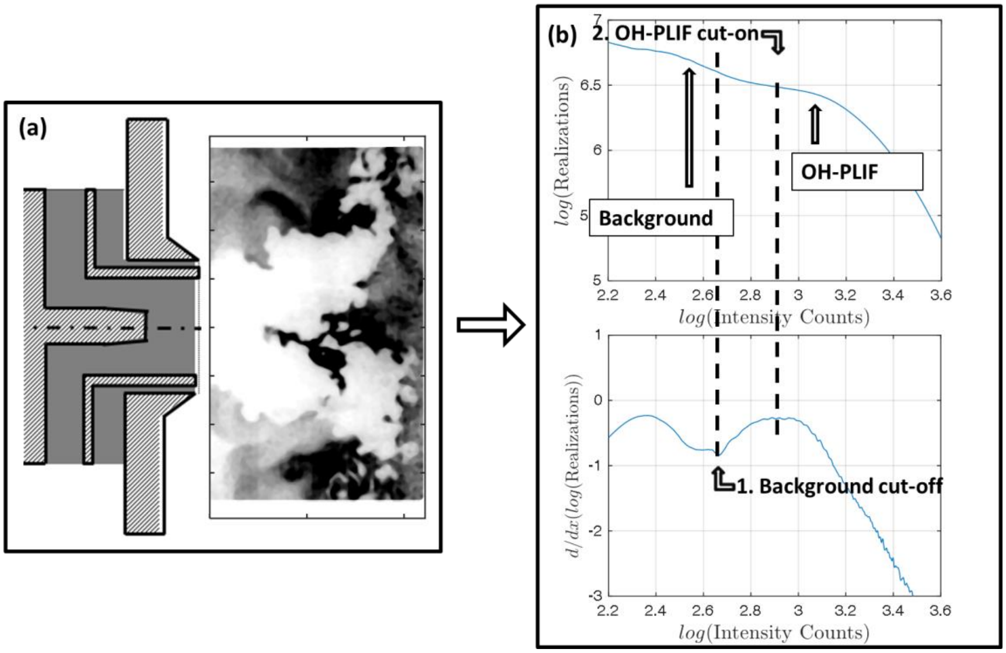

Figure 3.3: Extracting intensity thresholds from OH-PLIF histogram for case 1.

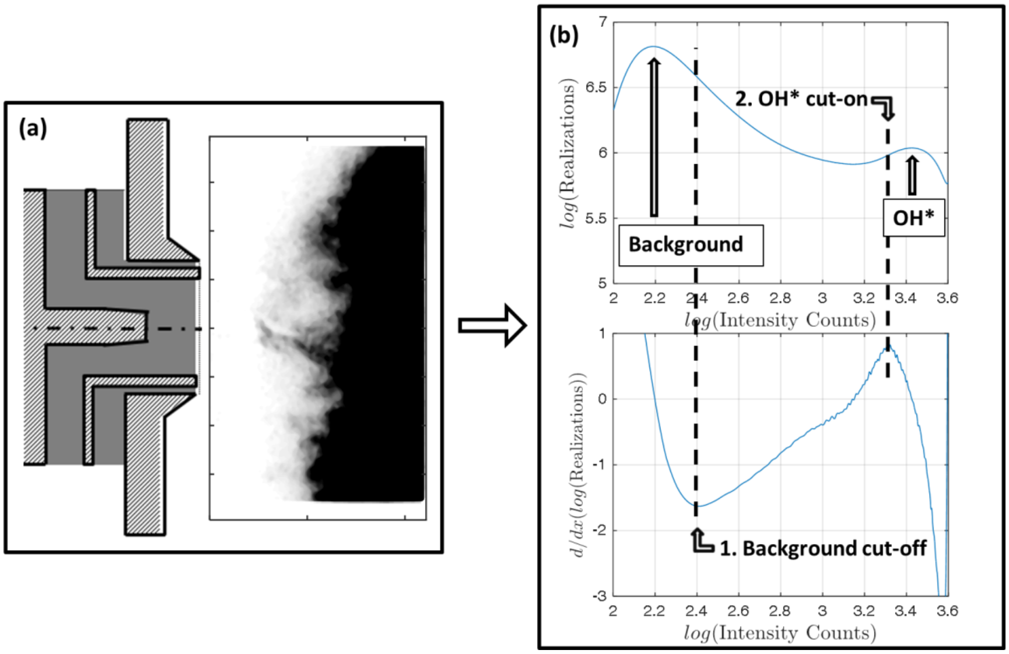

Figure 3.4: Extracting intensity thresholds from OH* histogram for case 1.

Extracting reaction progress variable fields

Reaction progress variable fields were computed by using the OH-PLIF-derived flame edge (per procedure above) to digitize the viewing area into values of zero for reactant and unity for products. These digitized images were then time-averaged to yield an average progress variable field, $\bar{p}_{OH}(r,z)$.

3.1.3. Flame Leading Edge Conditioning

In this section we outline how we identify and analyze characteristics of the flame dynamics at the global most upstream point, which we will refer to as the “flame leading edge”. As described earlier, in the quasi-steady limit, the leading edge plays a key role in stabilizing aerodynamically stabilized flames. In other words, the spatial location of every point on the flame downstream is controlled by the local balance between turbulent burning velocity and flow velocity at this point, at least under quasi-steady conditions. Our hypothesis here is that leading edge and, hence, the flow and strain characteristics at this point, are similarly important in general in controlling flame stabilization. However, because of the three dimensionality of the field and the fact that this point is continuously moving, the leading edge of the instantaneous front will not typically lie in the measurement plane, see Figure 3.5(b). In order to make measurements that are conditioned on the flame leading edge lying in the laser sheet, see Figure 3.5(a), the planar and simultaneous line-of-sight chemiluminescence images are compared. These line-of-sight images will necessarily capture the flame leading edge at every time instant. By comparing overlays of the planar and line-of-sight measurements, images can be identified where the leading edge coincides with the laser sheet within some specified tolerance (we use 1.0mm here, which is 1/2 of the PIV sheet thickness). The radial and axial location of the leading edge within the measurement volume is denoted as (R_{le}(t), Z_{le}(t)).

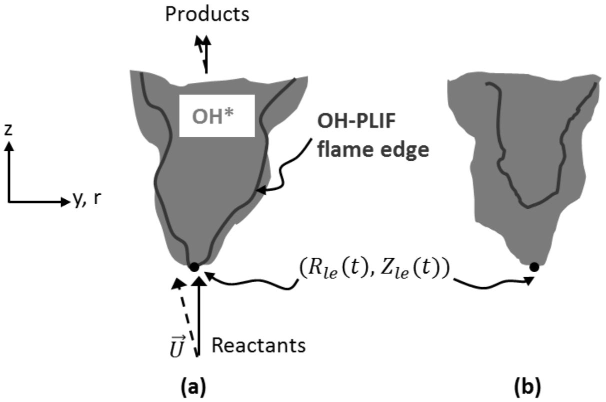

Figure 3.5: Planar interrogation of a 3-D flame surface. (a) Interrogation plane captures the leading edge ($R_{le}(z,t)$, $Z_{le}(r,t)$) of the flame surface. (b) The interrogation plane misses the leading edge of the flame surface.

Figure 3.6 provides examples from the data for case 1, showing a sequence of four images, 100 μs apart, with the in-plane velocity field indicated by red vectors, the OH-PLIF shown in blue, and the OH* shown in green. The axial velocity stagnation contour, $U_z(r,z,t)=0$, is shown with dotted red lines. Additionally, the OH-PLIF flame edge is indicated with yellow lines, the OH* flame edge with gray. Discussion of the flame edge extraction procedure is given later. In this frame sequence, the flame leading edge is passing through the laser sheet in images (b) and (c), but does not coincide with the measurement plane in images (a) and (d). In a similar fashion, four consecutive images are shown in Figure 3.7 for case 2. Here the leading edge is passing through the laser sheet only in image (b).

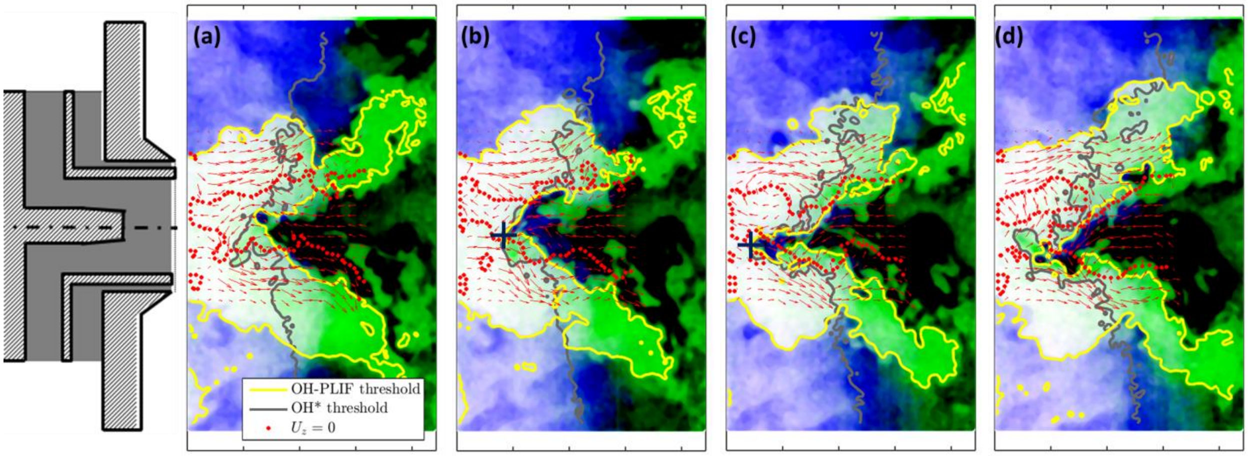

Figure 3.6: Sequence of four images 100 μs apart from case 1, at 70 m/s, showing the flame leading edge (marked with "+") passing through the laser sheet in images (b) and (c), and *lying outside* in (a) and (d). Blue OH-PLIF signal and green OH* signal with 3-component PIV data are shown. Yellow lines are the OH-PLIF flame edges, and blue lines are the OH* flame edges. Dotted red lines denotes the axial velocity stagnation isocontour ($U_z(r,z,t)=0$).

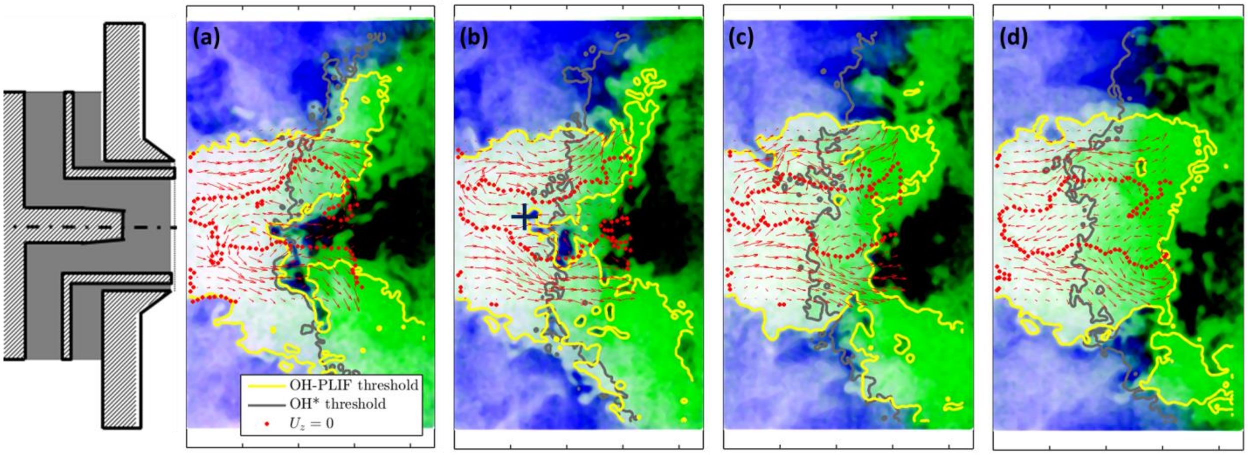

Figure 3.7: Sequence of four images 100 μs apart from case 2, at 45 m/s, showing the flame leading edge (marked with "+") passing through the laser sheet in image (b), and *lying outside* in (a), (b) and (d). Blue OH-PLIF signal and green OH* signal with 3-component PIV data are shown. Yellow lines are the OH-PLIF flame edges, and blue lines are the OH* flame edges. Dotted red lines denotes the axial velocity stagnation isocontour ($U_z(r,z,t)=0$).

The rest of this section explains the procedure for extracting these flame features from the raw images. The following post-processing steps are performed next:

1. *Composite image construction:* In order to visualize the simultaneous OH-PLIF and OH*, false color composite images are constructed, showing OH-PLIF in blue and OH* in green; see Figure 3.6 and Figure 3.7. The OH-PLIF flame edge is shown in yellow and the OH* in gray.
2. *Masking of outer shear layer flame edges*: The outer shear layer flame edges are usually upstream of the central flame and are removed using a static mask.
3. *Condition frames on capturing global most-upstream point:* This is the key step in this study. The most upstream edge of the flame is identified by retaining frames where the most upstream OH-PLIF and chemiluminescence edge points lie within 1mm of each other, as long as they are at least 3 mm downstream of the combustor dump plane to avoid laser scattering from the metal surface. Leading edges that are < 3mm constitute 2% of the retained images for case 1, and do not occur for case 2. The bias introduced to the axial flame leading edge location by this filtering step is very small (1/4 of PIV vector spacing). The images in Figure 3.6 (b) and (c) (case 1) and Figure 3.7 (b) (case 2) are images retained for subsequent analysis of the flame leading edge. Figure 3.8 shows a sample of four typical conditioned frames containing the flame leading edge for case 1. Only the flame edges are shown, and the flame leading edge is marked with "+". We note that the PIV measurements have coarser spacing than PLIF, and we wish to reactant-condition the flame stretch computations (see section 1.1.6). Therefore, we shift the flame leading edge obtained from PLIF upstream by half of a PIV window size (580 μm) and select the nearest PIV position.
4. *Outlier detection and removal:* The automated conditioning step (6) removes most (but not all) frames in which the flame leading edge is clearly not in the laser sheet, and has been verified to keep all potentially good ones, but final manual sorting is

required. For case 1, about ~ 10% of the frames are selected by this algorithm for manual consideration. Of these candidate images, approximately ~ 27% showed clear coincidence of continuous OH PLIF and OH* edges and were retained for the quantitative analyses described in the next section. These 271 unambiguous conditioned frames constituted ~ 2.8% of all acquired frames for this case. There was some ambiguity in classifying 71% of the candidate images, as they showed complex topologies such as multiple islands or pockets of OH. An example showing two such cases is shown in Figure 3.9 (a, b). Both images show that the most upstream point of the OH PLIF consist of islands which are separate from the main flame. These images are not considered further for this study. The remaining 2% contained frames in which the leading edge was not associated with the VBB and appeared to be associated with the OSL, as in Figure 3.9 (c, d). The case 2 frames were considered in a similar fashion with 4.1% of the images being unambiguously conditioned and retained for subsequent analysis.

Table 3.1: Percentage total frames selected by the automated algorithm as candidate frames. Percentage split into retained and ambiguous frames. Ambiguous frames further split into flame broken into "islands", and ambiguous, merged ISL/OSL flame structure.

			Candidate Split Ratio [%]		
Run #	# Images	Candidate Ratio [%]	Retained	Leading edge is Island	Leading edge not associated with VBB
1	9699	9.7	27	72	0.6
2	9699	14	31	68	0.8

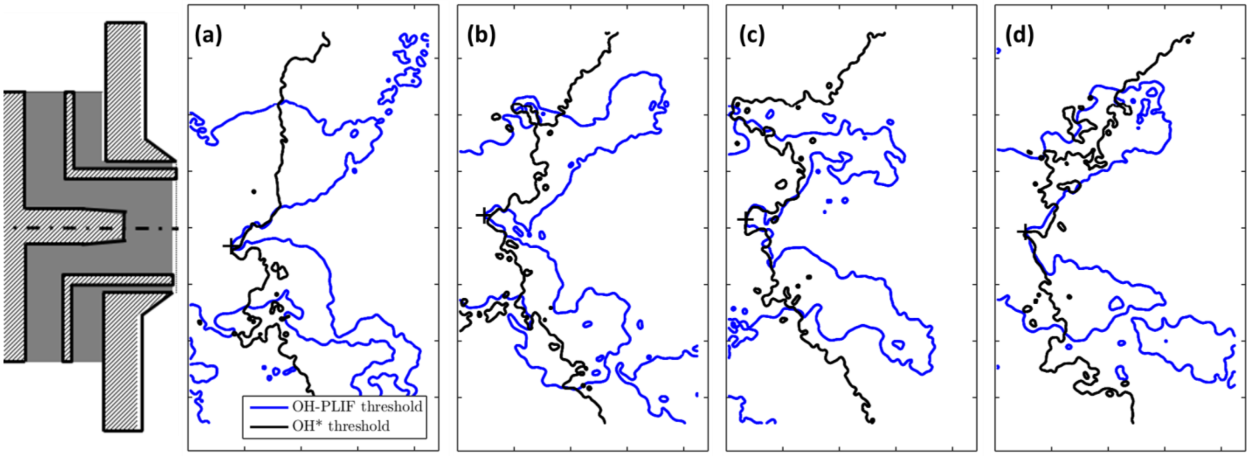

Figure 3.8: Sample conditioned frames containing the flame leading edge for case 1.

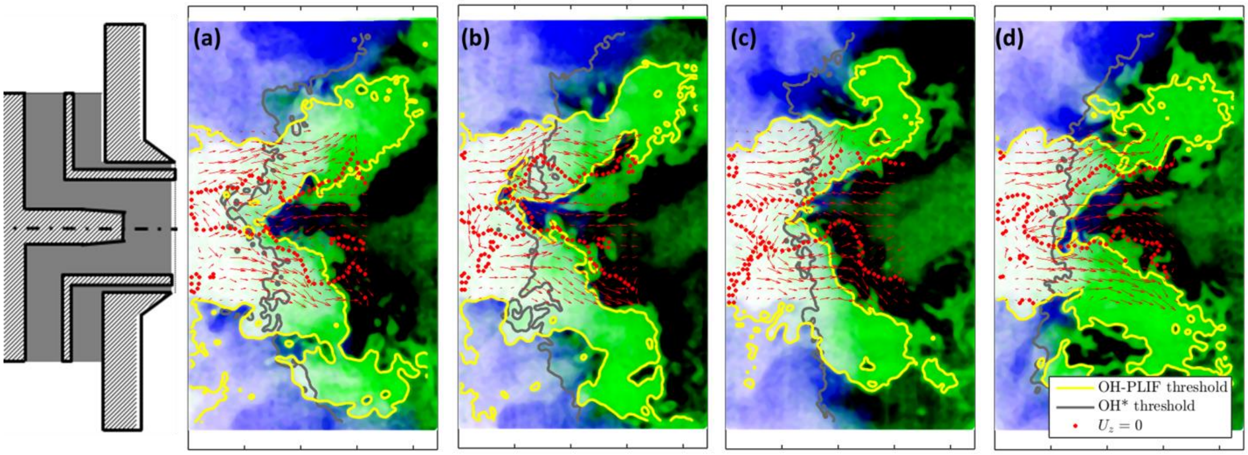

Figure 3.9: OH-PLIF and OH* overlays showing example images from case 1 that were not retained for the analysis for reasons discussed in the text: (a, b) islands disconnected from main flame, (c, d) leading edge not associated with VBB, as denoted by the OH* edge (gray line).

3.1.4. Converting Statistics from Cartesian to Polar Coordinates

Figure 3.10 shows the geometry and overlays two coordinate systems, a Cartesian (x-y) coordinate system and a polar (r-θ) coordinate system. Note that the measurements are extracted in a Cartesian coordinate system. Given the circular, axisymmetric nature of this combustor geometry, it is useful to convert the measured statistics to a polar coordinate system, which allows us to determine various statistics conditioned on radial location, r, in the combustor. Since the data are acquired in a volume defined by the laser sheet which is approximately constant thickness, the probability of the extracted flame leading edge lying within a given azimuthal arc angle decreases with increasing *r*. If uncorrected for, this effect leads to bias errors in estimates of the various quantities considered later, as they will necessarily be weighted toward the value of that quantity at smaller *r*. Hence, there is a need to convert the Cartesian probability distribution function (PDF) of the flame leading edge, $f_{Y_{le},C}(Y_{le})$, to the radial PDF, $f_{R_{le},r}(R_{le})$, and consequently correct the PDFs of all variables, x_{i}, i.e.: $U_{\mathrm{z,le}}(\mathrm{t})$, $\kappa_{\mathrm{s,le}}(\mathrm{t})$, etc.

This correction is straightforward. Referring to Figure 3.10, the number of realizations in a Cartesian differential element, $N_C(x_i, r)$, for any variable x_{i} is multiplied by its corresponding radius to obtain the corrected "number" of realizations in a polar element, $N_p(x_i, r)$, using eqn. (8):

$$N_p(\kappa_s, r) = 2\pi \cdot r \cdot N_C(\kappa_s, r) \tag{8}$$

Given this information, the polar cumulative density function (CDF), $F_{x_i}(x_i)$, is given by eqn. (9):

$$F_{x_i}(x_i) = \sum_{x_{i,arb}=-\infty}^{x_i} \sum_{r} r \cdot N_C(x_{i,arb}, r) \Bigg/ \sum_{x_{i,arb}=-\infty}^{\infty} \sum_{r} r \cdot N_C(x_{i,arb}, r) \tag{9}$$

The PDF is now obtained by taking the derivative of the CDF with respect to x_{i}: $f_{x_i}(x_i) = d/dx_i \, F_{x_i}(x_i)$. Intuitively, for $x_{\mathrm{i}} = R_{\mathrm{le}}$, the PDF correction from Cartesian to polar is given by eqn. (10):

$$f_{R_{le},p}(R_{le}) = f_{R_{le},C}(R_{le}) \cdot R_{le} \Bigg/ \sum_{R_{le}} f_{R_{le},C}(R_{le}) \cdot R_{le} \cdot \Delta R_{le} \tag{10}$$

Equations (8-10) all imply that the polar coordinate system correction multiplies the PDF's of variables by zero when $r = 0$, which causes a complex propagation of error in estimates of sample statistics, $x_{\mathrm{i}}(r)$, as well as introducing a bias in estimates of the mean. This error propagation depends on the relative shapes of the radial distribution of the given variable, $r|x_i$, and the variable's PDF, $f_{x_i,C}(x_i)$, and is highest when $r = 0$

coincides with a peak in the PDF. The PDF of the raw radial leading edge location, x_i = R_{le}, $f_{Y_{le},C}(Y_{le})$ has a peak at r = 0, while none of the other variables have r = 0 coinciding with a peak in the PDF. Therefore we discuss the error computed for $f_{Y_{le},C}(Y_{le})$, as the upper bound. A Monte Carlo simulation was used to numerically obtain the difference error between the true mean of a population of flame leading edge radial positions in r-θ space and a reconstructed population distribution obtained by applying the geometric correction of eqn. (10) to the distribution of the variable as "measured" within an imaginary interrogation volume. We fitted a normal distribution to the estimated distribution of $f_{R_{le},p}(R_{le})$, and used it to generate flame leading edge location points within a physical r-θ space corresponding to a cross-section of the combustor. We then selected a Cartesian sample defined by the laser sheet thickness, δ_{ls}, and the height of the interrogation window. The population size was set to produce a Cartesian sample size of roughly N = 300. Finally, we repeated the simulation M = 10,000 times. This Monte Carlo simulation showed that this radial correction procedure adds a bias error to the mean of 2.5%, and an additional random error with a standard deviation of 3.4%. This former value compares to a 2.8% uncertainty in the estimate of mean due to the sample size (standard error for a Gaussian distribution, $SE_{\bar{R}_{le}} = \sigma_{R_{le}} \big/ \sqrt{N}$).

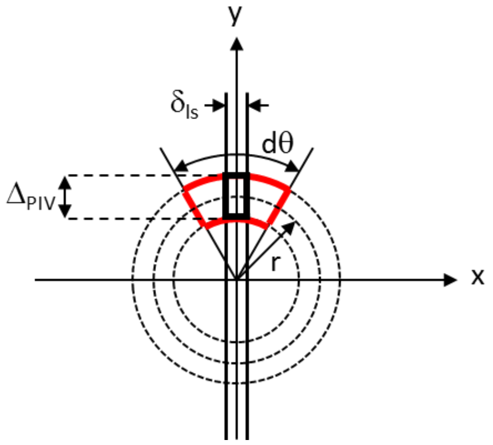

Figure 3.10: Geometry of the PIV interrogation window defined by the laser sheet and a hypothetical polar interrogation window. This view is from inside the combustor, facing the nozzle

3.1.5. Flow, Flame and Measurement Length and Time Scales

In order to understand the measurement spatial resolution limitations, we consider next various flow, flame and measurement length scales. For reference the Reynolds number, $\mathrm{Re} = UL/\nu$, in the products is between 2000 and 3000 depending on the nozzle velocity, where U is the reference velocity, L is the reference length, and ν is the kinematic viscosity. Figure 3.11 plots all three of these for case 1. Starting with flow length scales and working from largest to smallest (right to left on the plot), the largest one is the reference length L, taken here to be the approximate nozzle diameter, D_0 on the order of 2 cm. Next we estimate the longitudinal integral length scale of turbulence, l_{11}, from the PIV data by integrating the average from all frames of the two-point normalized correlations, f(r), over the entire spatial coordinate, as given by eqn. (11):

$$l_{11} = \int_0^\infty f(r)\,dr \tag{11}$$

The two-point normalized correlation, f(r) [154], is defined by eqn. (12):

$$f(r) = \frac{\langle U_z(z) U_z(z+r) \rangle}{\langle U_z^2 \rangle} \tag{12}$$

where r is displacement, and $\langle\ \rangle$ denotes expected value. The range of displacement was from 0 to 30mm, which also defined the upper limit of integration in eqn. (11). For cases 1 and 2, l_{11} was about 9mm both inside and jet and in the IRZ. Near the shear layers it was about 2mm. The flame leading edge is in the IRZ so we take l_{11} as 9mm. Finally we obtain a rough estimate of the Kolomogorov turbulence scale of smallest eddies [154], η, using eqn. (13):

$$\eta = \left[\frac{\nu^3}{\varepsilon}\right]^{1/4} \tag{13}$$

where the turbulence dissipation rate, $\varepsilon = u'^3 / l_0$, u' is the RMS velocity, and l0 is the length scale of the largest eddies, estimated using l_{11} from above. The Kolomogorov scale, η, estimated in this fashion is about 10μm. Next we have the laminar flame thickness, Δ_L=300μm, computed above for moderate values of stretch onto the flow scales. We need to consider how the turbulence intensity or eddy turnover velocity at these length scales compares to S_L. One way is to compute the Gibson scale, $l_G = S_L^3 / \varepsilon$, which is the length scale of eddies with sufficient turnover velocity to perturb the flame, i.e. S_L. Since l_G is estimated as 1 μm, we conclude that eddies of any size can push the flame front around. Lastly, we consider the measurement resolution, on the order of 100μm for PLIF (Δ_{PLIF}) and 1mm for PIV (Δ_{PIV}). Since our limiting accuracy is 1mm for PIV, it is clear that the measurement cannot resolve the flame thicknesses, Δ_L, and only some of the inertial range of turbulence.

To characterize the response of the flame to the flow perturbations and see how that compares with the data Nyquist frequency, we plot the inverse of these time scales, which are characteristic frequencies, in Figure 3.12. The sampling frequency, f_s, is 10000Hz, with a corresponding Nyquist frequency, f_N, of 5000Hz. We characterize the flame response time as a chemical time computed as S_L/δ_L. Since the temperature, T_{ph}, and fuel/air equivalence ratio, ϕ, are the same between cases 1 and 2, assuming a constant flame thickness, δ_L, the flame chemical frequency is in both cases estimated to be 1800Hz. In comparison, the flow characteristic frequency is estimated as U/L, and as such is higher at the higher velocity case 1, at 3500Hz, vs. 2000Hz for the lower velocity case.

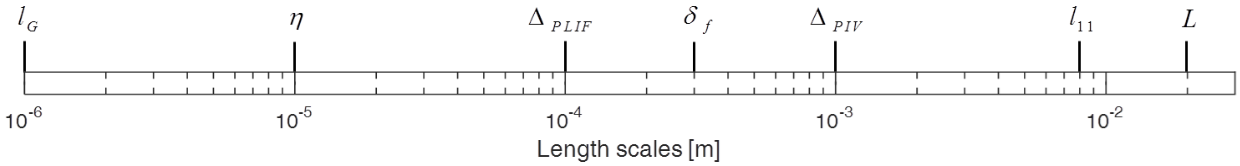

Figure 3.11: Measurement, flow and flame length scales.

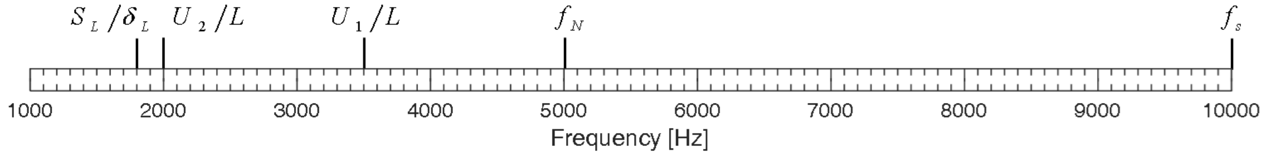

Figure 3.12: Flame and flow characteristic time (frequency) relative to data acquisition rate.

3.1.6. Flame Stretch Rate Estimation and Calculations

One of the key quantities considered at the flame leading edge is the local stretch rate, and its value relative to calculated extinction levels. The flame stretch rate is a function of the spatial location within the flame where it is estimated at and is a difficult quantity to measure, and so this section describes the issues associated with estimating it, as well as laminar flame calculations.

The general expression for flame stretch rate is given by eqn. (14):

$$\kappa = \underbrace{-n_i n_j \frac{\partial u_i}{\partial x_j} + \frac{\partial u_i}{\partial x_i}}_{\kappa_S} \underbrace{-S_L\left(\frac{\partial n_i}{\partial x_i}\right)}_{\kappa_{curv}} \tag{14}$$

where κ_s denotes flame stretch due to flow strain and κ_{curv} to flame curvature. Evaluation of κ_s, in general, requires measurements of velocity derivatives in three directions, something not possible with a single sPIV measurement plane. Planar measurements can be used to resolve the two dimensional component of hydrodynamic strain term κ_s at all points on the flame – note that discussion of the relation of two-dimensional stretch rate to the actual stretch rate is discussed extensively in the literature [65, 93, 155-158]. However, at the flame leading edge, $(R_{le}(t), Z_{le}(t))$, the two-dimensional measurement can resolve the full hydrodynamic strain term at an isosurface upstream of where significant density gradients occurs. This can be seen from eqn. (14). At the conditioned flame leading edge, the local flame unit normal vector is given by $\hat{n} = -\hat{n}_z$, and the only hydrodynamic term remaining is $\kappa_s = -dU_z/dz + (dU_x/dx + dU_y/dy + dU_z/dz)$. If this quantity is evaluated in a region just upstream of the flame where the density is constant, the bracketed terms add up to zero using the incompressible continuity equation $dU_x/dx + dU_y/dy + dU_z/dz = 0$. In this case, $\kappa_{s,incomp}(z,t) = -dU_z/dz$, and significantly, this quantity is fully resolved by the two-dimensional measurement. The flame stretch measurements we report use this incompressible flame stretch estimate.

The curvature stretch component, κ_{curv}, cannot be resolved with a planar measurement, but it is small relative to κ_{s}. The flame surface is nominally curved away from the reactants, and hence, the curvature component of stretch, $\kappa_{\mathrm{curv,le}}$, is positive. As an estimate of a typical value, we multiply S_{L} (~ 1m/s) by a characteristic radius of curvature (~ 5mm) from Figure 3.6 and Figure 3.7, to obtain $\kappa_{\mathrm{curv,le}}$ ~ 200 [1/s]. As will be presented in the results section, the average measured flame leading edge hydrodynamic strain, $\overline{\kappa_{s,le}}$ ~ 10,000 [1/s] for the high premixer velocity case 1, and ~700 [1/s] for the slower case 2.

Laminar stretched flamed calculations provide useful reference flame velocity and stretch rate scales. A convenient model problem for stretch computations is a symmetric opposed jet premixed flame, which is representative for an aerodynamically stabilized flame. We note that for a lifted shear stabilized flame, non-adiabatic conditions, as well as products mixing with the reactants, alter the flame properties and warrant modifications to the opposed jet problem [93]. Figure 3.15 shows a calculation, obtained using detailed kinetics of symmetric opposed flow premixed flames, using CHEMKIN OPPDIF [93]. GRI 3.0 mechanism was used for transport coefficients, thermodynamic properties and chemical kinetics. The flame stretch is calculated with respect to some isosurface. As discussed above, this isosurface is often chosen near the leading edge of the flame where the density change is negligible. For an opposed jet flame, assuming incompressible flow, the stretch rate is given by eqn. (15):

$$\kappa_{s,incomp} = -\frac{\partial U_z}{\partial z} \tag{15}$$

If the isosurface at which flame stretch is calculated lies inside the flame where the gas density, ρ, is not constant, the stretch rate is given by the "compressible form" in eqn. (16):

$$\kappa_s = -\frac{\partial U_z}{\partial z} - \frac{U_z}{\rho}\frac{\partial \rho}{\partial z} \tag{16}$$

Figure 3.15(a) plots the flame stretch, $\tilde{\kappa}_s(z)$, OH mole fraction, $\tilde{\chi}_{OH}(z)$, and axial velocity, $\tilde{U}_z(z)$ profiles (the tilde indicates that the variable is normalized by its maximum value). We have also plotted for reference the flame stretch at each location, showing its actual value and its value assuming an incompressible flow, $\tilde{\kappa}_{s,incomp}(z)$. In the coordinates of Figure 3.15(a), z = 1 mm corresponds to the opposed jet stagnation plane. Note the monotonically decreasing axial velocity, except for the jump due to heat release in the flame reaction zone near z = 0.9mm. The OH mole fraction rapidly jumps from zero also near z = 0.9mm and indicates the flame reaction zone. Upstream of the reaction zone, $\kappa_{\mathrm{s,incomp}} = \kappa_{\mathrm{s}}$, as is to be expected. Note that the reaction zone thickness for the flames of Figure 3.15 is ~ 100μm, and the PIV resolution, Δ_{PIV}, is ~ 1mm. Hence, these internal flow adjustments are spatially filtered in the PIV measurements.

The PIV velocity flame stretch estimate is based upon a central difference gradient, using one interrogation window before and after the interrogation window, which lies upstream of and adjacent to the flame edge, as determined by the OH. Because of the coarseness of the PIV with respect to the flame thickness (a large viewing window was needed because of the significant flame motion), there was concern about the sensitivity of the estimated flame stretch rate with respect to the location at which the derivative was estimated. For this reason, we performed two different sensitivity studies. First, flame stretch statistics were also compared by calculating the velocity derivative at an interrogation window centered one cell upstream, as well as one cell downstream of its nominal position. The resulting PDF's for both cases are shown in Figure 3.13. It is apparent that the PDF's do not change qualitatively for both cases. For case 1, shifting the interrogation window upstream decreases the mean stretch value, $\overline{\kappa_{s,le}}$, by 40%, while shifting it downstream increases $\overline{\kappa_{s,le}}$ by 30%. For case 2 the mean stretch value remains the same within 10%. Neither of these changes is sufficiently large to alter the flame stretch conclusions described later.

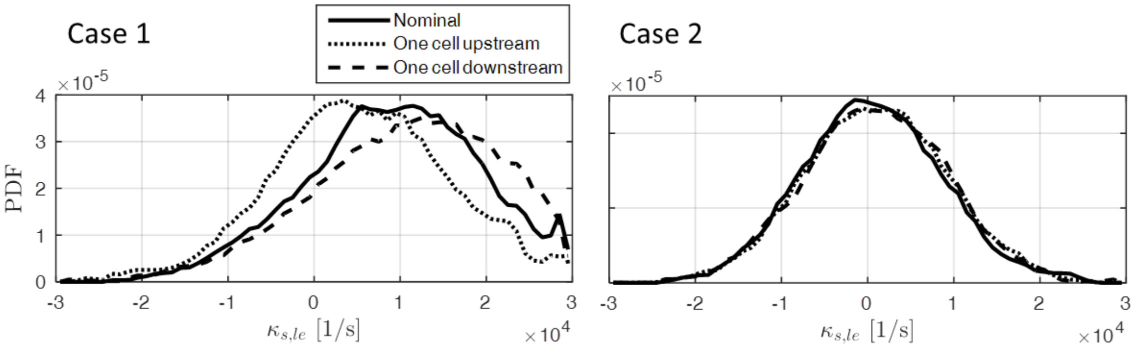

Figure 3.13: Sensitivity of flame leading edge hydrodynamic strain rate PDF, $f_{\kappa_{s,le},p}(\kappa_{s,le})$, to shifts in the interrogation window for cases 1 and 2.

Second, we checked the sensitivity of the flame stretch average to PIV resolution by artificially decreasing the resolution by factors of 2, 4, and 8, using a sliding spatial filter, for the central difference estimate of dU_z/dz at the flame. For case 1, $\overline{\kappa_{s,le}}$ changed by less than 4% for interrogation windows of 2X and 4X, and dropped by 19% for 8X. As expected the (root-mean-square) RMS of $\kappa_{s,le}(t)$ dropped with increasing filter width, by about a factor of three for both cases.

Third, we check the response of the local maximum of the axial profile of the axial velocity gradient near the flame leading edge to increasing width of an averaging filter applied to the velocity data. As the gradient of axial velocity in the vicinity of the flame leading edge is positive and high but often near constant for several interrogation windows, its maximum represents the measurement's ability to pick out sharp gradients. We computed the average local maximum of axial velocity gradient across 10 frames which show monotonic behavior. The results are plotted in Figure 3.14; a filter width of 1 corresponds to the raw, unfiltered data. As expected the local gradient maximum drops sharply with filter width. An exponential function is fitted to the data, and extrapolating to a filter width of "zero" indicates that the gradient is ~ 25% higher. Of course, in reality increasing the measurement resolution would allow resolving smaller scales, but this result provides significant confidence in the measured value providing a useful representative flame stretch value.

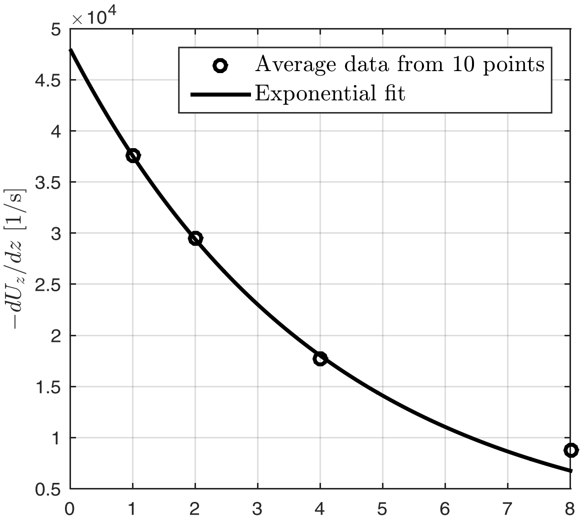

Figure 3.14. Extrapolation of exponential curve fit to gradient maximum near flame leading edge vs. filter width to estimate true maximum gradient. Filter width of 1 corresponds to the raw PIV gradient calculation. The extrapolation point of filter width zero corresponds to true flow gradient before beign spatially filtered by the measurement volume. Gradient maximum was selected from 10 representative data points in which the gradient had monotonic behavior near the flame leading edge for at least 8 filter widths.

Having considered the issues of estimating flame stretch, we next consider a reference extinction value for the flame stretch. Since the stretch rate varies through the flame, this requires calculation of a reference location. A convenient reference location for the flame stretch calculation is the edge of the flame reaction zone, $\partial U_z / \partial z = 0$. We refer to the corresponding stretch rate as κ_s^{RZ}. Figure 3.15(b) illustrates the calculated effect of flame stretch on flame speed for the symmetric, opposed flow configuration. For this lean methane/air flame, positive flame stretch enhances the flame speed up to a turning point, after which increasing stretch further decreases the flame speed. Eventually, a critical value is reached at which the flame will extinguish, known as the extinction stretch rate, κ_{ext}^{RZ}. The figure shows that the maximum stretched laminar flame speed (more precisely, the displacement speed, which is the velocity at *z*, where $\partial U_z / \partial z = 0$) and extinction stretch rate are S_d = 102cm/s and κ_{ext}^{RZ} =2600 [1/s], respectively.

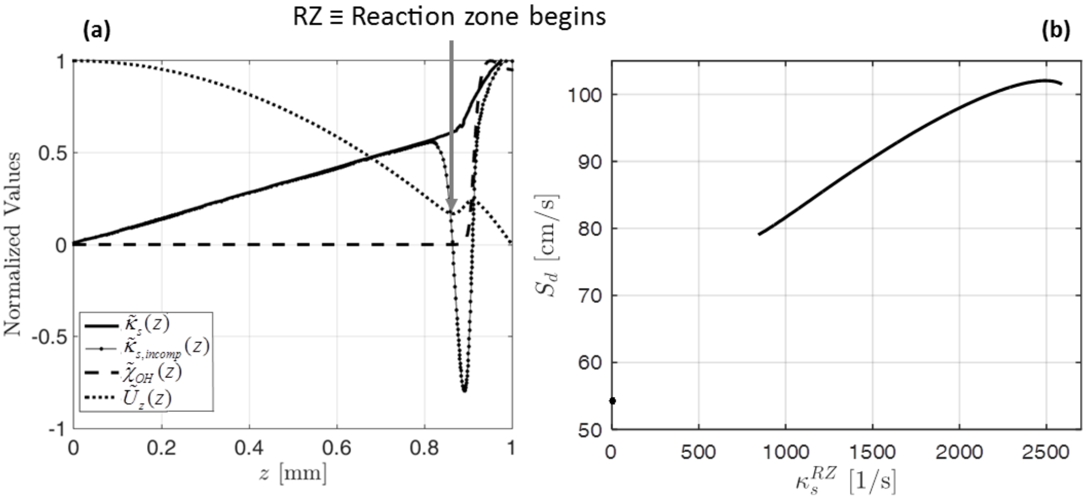

Figure 3.15: Laminar stretched flame computations for CH_4/air, ϕ = 0.60, T_{ph} = 566K. (a) Normalized flame stretch, incompressible term of stretch, mixture fraction of OH, and velocity. (b) Dependence of laminar flame speed on positive flame stretch; the unstretched laminar flame displacement speed, $S_{d,0}$ = 54.3cm/s, and extinction stretch rate at the edge of the flame reaction zone, κ_{ext}^{RZ} = 2600 [1/s].

3.2. High Pressure Jet Fuel High Shear Swirler

3.2.1. Spray OH-PLIF/Fuel-PLIF Signal Separation

This section describes the OH/fuel-PLIF signal separation procedure. Due to intrinsic non-linearity in the response of the intensifiers, especially with brighter signals, combined with temporal and spatial variations in the fuel emission spectrum, the fuel image cannot be directly subtracted from the OH + fuel image. As such, a more involved procedure is needed to differentiate fuel and OH signals. We use the fuel-PLIF to instantaneously identify regions of liquid fuel, which is then used to mask those from the OH-PLIF + fuel-PLIF camera images. We start with synchronized images from the mixed OH-PLIF + fuel-PLIF camera and the fuel-PLIF camera.

First the images from the two flame imaging cameras are corrected for the camera/intensifier/lens system response and laser sheet profile as described in detail above by beginning with a raw image from each camera: (1) dark image subtraction to compensate for the camera sensor offset at zero light; (2) flatfield correction for spatial variation in the optical system intensity response; (3) time-averaged laser sheet intensity correction using acetone-PLIF; (4) image registration and LaVision's self-calibration on PIV and PLIF cameras. Note that we do not correct for the absorption of the laser along its beam path. As also noted by Frank et al. in a series of OH-PLIF measurements in a liquid-fueled combustor at high pressure [120], the bottom halves of the OH/fuel emission images are significantly dimmer due to absorption of the laser energy (Frank et al. noted how this varied with pressure and fuel/air ratio). Consequently, the analysis here is confined to the top halves.

Next the fuel and OH + fuel images are post-processed to produce composite images revealing regions of OH, fuel and overlapping OH and fuel:

1. *Noise reduction:* 6x6 pixel median filter applied twice to the fuel and OH + fuel images for noise reduction while preserving the edges.
2. *Extraction of fuel-PLIF intensity thresholds:*

The detectable fuel-PLIF signal corresponds to liquid fuel (plus some background). The vapor fuel-PLIF is much dimmer and cannot be detected, mostly due to the difference in density. Let's assume that the liquid and vapor fuel have a low absorption so that there are no laser depletion effects. Furthermore, let's assume that the vapor fuel has similar absorption and fluorescence yield as the liquid, i.e. the vapor is not undergoing pyrolysis which could change those properties. Fluorescence scales linearly with the number of molecules, but inversely with the quenching. For example, the highest possible pure gaseous to pure liquid fuel density ratio for the cases considered here is about 2%. Regions of pure liquid are observed where there are fuel ligaments close to the nozzle lip. Quenching in the gas phase is higher, which reduces the gaseous fuel-PLIF yield, so that PLIF from gaseous fuel is lower than 2% of an equivalent volume of liquid fuel. Therefore, vapor fuel-PLIF does not register on the camera within the noise/background level of 10% of full scale for our 12-bit camera as shown in Figure 3.16 for case 1. The results are similar for all other cases.

An intensity histogram of the fuel-PLIF image (computed from the entire top half of the interrogation plane) computed for all frames of a given run is shown in Figure 3.16. The histogram reveals three populations, first corresponding to a weak background signal, second to weak fuel emission, and third to stronger fuel emission. These different populations can be seen more readily from the lower figure which plots the derivative. In order to ensure that these different regions were not due to fundamentally different instantaneous images, histograms were also computed for smaller number of images which showed similar behaviors. The histograms of the fuel images from all cases look qualitatively similar to histogram shown in Figure 3.16 (case 1 at 2.1 bar).

We speculate that the multimodal distribution of the "signal" portion of the fuel histograms is linked to the atomization properties of the subject airblast filming nozzle (see Figure 2.6 in section 2.1.3). Namely, the weaker signal population derives from a distribution of fine droplets with diameters smaller than the resolution of the imaging system (e.g., multiple small droplets in a given pixel), which cannot be resolved by the imaging system, while the stronger signal originates from a distribution of larger droplets or ligaments, which are readily resolved. Two thresholds are defined which appear naturally from the inflection points of the histogram, as shown in Figure 3.16. We call the first one the “weak cut-off” and the second one the “signal cut-on”. Note that for most cases the background and weak-fuel population are hardly distinguishable, so later we will use the “weak cut-off” as the detectable fuel threshold.

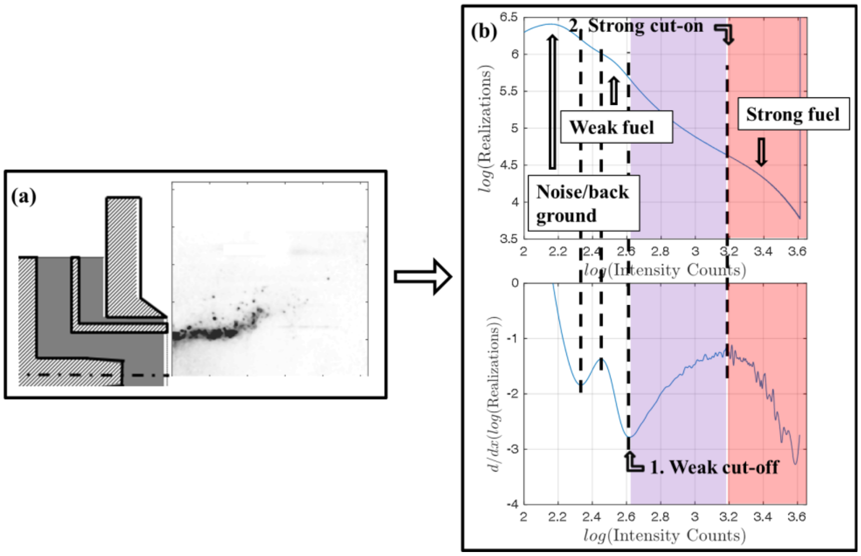

Figure 3.16: Extracting intensity thresholds from the fuel-PLIF histogram for case 1. Other cases produce similar results. (a): raw fuel-PLIF image. (b): fuel-PLIF intensity histogram and derivative.

To illustrate the plausibility of our population model above we simulated a background-polluted fuel-LIF signal population, composed of a sum of three normal distributions, with associated means and standard deviations, one for the background, fine droplets, and large droplets or ligaments. In reality the fuel-LIF signal will not be normally distributed even if the droplet diameter nearly is, because within our assumptions, LIF signal scales with the volume of fuel within the interrogation volume. However, normal distributions are simple and convenient, and work well for qualitative results. We plot the simulated fuel-LIF histogram in Figure 3.17 (left), next to the histogram from pre-processed data from case 1 (right) to show that this simple model captures the correct histogram shape. For reference, Table 3.2 lists the normal distribution parameters used: the mean, μ, standard deviation, σ, and relative amplitudes.

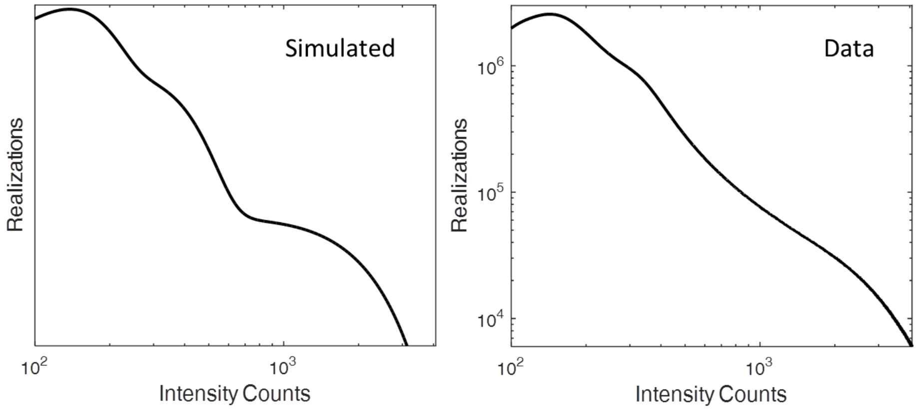

Figure 3.17: Simple simulated histogram of a background-polluted fuel-LIF signal compared to the histogram from data (case 1)

Table 3.2: Normal distribution parameters used in simulated histogram of Figure 3.17

	μ	σ	Relative Amplitude
Background	135	55	(1.0)
Fine spray	225	150	0.8
Ligaments	400	1200	0.4

3. *Composite image construction:* Next the information from OH and fuel-PLIF is combined into composite images. This process is illustrated in Figure 3.18. Using the thresholds obtained above from the fuel-PLIF image, we identify three regions within the OH + fuel camera field:

   a) Intensity is below the “weak cut-off”, so ***there is no detectable fuel*** on the fuel-PLIF camera. Therefore any signal on the OH + fuel camera is from OH.

   b) Intensity is larger than the “weak cut-off” threshold, but lower than the “strong fuel signal cut-on” threshold. There are smaller fuel droplets and OH or for short ***“fuel + OH”*** in this region.

c) Intensity is greater than the “strong fuel signal cut-on” threshold. Therefore, any signal in this region on the OH + fuel camera is dominated by fuel. Furthermore, in the midst of dense regions of spray, we expect no combustion, and therefore, no OH. We conclude there is ***fuel only*** in this region.

We construct composite false color images as in Figure 3.18 showing the “***fuel only” in red***, the “***fuel + OH” region in purple***, and “***no detectable fuel” in blue***. To check the sensitivity of these levels, we computed and compared the thresholds for light spray frames (one standard deviation dimmer than average) and heavy spray frames (one standard deviation brighter than average). The resulting “***fuel only”*** and “***elevated OH”*** thresholds were within 1 mm of each other on the flame images, while the ***“no detectable fuel”*** thresholds were within 3 mm of each other. See next subsection for more details.

4. *OH containing regions and flame location*: In order to extract information about the flame location we examine relative signal values from the masked OH-PLIF images (i.e., the region outside the “weak cutoff”, shaded in blue in Figure 3.18). Although the masked OH-PLIF images are not intended to provide OH concentrations, the histograms clearly indicates three different regions:

   a) Background emission signal

   b) Spatially diffuse, low level OH signal, predominantly found in the inner/outer recirculation zone (IRZ/ORZ) regions, and suggest that they originate from OH in recirculating product gases. This signal levels are roughly three times higher than the background.

   c) Elevated OH in regions. These elevated OH levels occur immediately outside the fuel jet and in plumes downstream of the flame zone which appear to be closely associated with the super-equilibrium OH in and downstream of reaction zones. The background subtracted signal levels are roughly twice the low level OH levels.

We note that lower part of the histogram, including the low level OH, are affected by the masking of the images as some OH is contained in the overlapping (purple) region and not retained by the masking. The elevated OH regions are defined from the inflection point shown in Figure 3.19 for case 1. As shown in Figure 3.19(b), the histogram shows three sub-population distribution peaks, corresponding to the three signal levels above. Again, the results are similar across all cases. Note that the ratios between the three signal levels noted above can be extracted from the histogram. As seen in Figure 3.19(b) the first derivative local maximum, identifies the cut-on point of the elevated OH level population. This threshold, shown in Figure 3.18 is later used to binarize masked OH-PLIF fields.

The signal-to-noise ratio SNR was calculated to be about 100 for the fuel signal in the fuel camera, and about 30 for the OH signal in the OH+fuel camera. The ratio was computed for a few representative frames as the mean over RMS, for a region of interest selected in a region of the camera view where the signal fuel/OH distribution appeared uniform. Since the laser UV output was modest, with pulse energies of 300 μJ, we anticipate higher SNR ratios can be achieved with higher pulse energies.

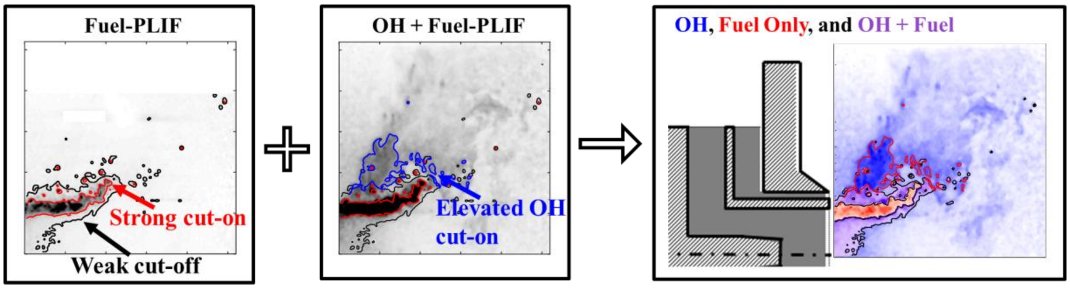

Figure 3.18: Constructing a false color OH/fuel-PLIF image for case 1. Thresholds lines from Figure 3.16 are used to split each frame into three regions and create a composite, false color image. The red region contains fuel only signal and is taken from the fuel-PLIF camera; the purple region contains OH + fuel and is taken from the OH/fuel-PLIF camera; the blue region shows only OH signal.

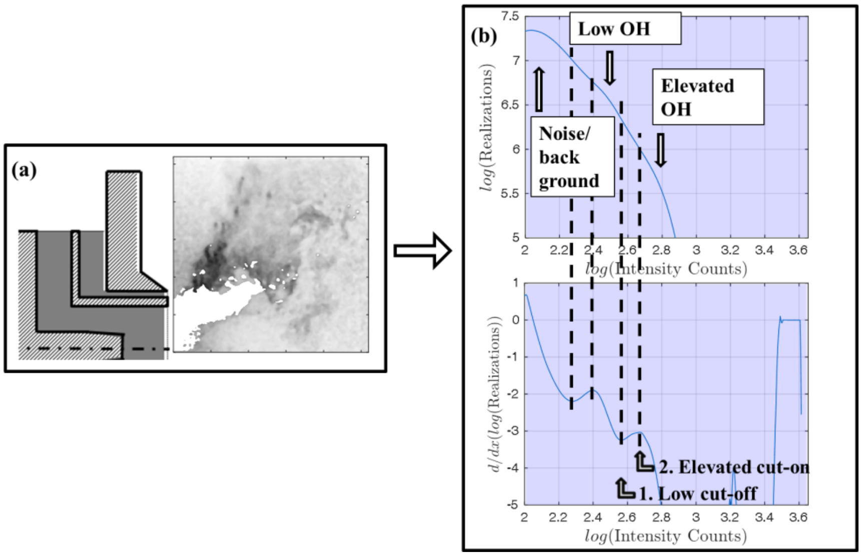

Figure 3.19: Extracting elevated level cut-on thresholds from the masked-OH-PLIF histogram for case 1. (a): OH-PLIF image, with fuel containing regions masked out using thresholds from Figure 3.16. (b): Masked OH-PLIF intensity histogram from full data set.

Lastly, the processed fuel-PLIF images and weak cut-off threshold, as illustrated in Figure 3.18, are used to separate the PIV vectors into those representing the gas or liquid/droplet velocity. As discussed in the introduction, this is necessary because large droplets do not follow the flow and so estimates of gas phase velocity that do not account for this will have bias errors. To estimate the minimum detectable liquid droplet diameter, we assume again that the liquid and vapor fuel have similar low absorptivity and similar fluorescence gains. The low absorptivity assumption allows us to ignore laser energy depletion. Then we compute the ratio of the fuel fluorescence camera detectable fuel signal level to the full scale level, where full scale corresponds to 100% liquid corresponding to large ligaments near the nozzle. We use that ratio to estimate the volume of the smallest detectable spherical droplet by scaling the volume of the interrogation volume defined by the region of interest in physical space of a camera pixel multiplied by the laser sheet thickness. For example, the smallest detectable droplets are estimated to be ~ 45μm in diameter, for which equations 24b and 25 from Mei[149], compute a cutoff frequency based on 50% energy following for 450K air as 54Hz.

Finally, we check the sensitivity of our full scale intensity calibration. If what we assume to be 100% liquid is 10% liquid, the droplet diameter estimate would be smaller by $10^{1/3}$ or ~ 21μm.

To illustrate the separation process, the blue region in Figure 3.18 is used as a gas phase mask, and the red region as a spray mask, while data in the purple region is not used. The velocity vector extracted from each interrogation window is then binned into gas or liquid phase, resulting in two non-equally spaced, velocity time series in each interrogation window. Depending upon spatial location, the relative fraction of velocity values binned as either gas or liquid phase varies significantly. Therefore, different regions of the averaged fields have different number of realizations, and we have removed time-averaged vectors with fewer than 2% realizations to reject non-converged data.

3.2.2. Checking Signal Separation Method for Robustness

The fuel spray originates at the dump plane, but the penetration of liquid fuel into the combustor varies in time, and the spray can move around. As indicated above, the histogram region of interest needs to fully encompass the bulk of the spray. This is important in order to make sure the histogram reflects all of the spray, and the histogram is unaffected by the spray's motion. However, the spray density is highly unsteady. The spray unsteadiness due to the nature of turbulent swirl combustion is exacerbated by the non-uniform pattern created by the six injection holes, and in some frames the spray is very light, while in others very heavy. Since we use intensity based thresholding, it is important to demonstrate the robustness of the current method. To determine the sensitivity of the threshold isolines to spray density, we computed them from the histograms of only dim frames, bright frames, and nearly average frames. We used the following criteria:

1) If total integrated intensity is more than one standard deviation above the average, then it is an *intense spray*
2) If total intensity is within ½ standard deviation of the mean, then it is an *average spray*
3) If total integrated intensity is less than one standard deviation below the average, then it is a *weak spray*

Figure 3.20 below illustrates the three classes of spray intensity. Figure 3.21 shows the region encompassed by the threshold isolines computed from histograms of the different classes of spray intensity frames for two instances. The thresholds change by as much as 25%, but because the intensity gradients near the threshold isolines are high, this translates to a low uncertainty of about 1 mm for the “***fuel only”*** and “***elevated OH”*** lines, and about 3 mm for the ***“no detectable fuel”*** line. This is indicated in Figure 3.21 by the maximum thickness of the black shading. As expected, the values thresholds for the nearly averaged frames were between the values of the thresholds for the dim and the bright frames.

Intense Spray Sample Frames:
$X > (\mu_x+\sigma_x)$

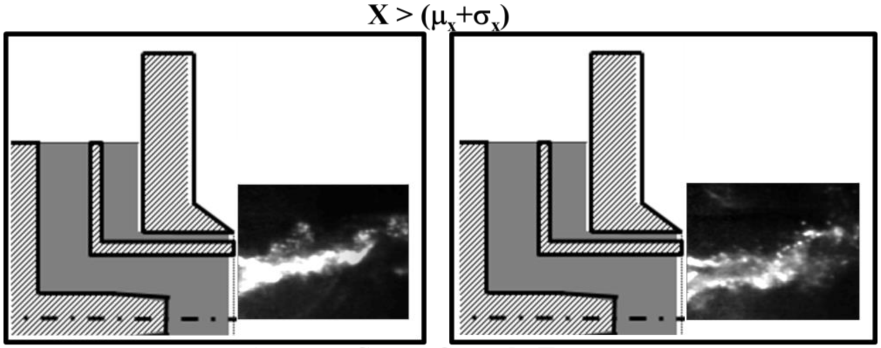

Average Spray Sample Frames
$(\mu_x-0.5\sigma_x) < X < (\mu_x+0.5\sigma_x)$

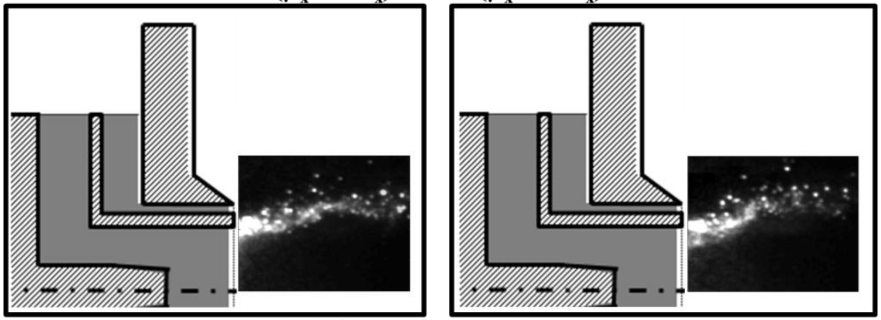

Weak Spray Sample Frames
$X < (\mu_x-\sigma_x)$

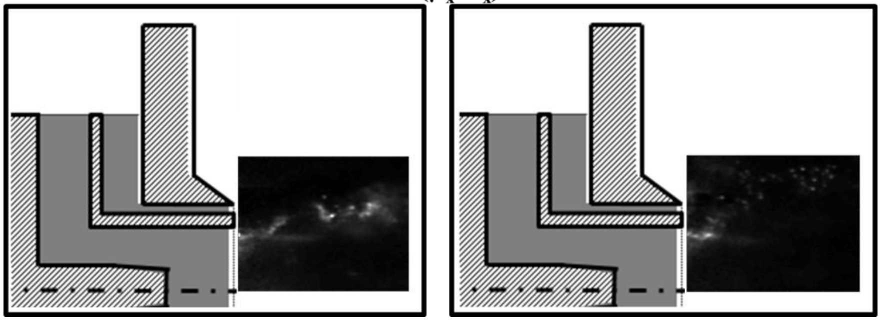

Figure 3.20: Representative intense, average, and weak spray frames. *X* is the integrated intensity of the region of interest.

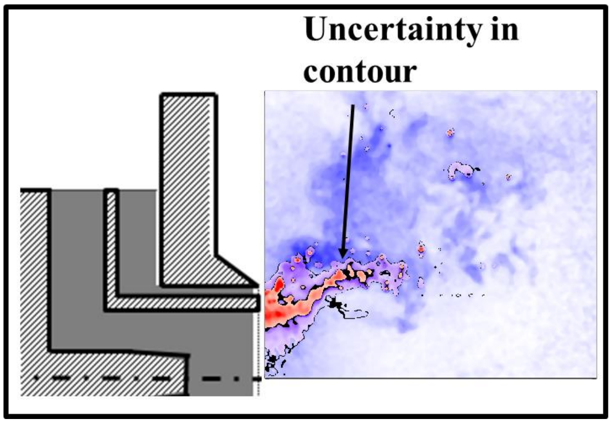

Figure 3.21: Estimated uncertainty region in the thresholding isolines produced by spray intensity variation. The shaded region is the region encompassed by the various thresholds indicated by the histograms of weak, average and intense spray frames. Maximum uncertainty is about 1mm for "*fuel only*" and "*elevated OH*" thresholds and 3mm for the *"no detectable fuel"*.

CHAPTER 4

RESULTS – PREMIXED FUEL

This chapter presents results and supporting calculations from our atmospheric premixed methane/air studies of first, vortex breakdown stagnation point precession effects on time-averaged quantities in Section 4.1, and second, flow field characteristics at the leading edge of aerodynamically stabilized flames in Section 4.2. Each section follows the layout from the scope of work in the Introduction, Background, Motivation and Scope Chapter 1. In brief summary, the studies in both sections are motivated by the presence of aerodynamically stabilized flames in swirling combustors with vortex breakdown. These flames' position is affected by large scale motion such as the commonly observed precession of the inner recirculation zone. In the case of vortex breakdown with an interior stagnation point, the flame follows the precessing stagnation point, which results in substantial differences between the instantaneous and time-averaged flow field and flame position. Section 4.1 focuses on these differences as they are key to predicting accurately quantities such as flame position, emissions and pattern factor for combustor design and comparisons with CFD. Furthermore, for vortex breakdown flow fields without interior stagnation points, the flames can be aerodynamically stabilized by instantaneous stagnation points created by large scale helical vortical structures in regions of the flow with negative time-averaged velocity. This gives rise to important questions such as why the flame does not flash back, and how important are effects such as flame stretch. Section 4.2 uses data from an aerodynamically stabilized flame by the atmospheric, premixed methane/air high shear swirler with a centerbody and centerline reverse flow on average to analyze the local flow field and flame stretch.

4.1. Precession Effects on the Relationship between Time-Averaged and Instantaneous Reacting Flow Characteristics

In this section we discuss the precessing flow field from the premixed, atmospheric methane/air dual annular counter-rotating swirler (DACRS) nozzle without a centerbody. We first develop a simple model of a precessing flow field characteristic of the one produced by the nozzle to build intuition. Then we develop reverse flow probability maps as a nonlinear averaging tool to supplement information obtained from conventional time averages. We illustrate precession of varying strength using reverse flow probability maps obtained from data and the model problem. Next we show how precession can create central regions of centerline positive flow, cause a substantial difference between the location of instantaneous and time-averaged stagnation points, and cause asymmetric time-averaged flow fields.

4.1.1. Model Problem of a Precessing Flow Field

In order to build insight into the effects of precession on the time-averaged flow field, this section presents a simple conceptual model of typical combustor flow fields with vortex breakdown – namely a region of positive axial flow, and a reverse flow region. The reverse flow region is precessing. The interface between these two zones is described by a surface in three-dimensional space, which discontinuously divides the regions of positive and negative axial flow. In reality, there will be some velocity transition region between the two zones which is not incorporated here for simplicity. The reverse flow region is demarcated by a paraboloid of revolution which precesses in a circular orbit and undulates axially.

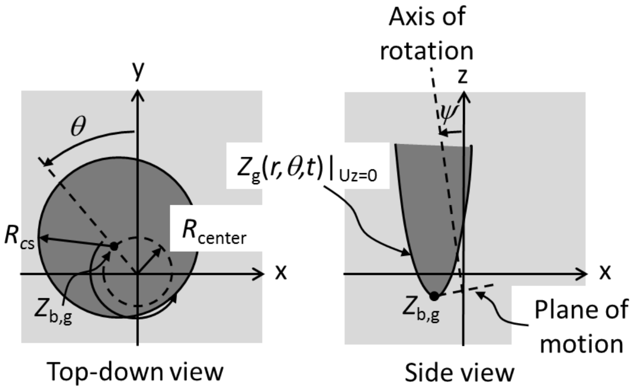

Figure 4.1: Two views of the two-zone flow model. Flow is in the *z* direction. Circular path of precession with radius R_{center}. Reverse flow is dark colored and positive flow is light. Axial velocity stagnation contour and most upstream stagnation point denoted.

Figure 4.1 introduces the geometry. The velocity is assumed to be spatially uniform in each zone, and equal to U_f (light) and U_b (dark). We introduce a backflow parameter as the backflow to forward flow ratio, $\beta = U_b/U_f$. At each axial location the precessing reverse flow region has a circular shape, with radius $R_{cs}(z)$, and the instantaneous center of this reverse flow region is given by the polar coordinates $R_{center}(z)$, and $\theta_{center}(z,t)$. In addition to precessing, the reverse flow region can also move up and down axially.

This model matches well the flowfield produced by the present atmospheric DACRS nozzle, as well as the nozzle from Basu's group [159] (see Figure 4.5). As discussed previously in Experimental Setup, Section 2.1.1., and shown in Figure 4.2 below, the DACRS nozzle produces positive flow along the centerline coming out of the nozzle by virtue of a central jet instead of a centerbody. This positive jet meets the reverse flow from the IRZ creating an interior stagnation point, which is subject to perturbations from a PVC and other disturbances. The IRZ of this facility precesses, observed as side-to-side motion in the radial-axial interrogation plane of our data (see Figure 4.6 ahead). The instantaneous (and time-averaged) axial velocity stagnation contours have parabolic shapes (see Figure 4.2 and Figure 4.6), with of course the instantaneous contours highly distorted by large scale dynamics.

We note that a combustor nozzle with a centerbody, either flush with the dump plane or recessed, will produce negative flow throughout the entire centerline. For the flush centerbody case, the centerbody wake would of course affect the flow near the centerbody. In such geometries the VBB stagnation point would be essentially “locked” in place, and the inner shear layers would be prominent and anchored to the centerbody. Furthermore, the time-averaged axial velocity stagnation contour would be no longer parabolic but constitute of two lines, parallel to the shear layers and also attached to the centerbody (see Figure 2.5 in Experimental Setup, section 2.1.2. and, Figure 4.13 and Figure 4.14 below for the HSS nozzle which has a recessed centerbody). The stagnation point would not be able to precess (much), but the IRZ would still be subject to helical disturbances (PVC), and an aerodynamically stabilized flame, supported by instantaneous stagnation points as discussed in Chapter 1, could still precess. There is further discussion later in this section.

Consider next some definitions. In three-dimensional space, the axial position of the instantaneous axial velocity stagnation point is denoted as $Z_{b,g}(t)$, defined as the most upstream location of the instantaneous axial velocity stagnation contour, with the subscript “g” (for “global”), given by eqn. (17):

$$Z_{b,g}(t) \equiv \min[Z_g(r,\theta,t)\big|_{U_z=0}] \tag{17}$$

where $Z_g(r,\theta,t)|U_{z=0}$ defines the axial velocity stagnation surface. The time-averaged position of $Z_{b,g}(t)$ is given by $\overline{Z_{b,g}}$. The stagnation point of the time-averaged axial velocity is denoted as $Z_{b,g,ave}$, defined as the most upstream location of the time-averaged axial velocity stagnation contour by eqn. (18):

$$Z_{b,g,ave} \equiv \min[Z_g(r,\theta,t)\big|_{\overline{U_z}=0}] \tag{18}$$

As the experimental measurements are obtained from the laser sheet plane, we also define analogous definitions of these quantities for an *x*-*z* plane (*y* = 0), dropping the subscript “g” (for “global”) so that:

$$Z_b(t) \equiv \min[Z(x,t)|_{U_z=0}] \tag{19}$$

and

$$Z_{b,ave} \equiv \min[Z(x,t)|_{\overline{U_z}=0}] \tag{20}$$

The time-averaged position of $Z_b(t)$ is $\overline{Z_b}$.

While this model is quite general, in order to show specific results, in the illustrative results shown later, we will assume that R_{center} is not a function of *z*, and that the reverse flow region radius grows axially as:

$$R_{cs}(z) = \frac{z^2}{R_0} \tag{21}$$

Assuming that the motion is time harmonic, the precession region center, $\theta_{center}(z,t)$, is located by eqn. (22):

$$\theta_{center}(z,t) = \sin(\omega_p t - \phi_{0,p}) \tag{22}$$

where ω_p is the precessing angular frequency and $\phi_{0,p}$ is the precession initial phase.

We assume time harmonic axial oscillations so that the position of the leading edge of the recirculation zone, $Z_{b,g}(t)$ is given by eqn. (23):

$$Z_{b,g}(t) = A_{pert,z} \sin(\omega_{pert,z} t - \phi_{pert,z}) \tag{23}$$

where $\omega_{pert,z}$ is axial oscillation angular frequency and $\phi_{pert,z}$ is the precession initial phase.

In the case of frequency-locked axial and azimuthal motion, i.e., $\omega_p = \omega_{pert,z}$, the precession axis simply tilts with the following angle, shown in Figure 4.1:

$$\psi = \tan^{-1}\left(\frac{A_{pert,z}\sin(\Delta\phi)}{R_{center}}\right) \tag{24}$$

where $\Delta\phi = \phi_{pert,z} - \phi_0$.

To summarize, the key dimensionless parameters controlling this model flow field are the dimensionless precession radius, $\rho = R_{center}/R_0$, the tilting angle of the axis of rotation, ψ, and axial perturbation, $A_{\mathrm{pert,z}}/R_0$.

4.1.2. Reverse Flow Probability Maps

While precessing flow features can be extracted in a straightforward way from 3-D data, such as computations, the most typical data sets consist of planar *r-z* cuts. While such data generally capture precession, time-averaged flow fields mask these features. One of the reasons for this has to do with the significant differences in velocities of the forward and reverse flow. The forward flow velocities are high, being on the order of nozzle exit velocities, while peak reverse flow fields are much lower; e.g., backflow ratios β range between 0.10 and 0.20 from the results from a variety of different swirl combustor data sets from our lab. As such, the smoothly varying velocity fields shown in time averages of *x-z* cuts do not allow one to see that this average is actually composed of a spatially varying weighted average of the $U_z > 0$ and $U_z < 0$ instants. For example Figure 4.2 shows the time-averaged velocity field from experiments. The image clearly shows the high velocity annular jet, as well as the center recirculating fluid, well known time-averaged features in high swirl flows of this kind.

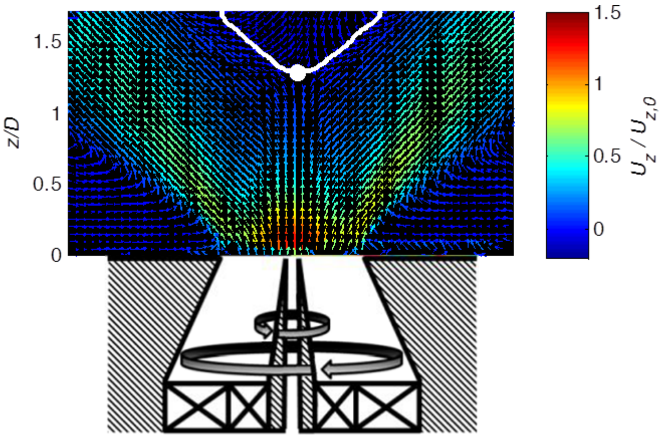

Figure 4.2: Time-averaged *x-z* plane velocity vector fields with axial velocity stagnation contours shown by white line. Time-averaged field axial stagnation points marked with a filled circle.

Additional insight into the flow field comes from binarizing the velocity field data into values of unity and zero, corresponding to values where U_z is less than or greater than some reference value, $U_{z,ref}$. Using $U_{z,ref} = 0$, the time average of the binarized image then provides a "Reverse Flow Probability" (RFP) map of the fraction of time that the flow field at a given position is reversed. The RFP map for the same data set shown in Figure 4.2 is shown in Figure 4.3. The key new qualitative feature that is evident in this figure, relative to its time average in Figure 4.2, is *the double tail structure*, i.e., the two off-center dips in the RFP isocontours, first seen near the nozzle exit at $z/D_0 \sim 0.3$. This double tail structure is consistent with precession, as it shows higher probability of reverse flow off axis, than it does on-axis. The RFP map also shows evidence of axial motion of the reverse flow region by virtue of the low axial gradient in the tails. As a side note, the RFP maps provide no indication of helicity in the reverse flow region, as all phase information is lost by averaging.

As also shown in Figure 4.3, in contrast to the DACRS nozzle, no such feature is present in the high shear swirler or bluff centerbody [35] configurations. However, the bluff centerbody RFP map shows that the center flow is sometimes positive near the dump plane even though it is reversed everywhere on the average flow field. This is due to axial motion of the VBB, as the recirculation zone occasionally lifts from the centerbody, evidenced by the appearance of instantaneous centerline stagnation points. Precession in the bluff geometry does occur as the stagnation point is in the centerbody wake and can move side-to-side slightly. For the high shear swirler, the recirculation zone starts along the centerline somewhere in the nozzle and is “locked” in place, but is free to precess further downstream. Instantaneous r-θ cuts clearly indicate precession, but it is not obvious from this image. Similar behavior would be observed in the model problem for the situation where $R_{\text{center}}(z)$ starts near zero and grows downstream, i.e. increasing precession radius.

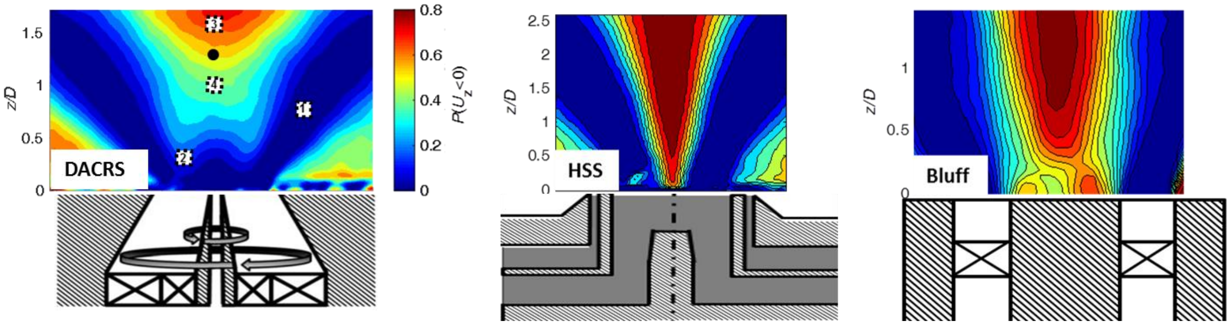

Figure 4.3: Reverse flow probability maps from data DACRS nozzle, gaseous HSS and annular swirler with bluff centerbody [35]. Stagnation contours of time-averaged axial velocity in black. Time-averaged axial velocity stagnation point $Z_{b,ave}$ marked with a filled circle. For the HSS, (1), (2), (3) and (4) denote the averaging region of 3 by 3 vectors where the convergence behavior of the averages is plotted in Figure 4.11.

As one might expect, the ratio of the precession radius to the recirculating flow radius, ρ, is a key parameter influencing whether this double tail structure does ($\rho >> 1$) or does not ($\rho << 1$) exist. In addition, the axial development of the precession radius also controls the nature of the tail region as, for instance, if R_{center} starts near zero at $z = 0$ and grows downstream, such as it might in geometries where the central recirculation zone is connected to a geometric feature such as a centerbody. Example calculations are shown in Figure 4.4 below, showing RFP maps for the model problem for increasing values of this parameter, ρ. Note the growing reverse flow probability off axis with increasing ρ

values. Note also how the flow is always positive on the centerline for large enough values of ρ.

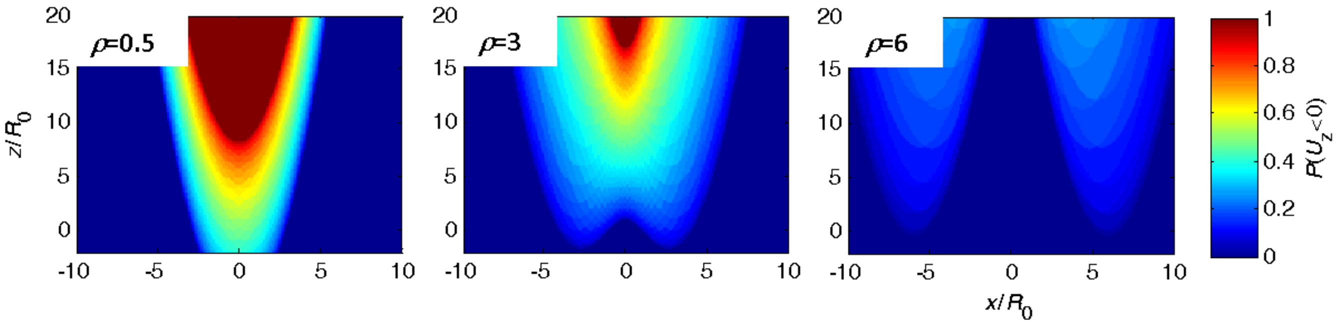

Figure 4.4: Effect of precession parameter ρ on reverse flow probability map shape from model problem. $A_{pert,z}/R_0 = 8$ used here to simulate a more realistic appearance of the blurring of the double tail.

Such time-averaged centerline axial jets have been observed and commented on a number of times in the literature, e.g., [12, 30, 31, 159, 160]. One of the most extensive parametric characterizations of the conditions under which such centerline jets do and do not exist have been described in [159, 160]. Two example time-averaged flow fields from their data are shown in Figure 4.5. The right half of the image shows a condition where the time-averaged recirculation zone is a single bubble, with reverse flow on the centerline. The left half shows a condition where the recirculation zone has the shape of a torus, with a centerline jet. Their papers show regime maps characterizing the conditions where the bifurcation in time-averaged recirculation cell topology exists. The results of the model problem presented in the present study *shows that flows with positive or negative time-averaged centerline velocity need not be qualitatively different in character, but rather may simply reflect quantitative differences in the precession parameter ρ*. In other words, a smooth monotonic variation in precession parameter, ρ, can lead to a bifurcation in the time-averaged recirculation zone topology. Of course, this result does not prove that this precession effect is the exclusive cause of axial centerline jets in swirling flows, but does show one mechanism for their occurrence.

Another important point that can be seen from this result is that flows which have instantaneous stagnation points need not have stagnation points in the time-averaged velocity. Again, for the ρ = 6 case, the flow will be positive along the centerline (since the RFP map reads zero along the centerline) even though instantaneously we have stagnation points on either side of the centerline as the paraboloid precesses.

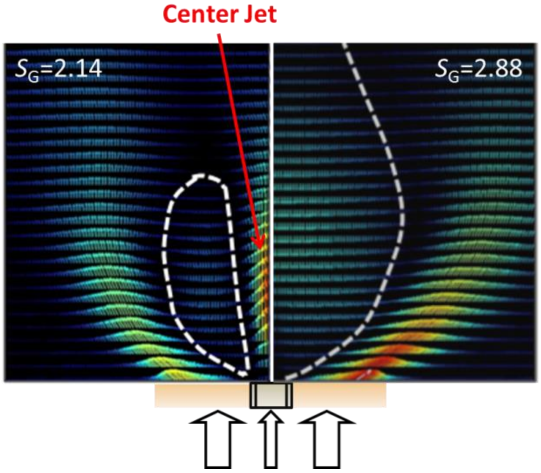

Figure 4.5: Experimental data from Basu's group [159] at two different geometric swirl numbers, S_G. The flow on the left has a centerline axial jet while the one on the right has centerline reverse flow.

4.1.3. Precession Influences on Stagnation Points

Precession of flow stagnation points has important effects on the relationship between instantaneous and time-averaged stagnation regions. As defined previously, $Z_b(t)$ defines the leading edge of the instantaneous axial velocity, and $Z_{b,ave}$ is the stagnation point of the average axial velocity. We denote $Z_b(t)$ with an empty circle and $Z_{b,ave}$ with a filled circle throughout this paper. The time average of $Z_b(t)$ is denoted as $\overline{Z_b}$, and marked with a square.

To illustrate these quantities, consider Figure 4.6, which illustrates instantaneous results. The leading edge of the average axial velocity stagnation contour is denoted by a filled circle and is located at $Z_{b,ave}/D = 1.3$. The dashed white line denotes the instantaneous contour of zero axial velocity, and the empty circle denotes its instantaneous leading edge, $Z_b(t)$. Note how $Z_b(t)$ moves from side to side, as would be expected of a precessing flow. Finally, the solid red line denotes the leading flame edge, estimated from PIV seeding density gradient edges. Note that the instantaneous leading edge point of the flame always lies either on or below the instantaneous stagnation contour. The key feature to note from this figure is that *the instantaneous stagnation point lies below the stagnation point of the average flow field most of the time*. In other words $\overline{Z_b} \neq Z_{b,ave}$; rather $\overline{Z_b} < Z_{b,ave}$. For this case $\overline{Z_b} / D = 0.48$ and is marked with a square, while $Z_{b,ave}$ = 1.3 and is marked with a filled circle.

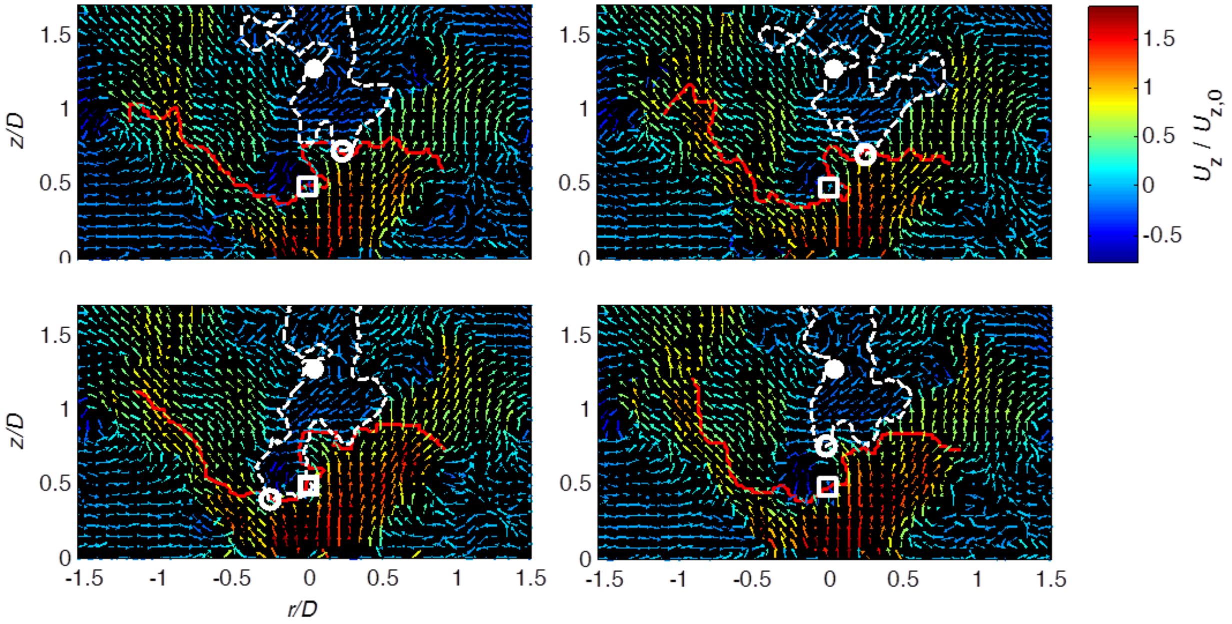

Figure 4.6: Sequence of instantaneous r-z velocity vector fields showing side-to-side motion of stagnation point. The filled circle represents $Z_{b,ave}$, the empty circle represents $Z_b(t)$, and the square is $\overline{Z_b}$. The white line is the axial velocity stagnation contour, and the red line is the flame edge extracted from the PIV images using seeding density gradients.

This result has significant implications on prediction of average flame location for aerodynamically stabilized flames in precessing flows. Specifically, it shows that the time-averaged stagnation point has no relevance to the time-averaged flame position, unless the ratio $\rho \ll 1$. Moreover, it shows that even if a Reynolds Averaged Navier Stokes (RANS) calculation perfectly predicts the time-averaged flow and has a perfect turbulent flame speed closure model, it can still completely miss the average flame location. To illustrate, consider a RANS calculation with a flamelet closure: The RANS calculation will position the time-averaged flame position where the time-averaged velocity matches the turbulent flame speed. As shown above, the regions of low time-averaged axial velocity need not have a relationship to the regions of low instantaneous axial velocity. In order for the RANS calculation to correctly predict the flame position, the "effective" turbulent flame speed closure would need to include a vortex precession radius, ρ, as a flame speed parameter.

To understand better the relationship between time-averaged and instantaneous stagnation points, consider Figure 4.7 below, which shows a cross-sectional cut of a paraboloidal VBB in simple orbit from the model problem. Areas inside the parabolic cut are of reverse flow, and regions outside are of positive flow. In this case, the empty circle shows the location of $Z_b(t)$, and the filled circle shows $Z_{b,ave}$. The dotted line shows the path of the instantaneous stagnation point in the center plane or $Z_{b,g}(t)$. These features are also shown in a corresponding RFP map in Figure 4.8. For the model problem, the flow above $Z_{b,ave}$ is always negative and the flow below it is always positive. Furthermore, even though $\overline{Z_b}$ is in a region of flow that is always positive, the path of the instantaneous stagnation point is always outside of this region.

The influence of precession on $Z_{b,ave}$ can be seen explicitly for this model problem, where:

$$Z_{b,ave} = \rho^2 R_0 \tag{25}$$

This relationship is not affected by *sinusoidal axial motion, and f*urthermore, $\overline{Z_b}$ is always given by:

$$\overline{Z_b} = Z_{b,ave}/2 \tag{26}$$

This is in contrast to the global values where:

$$Z_{b,g,ave} = \rho^2 R_0 \tag{27}$$

but $Z_{b,g}(t) = \overline{Z_{b,g}} = 0$.

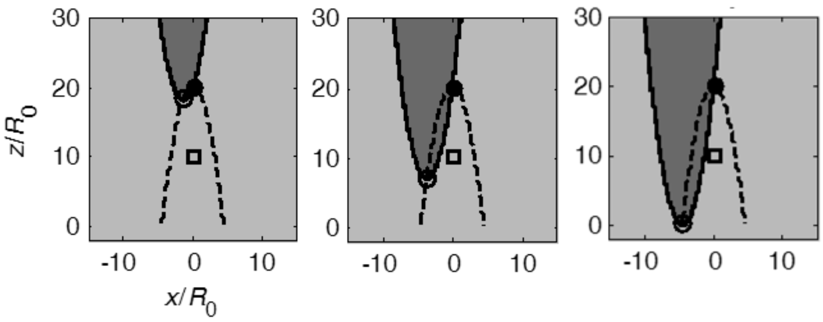

Figure 4.7: Simulated precession of paraboloid slice in *x-z* plane for ρ = 4.5, $A_{pert,z}/R_0$ = 0. The filled circle denotes $Z_{b,ave}$, the empty circle is $Z_b(t)$ and the square is $\overline{Z_b}$. Reverse flow is dark colored and positive flow is light.

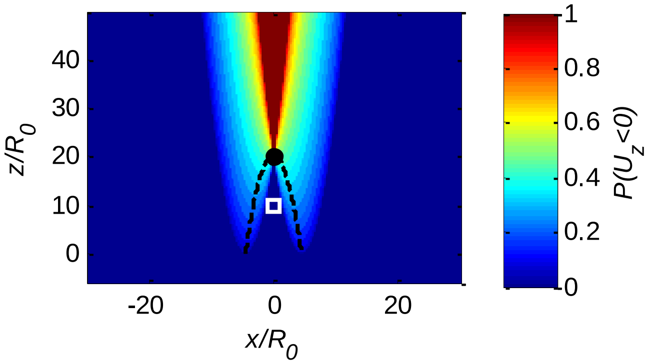

Figure 4.8: Reverse flow probability map for a model precessing paraboloid for ρ = 4.5, $A_{pert,z}/R_0$ = 0. Dotted line is locus of $Z_b(t)$, the filled circle is $Z_{b,ave}$, and the square is $\overline{Z_b}$.

4.1.4. Axial Asymmetry for Precessing Wake Model

It is a common observation that measurements of time-averaged velocity fields in nominally axisymmetric geometries are not symmetric. In this section, we demonstrate that phase-locked azimuthal and axial motion of the precessing region can introduce asymmetry in the time-averaged flow. For example, a nonzero precession axis angle ψ leads to non-symmetric velocity fields for the model problem. Figure 4.9 shows a series of example calculations of the paraboloid precessing on an inclined plane, showing the growing degree of non-symmetry of the flow field as the inclination angle ψ increases.

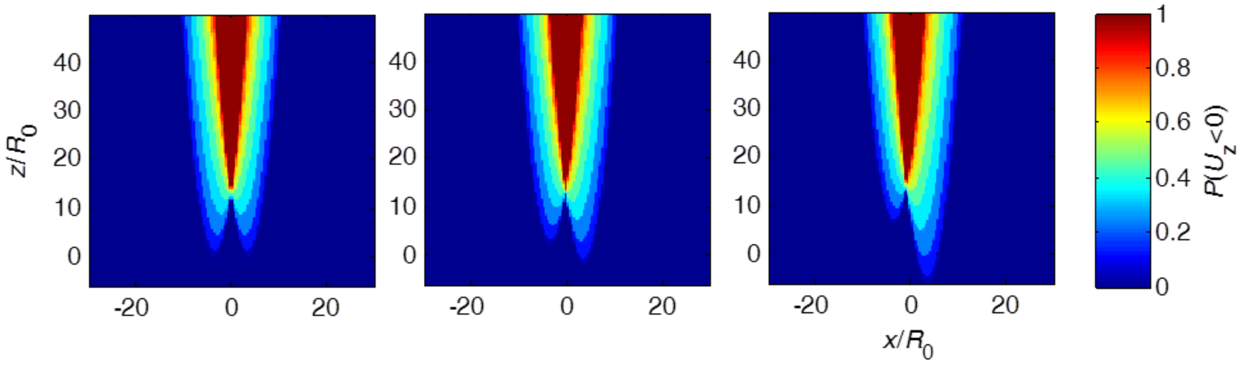

Figure 4.9: Effect of tilt angle ψ upon time-averaged reverse flow probability maps, $\rho = 4.5$, $A_{pert,z}/R_0 = 0$.

Of course, in any real turbulent flow, random phase jitter of the azimuthal rotation of this tilted precession axis would render the time-averaged velocity to be axisymmetric, given sufficient averaging time. However, this could occur slowly and so statistical convergence to a symmetric flow field could require substantially longer averaging time intervals than what might be expected based upon typical approaches for estimating confidences in the mean, based on assumptions of uncorrelated, Gaussian statistics. This point is discussed further in the next section.

4.1.5. Statistical Convergence of Time-Averaged Axial Velocity for Precessing Flows

This section addresses the convergence of estimates of time-averaged quantities in swirl flows. We focus upon the influence of coherent motion and/or a tilted axis of precession, which can cause non-Gaussian statistical convergence of sample statistics. We show in this section that the rate of convergence of averages decreases monotonically with the reverse flow probability value of the flow at the measurement point.

Figure 4.10 plots PDF's of the axial velocity at the four points in the nozzle flow shown in Figure 4.3, corresponding to the jet, "tail region", deep recirculation zone, and a point at $z/D = 1$, $r/D = 0$. The PDF's are normalized as $(U_z\text{-}U_{z,\text{ave}})/\sigma$, where $U_{z,\text{ave}}$ and σ denote the average and standard deviation of the axial velocity, estimated from 10,000 data points. As Figure 4.10 shows, the PDF's are similar to a Gaussian distribution, also shown in the figure. The PDF deep in the recirculation zone deviates from Gaussian the most. Note, however, that none of these PDF's are bimodal, such as the case discussed in the introduction.

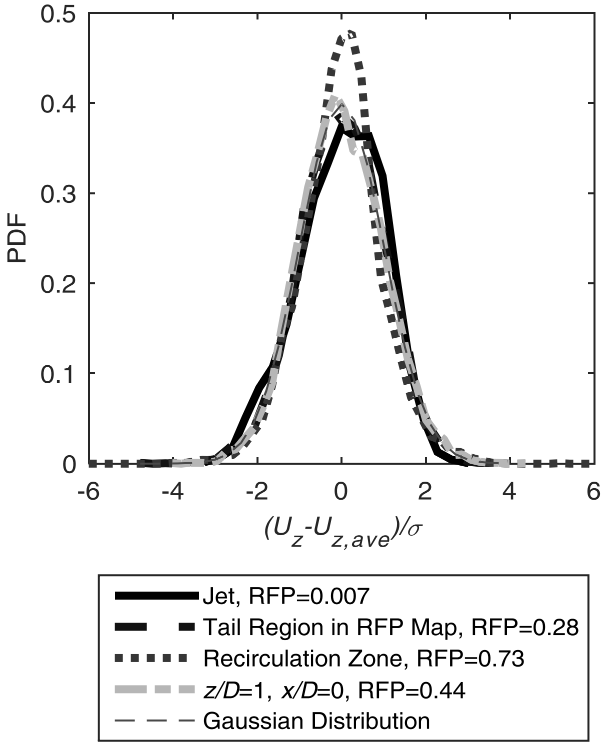

Figure 4.10: Normalized probability distribution functions of axial velocity for the three flow regions from Figure 4.3.

Consider next the convergence behavior of the time average for these same three data sets. Define the sample mean by: $U_{z,n} = \sum_{j=1}^{n} U_z$, where n denotes the sample size. The population mean, $U_{z,ave}$, and standard deviation, σ, is determined from this expression using the entire sample, where $N_{\text{pop}} = 10,000$. For large sample sizes of normally distributed data, the squared normalized convergence error of the sample mean relative to the population mean is given by [161]:

$$\frac{(U_{z,n} - U_{z,ave})^2}{\sigma^2} = \frac{1}{n} \tag{28}$$

Figure 4.11 plots the dependence of the convergence behavior in the three regions of the DACRS nozzle flow shown in Figure 4.3 as a function of sample size, *n*, up to a value of n_{max} = 500 (corresponding to 50ms of sampling time). The three lines correspond to reverse flow probabilities of 0.007, 0.28, and 0.73, respectively. Also indicated with a green dashed line is Eq. 12, corresponding to the convergence behavior of large sample size, random Gaussian data. The squared normalized convergence error defined above is calculated and averaged over 1000, 96% overlapping ensembles. Nine neighboring locations (from a 3 by 3 vector location region of interest) are averaged to further smooth the data. From the figure, it is clear that the data increasingly departs from the Gaussian line with increasing reverse flow probability values. In the core of the annular jet, the convergence is closest to random normal data, but well into the recirculation region, convergence is much slower. A better indicator of the data is a two zone behavior with a slow initial decay, followed by a decay rate that more closely parallels the Gaussian line.

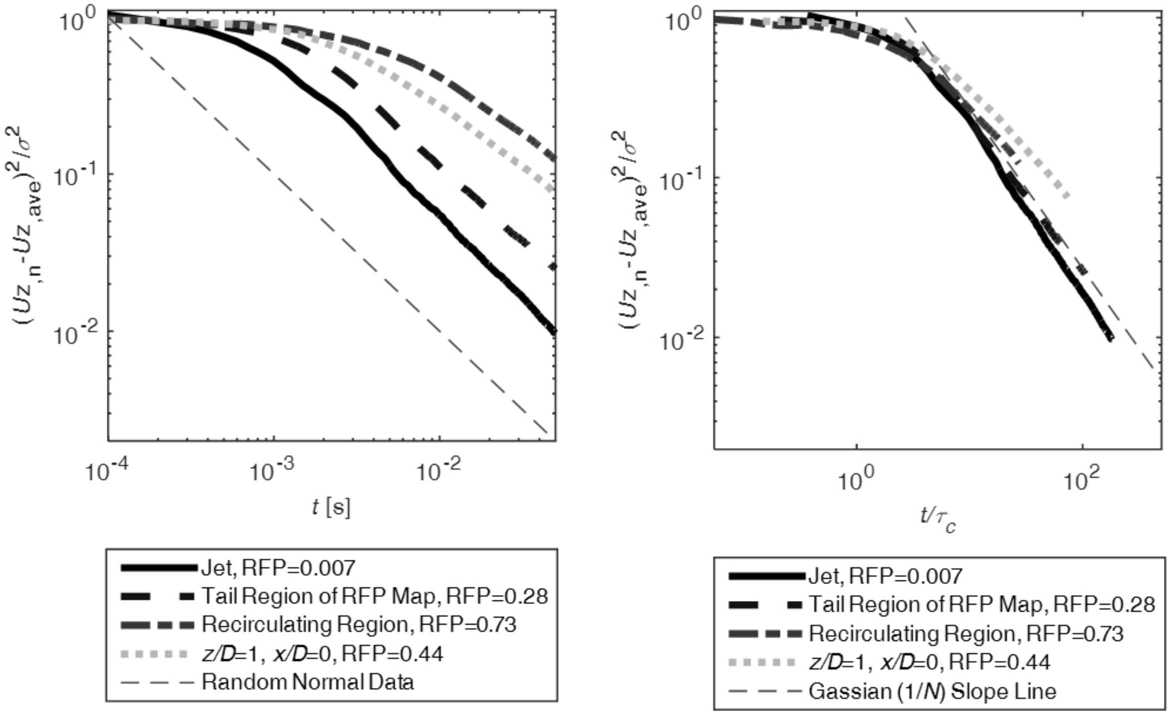

Figure 4.11: Convergence behavior of average axial velocity. Left: as a function of number of time at the four regions of the flow from Figure 4.3 corresponding to different RFP values. Right: as a function of time normalized by the integral time of turbulence, τ_c, at the 4 regions of the flow from Figure 14. Gaussian, uncorrelated (1/*n*) line shown.

To better see the temporal behavior of these three regions, Figure 4.12 plots the ensemble-averaged power spectra of the axial velocity. The spectra do differ, but do not indicate any particularly narrowband features. An additional spectrum is shown at $z/D = 1$, $r/D = 0$, where more narrowband energy at 150Hz is evident. This peak only shows up at radial locations smaller than $|x/D| < 0.5$ and at axial locations lower than $z/D = 1.5$. However, the spectrum rolls off at a much lower frequency in the recirculation zone, indicative of a longer correlation time of the motions. These results suggest that the frequency at which the power spectrum rolls off, or the correlation time, is indicative of the rate of convergence from Figure 4.11 (left).

To capture the effect of correlation time, the integral time scale of the axial flow disturbances, τ_c, was estimated from the time integral of the autocorrelation function $r(\tau)$:

$$\tau_c = \int_0^{T_{1/2,e}} r(\tau)d\tau \tag{29}$$

where the upper integral limit $T_{1/2,\mathrm{e}}$ was selected as one half of the ensemble duration. The autocorrelation function was ensemble-averaged over 1000, 96% overlapping ensembles like in the previous calculations. The autocorrelation function, $r(\tau)$, is defined as [154]:

$$r(\tau) = \frac{\left\langle U_z(t)U_z(t+\tau)\right\rangle}{\left\langle U_z{}^2\right\rangle} \tag{30}$$

where τ is time delay and $\langle\ \rangle$ denotes expected value, in this case evaluated as:

$$r(\tau) = \frac{\sum_1^{n_{1/2,e}} U_z(t)U_z(t+\tau)}{\sum_1^{n_{1/2,e}} U_z{}^2} \tag{31}$$

where $n_{1/2,\mathrm{e}}$ is the number of elements in the first half of the ensemble. The data in Figure 4.11 (Left) are replotted in a normalized manner in Figure 4.11 (Right). This figure shows a much better collapse of the data.

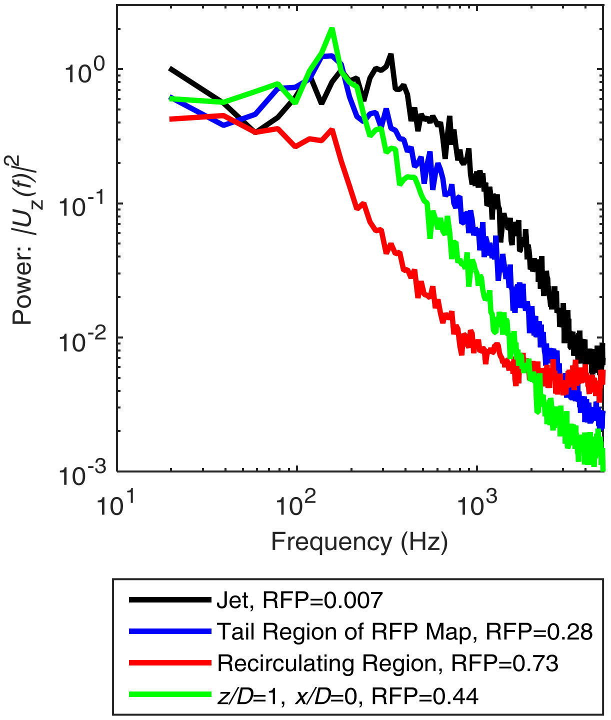

Figure 4.12: Power spectra of axial velocity from the three flow regions from Figure 4.3 and a fourth region (green). $U_z(f)$ are the FFT coefficients. Spectra are averaged from 10 ensembles each, from 9 adjacent locations.

The slower rate of convergence relative to Gaussian random data has the important implication that the standard error of the mean estimates in these flows is larger than the $\sigma/\sqrt{n}$ for random Gaussian data. This is an important point in analysis of results from computational studies in which a low number of flow-through times may be available.

4.2. Velocity and Stretch Characteristics at the Leading Edge of an Aerodynamically Stabilized Flame

In this section we present statistics of the calculated quantities at the flame leading edge of the aerodynamically stabilized flame with the atmospheric, premixed methane/air high shear swirler. This flame is stabilized by instantaneous stagnation points created by helical vortical structures. As described earlier, the two data sets at different nozzle velocities were processed to produce leading edge realizations for cases 1 and 2, which are analyzed in this section. The next subsection summarizes the time-averaged flow features, followed by three subsections which compare the (1) flame leading edge axial and transverse location, (2) local velocity field and (3) flame stretch.

4.2.1. General Flame and Flow Features

Figure 4.13 and Figure 4.14 display the general flame and flow features for cases 1 and 2, respectively, with subplot (a) displaying the time-averaged axial velocity field, $\bar{U}_z(r,z)$, subplot (b) the negative axial gradient of time-averaged axial velocity, $-d\bar{U}_z(r,z)/dz$, and subplot (c) the fraction of time that the flow at that point is negative, denoted as the reverse flow probability field, $p\left(U_z < 0\right)$. This last plot is a nonlinear averaging technique introduced in Section 4.1 to better illustrate the intermittent structure of the recirculating flow. These figures show the typical topology of a high swirl number flow with vortex breakdown – i.e., the high velocity annular jets with a recirculating core flow. Several lines are drawn in to indicate key flow features. The locus of points of maximum magnitude of the 3-component time-averaged velocity, the "jet core", is indicated by the dashed black line. The inner (below the jet core) and outer (above the jet core) shear layers are displayed, extracted as the locus of maximum out-of-page component of time-averaged vorticity. Reaction progress variable field is displayed as obtained from binarized OH-PLIF instantaneous images, $\bar{p}_{OH}(r,z)$. Finally, the time-averaged axial velocity stagnation line, $\bar{U}_z(r,z) = 0$, is plotted. Furthermore, we have conditioned the flame leading edge the radial and axial coordinates, $R_{\mathrm{le}}(t)$ and $Z_{\mathrm{le}}(t)$, on each other as follows: First, values of $R_{\mathrm{le}}(t)$ are conditioned on values of $Z_{\mathrm{le}}(t)$. This is done by binning the $R_{\mathrm{le}}(t)$ data according to corresponding values of $Z_{\mathrm{le}}(t)$. The red dots in Figure 4.13 and Figure 4.14 are the average value of $R_{\mathrm{le}}(t)$ for each bin, and are denoted as $\overline{R_{le}|Z_{le}}$. This process is performed in a similar way for $Z_{le}(t)$ to produce the black dots, $\overline{Z_{le}|R_{le}}$.

Turning our attention to the flame location, we note that the flame is in an "M-shape" configuration, stabilizing in the outer shear layer and near instantaneous stagnation points in the inner recirculation zone, created by helical vortices accompanying a precessing vortex core PVC. Note that cases 1 and 2 are topologically similar, with the notable exception of the flame location. The flame leading edge time-averaged location lies along the inner shear layer for case 1 in a region of highly positive axial velocity, while for case 2 the leading edge is further downstream, a little outside of the shear layer and in a region of lower positive axial velocity. The time-averaged flame position is also shifted downstream for case 2 relative to case 1. We will return to these features for more detailed discussions to follow.

Note that extensive sets of statistical plots are presented in Appendices A and B. Appendix A contains a complete sets of bi-variate statistics for the 6 measured quantities, $Z_{le}(t)$, $R_{le}(t)$, $U_{z,le}(t)$, $U_{r,le}(t)$, $U_{\theta,le}(t)$, and $\kappa_{s,le}(t)$, for both cases. Appendix B presents polar histograms of the flow angle at the flame leading edge from three "viewing angles," and histograms of the time between instances when the flame leading edge crosses the interrogation plane.

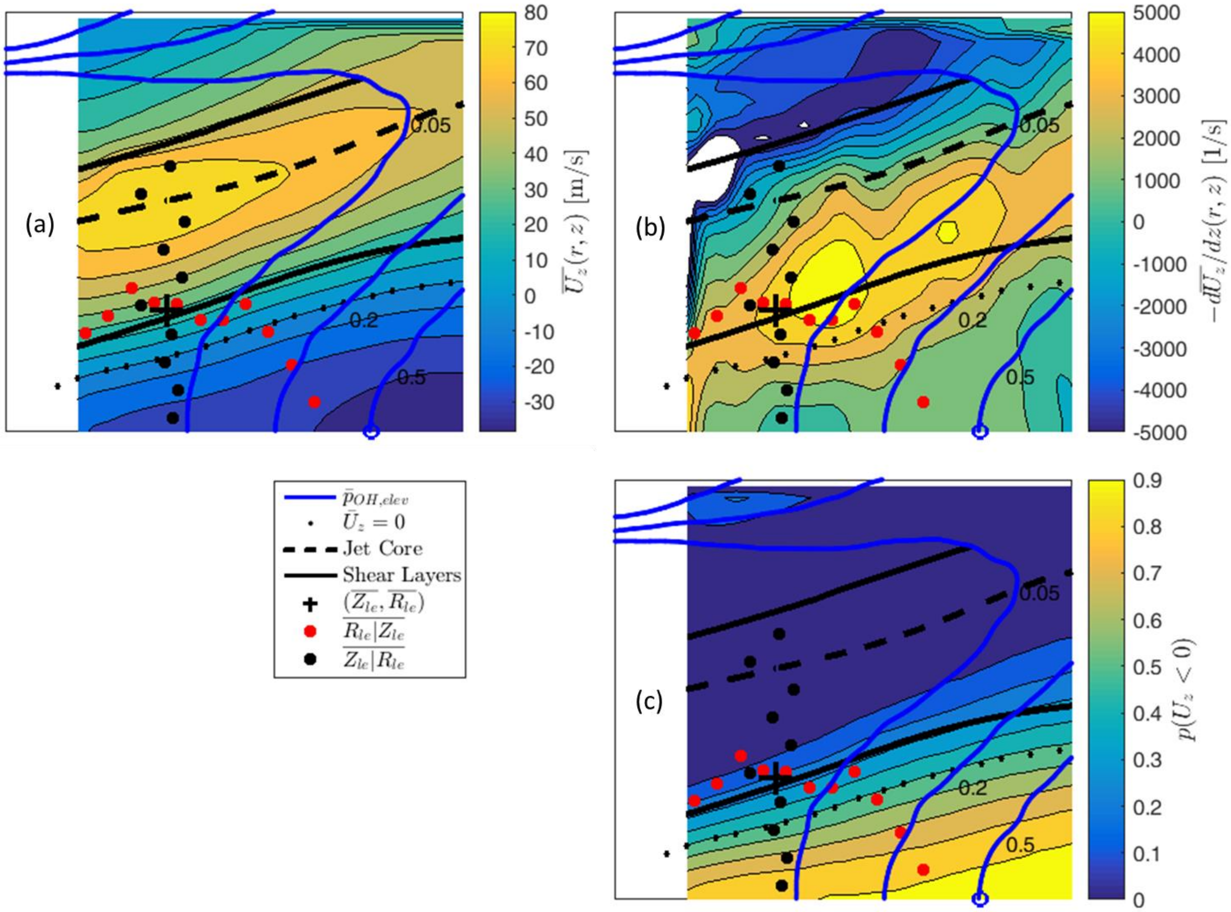

Figure 4.13: Spatial dependence of the (a) time-averaged axial velocity field, $\bar{U}_z(r,z)$, (b) negative axial gradient of the time-averaged axial velocity field, $-d\bar{U}_z(r,z)/dz$, and (c) reverse flow probability field, $p\left(U_z<0\right)$, for case 1. Isolines indicate jet core, shear layers, progress variable isocontours, $\bar{p}_{OH}$ (values of $\bar{p}_{OH}=0.05, 0.2, 0.5$ are indicated), and time-averaged axial velocity stagnation line, $\bar{U}_z(r,z)=0$. The flame leading edge time-averaged location, $\left(\overline{R_{le}},\overline{Z_{le}}\right)$, is shown with a "+". The black dots show the average z-position for a given r, $\overline{Z_{le}|R_{le}}$, while the red dots show the average r-position for a given z, $\overline{R_{le}|Z_{le}}$ (these points are also indicated in Figure 4.15).

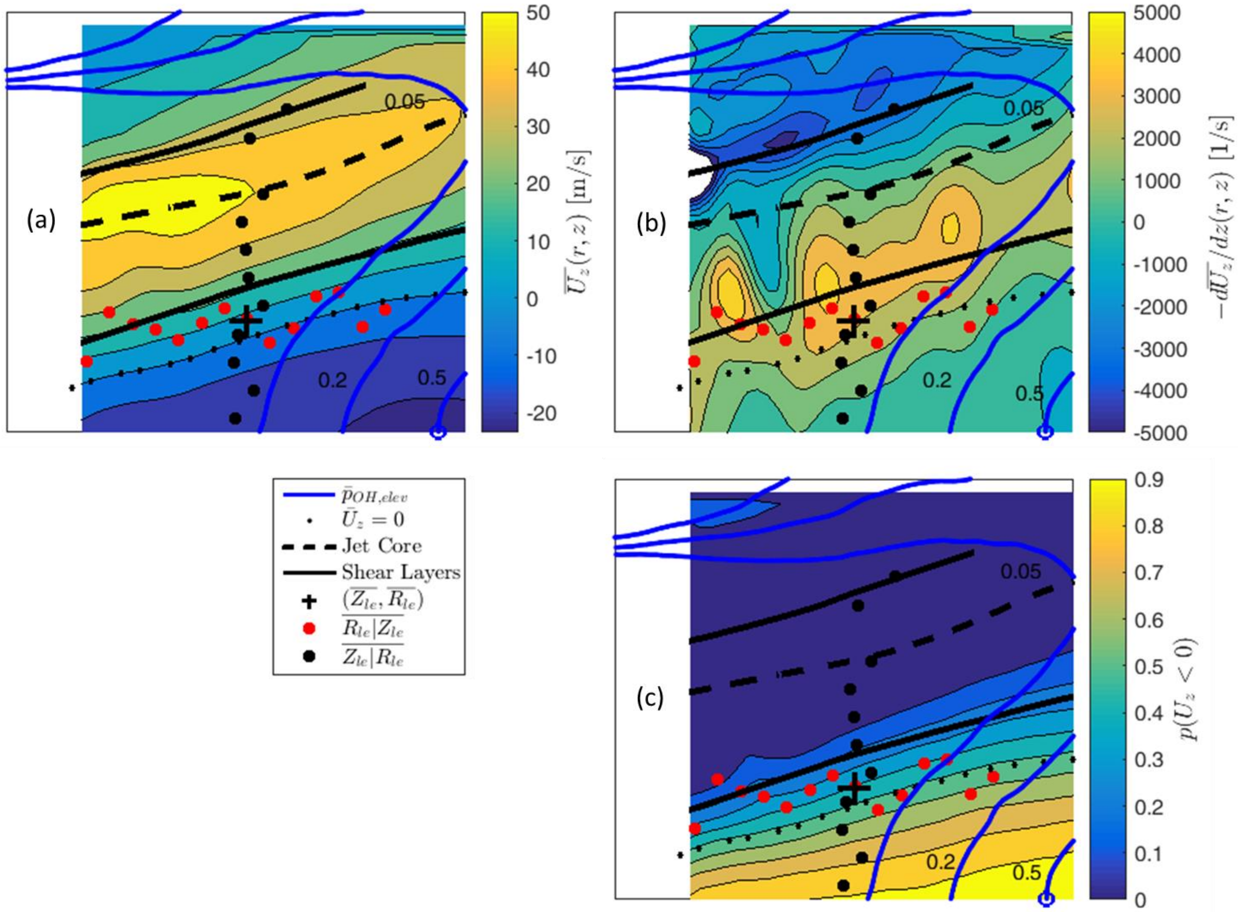

Figure 4.14: Spatial dependence of the (a) time-averaged axial velocity field, $\bar{U}_z(r,z)$, (b) negative axial gradient of the time-averaged axial velocity field, $-d\bar{U}_z(r,z)/dz$, and (c) reverse flow probability field, $p(U_z<0)$, for case 2. Isolines indicate jet core, shear layers, progress variable isocontours, $\bar{p}_{OH}$ (values of $\bar{p}_{OH}=0.05, 0.2, 0.5$ are indicated), and time-averaged axial velocity stagnation line, $\bar{U}_z(r,z)=0$. The flame leading edge time-averaged location, $\left(\overline{R_{le}}, \overline{Z_{le}}\right)$, is shown with a "+". The black dots show the average *z*-position for a given *r*, $\overline{Z_{le}|R_{le}}$, while the red dots show the average r-position for a given *z*, $\overline{R_{le}|Z_{le}}$.

4.2.2. Location of Flame Leading Edge

Figure 4.15 presents the corrected statistics of the radial and axial location of the flame leading edge position for case 1. The central figure plots the radial and axial coordinates, R_{le}(t) and Z_{le}(t), conditioned on each other as just explained, $\overline{Z_{le}|R_{le}}$ and $\overline{R_{le}|Z_{le}}$, respectively. Furthermore, the RMS of each binned average point is indicated with “error” bars. Corrected PDFs of the axial and radial locations of the flame leading edge are also indicated to the side and below. Several observations are immediately evident – first, the figure shows that the average radial flame leading edge location, $\overline{R_{le}/D_0}$, is off center, i.e., for this case, it is located at $\overline{R_{le}/D_0} = 0.22$. This result indicates that the flame leading edge precesses off the centerline, $r = 0$ axis. Such a result was expected, as the center of rotation and flow stagnation points in high swirl flows are well known to precess off-axis, as discussed in the Introduction. For reference, Figure 4.16 shows the uncorrected PDF of the flame transverse location Y_{le}. Note that its PDF is symmetrically distributed around $y = 0$, with $\overline{Y}_{le} \approx 0$. This is a qualitatively different conclusion than the $\overline{R_{le}/D_0} = 0.22$ result presented above, illustrating the critical importance of correcting planar data for estimates of statistics in a round geometry. This leading edge location is indicated by the ‘+’ symbol in Figure 4.13, which shows that it lies between the location of average maximum vorticity and zero axial velocity.

Consider next the statistics of the axial leading edge location. The mean of the instantaneous axial locations, $Z_{le}(t)$, is given by $\overline{Z_{le}/D_0} = 0.33$, which is *upstream* of the leading edge of the mean unconditioned flame edge (i.e., the 0.5 progress variable value) of $Z_{f,mean}/D_0 = 0.92$ from Figure 2.5, also plotted in Figure 4.15. This is an important point, and was alluded to earlier in Section 4.2.1, noting the significance of precession in controlling the relationship between instantaneous and time-averaged flow features. In this case, it clearly shows that the time-average location of flame stabilization is systematically different than what would be inferred from a time-averaged velocity field. A similar conclusion is reached for case 2, with the lower premixer velocity, $U_{z,0}$ = 45 m/s, where the mean radial position of the flame leading edge has a slightly lower value of $\overline{R_{le}/D_0} = 0.20$, while the mean axial position is significantly further downstream, at $\overline{Z_{le}/D_0} = 0.50$.

Although not shown in the figure, there is no correlation between these instantaneous axial and radial locations of the flame leading edge. This result suggests the following physical picture of the flame leading edge location – it precesses around the flow centerline at a given axial location, with significant random axial and radial perturbations.

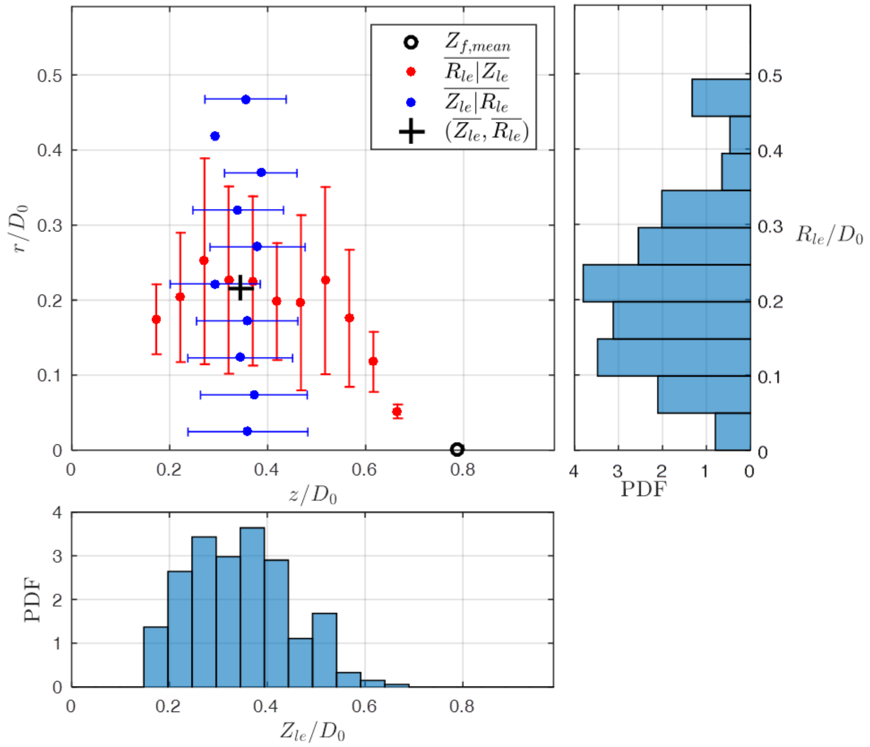

Figure 4.15: Corrected statistics of the flame leading edge position (Z_{le}(t), R_{le}(t)) in the *r*-*z* plane for case 1. PDFs of each coordinate are shown below and to the right. The average flame leading edge and the leading edge of the unconditioned mean flame edge, $Z_{f,mean}$, are also plotted.

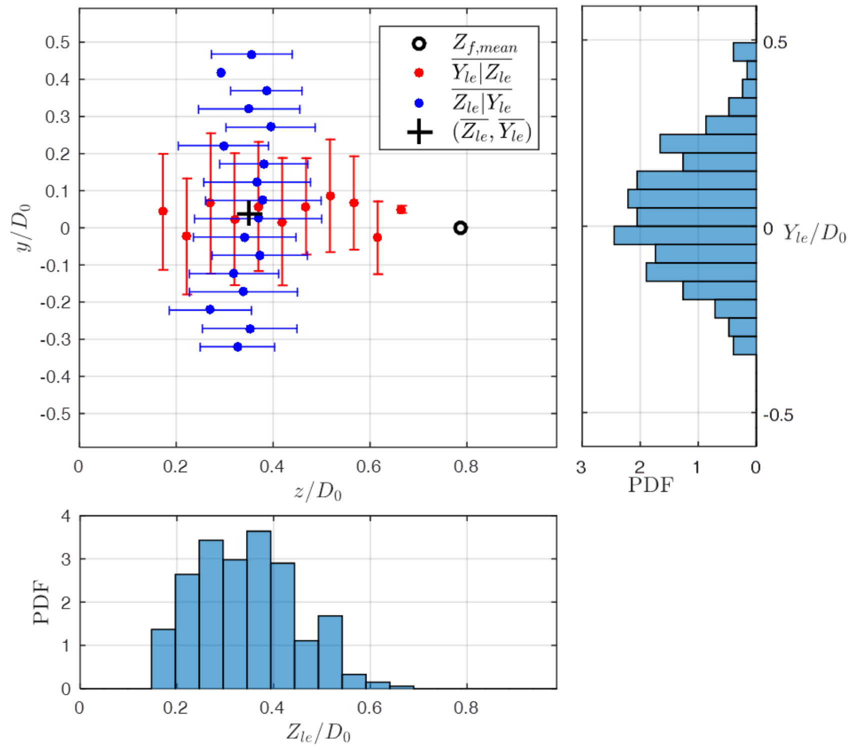

Figure 4.16: Uncorrected statistics of the flame leading edge position (Z_{le}(t), Y_{le}(t)) in the y-z plane for case 1. Each coordinate is plotted conditioned upon the other by binning and averaging. The RMS of each binned average point is indicated with error bars. PDFs of each coordinate are shown below and to the right. The average flame leading edge and the leading edge of the unconditioned mean flame edge, $Z_{f,mean}$, are also plotted.

4.2.3. Local Velocity Field

We next consider the conditioned velocity at the leading edge. Figure 4.17 plots several representative results from both cases showing the dependence of the axial velocity, $U_z(r = R_{le}, z, t)$, upon axial location, referenced to the instantaneous leading point position, using the coordinate z-Z_{le}(t). Figure 4.17 shows that for case 1, Z_{le}(t) generally lies at a location where the absolute value of the flow velocity is decelerating; i.e., in regions where $\kappa_s = -dU_z/dz > 0$. This velocity gradient would be expected based on time-averaged considerations, as the high velocity nozzle flow decelerates as it enters the much larger diameter combustor.

For comparison, case 2 shows that Z_{le}(t) does continue to lie at a location where $dU_z/dz < 0$ in some cases, but there are relatively more instances compared to case 1 where the gradient direction is reversed. In other words, even though the bulk flow is decelerating on average, the flame instantaneously lies in regions of accelerating flow. This result is not necessarily surprising, as there are significant large scale flow structures that cause the flow to oscillate between forward and reverse flow. However, the implications are quite significant – as can be quantified from the PDFs shown in Figure 3.13 above, the flame is positively stretched in ~ 85% of the realizations for case 1, and dropping to ~ 55% in case 2. This leads to the significant difference in average flame stretch rate (case 2 is 14 times lower than case 1) discussed in the next subsection.

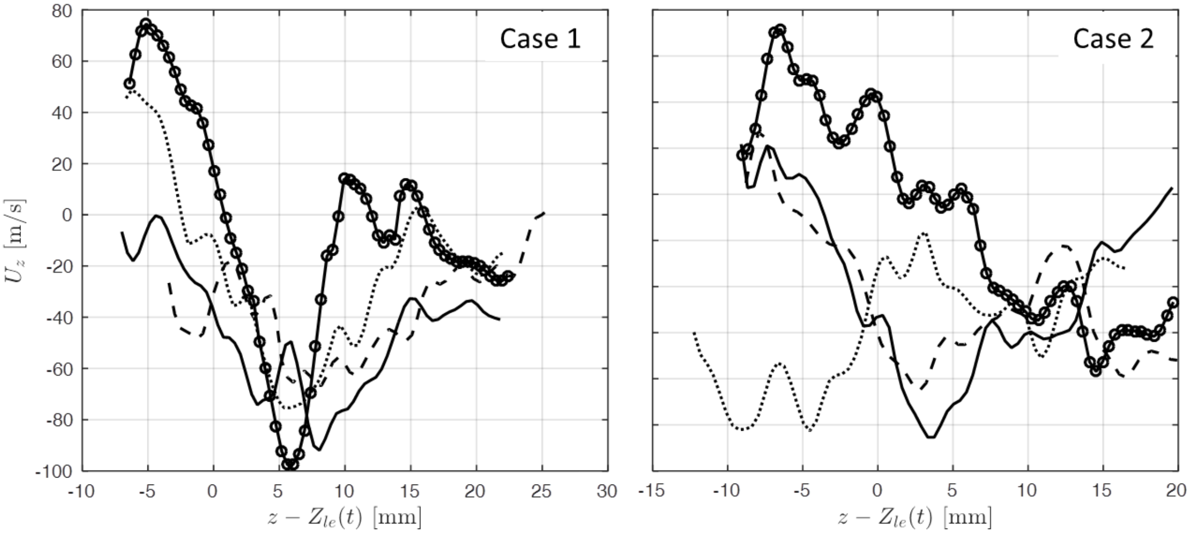

Figure 4.17: Axial dependence of the axial velocity, $U_{z,le}$(t), for four representative realizations from case 1 and case 2. The abscissa is referenced to the instantaneous leading edge. The computed slope dU_z/dz using a central difference scheme centered at z-Z_{le}(t) = 0.

Figure 4.18 presents the statistical relationship for case 1 between flame leading edge axial velocity, $U_{z,le}(t)$, and its axial location, by plotting $U_{z,le}(t)$ and $Z_{le}(t)$ conditioned on each other by binning and averaging, i.e. $\overline{U_{z,le}|Z_{le}}$ and $\overline{Z_{le}|U_{z,le}}$. Similarly the radial statistics of the flame leading edge axial velocity, $U_{z,le}$(t), are shown by plotting

$\overline{U_{z,le} | R_{le}}$ and $\overline{R_{le} | U_{z,le}}$. For reference, this plot also overlays axial and radial profiles of the measured mean value of the axial velocity at the mean radial or axial location of the flame leading edge; i.e. $\bar{U}_z(r, z = \overline{Z_{le}})$ and $\bar{U}_z(r = \overline{R_{le}}, z)$. The velocity histogram in Figure 4.18 indicates that the majority of the flame leading edges lie in regions of positive axial velocity; i.e., in the boundary between the recirculation bubble and annular jet, with a mean value of $\overline{U_{z,le}} = 9\, m/s$. The mean axial velocity evaluated at the mean flame leading edge is $\bar{U}_z(r = \overline{R_{le}}, z = \overline{Z_{le}}) = 36\, m/s$ (for reference, Figure 4.13 shows the time-averaged flame leading edge location). The factor of four difference between this 36m/s value and the actual mean velocity at the conditioned leading edge ($\overline{U_{z,le}} = 9\, m/s$) shows the significant influence of flame movement on averaged flame statistics. Figure 4.19 shows similar statistics for case 2. However, in this case the proportionality between the mean conditioned velocity at the leading edge, $\overline{U_{z,le}} = 10\, m/s$, and the mean velocity at the mean flame edge, $\bar{U}_z(r = \overline{R_{le}}, z = \overline{Z_{le}}) = 5\, m/s$, is reversed. In other words, the ratio $\overline{U_{z,le}} / \bar{U}_z(r = \overline{R_{le}}, z = \overline{Z_{le}})$ = 4 and ½ for cases 1 and 2. This result suggests a fundamental difference in flame stabilization for the higher velocity case, which is closer to blowoff.

Note also how these velocities compare at each radial location. For instance in case 1, Figure 4.18 shows that the mean of the velocity conditioned on the flame leading edge realizations, $\overline{U_{z,le} | R_{le}}$, at each radial location, r, is consistently below the mean velocity at that same radial location $\bar{U}_z(r, z = \overline{Z_{le}})$; i.e., the red dots are consistently below the black line. In contrast, for case 2 the conditioned mean at each radial location is much closer to the unconditioned mean.

Note again that the correction of the statistics is critical for successful interpretation of the results – the uncorrected values of $\overline{U_{z,le}} = -10\, m/s$ for case 1 and -5m/s for case 2 would lead one to think that the flame on average has a negative flame speed (indeed, this puzzling result led us to realize the need for the correction).

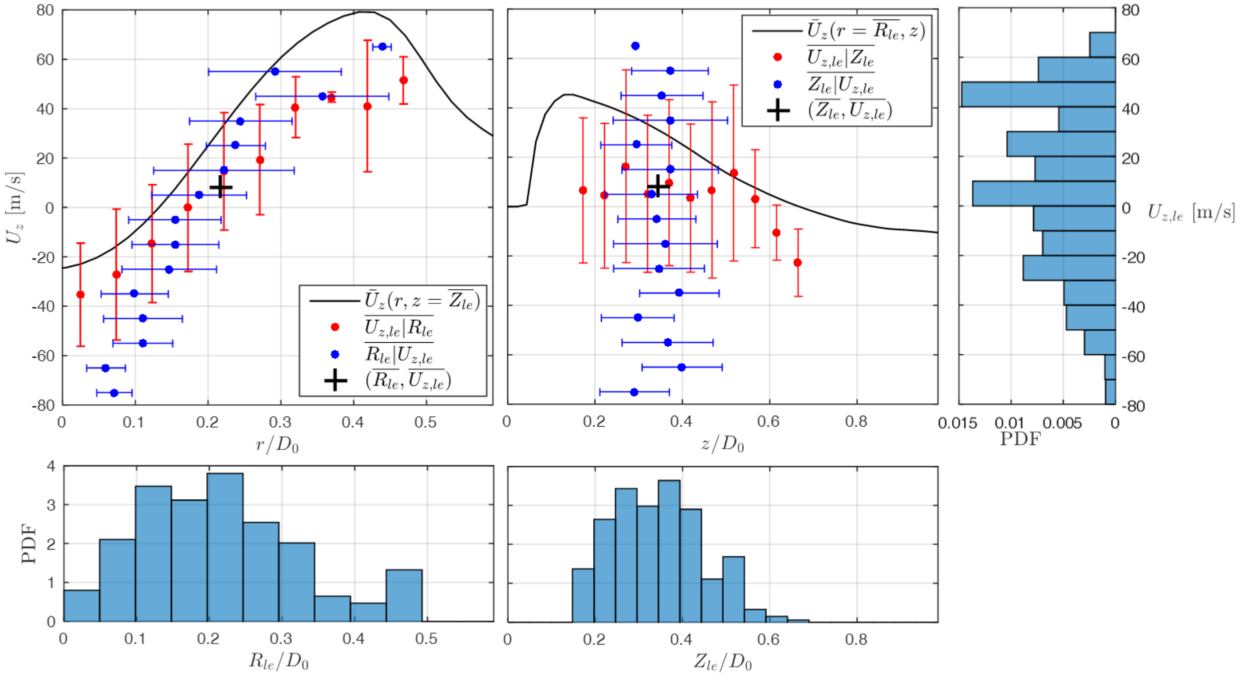

Figure 4.18: Corrected joint statistics of the flame axial velocity, $U_{z,le}$(t), vs. radial position, R_{le}(t), and vs. axial position, Z_{le}(t), at the flame leading edge for case 1. Each coordinate is plotted conditioned upon the other by binning and averaging. The RMS of each binned average point is indicated with error bars. PDFs of each coordinate are shown below and to the right. The mean values are plotted with a cross. The mean axial velocity radial profiles evaluated at the axial/radial position of the mean flame leading edge, $\bar{U}_z(z=\overline{Z_{le}}, r)$, are plotted for reference.

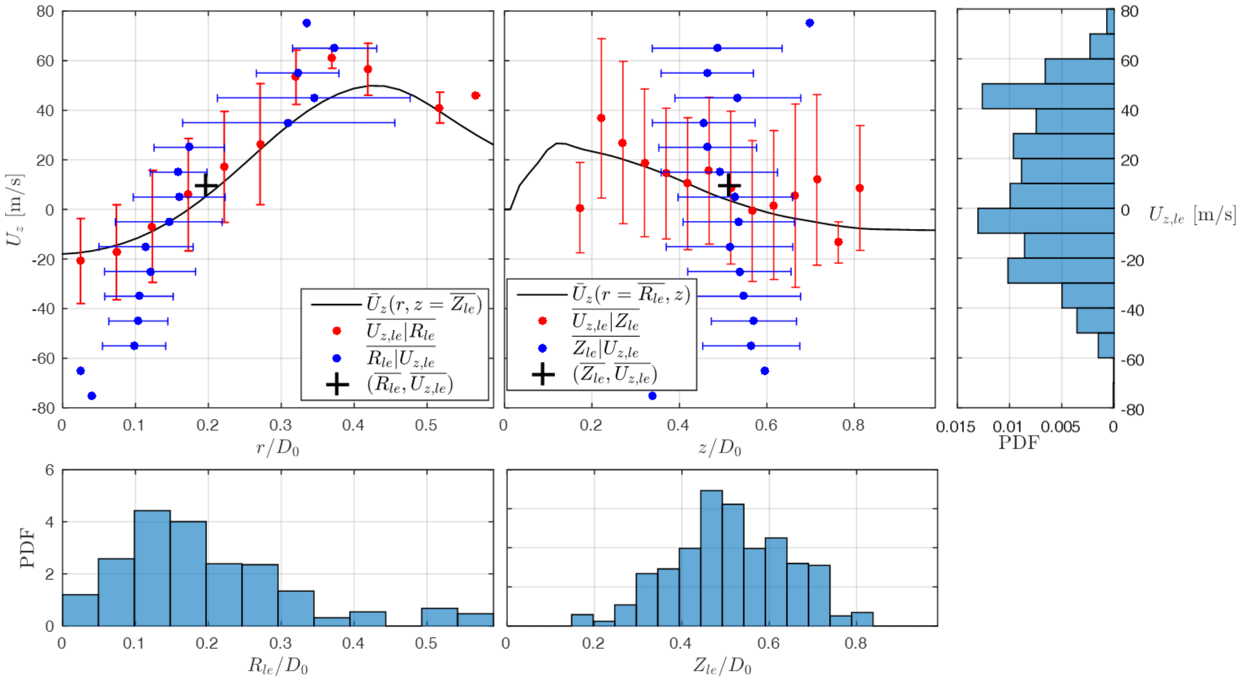

Figure 4.19: Corrected joint statistics of the flame axial velocity, *U*$_{z,le}$(t), vs. radial position, *R*$_{le}$(t), and vs. axial position, *Z*$_{le}$(t), at the flame leading edge for case 2. Each coordinate is plotted conditioned upon the other by binning and averaging. The RMS of each binned average point is indicated with error bars. PDFs of each coordinate are shown below and to the right. The mean values are plotted with a cross. The mean axial velocity radial profiles evaluated at the axial/radial position of the mean flame leading edge, $\bar{U}_z(z=\overline{Z_{le}}, r)$, are plotted for reference.

4.2.4. *Flame Stretch*

This section considers the conditioned stretch rate at the flame leading edge, and its value relative to extinction. Figure 4.20 plots the radial and axial statistics of the flame hydrodynamic stretch, $\kappa_{s,le}$(t), for case 1. As in the previous figures, $\kappa_{s,le}$(t) and R_{le}(t) are plotted conditioned on each other by binning and averaging, i.e. $\overline{\kappa_{s,le}|R_{le}}$ and $\overline{R_{le}|\kappa_{s,le}}$ for the radial statistics, and $\overline{\kappa_{s,le}|Z_{le}}$ and $\overline{Z_{le}|\kappa_{s,le}}$ for the axial. For reference, this plot also overlays radial and axial profiles of the negative of the gradient of the mean value of the axial velocity at the mean axial or radial location of the flame leading edge; i.e. $-d\bar{U}_z(r,z=\bar{Z}_{le})/dz$ and $-d\bar{U}_z(r=\bar{R}_{le},z)/dz$. Also shown to the side and bottom of the central figure are PDFs of the stretch rate and corresponding coordinate. The laminar extinction stretch rate from the CHEMKIN OPPDIF calculations $\kappa_{ext}^{RZ} = 2600\,[1/s]$ is also indicated. Finally, reference curves of the mean radial and axial strain rates are overlaid. The results show that the mean hydrodynamic strain, $\overline{\kappa_{s,le}} = 9500\,[1/s]$, a value that is 3.5 times higher than the calculated extinction flame stretch, $\kappa_{ext} = 2600\,[1/s]$. Prior workers have observed that unsteady laminar flames [162-165] can withstand instantaneous stretch rates substantially higher than corresponding laminar flame extinction stretch rates. However, here it is the mean value of the measured stretch rate that is higher than the steady extinction value. One possibility for this result is that stretch rate uncertainty is very high. However, the uncertainty of the estimate in the mean of the stretch rate, or standard error assuming Gaussian distribution, $SE_{\bar{\kappa}_{s,le}} = \sigma_{\kappa_{s,le}} \big/ \sqrt{N}$ (see the uncertainty section, Chapter 2.2.2.), is 650 [1/s], suggesting a 95% confidence interval (2σ) of 9500 ±1300 [1/s]. Even with this value, the mean stretch rates substantially exceed the computed extinction values. We do not fully understand how the flame can withstand such high stretch values, a topic that requires further study. However, we suspect that buoyancy forces associated with the high centrifugal loadings (estimated as ~5000 g using, D_0, $U_{z,0}$, and S_m~1), along with non-normal flame propagation (see Appendix B) may be responsible.

A follow up question is whether or not there is evidence of extinction in the high stretch data case 1. We expect extinction to be accompanied by flame surface breaking up due to local extinction events. It is difficult to differentiate an extinction or pre-extinction broken up flame from a helically wrapped flame interrogated by the laser sheet. We would expect extinction in the higher stretch case, which would be accompanied by an increase in the ratio of instances in which the flame appears broken up to candidate frames, in which the OH* and OH-PLIF leading edges match. There is not a significant difference between these ratios for the two cases, and therefore we presently do not have any evidence of extinction.

Figure 4.21 plots the same results for case 2. The mean stretch rate is $\overline{\kappa_{s,le}} = 670\,[1/s]$ - this value is substantially less than the reference extinction stretch rate, $\kappa_{ext} = 2700\,[1/s]$. The standard error for case 2 is 330 [1/s] (see the uncertainty section, section 2.2.2.).

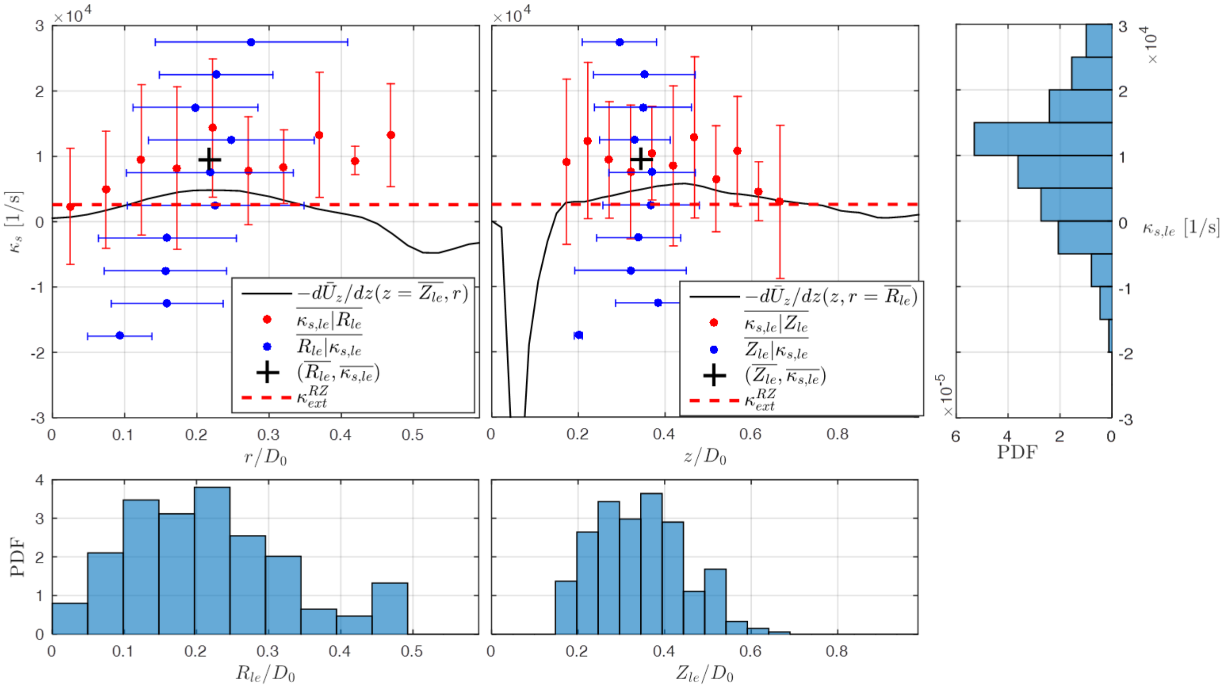

Figure 4.20: Corrected joint statistics of the flame hydrodynamic stretch vs. radial position, $\kappa_{s,le}$(t) vs. R_{le}(t), and vs. axial position, Z_{le}(t), at the flame leading edge for case 1. Each coordinate is plotted conditioned upon the other by binning and averaging. The RMS of each binned average point is indicated with error bars. PDFs of each coordinate are shown below and to the right. The mean values are plotted with a cross.

Comparing the stretch rate results for cases 1 and 2, note that the mean stretch rate in case 2 is 14 times lower than case 1. A basic stretch scaling of *U*/*L*, where *U* and *L* denote reference velocity and length scales, would suggest that the reference stretch should decrease by 70 [m/s] / 45 [m/s] = 1.6. Indeed, the unconditioned stretch rate, $-d\bar{U}_z/dz\,(r = \overline{R_{le}}, z = \overline{Z_{le}})$, calculated at the mean flame leading edge location, decreases from 4600 to 3100 [1/s], or 1.5 times, very nearly the expected value. Clearly, the actual mean stretch rate that the flame sees follows a much more complex scaling.

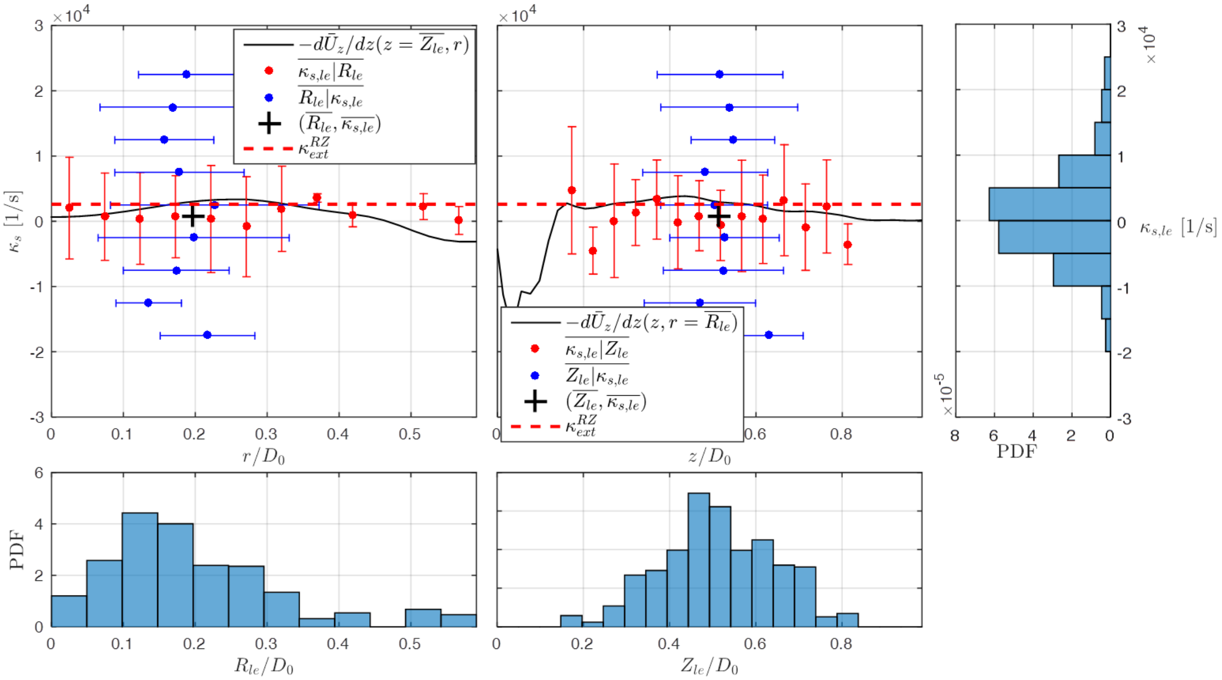

Figure 4.21: Corrected joint statistics of the flame hydrodynamic stretch vs. radial position, $\kappa_{s,le}$(t) vs. R_{le}(t), and vs. axial position, Z_{le}(t), at the flame leading edge for case 2. Each coordinate is plotted conditioned upon the other by binning and averaging. The RMS of each binned average point is indicated with error bars. PDFs of each coordinate are shown below and to the right. The mean values are plotted with a cross.

CHAPTER 5

RESULTS – LIQUID SPRAY FUEL

This chapter presents results after studying the physics of high pressure, liquid fueled combustion with the high shear swirler. These data were only available for analysis after performing combined fuel, OH-PLIF and two-phase stereo PIV, and reducing the data to separate the fuel and OH-PLIF fields, as well as liquid vs. gas phase PIV, as detailed in the Data Reduction Chapter 3. Again, this section follows the layout from the scope of work in the Introduction, Background, Motivation and Scope Chapter 1. This work is motivated by the lack of detailed experimental data sets of simultaneous fuel and heat release distribution fields in the literature due to the challenging nature of high pressure, liquid fueled experiments. The goal of these studies is to reveal general internal combustor physics such as characterizing the flame shapes, flow field and spray distribution. These scalar and vector fields are essential to combustor design for low emissions, broad operability limits, good pattern factor and hardware longevity.

5.1. Simultaneous Imaging of Fuel, OH, and Three Component Velocity Fields in High Pressure, Liquid Fueled, Swirl Stabilized Flames at 5 kHz

We next present results illustrating basic flow features and combustion physics using simultaneous velocity and scalar two-phase data with the liquid fueled, high pressure, high shear swirler. As noted above, PLIF images are only shown for the upper half of the flow.

5.1.1. General Flame and Flow Features

Figure 5.1 illustrates key swirl flow features, along with characteristics of the spray and OH distribution. As illustrated in Figure 3.18 and also shown in Figure 5.1 below, the red shading denotes fuel only, with signal coming from large droplets and ligaments, while the blue shading outside of the second black contour is signal from OH. The region between the two black contours is shaded purple, as also illustrated in Figure 5.1, where small fuel droplets and OH coexist and fuel/OH cannot be differentiated with this technique. From this figure, various features can be noted in the flame and flow that are of interest, including: (1) degree of fuel spray penetration, (2) swirling annular jet flow, (3) outer recirculation zone (ORZ), (4) elevated OH level outside and the annular jet, (5) helical vortex shedding from the nozzle shear layers (6) internal recirculation zone (IRZ) and centerline reverse flow, and (7) low OH level inside the annular jet, in the IRZ.

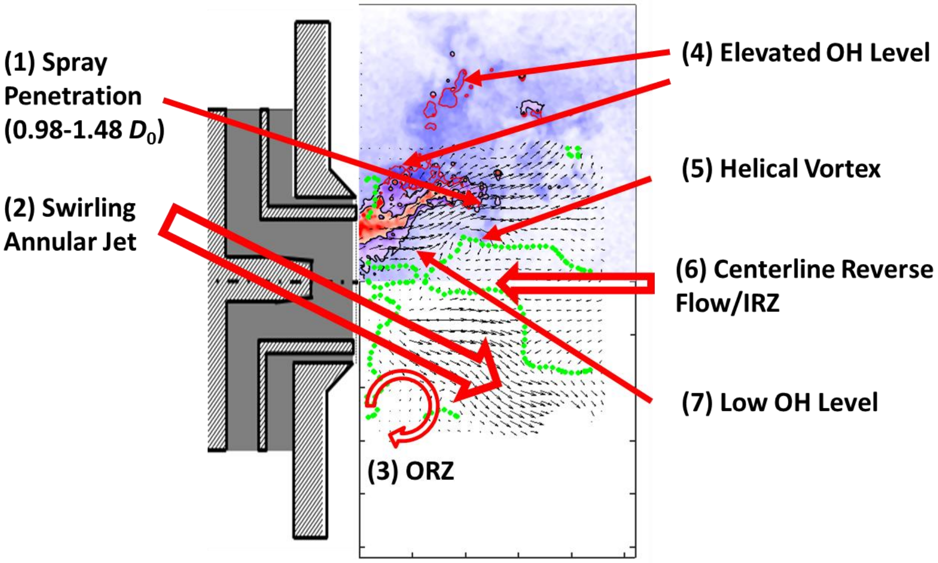

Figure 5.1: Overlay of instantaneous flow velocity, OH (blue), fuel (red), and OH+fuel (purple), showing general flow topological features for Case 1.

Additional instantaneous results for this case are shown in Figure 5.2 as a filmstrip of 6 consecutive frames 200μs apart. Each frame consists of part (a): two components of PIV, $U_z = 0$ line in green, and the regions of OH, fuel, and OH+fuel; and part (b): all components of PIV with the out-of-page component color coded, and the $U_\theta = 0$ line in black. In this sequence, the highly dynamic nature of the spray is evident. The helical vortex noted in Figure 5.1 advects axially as the 3-D vortex structure rotates and passes through the laser sheet. By comparing the images, flapping of the annular jet and spray is evident as well. The sPIV reveals that the swirling, out-of-plane velocity is highest in this annular jet region, similar to the axial velocity, indicating that the jet edges are regions of high shear in both the azimuthal and axial directions. The region of overlap between spray and OH is fairly wide compared to the region of pure spray (and no OH). The OH-PLIF (blue) signal is concentrated outside of the annular jet, in the ORZ. Note, as mentioned before, the presence of both elevated OH signal regions in certain regions (e.g., right outside the fuel jet and downstream of it in the annular jet), as well as a more diffuse background. This elevated OH region is likely the super-equilibrium OH present in the reaction and recombination zone, while the diffuse background is likely near equilibrium OH in the combustion products. Laminar flame CHEMKIN OPPDIFF calculations for decane at 5 bar, T_{ph} = 450K, and $\phi = 0.7$, show that the OH mole fraction peaks to a value about 4.5X its equilibrium value, and the OH recombination zone is at least 20 times thicker than the heat release zone. This suggests that it is reasonable to observe super-equilibrium OH for the present conditions. Note the structure of the elevated OH regions which forms a plume downstream of the liquid jet. Both small scale and large scale rollup of the edges of these plumes is evident in the images. Note the pocket at the end of the liquid jet with no OH, presumably consisting of air.

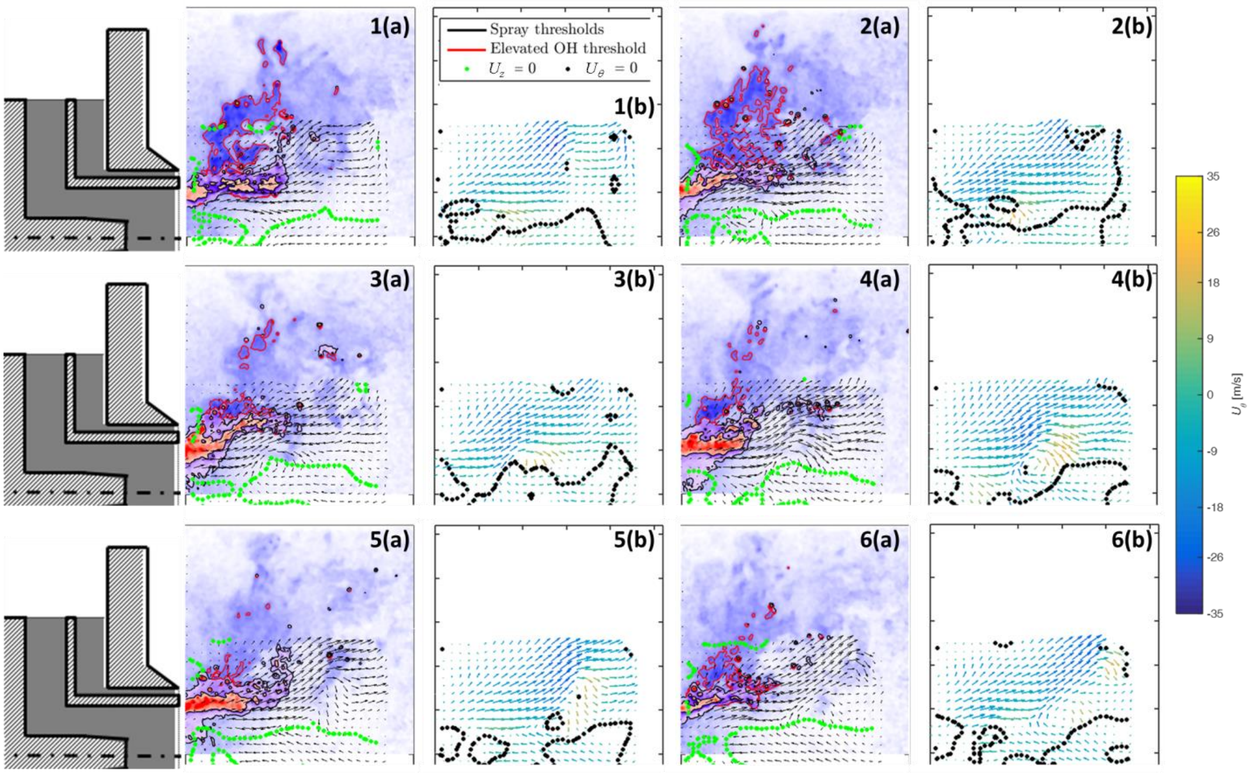

Figure 5.2: Case 1 instantaneous data. Six frame sequence ($\Delta t = 200\mu s$) of OH-PLIF (blue), fuel-PLIF (red), mixture of fuel and OH (purple) and sPIV in (a). Two components of sPIV are shown in (a) with black arrows and all three in (b). $U_z = 0$ line plotted in (a) (green) and $U_\theta = 0$ line plotted in (b) (black).

A film strip of instantaneous images from case 3, which is at a higher pressure and ϕ relative to case 1 is shown in Figure 5.3. Again, both the spray and flowfield are highly unsteady. One important difference relative to the above case is that there is flame now on both sides of the jet, vs. only on the outside for case 1.

Instantaneous filmstrips for three more cases, including the one with C-5 fuel are presented next. Figure 5.4 shows some instantaneous frames for the highest pressure case 5; time averaged results from this case were presented in the main body. Figure 5.5 shows three frames from the high preheat case 4 at T_{ph} = 570K. Relative to case 3, the fuel/air ratios and operating pressures are the same within 5%, while the nozzle velocity at the high preheat is 10% higher. The elevated OH-containing regions are larger. Figure 5.6 presents case 2, which is at the same pressure and preheat temperature as case 3, but with C-5 and at a lower global ϕ = 0.38 vs. 0.61. C-5 has a notably lower 90% boiling point of 438 K, relative to 518 K for Jet-A and should evaporate more quickly.

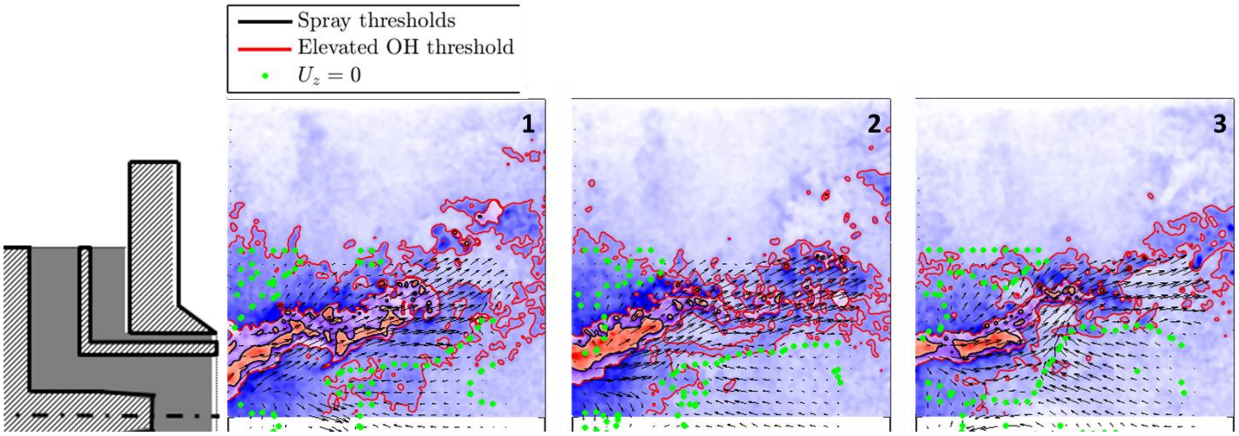

Figure 5.3: Case 3 instantaneous data. Three frame sequence (Δt = 200μs) of OH-PLIF (blue), fuel-PLIF (red), mixture of fuel and OH (purple), and sPIV (black arrows). U_z = 0 line in green.

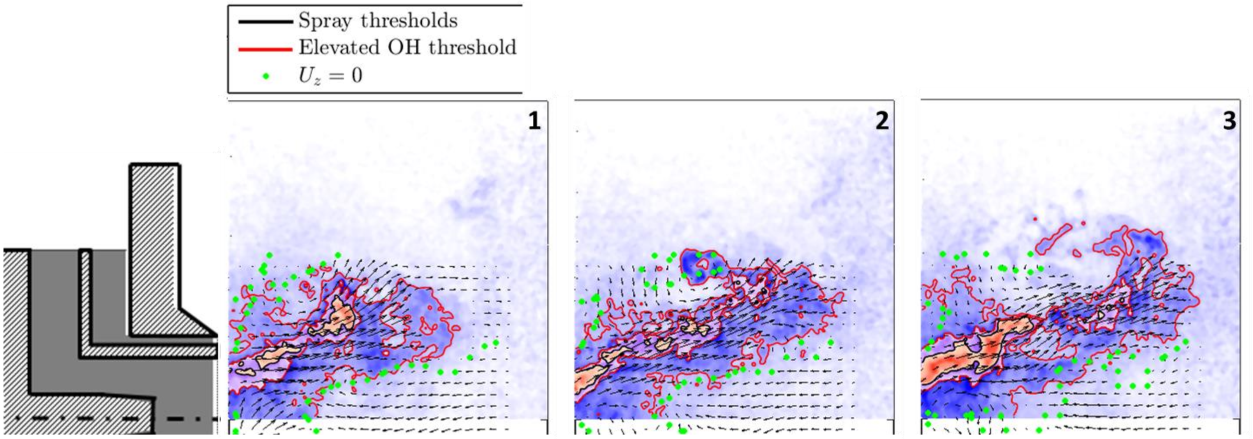

Figure 5.4: Case 5 instantaneous data. Three frame sequence (Δt = 200μs) of OH-PLIF (blue), fuel-PLIF (red), mixture of fuel and OH (purple), and sPIV (black). U_z = 0 line plotted in green.

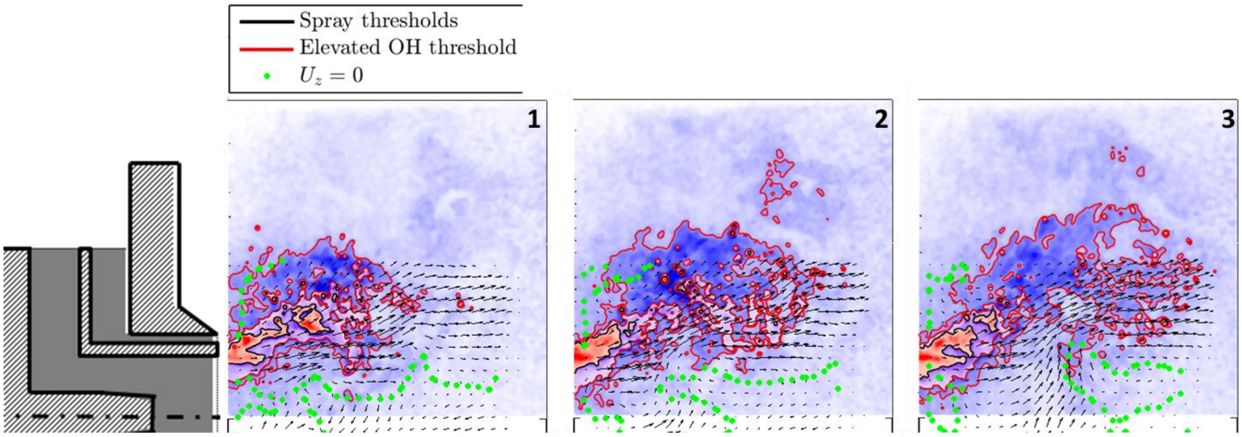

Figure 5.5: Case 4 instantaneous data. Three frame sequence (*Δt* = 200 μs) of OH-PLIF (blue), fuel-PLIF (red), mixture of fuel and OH (purple), and sPIV (black). U_z = 0 line plotted in green.

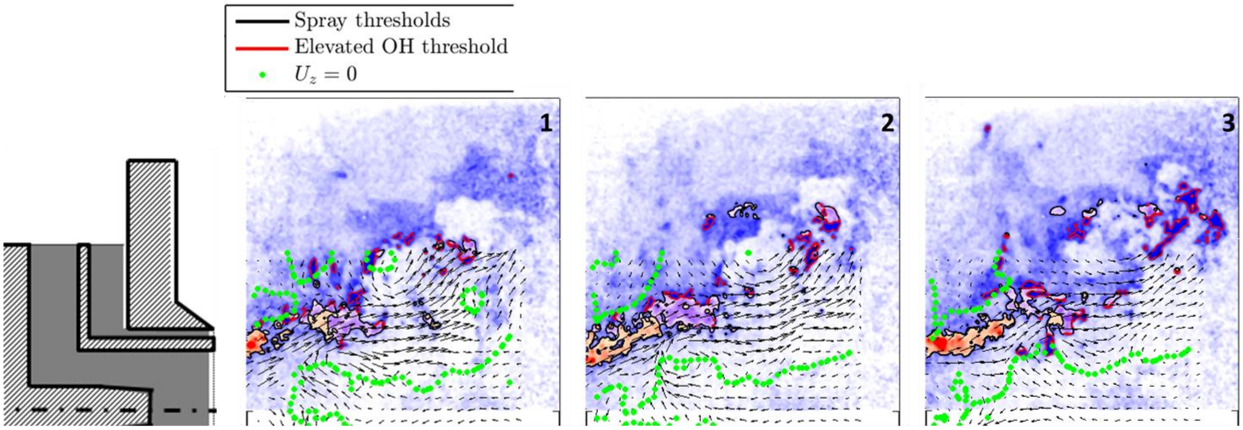

Figure 5.6: Case 2 instantaneous data. Three frame sequence (*Δt* = 200μs) of OH-PLIF (blue), fuel-PLIF (red), mixture of fuel and OH (purple), and sPIV (black). U_z = 0 line plotted in green.

Various time-averaged measures can be used to define quantitative metrics for the flow, spray, and flame. However, direct averaging of the scalar PLIF fields is not useful, as it is not entirely clear that the actual quantitative values of the OH fields are meaningful, or what the averages would be useful for. Therefore, we focus on probability fields, obtained by defining a threshold to binarize the field, and then averaging the instantaneous binarized fields. Figure 5.7 presents the time-averaged gas phase velocity field, as well as fuel spray $\bar{p}_1 = 0.5$ and $\bar{p}_2 = 0.5$ lines, and a few $\bar{p}_{OH,elev}$ lines. $\bar{p}_1$ is the probability field for *detectable* fuel spray, obtained by binarizing the instantaneous field into values of unity for intensities above the weak fuel cut-on threshold (from Figure 3.16 and Figure 3.18) and zeros elsewhere, and averaging the binarized images. The $\overline{p}_1 = 0.5$ ***line (purple) corresponds to 50% probability of finding <u>detectable</u> fuel***. This line can also be thought of as an OH boundary; i.e., there is predominantly OH outside. Similarly, $\overline{p}_2$ is the probability field for finding fuel spray only, see Figure 5.7(b), obtained by averaged binarized fuel images assigned ones for intensities above the strong fuel threshold and zeros elsewhere. The $\overline{p}_2 = 0.5$ ***line (red) corresponds to 50% probability of finding fuel spray <u>only</u>***. Although the $\overline{p}_1$ and $\overline{p}_2$ probability fields are indicative of the fuel evaporation, they are also affected by the unsteady motion of the spray. In other words, strong flapping of the spray will cause separation of iso-$\overline{p}_1$ and $\overline{p}_2$ values. Note that there is some OH in the region between $\overline{p}_1 = 0.5$ and $\overline{p}_2 = 0.5$, and its thickness is related to the distance between the flame and the bulk of the spray, as well as the unsteady motion of the spray. Finally, $\overline{p}_{OH}$ ***(blue lines) is the probability field for elevated OH levels***.

Figure 5.7(a) overlays several of these time averaged quantities in order to provide a picture of the reacting flow structure. Several scalar values are shown indicating the region where pure fuel, detectable fuel, and elevated OH exist – the $\overline{p}_1 = 0.5$ (purple), $\overline{p}_2 = 0.5$ (red), and a few $\overline{p}_{OH,elev}$ (blue) lines. The structure of the flow field is shown by indicating the time-averaged in-plane components of gas phase PIV (note some blanked regions in the fuel only region, for the reasons indicated in the “Data reduction” section on separating PIV into gas phase and liquid phase), the axial velocity stagnation line, $U_z = 0$ (green), the jet core (locus of maximum velocity magnitude) in a dashed black line, and inner and outer shear layers (ISL and OSL , respectively, defined as the locus of maximum out-of-plane component of vorticity) in black. Several observations can be made from this combined picture. First, note that, for this case, elevated OH is predominantly found *outside* of the OSL, in the ORZ; i.e., not in the IRZ (this is not always the case as shown later). As seen in the instantaneous frames from Figure 5.2 OH is detected inside of the ISL as well as along the annular jet, although not at these elevated levels for this case, but we will show other cases in which there are elevated levels of OH in the jet. The lower levels of OH are likely associated with the recirculating combustion products in the IRZ, and not indicative of a reaction front. The annular jet spreading is evident from the jet core. The jet core lines are almost identical for the cases 1 through 5 shown here, and so are not plotted. The dotted $U_z = 0$ line shows the recirculation bubble boundary, and also does not vary much across cases. The $\overline{p}_2 = 0.5$ contour penetrates about 0.49 D_0, and the $\overline{p}_1 = 0.5$ contour lies outside of that. Note also the location of the spray and elevated OH with respect to the key flow features. Specifically the “detectable fuel” and “fuel only” regions lie *between* the jet core and outer shear layer; i.e., they are in the annular jet column but on the outside. This is consistent with the picture for these filming type injectors shown in Figure 2.6 (right).

In order to provide a feel for the distribution of the spray probability values, Figure 5.7b plots iso-$\overline{p}_2$ values for 0.1, 0.2 and 0.5, and the “detectable fuel” $\overline{p}_1 = 0.5$ contour. It shows that the 0.1 and 0.2 $\overline{p}_2$ isocontours are located as expected between the $\overline{p}_1 = 0.5$ and $\overline{p}_2 = 0.5$ lines of Figure 5.7a. The exact spacing and shape of these lines changes with fuel type and operating conditions as the fuel evaporation rate and vapor distribution are modified. The liquid phase PIV is plotted in Figure 5.7(b) in order to enable comparison with the gas phase velocity field. Recall that vectors are shown only in locations with more than 100 realizations, so there are no vectors shown outside of a given region, which happens to roughly follow the no fuel $\overline{p}_1 = 0.5$ line. The liquid PIV is not drastically different than the gas-phase PIV. The key differences between the velocity fields is that the liquid PIV field shows a higher spreading angle along the outermost radial location, and a lower spreading angle along the innermost radial location.

In order to relate these features to the out of plane velocity, Figure 5.7(c) plots the time-averaged azimuthal velocity component using a color bar along with the U_θ=0 line in black. The U_θ=0 line is along the centerline, as expected, for an axisymmetric time-averaged flow.

The rest of this chapter is organized into three more sub-sections, discussing the spray distribution, flame shape, and the nature of flame stabilization across the various conditions.

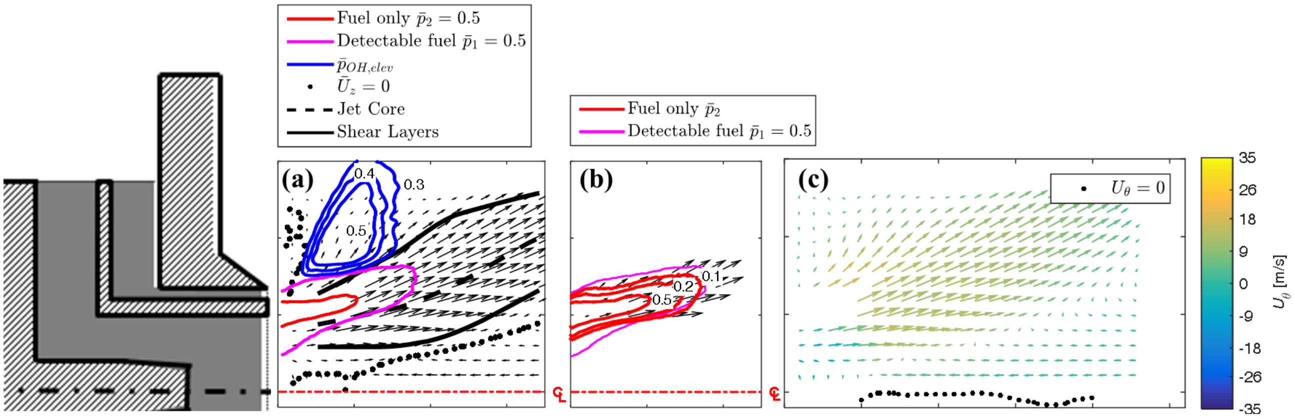

Figure 5.7: Case 1 time-averaged data. (a): Two components of gas phase sPIV shown along with U_z = 0 line (green). Fuel-PLIF $\bar{p}_2 = 0.5$ line (red) represents 50% probability of finding fuel spray only. Fuel-PLIF $\bar{p}_1 = 0.5$ line (purple) represents 50% probability of finding any detectable fuel. The jet core (dashed black) and maximum vorticity (solid black) lines are also shown. $\bar{p}_{OH,elev}$ field isolines are shown in blue, indicating the flame shape. (b): Fuel-PLIF $\bar{p}_2$ field and $\bar{p}_1 = 0.5$ line. (c): All three components of gas phase sPIV along with U_θ=0 line (dotted black). The combustor centerline, denoted C_L, is shown with a dashed red line.

5.1.2. Spray Distribution

The spray distribution is sensitive to preheat temperature, nozzle air velocity, fuel flow rate, pressure, and fuel composition. We can see it respond to changes in these quantities across test conditions. Note that the jet core and shear layers across the different cases are virtually identical, so results are only shown for one case. This also shows that the shifts in spray position and OH field discussed next are not due to shifts in time averaged gas flow field.

Figure 5.8 (a) enables comparison of cases 1, 3 and 5, representing our three operating pressures. We note that the fuel spray lines $\overline{p}_2 = 0.5$ and $\overline{p}_1 = 0.5$ are almost identical between case 1 and 3, although the pressure is about 75% higher and the fuel flow is increased as indicated by the higher ϕ. The $\overline{p}_2 = 0.5$ fuel spray contour for case 3 extends about 0.44 D_0, which is very similar to the 0.49 D_0 for case 1 despite the higher fuel/air ratio of 0.61 vs. 0.38 and elevated pressure of 3.4 vs. 2.1 bar. Also evident in Figure 5.8(a) is that the detectable fuel $\overline{p}_1 = 0.5$ lines are the same for cases 1 and 3.

The further increase in pressure and slight decrease in ϕ in going from case 3 to 5 results in the $\overline{p}_2 = 0.5$ line shifting upstream and penetrating axially 0.29 D_0. The OH boundary $\overline{p}_1 = 0.5$ line is significantly closer to the $\overline{p}_2 = 0.5$ fuel spray line, and extends only 0.59 D_0, relative to larger 0.84–0.88 D_0 values for the lower pressure cases. If increased fuel flow generally pushes the spray outward, it seems that increasing pressure brings the spray in, although the jet flapping may be different between the two cases and affecting the spray.

Figure 5.8(b) overlays $\overline{p}_1 = 0.5$ and $\overline{p}_2 = 0.5$ lines for cases 3 and 4. Everything else being equal, we expect the higher preheat case 4 to show faster evaporation by having a recessed fuel spray $\overline{p}_2 = 0.5$ line. Instead, we observe the OH boundary line $\overline{p}_1 = 0.5$ shifts axially downstream, from 0.84 to 0.98 D_0, and radially, from 0.74 to 0.93 D_0, and the fuel spray only $\overline{p}_2 = 0.5$ line also move out from 0.44 to 0.59 D_0. Apparently, this result is a manifestation of competing effects as we simultaneously increase the preheat temperature and nozzle velocity: First, although the fuel spray only $\overline{p}_2 = 0.5$ line moves outward, the closer spacing between fuel spray only $\overline{p}_2$ isolines, i.e. $\overline{p}_2 = 0.5$ and 0.1 lines (not shown for brevity but similar to Figure 5.7 (b), indicates the fuel is evaporating faster (an alternative explanation, of course, is that the liquid jet column is flapping less). Second, the faster evaporation likely produces a fuel-rich gas mixture, pushing out the OH boundary $\bar{p}_1 = 0.5$ line as observed. Third, the higher nozzle velocity would also push the spray and flame outward.

Figure 5.8 (b) also plots the fuel spray $\bar{p}_1 = 0.5$ and $\bar{p}_2 = 0.5$ lines, and shear layers for case 2 with the lower boiling point C-5 fuel. In the present case 2 the global ϕ is much lower, combined with a more volatile fuel resulting in much less spray. As expected, the fuel spray $\bar{p}_1 = 0.5$ and $\bar{p}_2 = 0.5$ lines move inward relative to cases 3 and 4.

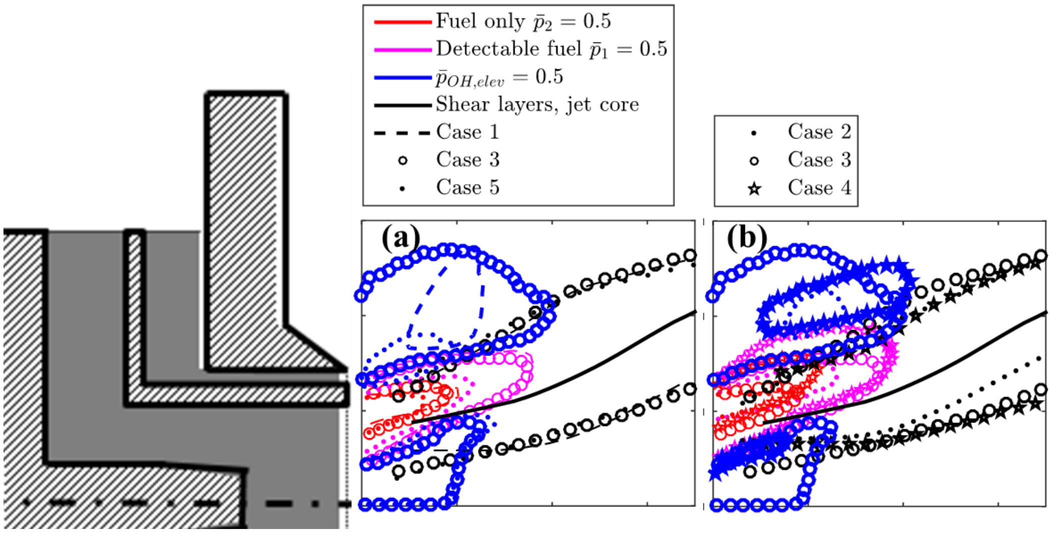

Figure 5.8: (a) Comparison across three pressures for cases 1, 3, and 5 with Jet-A. (b) A comparison of time-averaged data with fuel C-5 for case 2, and at two preheat temperatures for cases 3 and 4 with Jet-A. The time-averaged inner and outer shear layers (magenta) and jet core (same across cases - black) using gas phase velocity, $\bar{p}_2 = 0.5$ (red), $\bar{p}_1 = 0.5$ (purple) , and $\bar{p}_{OH,elev} = 0.5$ (blue) lines are shown. Note that for case 2, there is no $\bar{p}_{OH,elev} = 0.5$ isoline, and the highest probability line, 0.3, is shown.

5.1.3. Flame Shape

Prior work [35] in gaseous premixed flows shows that multiple flame topologies may exist in swirl flows of this nature, with the flame attaching itself to the ISL/OSL of the nozzle, or be stabilized aerodynamically in the center of the flow by vortex breakdown. In the present work we use super-equilibrium OH levels to indicate the flame location. We observe two flame configurations. The first one (Type I) appears for the low ϕ, low preheat temperature cases 1 and 2, with a flame wrapped around the outside of the OSL. In other words, we hypothesize that the OH in the center is not indicative of reactions, but with recirculating products. Note that case 2 is the only one with C-5 fuel, and fuel composition may be playing a role here. The second configuration (Type II) appears at higher ϕ and preheat temperature, with a flame appearing both outside of the OSL and around the inside of the ISL. The sensitivity of the flame shape to preheat temperature and equivalence ratio is illustrated in Figure 5.10 for all cases. Figure 5.10 (a) plots this sensitivity against preheat temperature and Figure 5.10 (b) against the combustion pressure, illustrating that the effect is dominated by change in equivalence ratio, although it is possibly also affected by preheat temperature and pressure.

These observations are illustrated using instantaneous frames comparing case 1 from Figure 5.2 with case 3 in Figure 5.3. The frames in Figure 5.2 from case 1 reveal very weak or even complete lack of OH-PLIF in the inside of the IRZ or in the center of the flow. In contrast, the frames from Figure 5.3 show super-equilibrium OH in both the ORZ and IRZ.

The observations on flame shape from instantaneous data are supported by time-averaged data. Figure 5.9 compares the time-averaged data for cases 1 and 3. In particular the $\overline{p}_{OH,elev}$ fields indicate the flame shape, and show a flame predominantly in the ORZ for case 1 and a flame in both the ORZ and IRZ for case 3. We note that OH is found throughout the combustor, i.e. the instantaneous images in Figure 5.2 from case 1 show low and even occasionally elevated levels of OH in the IRZ region, although the time-averaged flame is predominantly in the ORZ region.

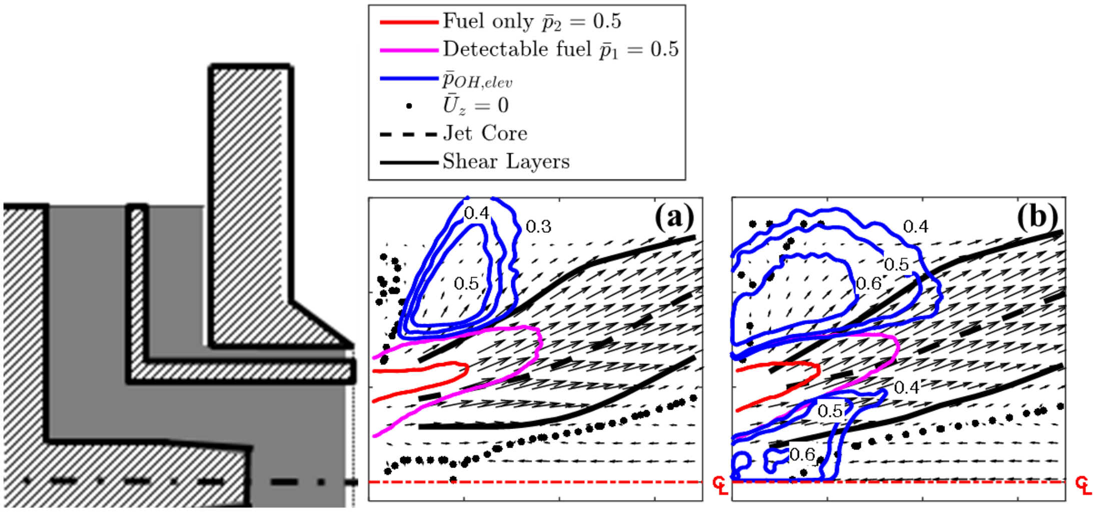

Figure 5.9: Comparison of two flame shapes encountered for cases 1(a) and 3(b). Two components of time-averaged gas phase sPIV shown along with $U_z = 0$ line (dotted black). Fuel-PLIF $\bar{p}_2 = 0.5$ line (red) represents 50% probability of finding fuel spray only. Fuel-PLIF $\bar{p}_1 = 0.5$ line (purple) represents 50% probability of finding any detectable fuel. The jet core (dashed black) and maximum vorticity (solid black) lines are also shown. $\bar{p}_{OH,elev}$ field isolines (blue) indicate the flame shape. (a) Case 1 has flame configuration I and (b) case 3 has flame configuration II. The combustor centerline is shown with a dashed red line.

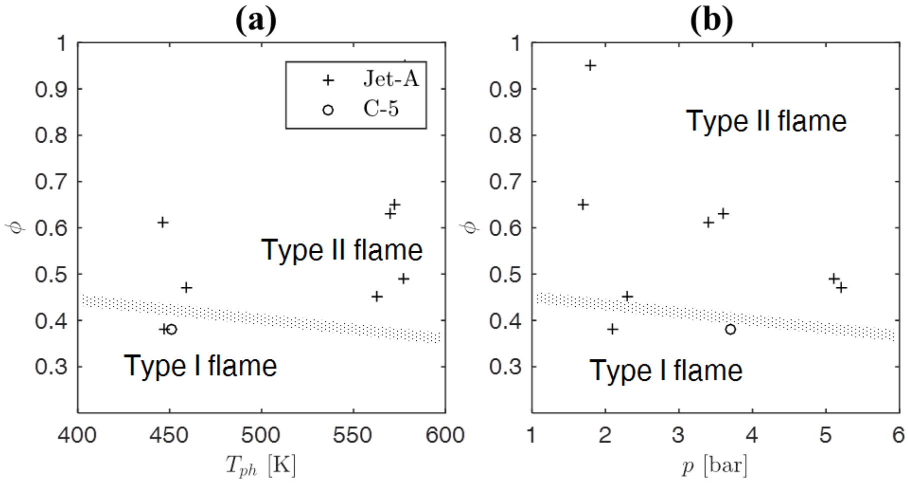

Figure 5.10: Sensitivity of the flame shape to fuel/air equivalence ratio and: preheat temperature (a), combustor pressure (b).

5.1.4. Flame Stabilization

This section considers first the points where reaction originates and compares and contrasts these spray flame results with premixed flames. We compare with the methane/air data with this identical nozzle in Section 4.2. In order to achieve uniform premixing, the fuel injection holes were not used in that study, and the fuel and air were mixed 2.0 m upstream of the nozzle. As the axial and radial distribution of heat release has such profound influences on combustor behavior, it is useful to reflect on the differences between this uniformly premixed flame reported previously and this spray flame.

As discussed in Section 1.1, premixed flames encountered in annular jet configurations like this have multiple configurations depending upon whether the flame is stabilized in the inner or outer shear layers of the annular jet, or is aerodynamically stabilized at interior stagnation points. From these stabilization regions, they then propagate into the reactant jet core, at an angle controlled by the ratio of turbulent flame speed and flow velocity. PIV/OH-PLIF data from the present nozzle show that the flame has an “M-shape” and stabilizes near the outer shear layers and partially in the inner shear layers and vortex breakdown bubble. This is shown in Figure 5.11 with a time-averaged velocity field and with a $\overline{p}_{OH,elev} = 0.5$ contour (blue). This iso- $\overline{p}_{OH,elev}$ line is determined in an analogous manner as in this liquid fuel study; i.e., by averaging intensity binarized OH-PLIF images, in which value of one corresponds to elevated OH and value zero elsewhere. The intensity threshold is determined in a similar way but much more straight forward way as the fuel and OH-PLIF thresholds discussed here, since the flowfield either does or does not have OH. Since the instantaneous isolines indicate the reaction zone for this premixed system, the $\overline{p}_{OH,elev} = 0.5$ isoline in Figure 5.11 represents the time-averaged reaction zone location.

Comparing the $\overline{p}_{OH,elev} = 0.5$ isolines in Figure 5.9 and Figure 5.11 shows some significant differences. In the premixed case (Figure 5.11), the flame originates in the low velocity shear layers and/or recirculating flow regions, as expected. Similarly, the outer spray flame (Figure 5.9) originates in the OSL, also near the indicated shear layers. In contrast, looking at all the spray flame results for cases where Type II flames are observed, note that the *inner flame always originates in the high velocity jet core itself* (e.g., see cases 3 and 5 in Figure 5.8, or the better view of case 3 in Figure 5.9). This would not happen in a premixed combustion system as the velocity inside the jet is too high relative to the turbulent flame speed. Rather, these results starkly illustrate the different controlling physics for flame location between the premixed case and spray flame – the spray flame sits right outside of the spray. As the outside of the spray is nearly coincident with the outer shear layer, the flame is also fortuitously coincident with the shear layer. However, the fact that the inside edge of the spray is well inside of the jet core allows us to differentiate the relative roles of the shear layer and spray placement, as the flame is clearly inside of the jet core. In contrast, as premixed flames stabilize via a propagating mechanism, they will originate in low velocity regions.

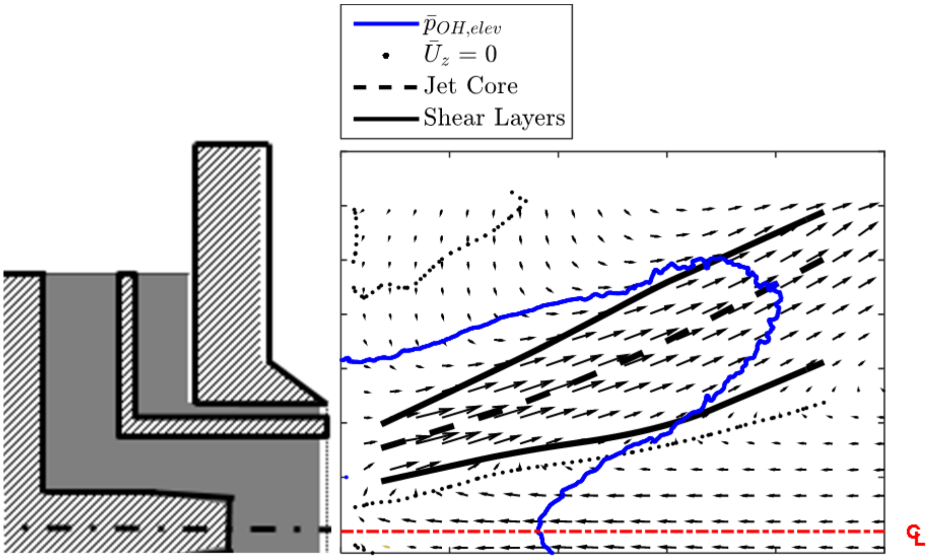

Figure 5.11: Gaseous time-averaged PIV/OH-PLIF data with present high shear swirler. Blue line is $\bar{p}_{OH,elev} = 0.5$ contour or the average location of the reaction zone. Solid black lines are the shear layers. Dashed black line is jet core. Thin dotted black line is $U_z = 0$. The combustor centerline is shown with a dashed red line.

CHAPTER 6

CLOSING REMARKS AND FUTURE WORK RECOMMENDATIONS

6.1. Closing Remarks

Design of efficient, low emission and reliable gas turbine combustors requires understanding of the internal physics. For example, flame shape and location influence and are important for understanding hardware heat loading and combustion instability limits. Pattern factor at the combustor exit is related to the flame shape and location, and is critical to proper inlet conditions for turbine design. Another related design property is low pollutant emissions, which is driven by increasingly stringent emissions requirements. This work generally focuses on swirl stabilized combustors for premixed and liquid fuel spray systems, and addresses different specific problems.

6.1.1. Stagnation Point Dynamics

One aspect of this work is inspired by the dynamic nature of swirl flows with vortex breakdown. These flow fields are subject to an interesting instability: the precessing vortex core, which translates to precession of the inner recirculation zone. The inner recirculation zone provides hot, low velocity regions, key to flame stabilization. Among the different possible flame shapes with these flow fields, aerodynamically stabilized flames are particularly interesting due to their lifted nature and potential to reduce hardware heat loading. Furthermore, their lifted nature means their location can move within the combustor. Precession of the flow field and flame can cause systematic differences between the instantaneous and time-averaged characteristics. Since these scalar quantities are often inferred from time-averages of CFD or experiments, it is important to understand the relationship between the time-averaged and instantaneous behavior.

A research question driving this work was how precession affects the location and existence of axial velocity stagnation points, as those are important to flame stabilization. We further asked how precession affects the symmetry of the time-averaged flow and the rate of convergence of means. These questions were addressed for an atmospheric, premixed methane/air aerodynamically stabilized flame, in a practical aero engine geometry: dual annular counter-rotating swirler without a centerbody.

Insight into topological features of the flow was obtained by a model problem, consisting of a dual zone forward and precessing reverse flow region. An important experimental observation, replicated in this model, is that precession around the central axis causes the average flow field stagnation point to be completely different from the mean location of the instantaneous stagnation point. This implies that average treatments of the flow field would place aerodynamically stabilized flames in a wrong location. It also shows that the presence or absence of a centerline axial jet is not indicative of some bifurcation in the instantaneous flow field, but may simply reflect a smooth, monotonic variation in the precession radius. Lastly, precession can cause axial asymmetry in flowfields, and average quantities to statistically converge slower than predicted by Gaussian statistics. An additional contribution is the implementation of progress variable fields to flow velocity as a nonlinear averaging technique to reveal swirl flow dynamics.

6.1.2. Aerodynamically Stabilized Flames

This work also focused on characterizing aerodynamically stabilized flames in a swirling flowfield with vortex breakdown and time-averaged reverse flow on the centerline. With the gaseous fueled high shear swirler the flame was stabilized by instantaneous stagnation points created by helical vortical structures. It was curious that the flame was not flashing back.

We focused on the flame leading edge, as in the quasi-steady limit this point controls flame stability. We specifically asked where the flame leading edge is located; what the local flow and flame stretch are at this point; and how these different quantities are correlated.

To answer these questions we applied a novel diagnostic based on simultaneous line-of-sight and planar flame imaging. The combination of the line-of-sight OH* chemiluminescence with the planar OH-PLIF allowed selecting instantaneous frames in which the flame leading edge lay in the interrogation plane. This also enables calculation of the full hydrodynamic flame stretch from PIV, a quantity that in general requires measurements of all velocity gradients in three dimensions.

The results show that the flame leading edge precesses off-axis, as might be expected in a high swirl flow with a precessing vortex core. The leading edge is also perturbed axially back and forth, but in an uncorrelated manner with the radial motions. This shows that the precession axis is not tilted off the axial direction. As such, the significant motion of the flame leading edge is associated with a precessing motion around a given average radial location, with significant additional radial and axial perturbations.

The results also indicate that the flame position adjusts itself to the dynamic flow conditions in a complex manner, as the high velocity annular jet and reverse flow region flap around. These cause the leading edge to be pushed axially back and forth and radially in and out. For example, the average axial velocity conditioned on the flame leading edge, $\overline{U_{z,le}}$, is 9m/s for case 1. In contrast, the average axial velocity, $\bar{U}_z(r = \overline{R_{le}}, z = \overline{Z_{le}})$, calculated at the mean flame leading edge location, is four times higher than the flame leading edge mean axial velocity. This clearly shows how kinematic effects cause the flame to locate itself in a region of high time-averaged velocity – in other words, the flame naturally moves forward and backward in regions of low and high velocity. In contrast, in the lower velocity and lower stretched case 2, the ratio between the flame leading edge and flow mean axial velocities are inverted – i.e., the time-averaged velocity is half the conditioned mean velocity.

Calculated stretch rates show much higher sensitivity to mean flow velocity than might be expected from basic scalings. In other words, the mean velocity decreases by 1.6 (from 70 to 45 m/s) for cases 1 and 2, respectively, but the corresponding conditioned stretch rate decreased by 14 times. For reference, the unconditioned stretch rate, $-d\bar{U}_z / dz\,(r=\overline{R_{le}}, z=\overline{Z_{le}})$, calculated at the mean flame leading edge location, decreases from 4600 to 3100 [1/s], or 1.5 times, nearly the expected value. Understanding this scaling is an important issue requiring further study. As noted by Lieuwen et al. [166], the scaling of flame stretch rates in shear layer stabilized flames also is much more complex than simply using a reference velocity and length scales. In that case, it was due to the superposition of shear and normal flow straining, which can have opposite signs and different length scale scaling. In this case, we are not aware of any prior work to consider flame stretch scaling. In addition, the measured stretch rate is about 3.5 times higher than the estimated extinction stretch rate for the high velocity case. The uncertainty in the estimate of the mean measured stretch rate is high, being a derivative of the velocity, but does not exceed 650 [1/s] for the high velocity case, and so even if the measured value is half of its estimate, it is still substantially larger than the computed κ_{ext}^{RZ} value (1.8 times). Of course, it is well known, that flames can withstand instantaneous stretch rates that exceed extinction values, if the stretch rate excursions are of fast enough time scale [162-165]. The difference here is that the *time-averaged* stretch rate exceeds the extinction value. This issue also requires further clarification. One interesting feature of this problem is the significant negative values of the instantaneous stretch.

Lastly, a general observation was that statistics of the flame leading edge revealed no correlation between radial and axial flame leading edge position, and no correlation between stretch and position or stretch and velocity. This suggested that for a given axial, radial and azimuthal velocity, or radial and axial position, the full range of flame stretch is observed.

6.1.3. Spray Combustion Physics Through Two-Phase PIV and PLIF

Liquid fuel combustion adds a few factors to combustor design relative to premixed combustion, due to the flow being dual phase and non-premixed. Examples are spray and gaseous fuel distribution, local equivalence ratio, and liquid and gas phase velocity. These quantities are not extensively studied due to the challenges associated with performing such measurements in high pressure, liquid fuel reacting flows. This work aims to provide insights into the combustion physics of liquid fuel in an aero engine type combustor at elevated pressures by applying simultaneous time-resolved (5kHz) sPIV, OH-PLIF, and fuel-PLIF. This work presents the first known to this author simultaneous measurements of these quantities. In particular we inquired into the simultaneous structures of the spray, flame position, and gas and liquid phase flow field. We were specifically interested in finding any differences between the flame shape and locations of the flame with respect to the flow for liquid spray vs. premixed combustion. Although the liquid spray work is at elevated pressures, while the premixed combustion is at atmospheric pressures, similar nozzle velocities were used and both flows exhibited bubble-type vortex breakdown with reverse flow along the centerline.

Thus, we have demonstrated a technique which uses a single dye laser to excite both the OH and fuel, and the signals are separated spectrally and temporally using two cameras and intensifiers. Intensity histograms are used to extract thresholds, which are used to identify regions of fuel, OH, and a mixture of fuel and OH.

In order to demonstrate the technique at multiple conditions, measurements were taken with Jet-A and C-5, (C-5 has a lower boiling point, higher aromatics content, and lower viscosity), and at different preheat temperatures of 450K and 570K, and pressures of 2.1, 3.5, and 5.2 bar. The resulting data enable simultaneous visualization of the flow field, spray, and flame location and enable a construction of key flow/flame features that are not possible to infer with a single measurement. At lower equivalence ratio, the flame exists only outside of the fuel jet in the ORZ, but increasing preheat temperature and equivalence ratio allows an M-shaped flame to exist, with a portion in the IRZ. The observation that multiple flame topologies are possible with the same fuel injector is well known for gaseous, premixed flames. Although expected, this observation is still very significant as these different flame shapes would have different liner heat loading characteristics, combustion instability characteristics, and emissions characteristics.

A second important observation is the location of the flame with respect to the jet flow and fuel features. These data clearly show the flame originating in the high velocity core just outside of the spray – i.e., the flame follows the fuel. Again, while this observation is not necessarily surprising, it was noted that premixed flames are located in low velocity regions, and that the location of the flame in a premixed configuration with this geometry would have been quite different. Again, this observation has important implication on the flame location and axial heat release distribution.

An additional result of this work was the adaptation of the nonlinear averaging technique used in the gaseous fueled portion of this work, based upon thresholding of the inferred spray and flame locations, to develop progress field maps to elucidate the general structure of the flow, spray, and flame. Such progress field maps are useful for quantifying statistics about the relative locations of these three key quantities, and for reducing (but not replacing) a large set of time-resolved data into a reduced set of results, useful for both understanding flow physics as well as comparison of results with computations.

It is important to discuss the sensitivity of these results to the thresholding approach, as well as the robustness of the inferred flow structures to these values. This was a question that we devoted significant attention to. As noted in Data Reduction, Section 3.2., we computed and compared the thresholds for different populations of systematically different kinds of images -light spray frames (one standard deviation dimmer than average) and heavy spray frames (one standard deviation brighter than average). The resulting thresholds were within 1–3mm of each other on the flame images. Moreover, we performed significant comparisons of the results where threshold values were systematically increased and decreased by up to 30%. The basic structure of the spray and flame location discussed above are quite robust to any reasonable variation of these parameters. As might be expected, the location of “detectable spray” is most sensitive to these variations, while the location of “fuel only” is the least sensitive.

6.2. Future Work Recommendations

6.2.1. Stagnation Point Dynamics

As alluded to previously, in geometries with a centerbody the vortex breakdown stagnation point can be attached to the centerbody and be nearly static. These geometries were not addressed by our experiments and model problem, but are interesting as flames can be stabilized aerodynamically by instantaneous stagnation points created inside the inner recirculation zone by large scale dynamics. This is the case with the high shear swirler also studied in this work with its aerodynamically stabilized flame, whose time-averaged position is in reverse flow. As some of the findings of this work were specific to swirling nozzles without a centerbody, a remaining research topic is to generalize the results to swirling geometries with centerbodies, and any other practically relevant variations. It appears that a time-averaged representation of this flowfield is incapable of properly predicting flame location. Therefore we ask if there is a high order statistic which can accurately reflect aerodynamic flame stabilization by instantaneous stagnation points created by helical vortical structures. This can begin with analysis of our aerodynamically stabilized flame with the premixed methane/air high shear swirler. Furthermore, this analysis can be performed on the liquid fueled high shear swirler data, in which lifted flames are equally relevant.

6.2.2. Aerodynamically Stabilized Flames

As noted above, several additional studies are motivated by this work. First, given the development of the conditioning technique, it will be useful for additional workers to make similar measurements on aerodynamically stabilized flames. This will enable checking several of the key observations described above for a larger range of flow conditions and geometries. Second, better understanding is needed of the flame stretch scaling for aerodynamically stabilized flames, as well as how the flame instantaneously adjusts itself to an evolving flow/strain field. For example, it would be useful to supplement our two velocity cases with several intermediate velocities, and study the flame location and local flow characteristics response. These intermediate cases would help answer the remaining question of why flames stabilized aerodynamically by instantaneous stagnation points in regions of time-averaged reverse flow do not flash back into the nozzle. Our current theory that the flow strain rate is prohibitively high any further upstream can be tested using such data from gradually increasing nozzle velocity, by looking for an upstream shift of the flame location, with corresponding increasing flame stretch. Finally, further analysis is needed for relating computed stretch sensitivities for model flames to measured values in complex, time evolving configurations as described here. For example, why are the time-averaged stretch values so high relative to laminar extinction stretch rate calculations? One potential reason is centrifugal force effects. As mentioned in the literature review section of the introduction Chapter 1, swirling flows can develop high G-forces on the order of thousands of g (estimated as ~5000 g using, D_0, $U_{z,0}$, and S_m~1). Precessing aerodynamically stabilized flames as the one studied in this work are, therefore, subjected to such accelerations. Induced buoyant forces can, in turn, modify flame flow field properties governing flame speed and stretch sensitivity. The flame leading edge centrifugal G-forces can be calculated and characterized for the present data. However, the present laminar flame speed calculations exclude buoyancy effects, and need to be modified for future studies. We suggest one approach by considering Cantera chemical kinetics open source codes to compute extinction flame stretch. Whatever model problem is chosen, e.g. symmetric opposed jet, the momentum equation may be modified to add centrifugal forces to deal with buoyancy effects.

A second potential reason is non-normal flame propagation, i.e. if the flow angle relative to the flame surface is non-normal, the flame stretch computed using our definition is not representative. Appendix B briefly discusses how the most frequent flow angle for the high stretch case 1 is 45 degrees, inflating the computed stretch by a factor of $\sqrt{2}$ by virtue of our definition. One way to deal with this is to condition the stretch values based on flow angle, or compute the gradient along the flow direction. Since our data sets have only a few hundred realizations, this work is left for future research.

6.2.3. Spray Combustion Physics through Two-Phase PIV and PLIF

For the spray fuel work, there is a need for continued improvement of scalar imaging in liquid fueled systems of this nature, particularly in flows with heavy levels of particulates. For example, many aircraft engine applications of the kind that motivated this work, actually operate with rich front ends, and thus the flame and flow are often surrounded by a particulate cloud (e.g., see Schroll, Klinner [113] or Meier, Heinze [114]). Moreover, the ability to simultaneously resolve other key scalars, such as those indicative of fuel-decomposition, soot formation, and pollutant formation would be very enlightening, both from providing insights into controlling physics, as well as for comparison with and validation of time-resolved computations of reacting sprays. For example, the present set of results can be used to benchmark calculations of the flow field and basic flame position features, but additional measurements would be needed to validate spatio-temporal locations of soot or NOx formation.

Interpretation of our PLIF data relies on intensity thresholding to identify regions of OH-PLIF and fuel-PLIF. Ideally the two PLIF signals would be detected independently. One solution would be to pick a specie other than OH, which can be excited and detected independently from fuel, but still provides important information about the heat release/flame distribution. One candidate, CH, is commonly used as a flame marker and can be excited with near visible or visible light for which the absorption of hydrocarbon fuels is much lower. Of course this experiment would require a second PLIF laser system, and the SNR for CH-PLIF would have to be assessed.

With that said, the current method needs further verification. First, the sensitivity to laser intensity and profile variations from shot to shot needs assessment. This can be done by simulating typical variation amplitudes and spatial wavelengths into the existing data to check the response of key characteristics, such as our inflection points. Ultimately this problem can be addressed by recording instantaneous laser sheet correction data. Second, laser depletion effects by fuel absorption need assessment. Some supporting fuel absorption measurements may be required, after which this affect can also be simulated into the existing data. Furthermore, it would be useful to define a relatively accurate statistics model capable of simulating the fuel and OH-PLIF intensity histograms observed. This way they can be fitted using the model to extract more useful quantities than these natural inflection points, which can be helpful for comparison with CFD. For example, extracting the locus of mean volume of droplets or ligaments is a natural quantity to compare with CFD.

We conclude with a few comments on experimental design, motivated by the remaining task to characterize the sensitivity to operating conditions of flame position and fuel spray distribution in respect to the flow. As mentioned before, the operating conditions parameters changed more than one at a time for the data points collected in the present work as the focus was more on developing the technique. It is desirable to obtain runs with changes only in equivalence ratio, preheat temperature, pressure, or fuel type, while holding the remaining parameters constant in order to analyze various parameter effects. Furthermore, the present orientation of the interrogation plane along a diameter makes the data (particularly fuel and OH distribution) sensitive to azimuthal variations in fuel distribution associated with the injector holes' orientation. The fuel distribution varies instantaneously and from case to case, making some cross-case comparisons difficult. A volumetric measurement could provide enough information to be able to track fuel concentration isolines across cases, but adds substantial complexity. A simpler approach would be r-θ plane cuts to capture azimuthal variations so that cases can be compared for a given axial position.

APPENDIX A

AERODYNAMICALLY STABILIZED FLAME LEADING EDGE FLOW CHARACTERIZATION VARIABLE DOUBLES PLOTS

For the aerodynamically stabilized flames with the methane/air, atmospheric, high shear swirler, the six measurements at the flame leading edge are: $Z_{le}(t)$, $R_{le}(t)$, $U_{z,le}(t)$, $U_{r,le}(t)$, $U_{\theta,le}(t)$, and $\kappa_{s,le}(t)$. There are 15 unique combinations of variable couples. Table 7.1 lists each combination and references the corresponding plot for the two cases. Each plot shows corrected statistics of a combination of flame leading edge measurements in the r-z plane for cases 1 and 2. Histograms of each coordinate are shown below and to the right. One variable is placed into bins conditioned by the other variable. The RMS is indicated with "error" bars. The average value is also plotted.

Table 7.1: Flame leading edge measurement combination plot set for cases 1 and 2

Number	Figure Axes	Case 1	Case 2
1	$U_{z,le}$ vs. $\kappa_{s,le}$	Figure 7.1	Figure 7.18
2	$\kappa_{s,le}$ vs. $U_{r,le}$	Figure 7.3	Figure 7.19
3	$\kappa_{s,le}$ vs. $U_{\theta,le}$	Figure 7.4	Figure 7.20
4	$\kappa_{s,le}$ vs. R_{le}	Figure 7.5	Figure 7.21
5	$\kappa_{s,le}$ vs. Z_{le}	Figure 7.6	Figure 7.22
6	$U_{z,le}$ vs. $U_{r,le}$	Figure 7.7	Figure 7.23
7	$U_{\theta,le}$ vs. $U_{z,le}$	Figure 7.8	Figure 7.24
8	$U_{z,le}$ vs. R_{le}	Figure 7.9	Figure 7.25
9	$U_{z,le}$ vs. Z_{le}	Figure 7.10	Figure 7.26
10	$U_{\theta,le}$ vs. $U_{r,le}$	Figure 7.11	Figure 7.27
11	$U_{r,le}$ vs. R_{le}	Figure 7.12	Figure 7.28
12	$U_{r,le}$ vs. Z_{le}	Figure 7.13	Figure 7.29
13	$U_{\theta,le}$ vs. R_{le}	Figure 7.14	Figure 7.30
14	$U_{\theta,le}$ vs. Z_{le}	Figure 7.15	Figure 7.31

15	R_{le} vs. Z_{le}	Figure 7.16	Figure 7.32

Case 1 Plots

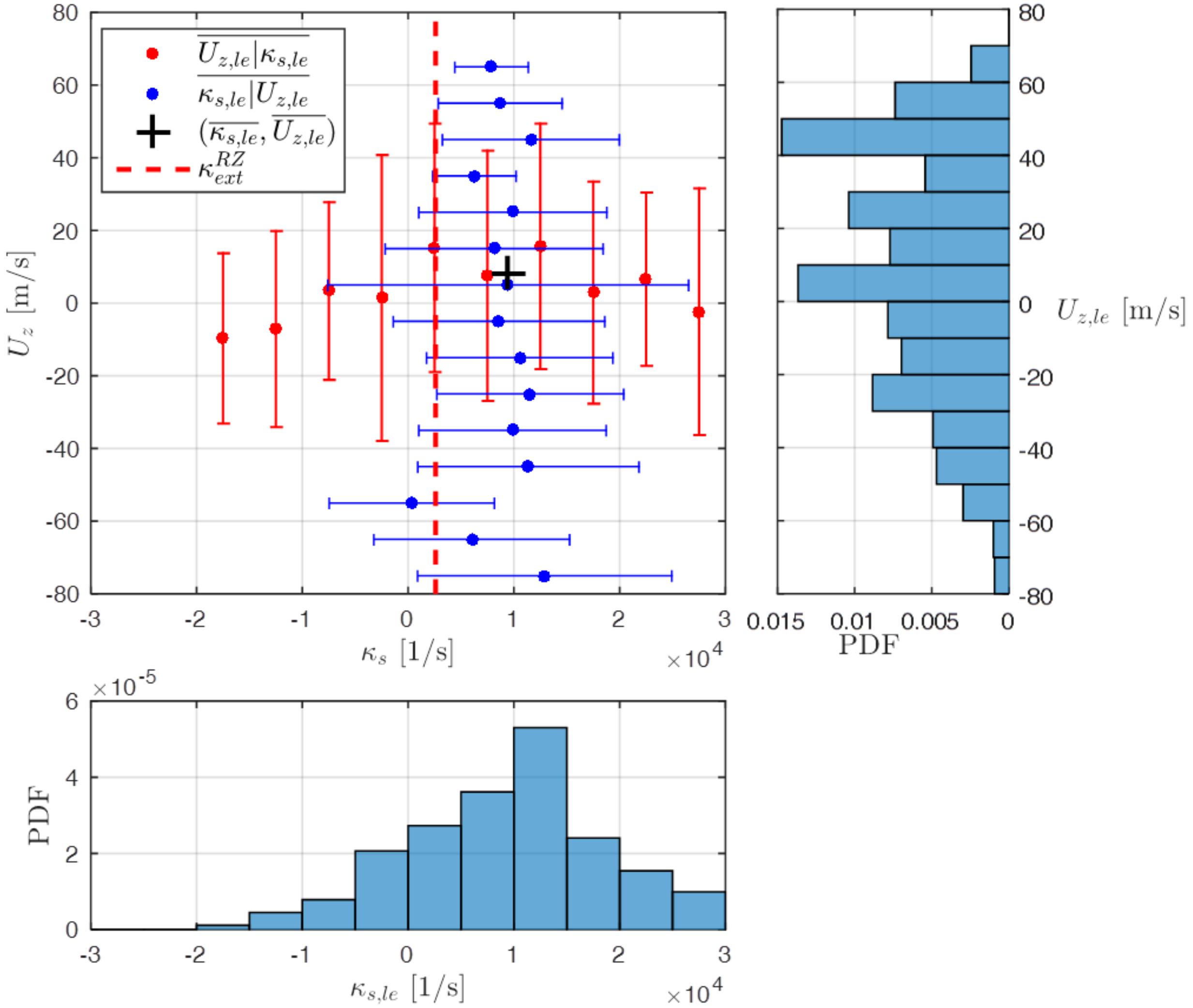

Figure 7.1: Case 1, plot 1, $U_{z,le}$ vs. $\kappa_{s,le}$

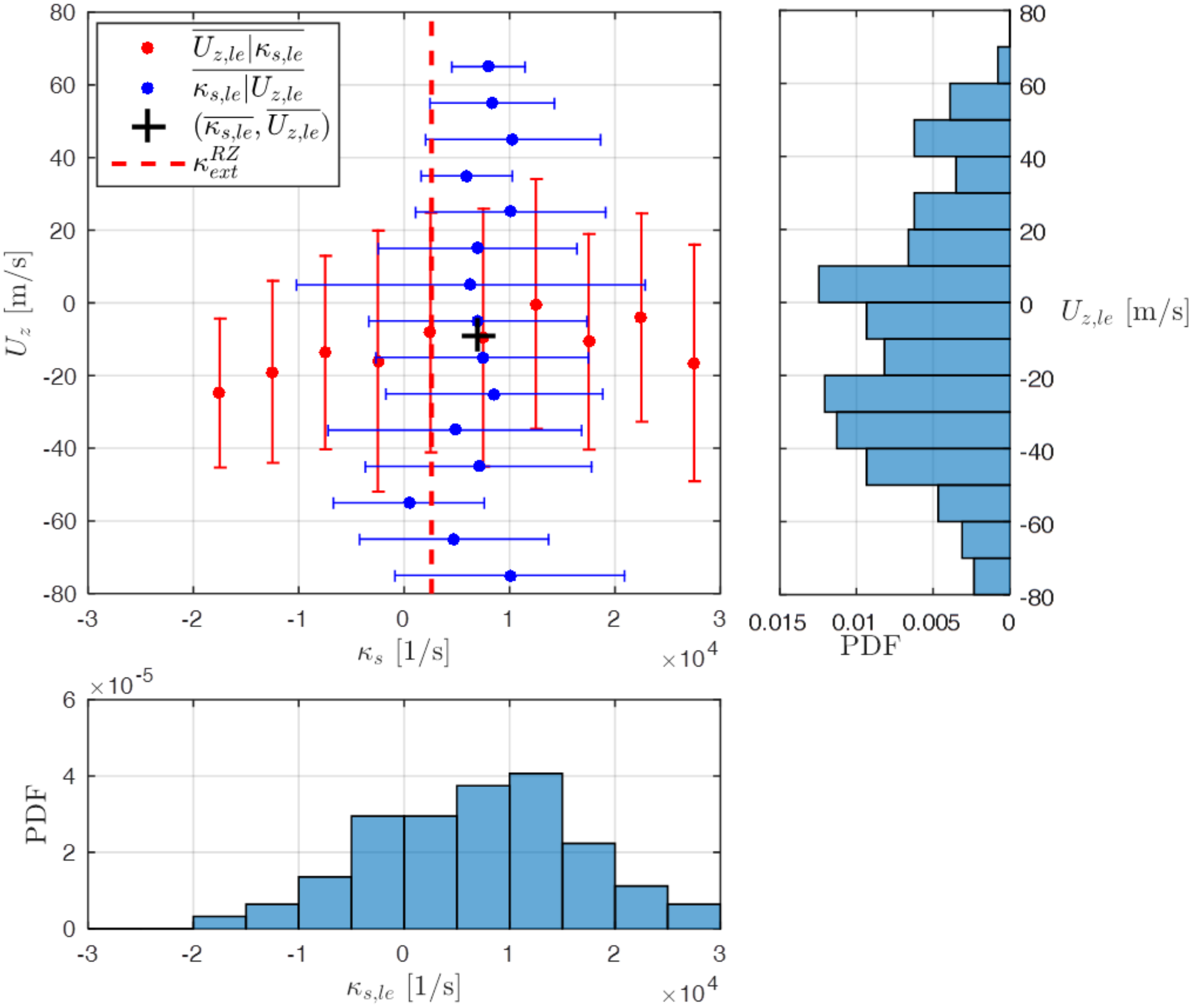

Figure 7.2: Case 1, uncorrected plot 1, $U_{z,le}$ vs. $\kappa_{s,le}$

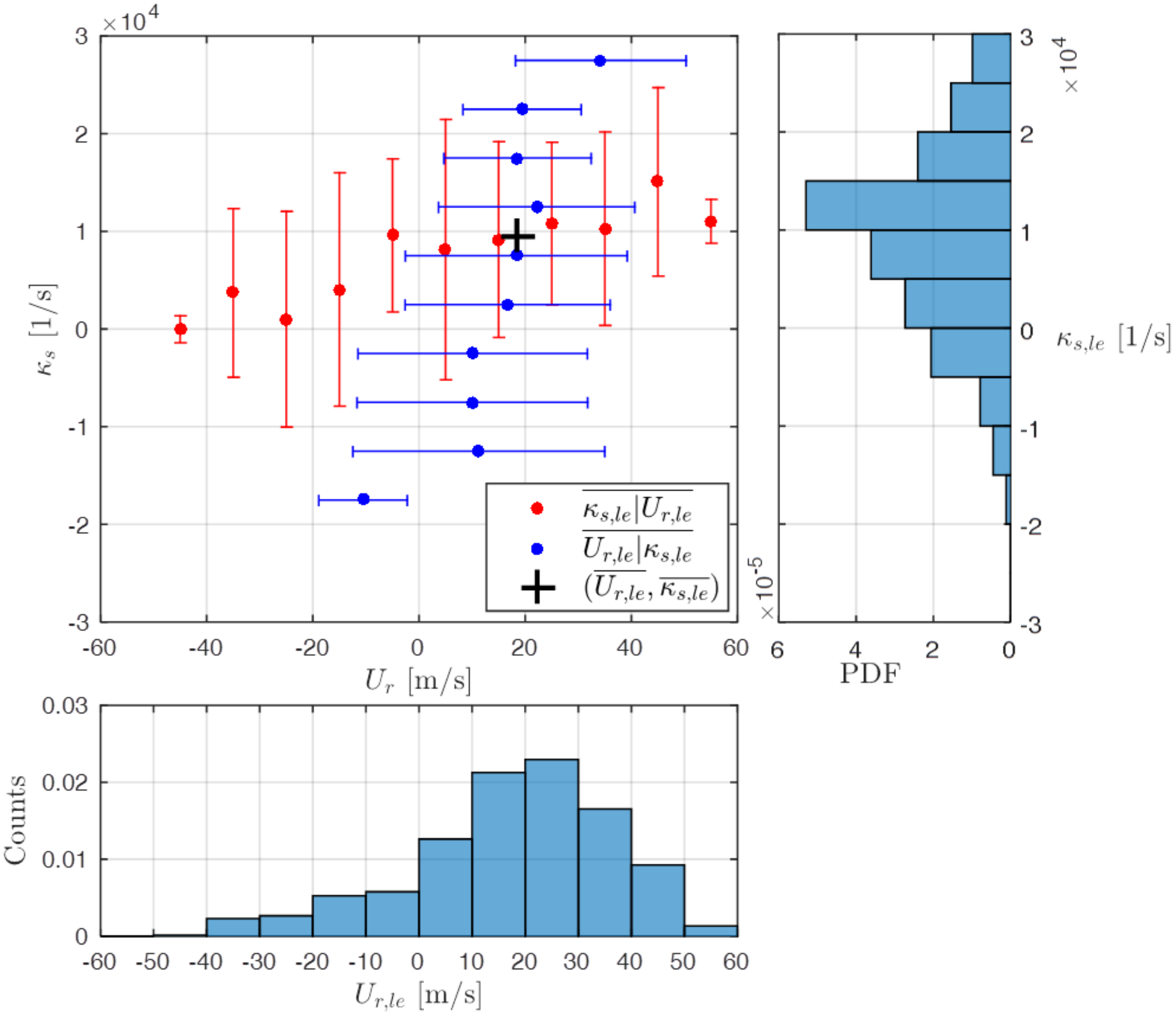

Figure 7.3: Case 1, plot 2, $\kappa_{s,le}$ vs. $U_{r,le}$

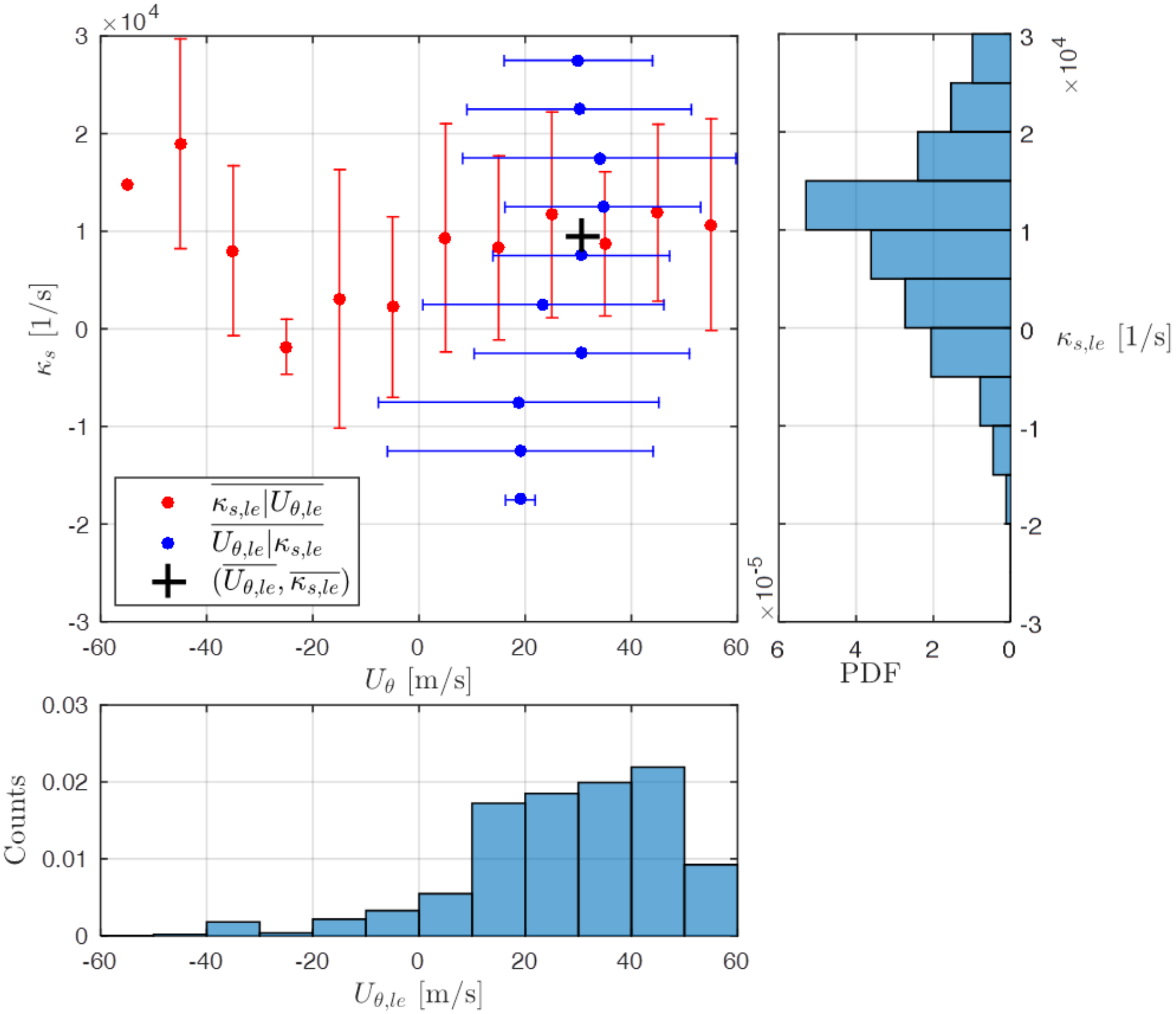

Figure 7.4: Case 1, plot 3, $\kappa_{s,le}$ vs. $U_{\theta,le}$

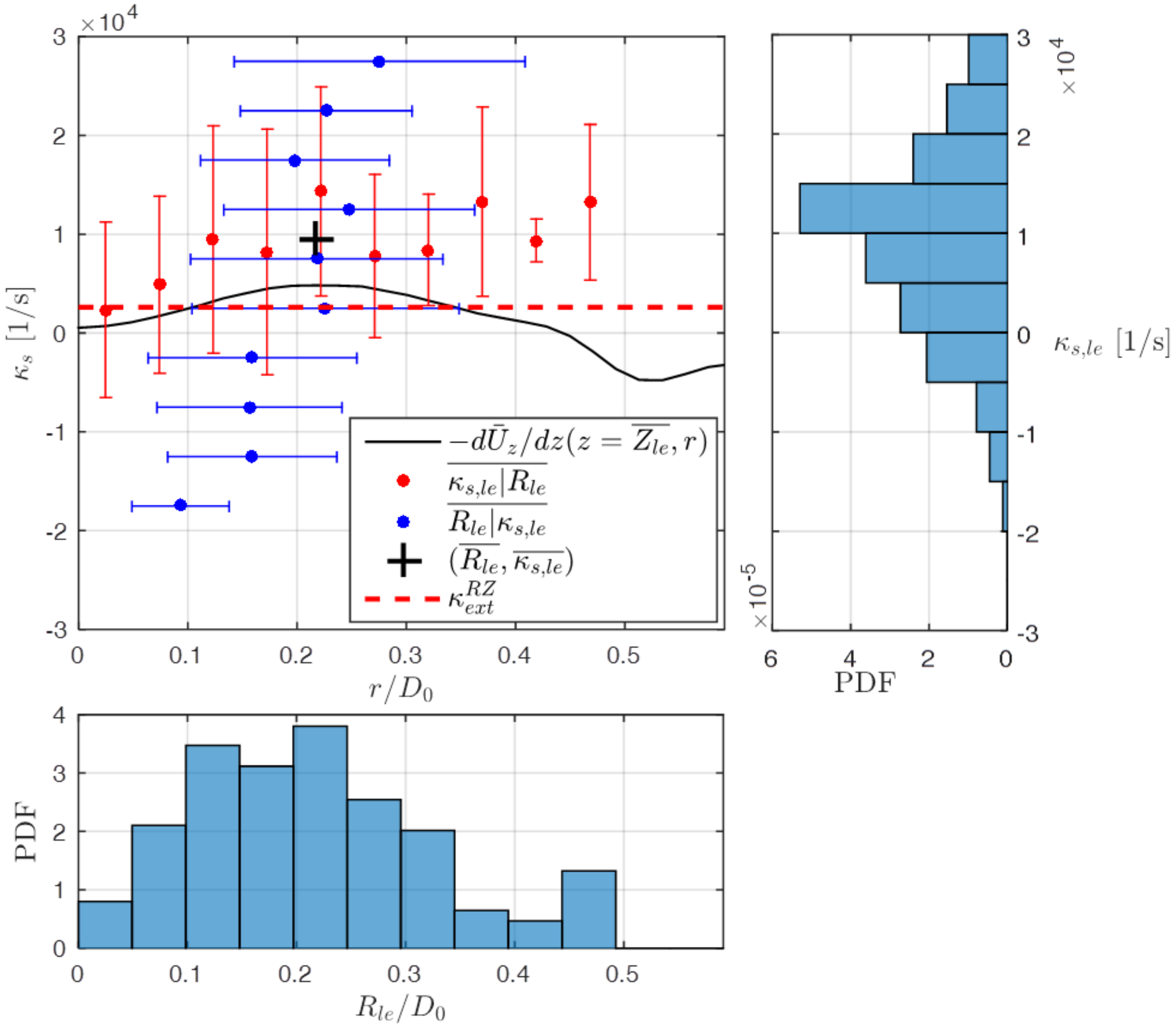

Figure 7.5: Case 1, plot 4, $\kappa_{s,le}$ vs. R_{le}

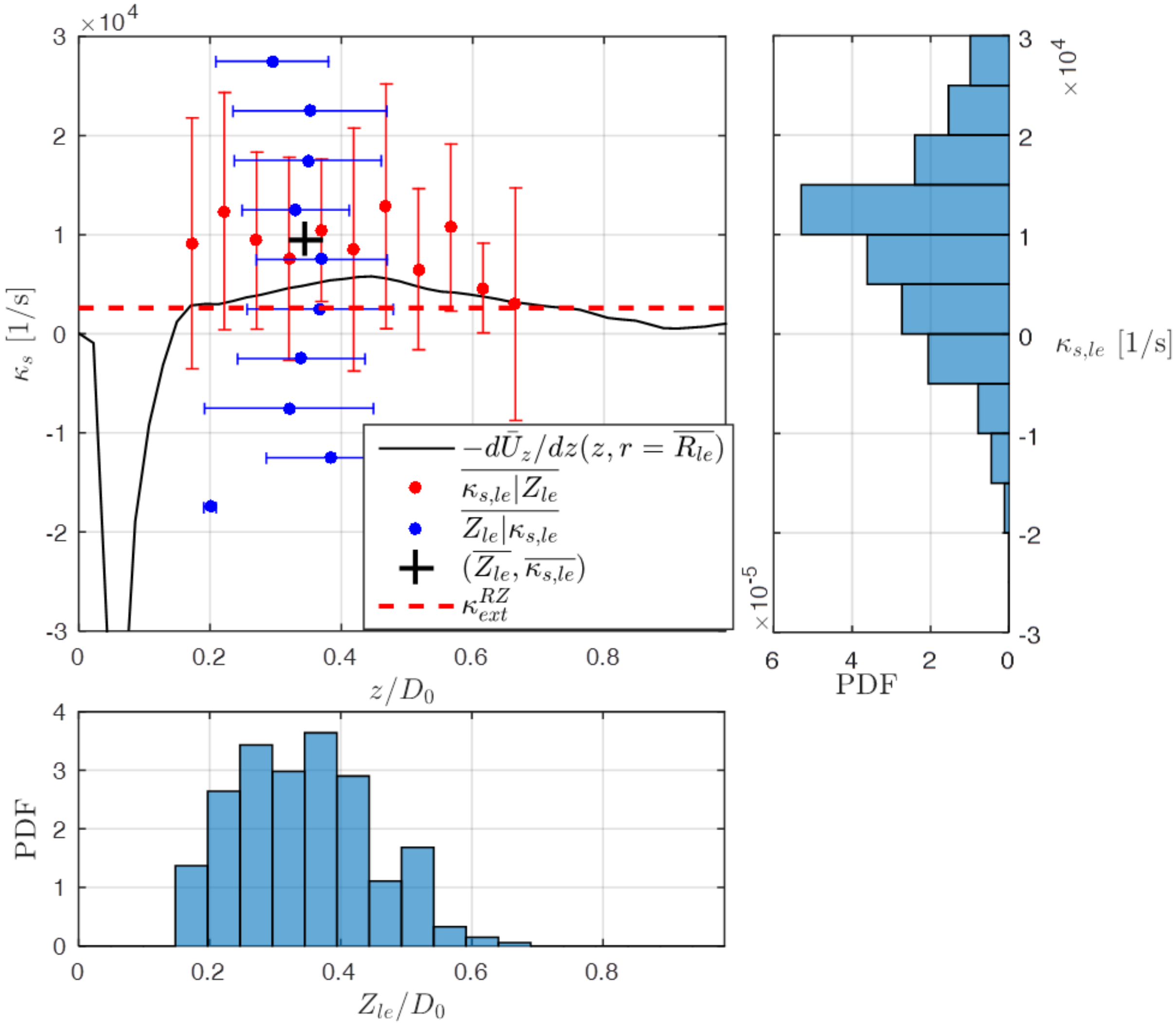

Figure 7.6: Case 1, plot 5, $\kappa_{s,le}$ vs. Z_{le}

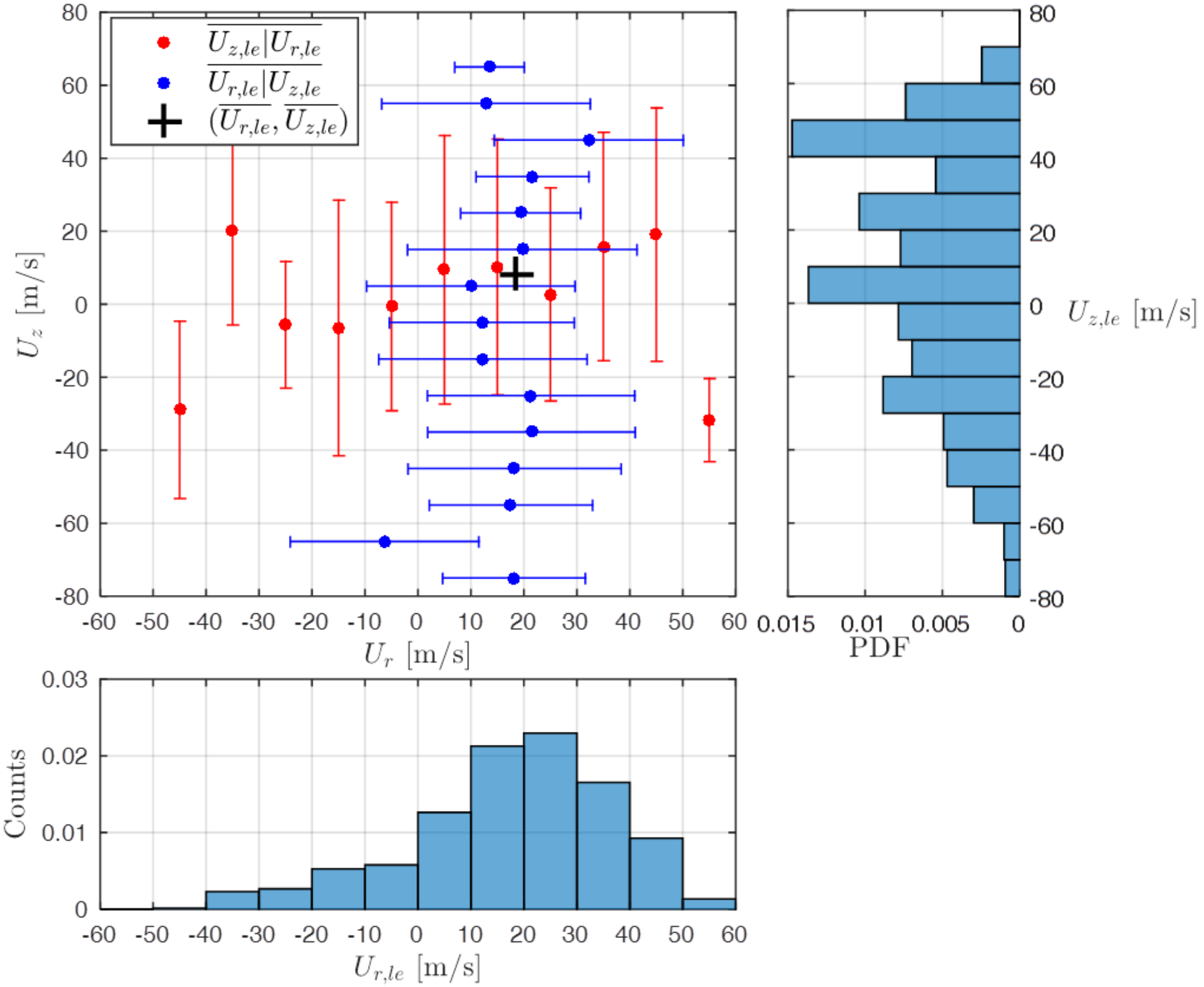

Figure 7.7: Case 1, plot 6, $U_{z,le}$ **vs.** $U_{r,le}$

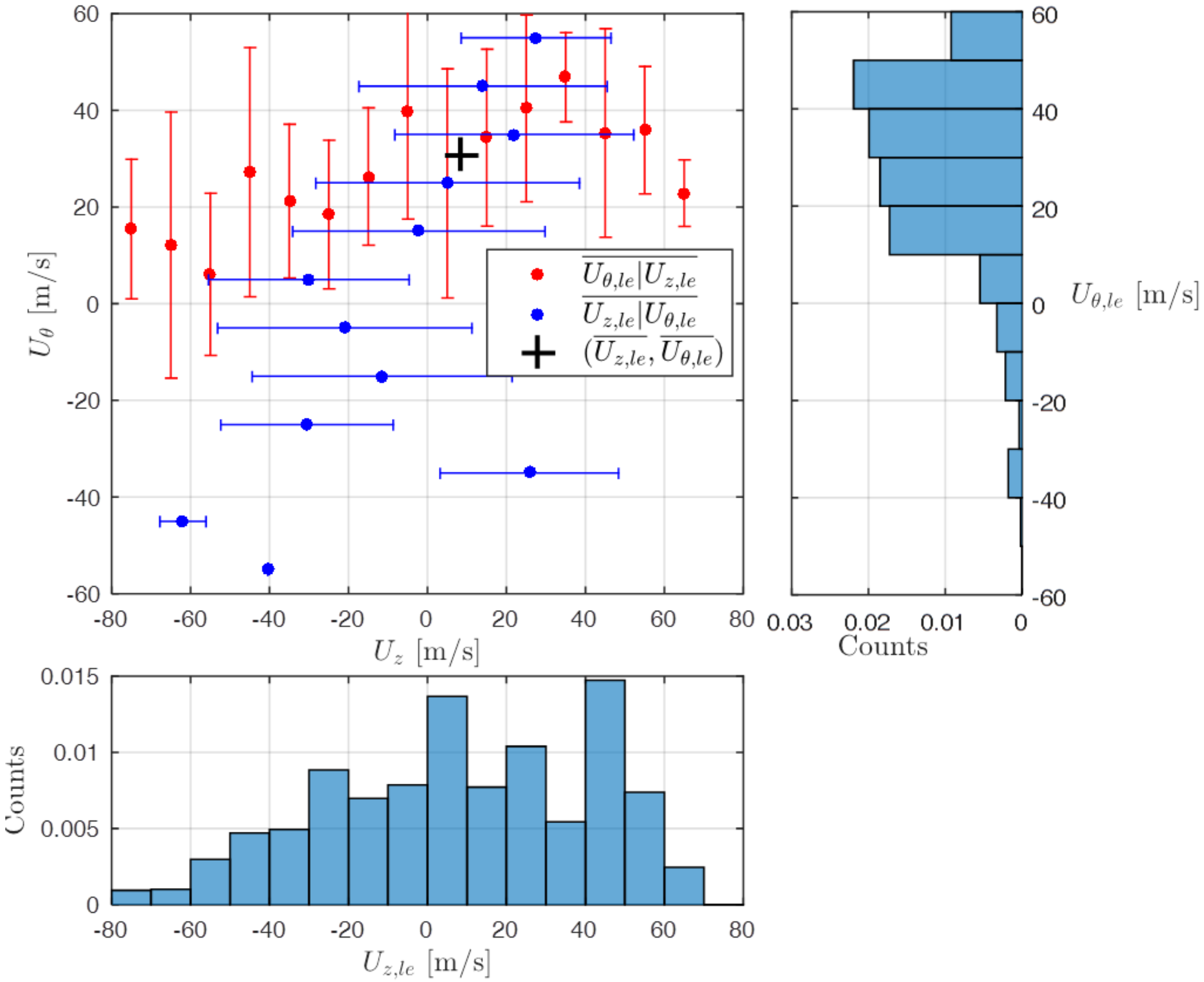

Figure 7.8: Case 1, plot 7, $U_{\theta,le}$ vs. $U_{z,le}$

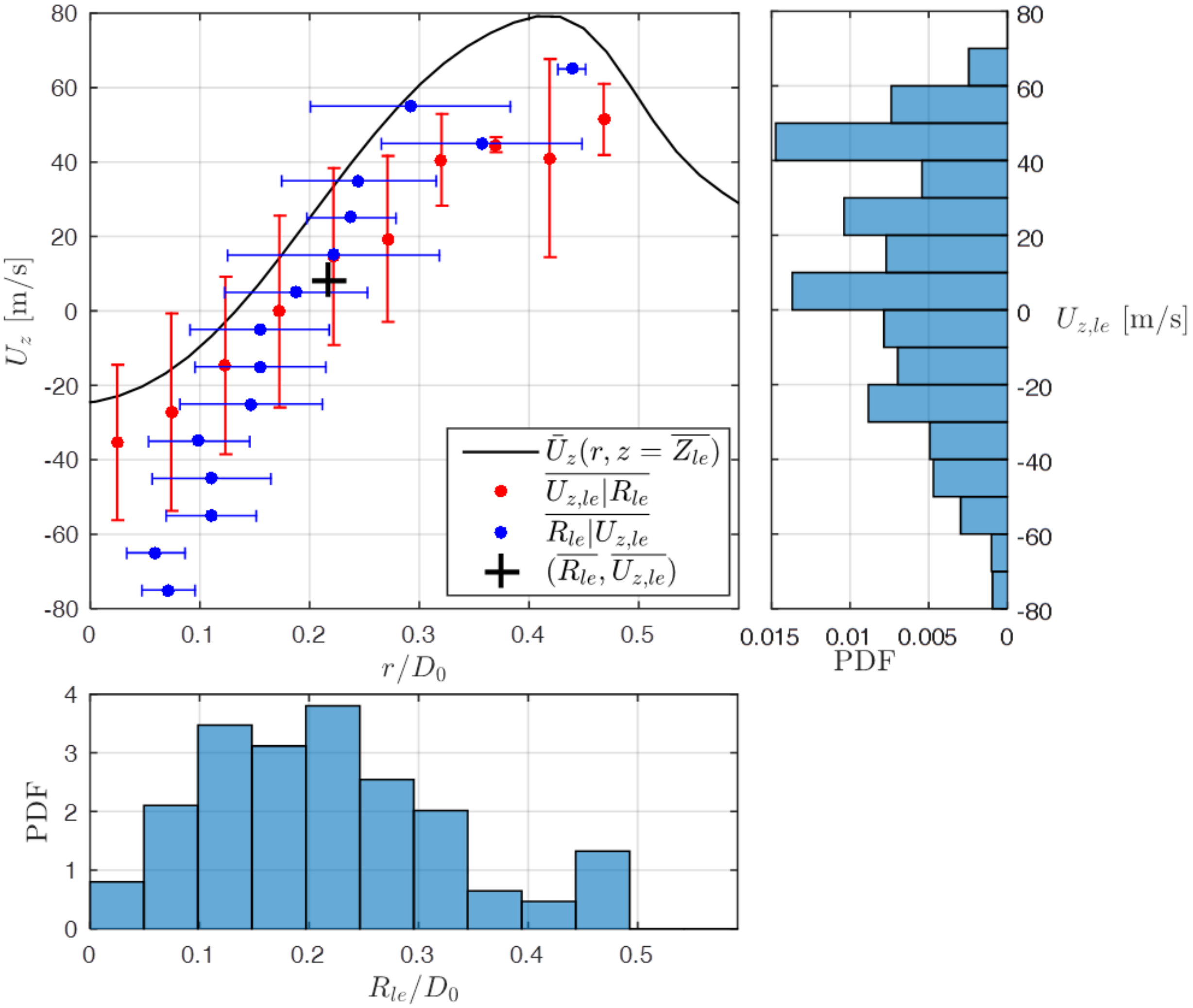

Figure 7.9: Case 1, plot 8, $U_{z,le}$ **vs.** R_{le}

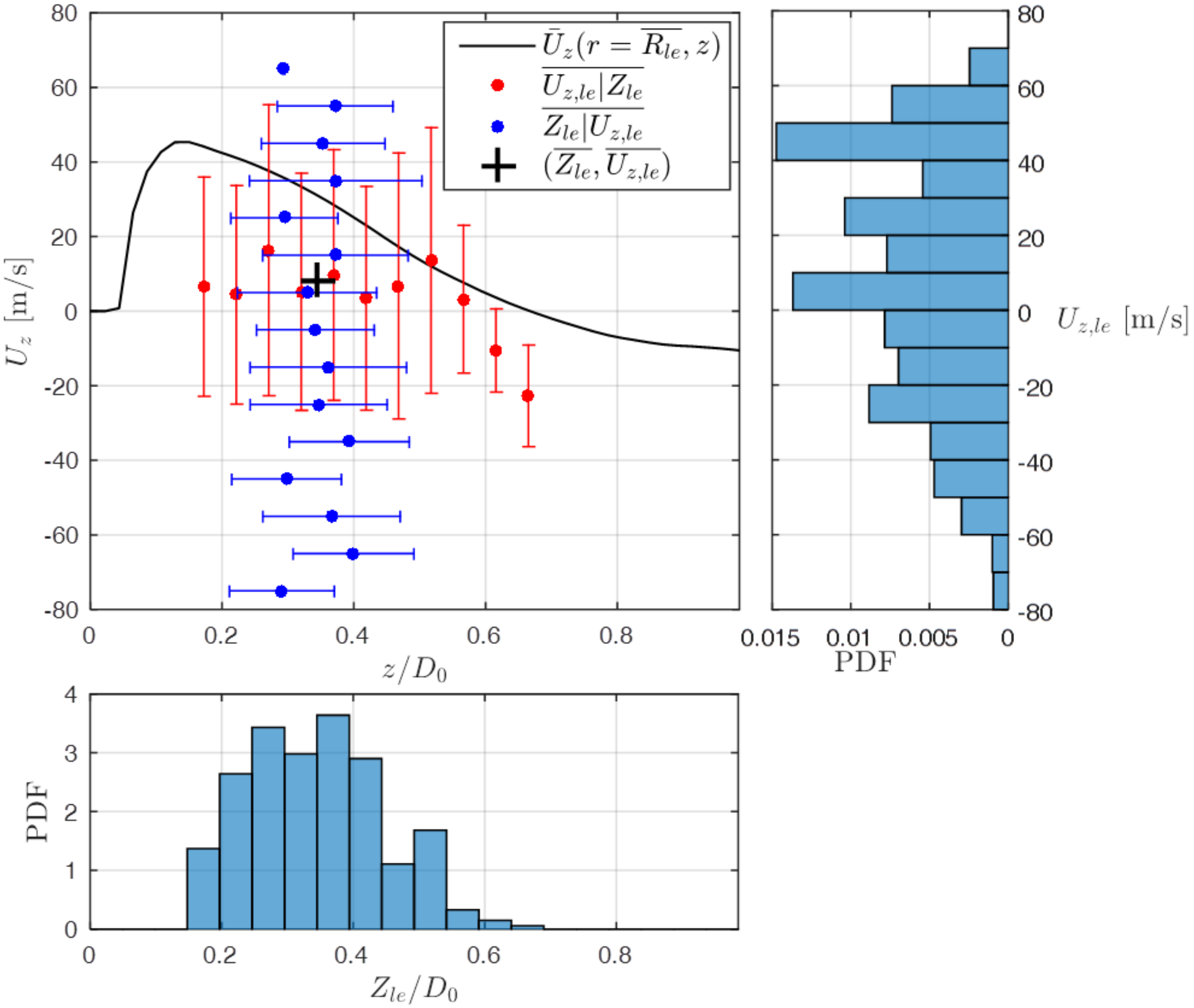

Figure 7.10: Case 1, plot 9, $U_{z,le}$ vs. Z_{le}

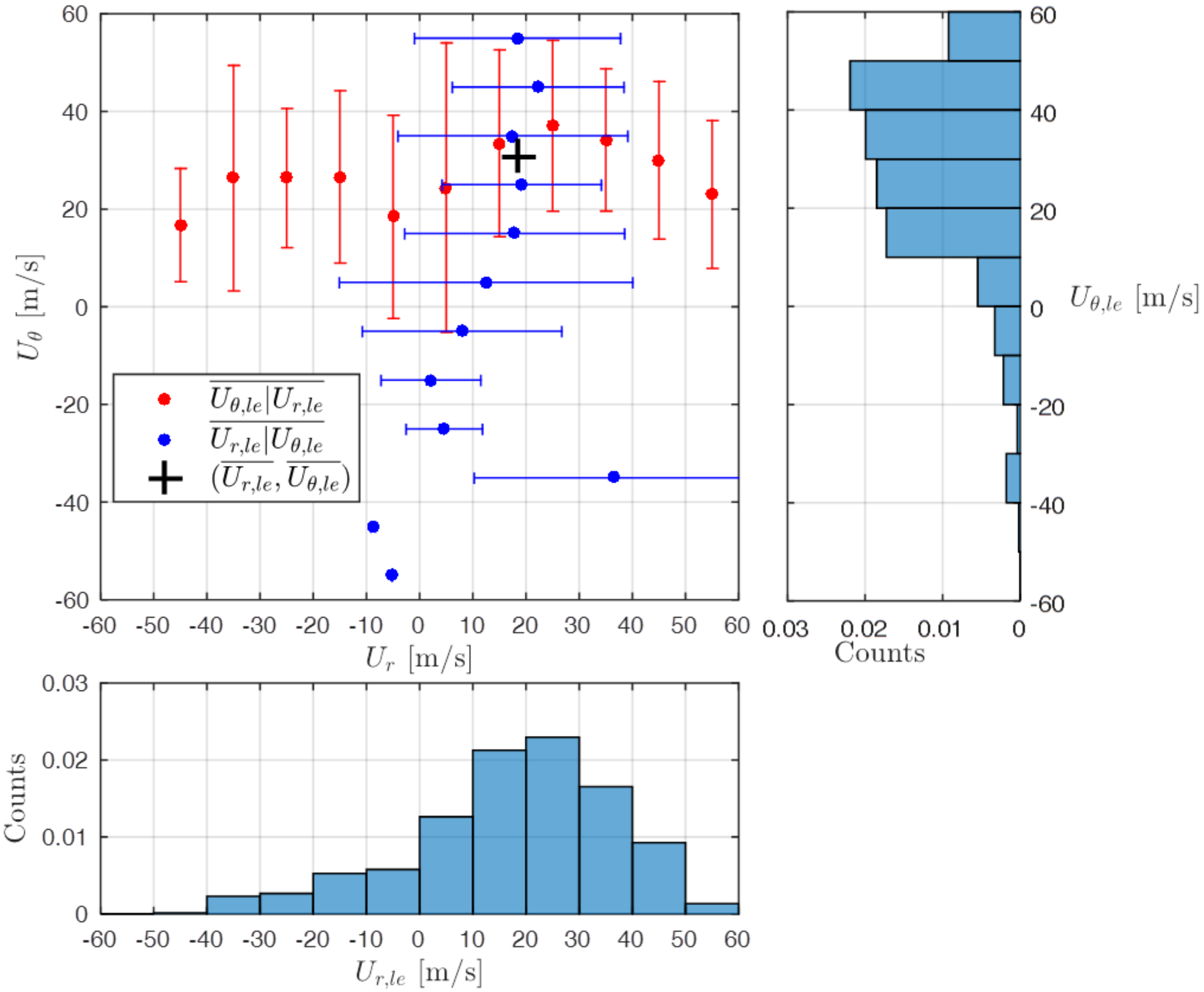

Figure 7.11: Case 1, plot 10, $U_{\theta,le}$ vs. $U_{r,le}$

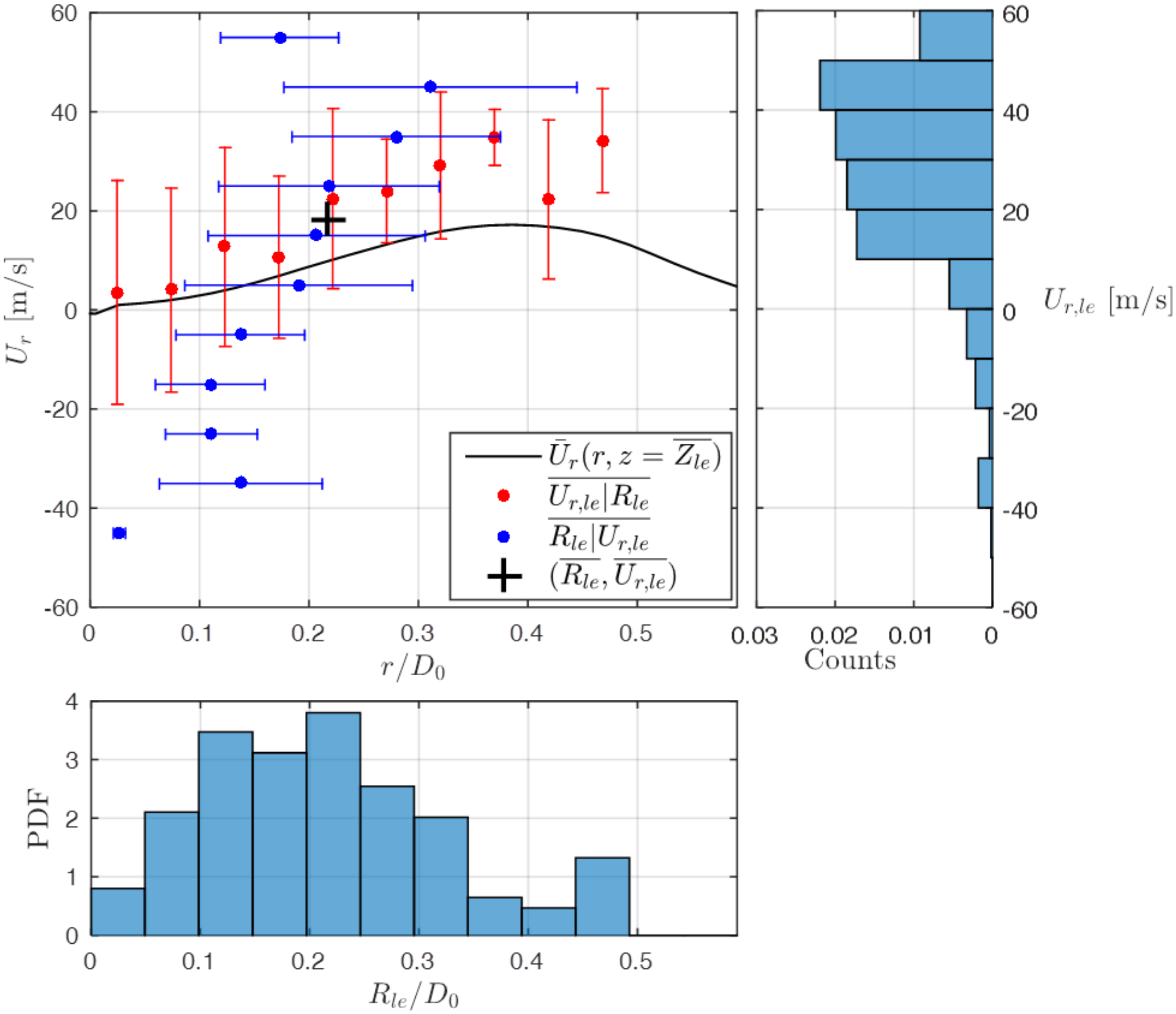

Figure 7.12: Case 1, plot 11, $U_{r,le}$ **vs.** R_{le}

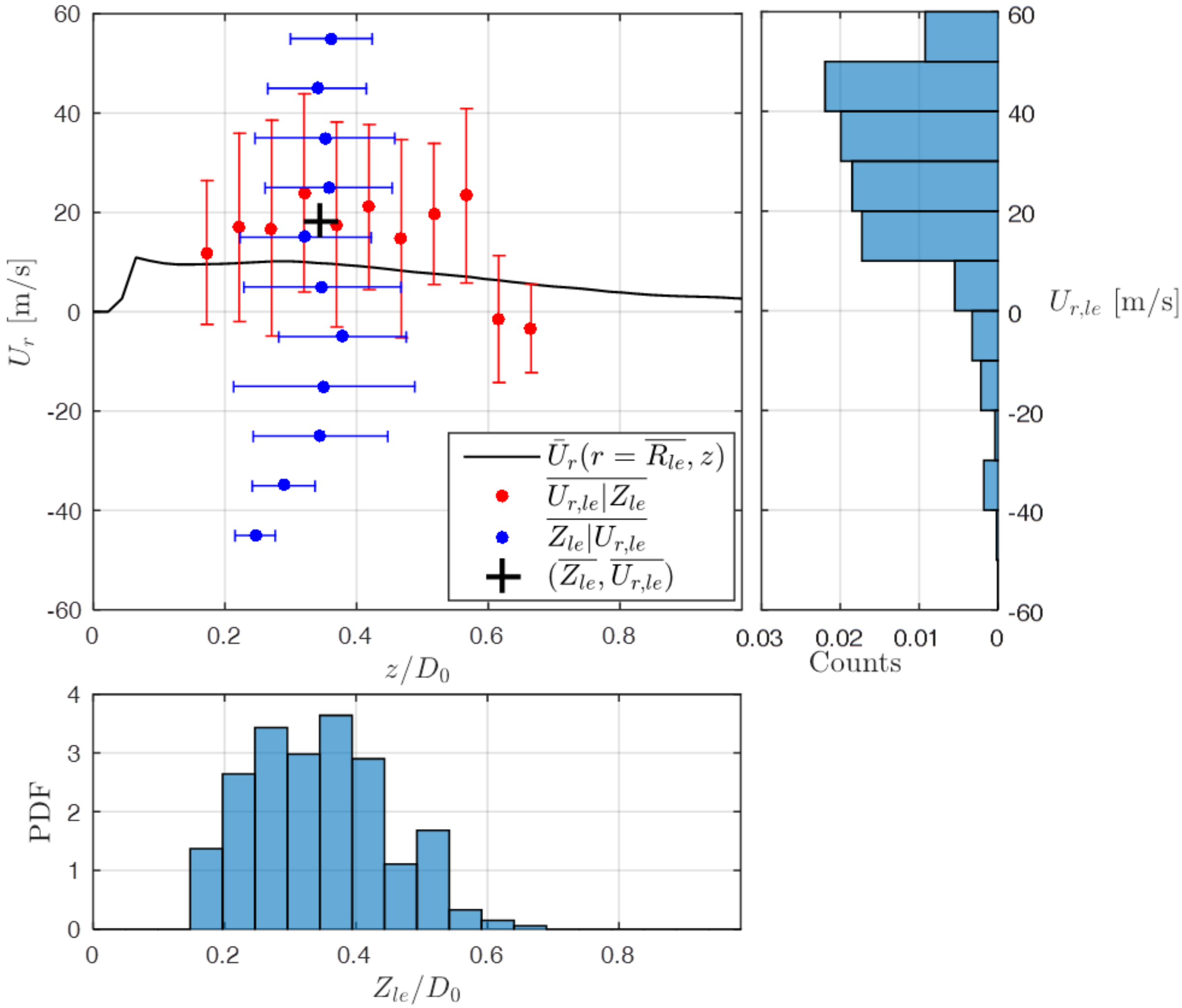

Figure 7.13: Case 1, plot 12, $U_{r,le}$ vs. Z_{le}

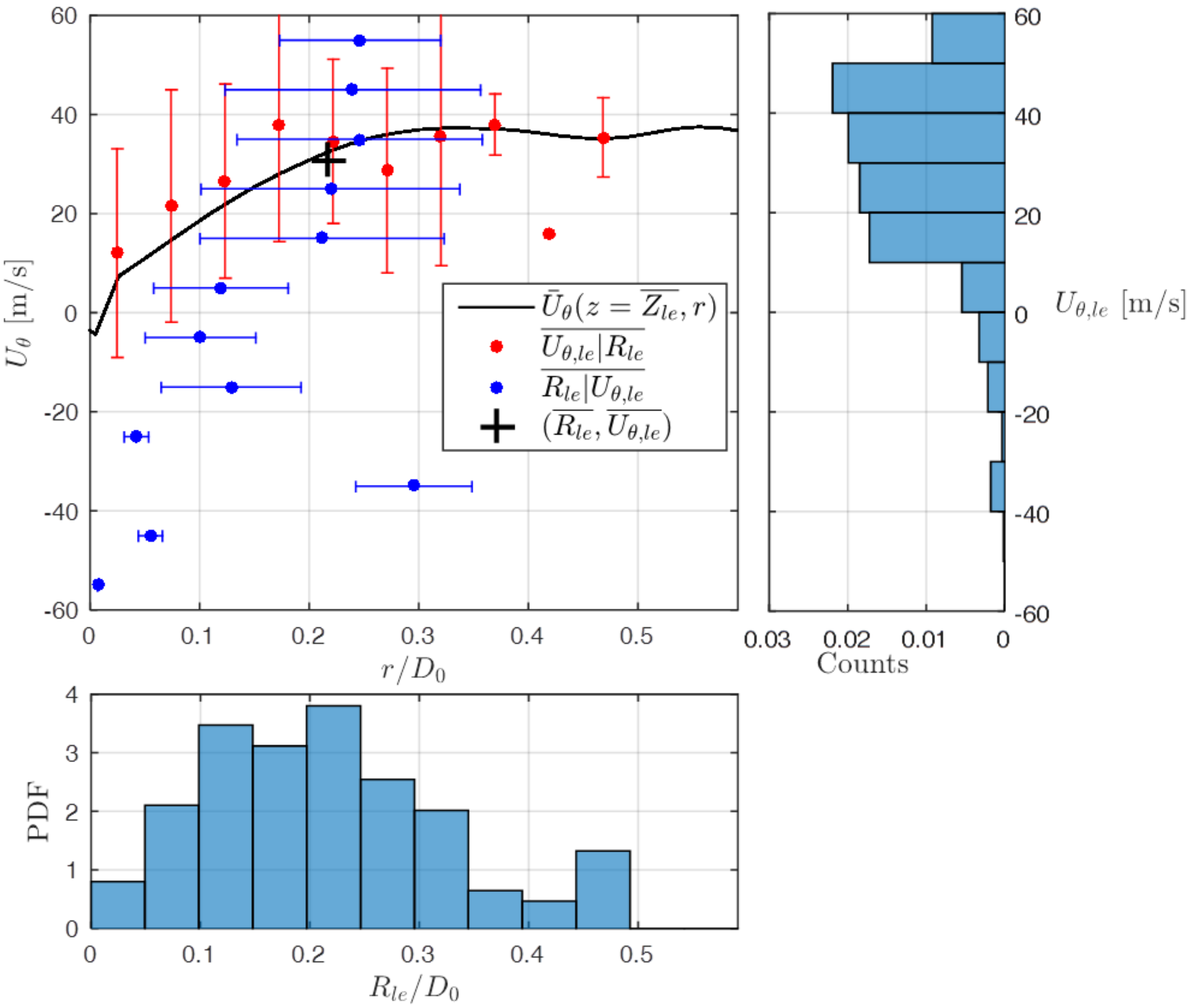

Figure 7.14: Case 1, plot 13, $U_{\theta,le}$ vs. R_{le}

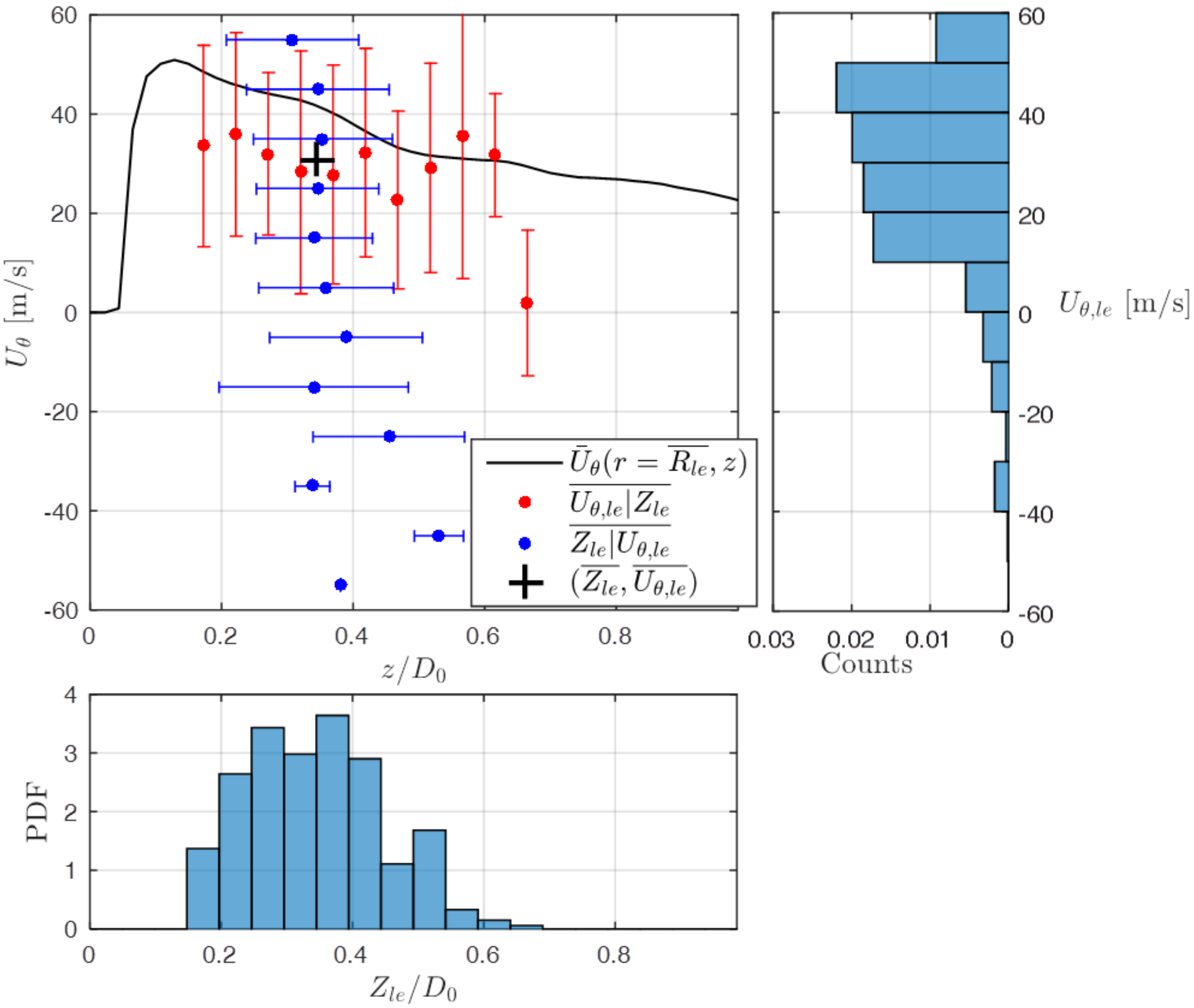

Figure 7.15: Case 1, plot 14, $U_{\theta,le}$ vs. Z_{le}

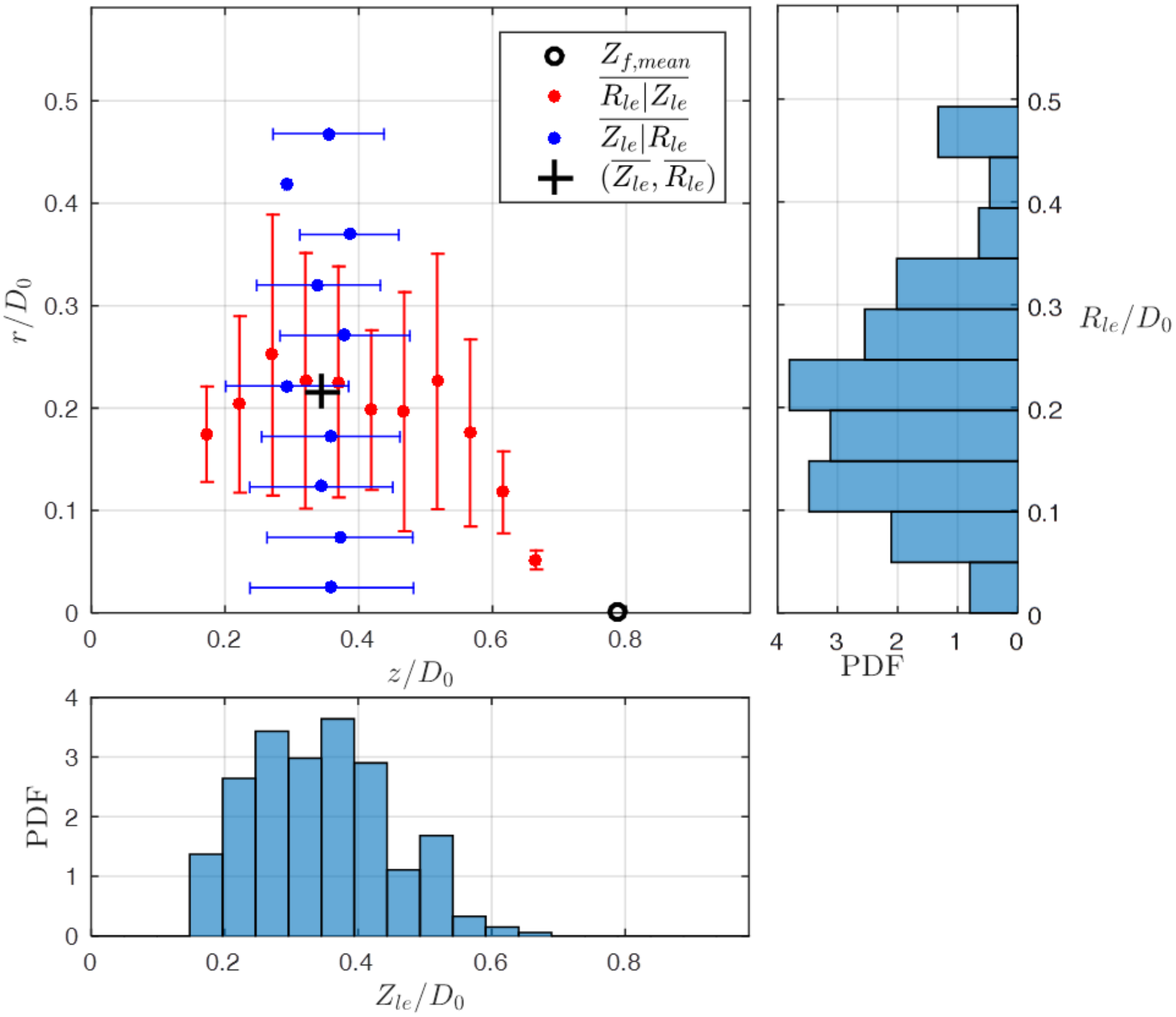

Figure 7.16: Case 1, plot 15, R_{le} vs. Z_{le}

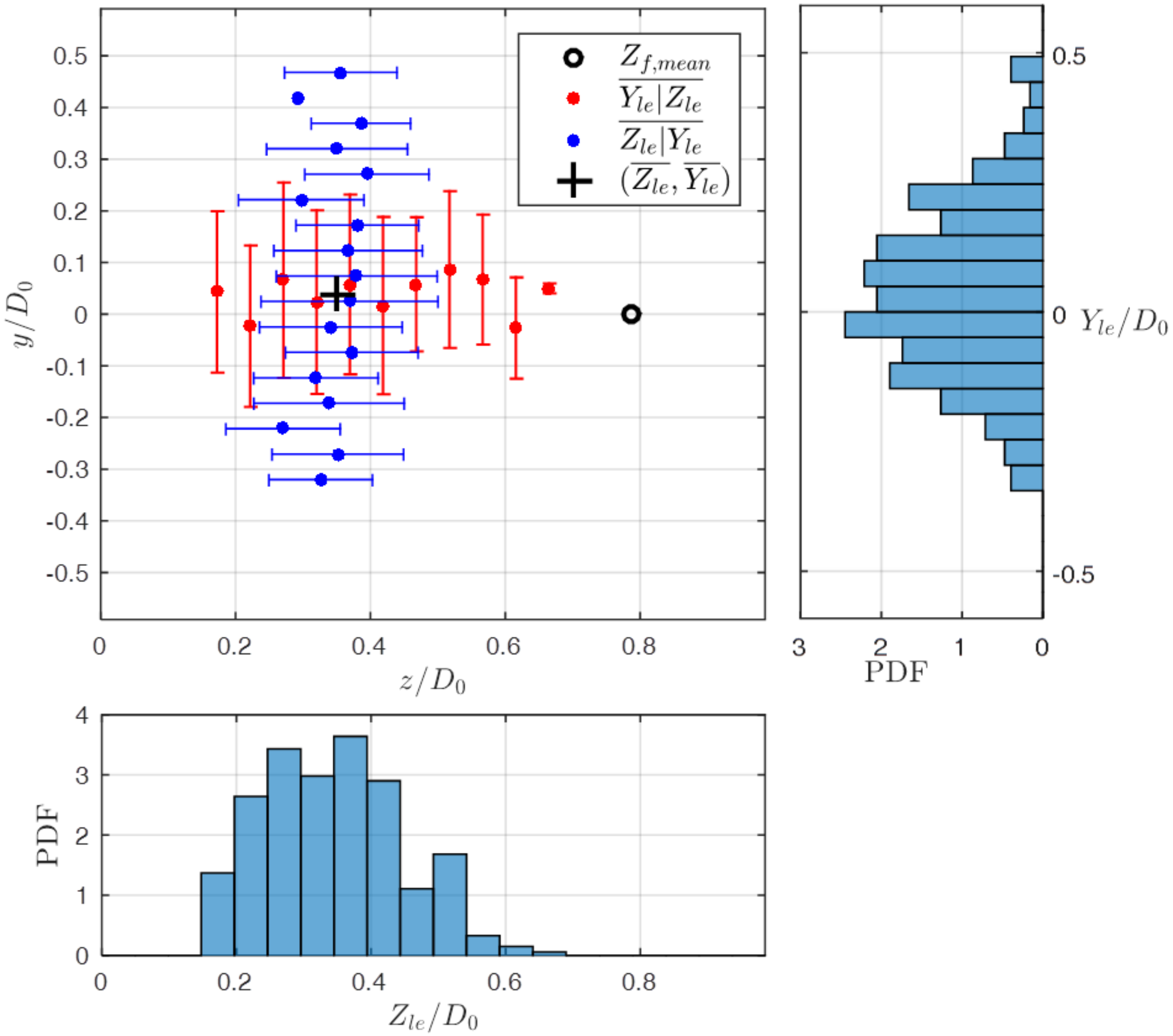

Figure 7.17: Case 1, plot 15, uncorrected R_{le} vs. Z_{le}

Case 2 Plots

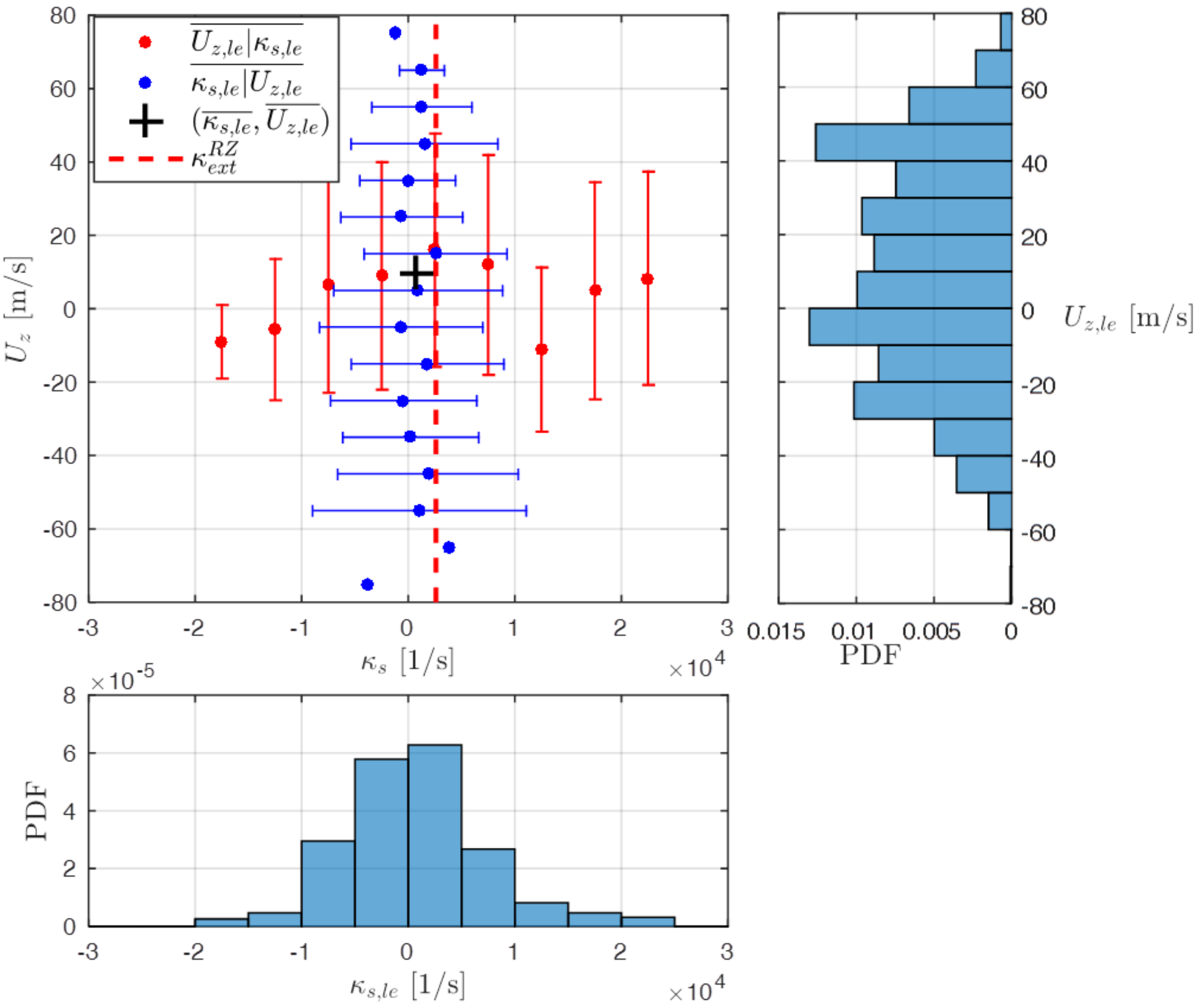

Figure 7.18: Case 2, plot 1, $U_{z,le}$ vs. $\kappa_{s,le}$

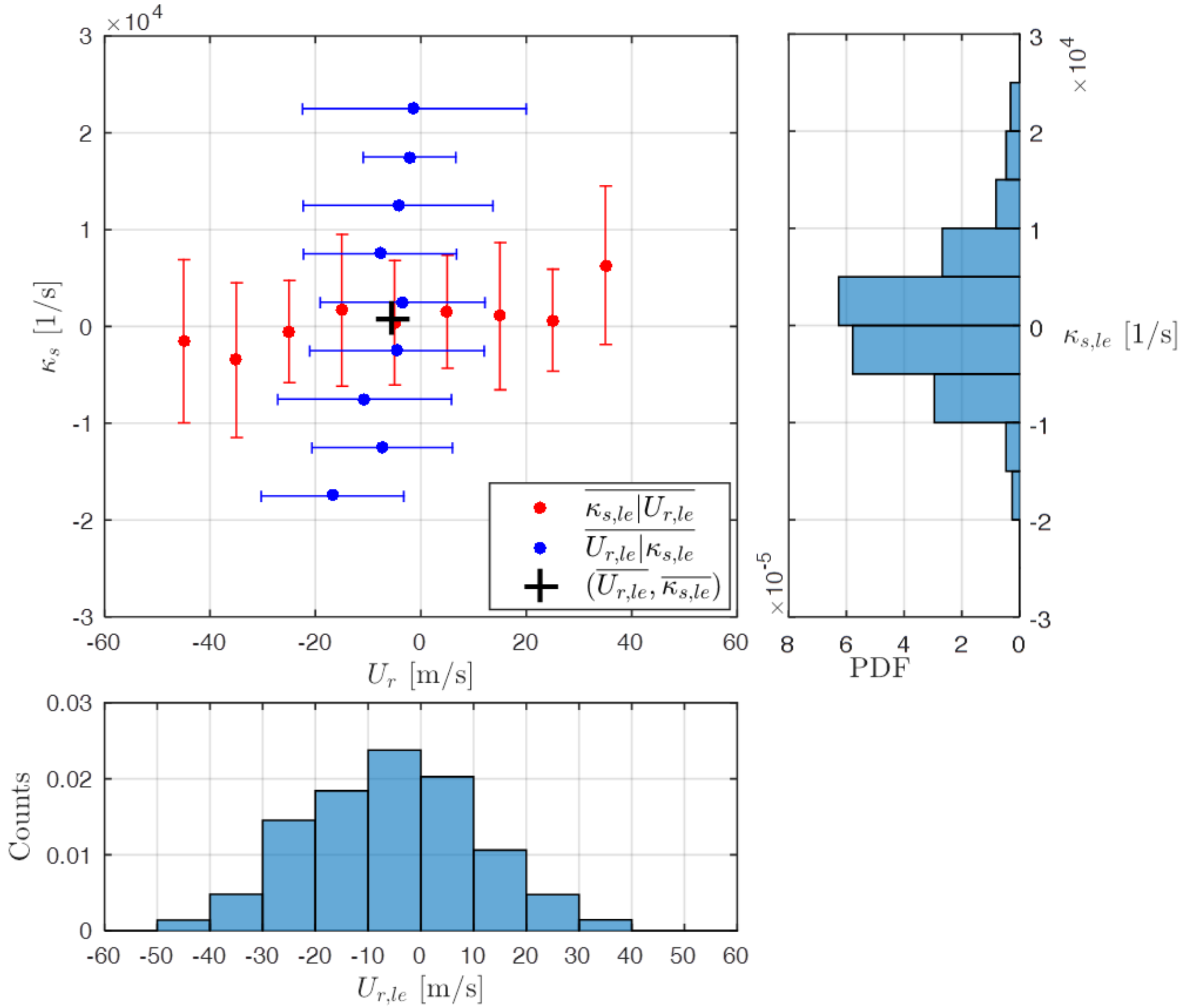

Figure 7.19: Case 2, plot 2, $\kappa_{s,le}$ vs. $U_{r,le}$

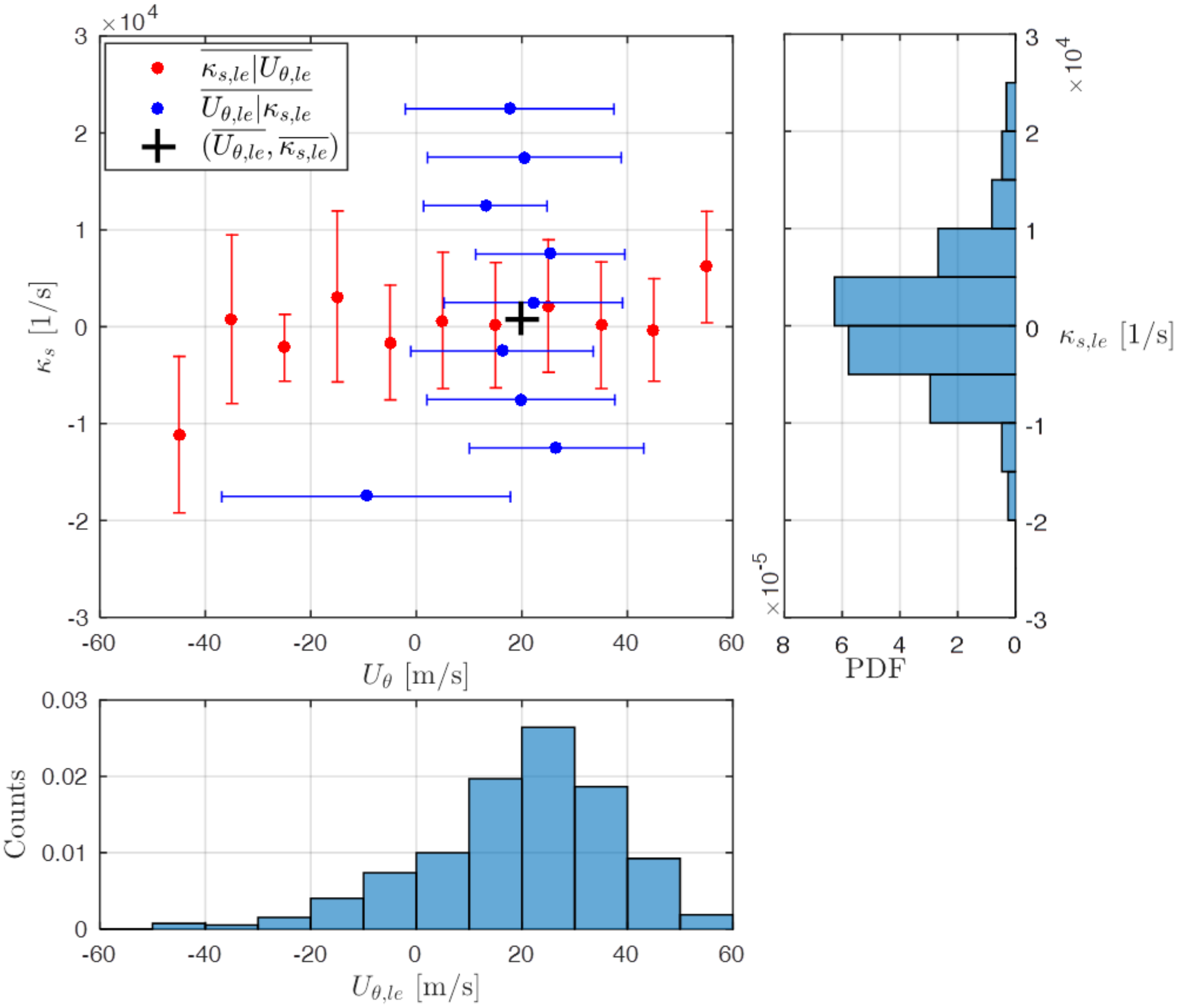

Figure 7.20: Case 2, plot 3, $\kappa_{s,le}$ vs. $U_{\theta,le}$

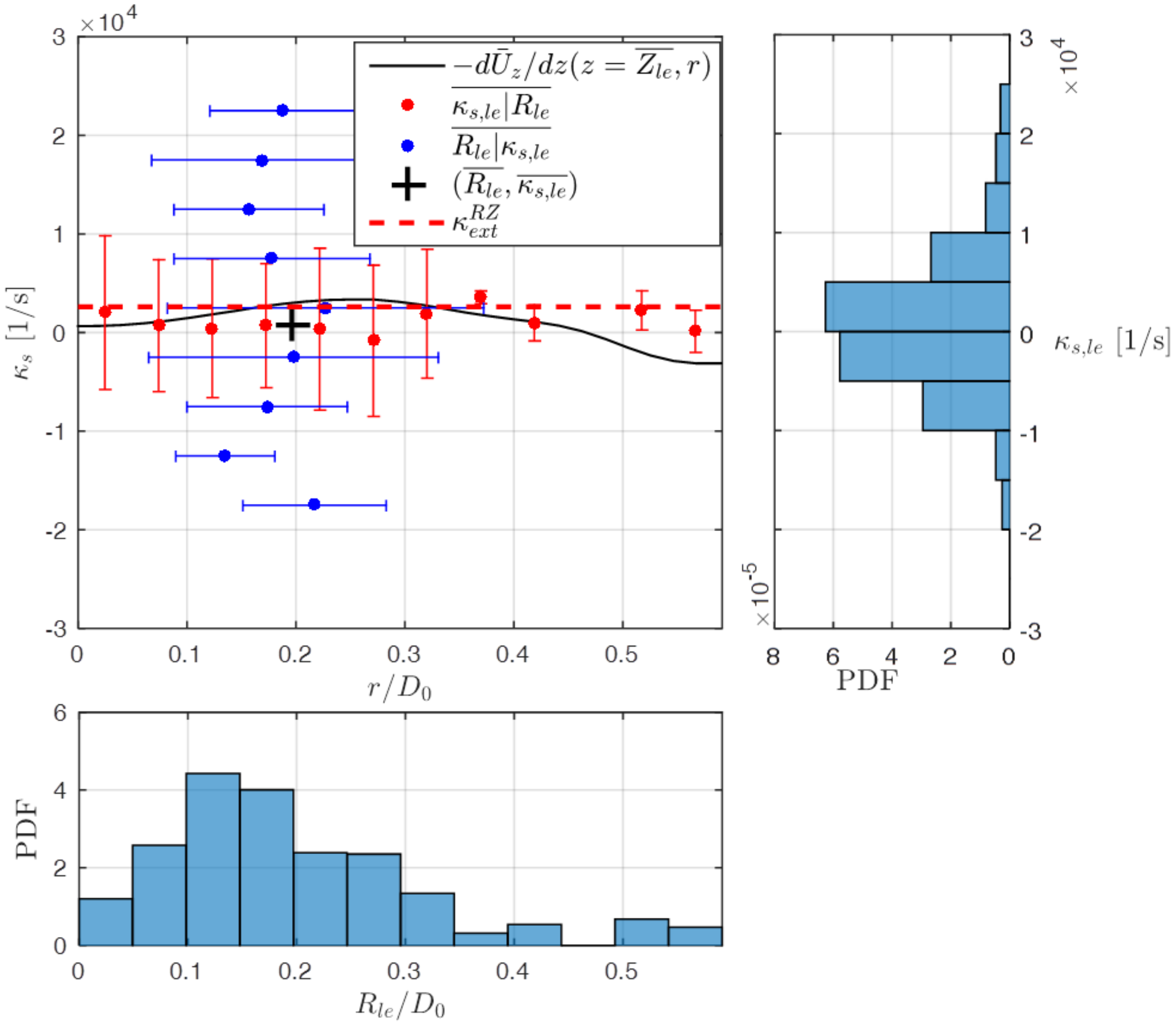

Figure 7.21: Case 2, plot 4, $\kappa_{s,le}$ vs. R_{le}

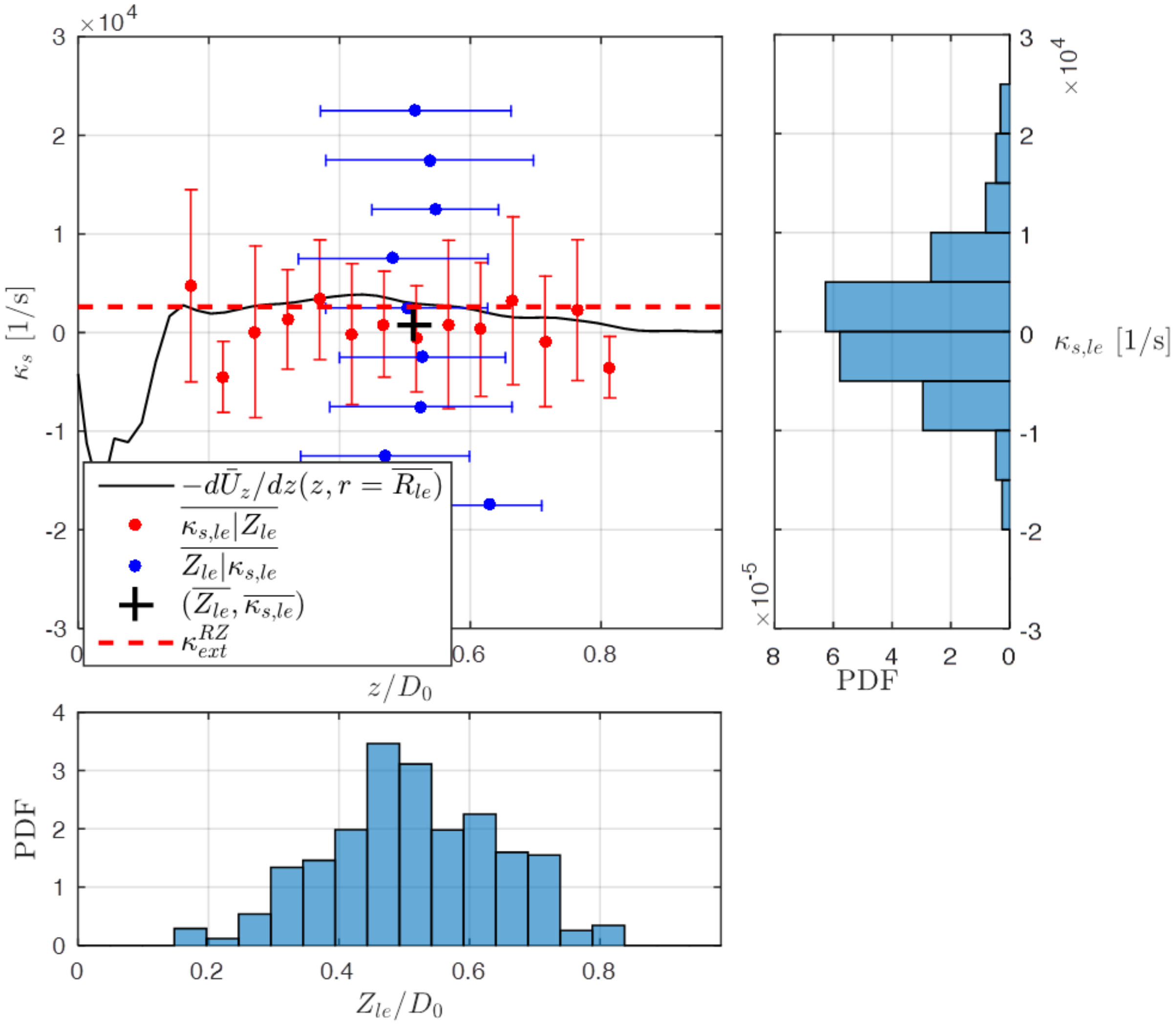

Figure 7.22: Case 2, plot 5, $\kappa_{s,le}$ vs. Z_{le}

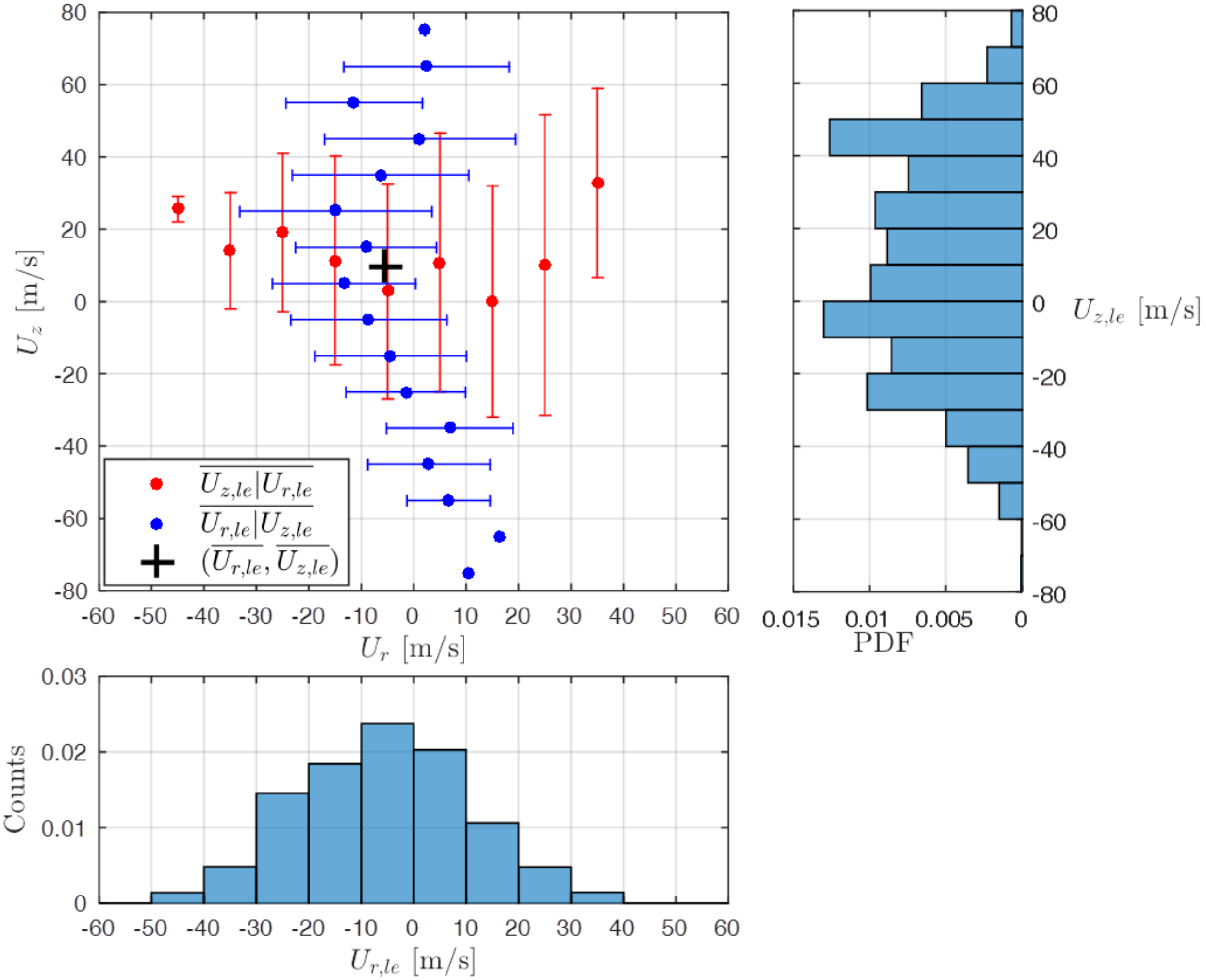

Figure 7.23: Case 2, plot 6, $U_{z,le}$ **vs.** $U_{r,le}$

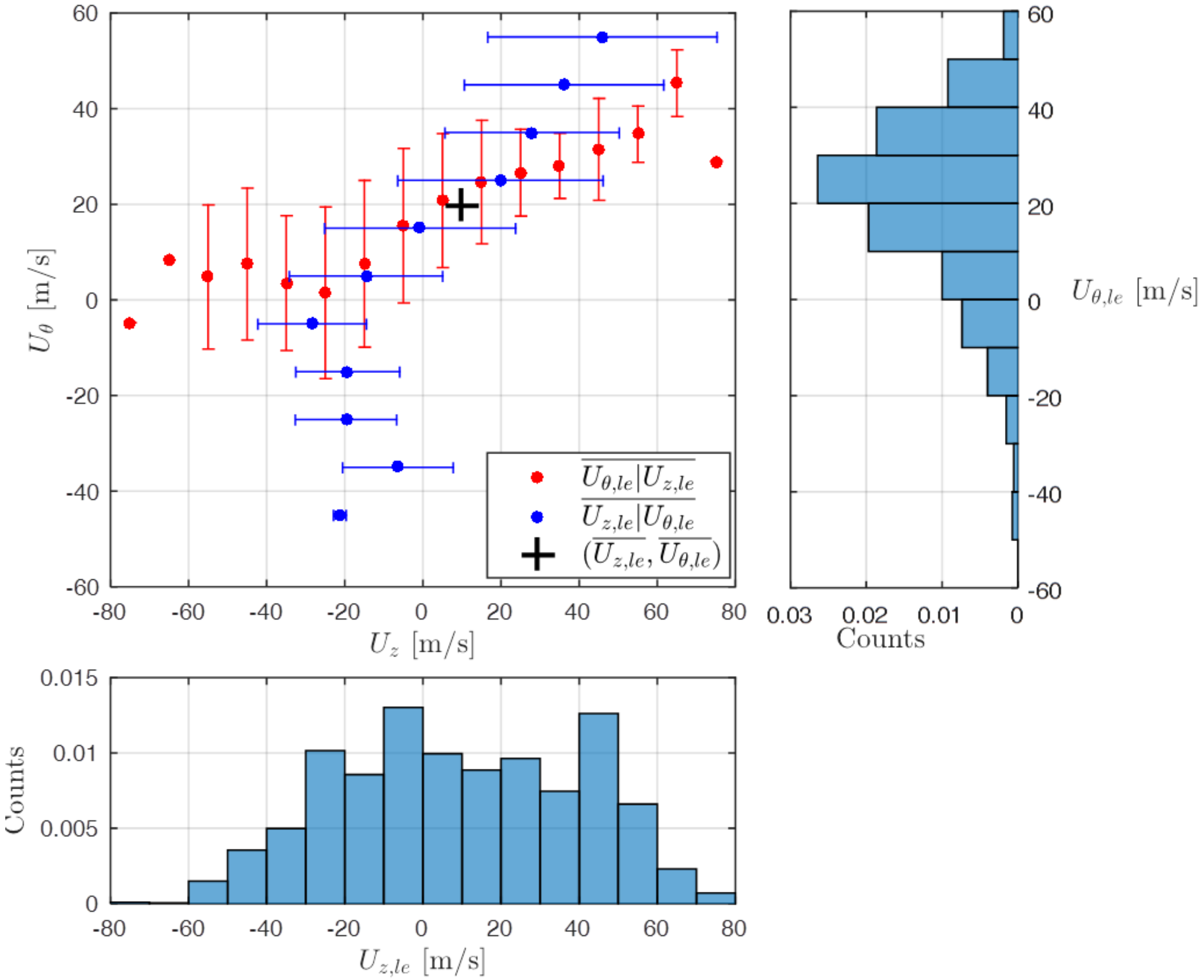

Figure 7.24: Case 2, plot 7, $U_{\theta,le}$ vs. $U_{z,le}$

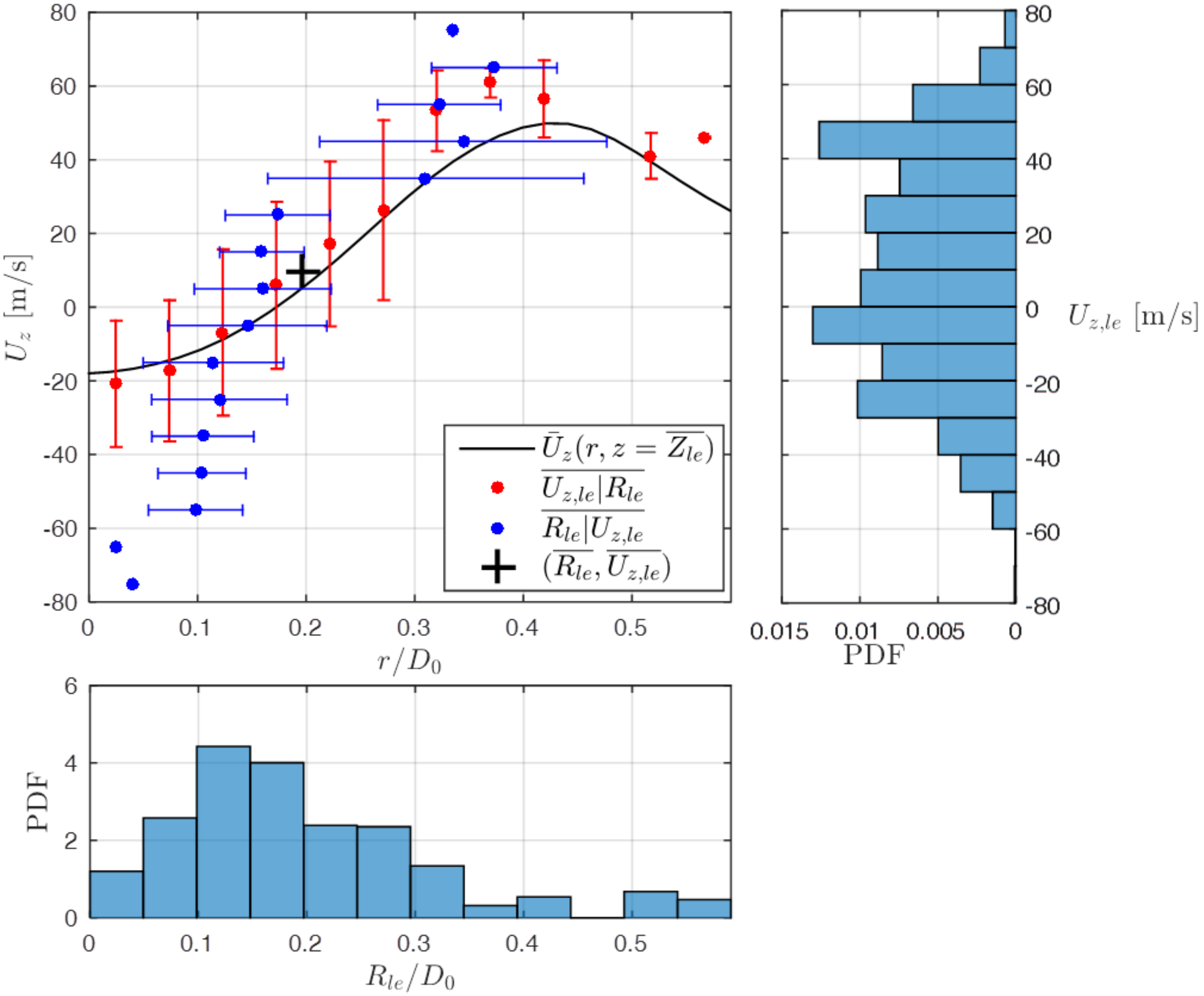

Figure 7.25: Case 2, plot 8, $U_{z,le}$ vs. R_{le}

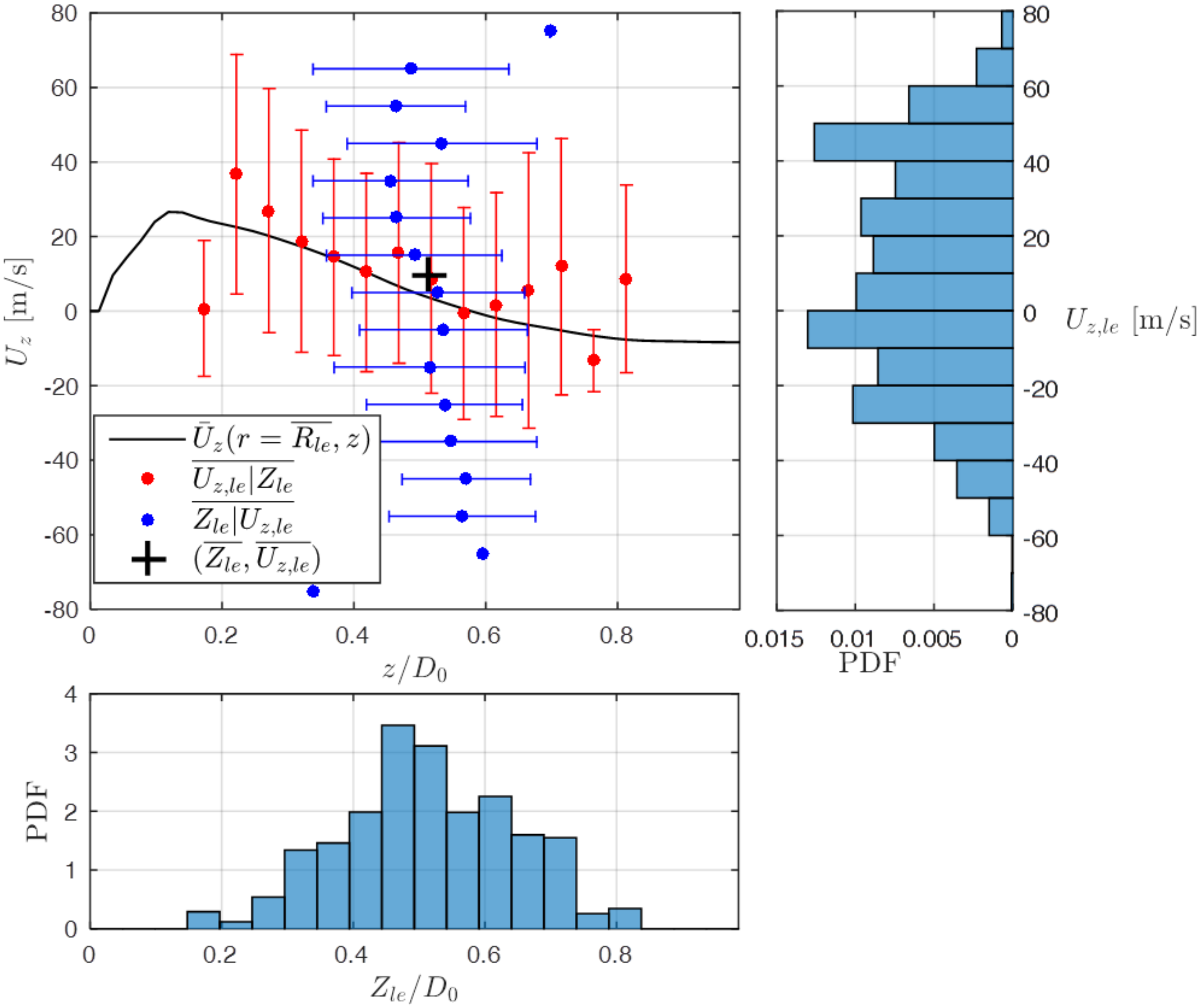

Figure 7.26: Case 2, plot 9, $U_{z,le}$ vs. Z_{le}

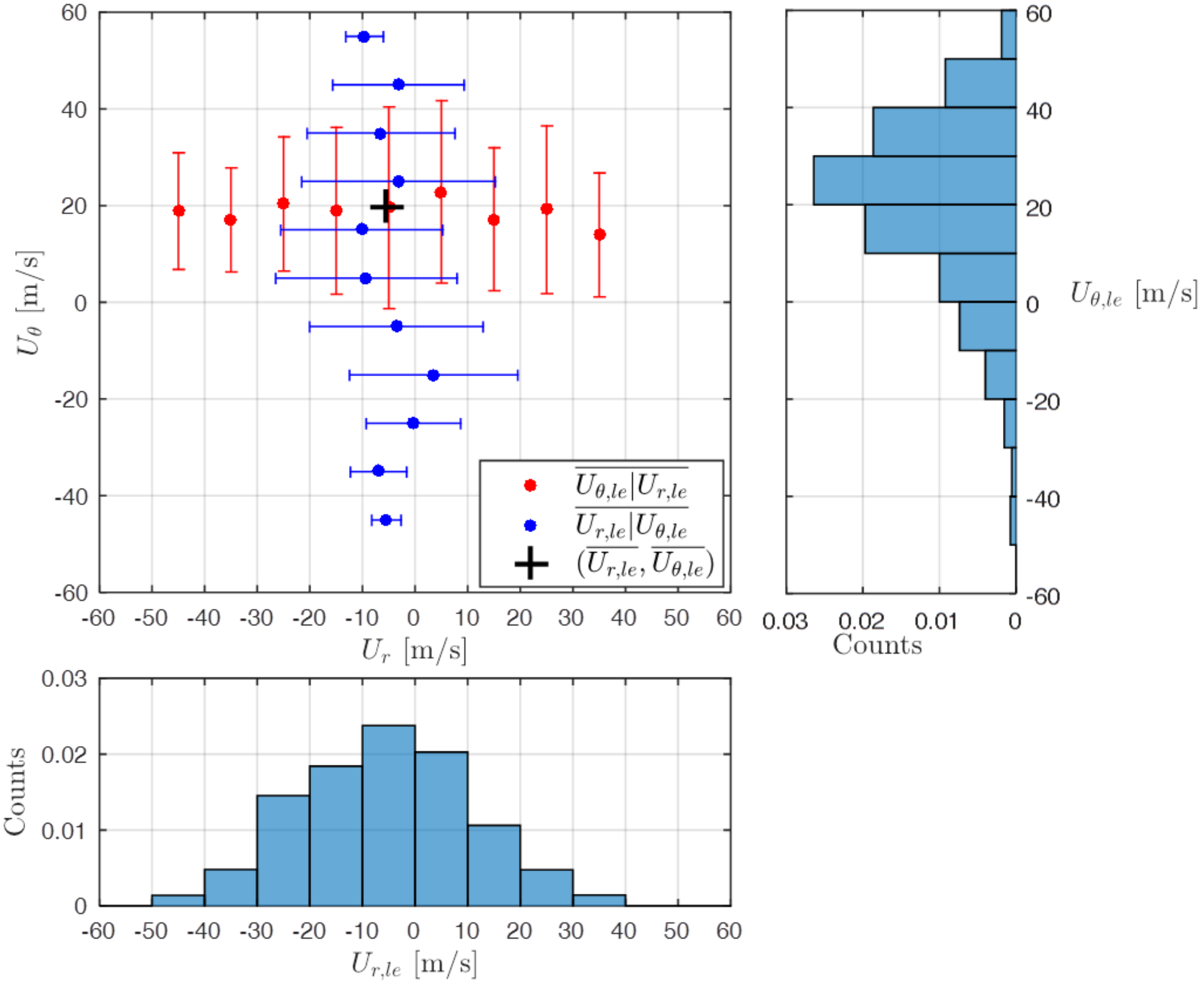

Figure 7.27: Case 2, plot 10, $U_{\theta,le}$ vs. $U_{r,le}$

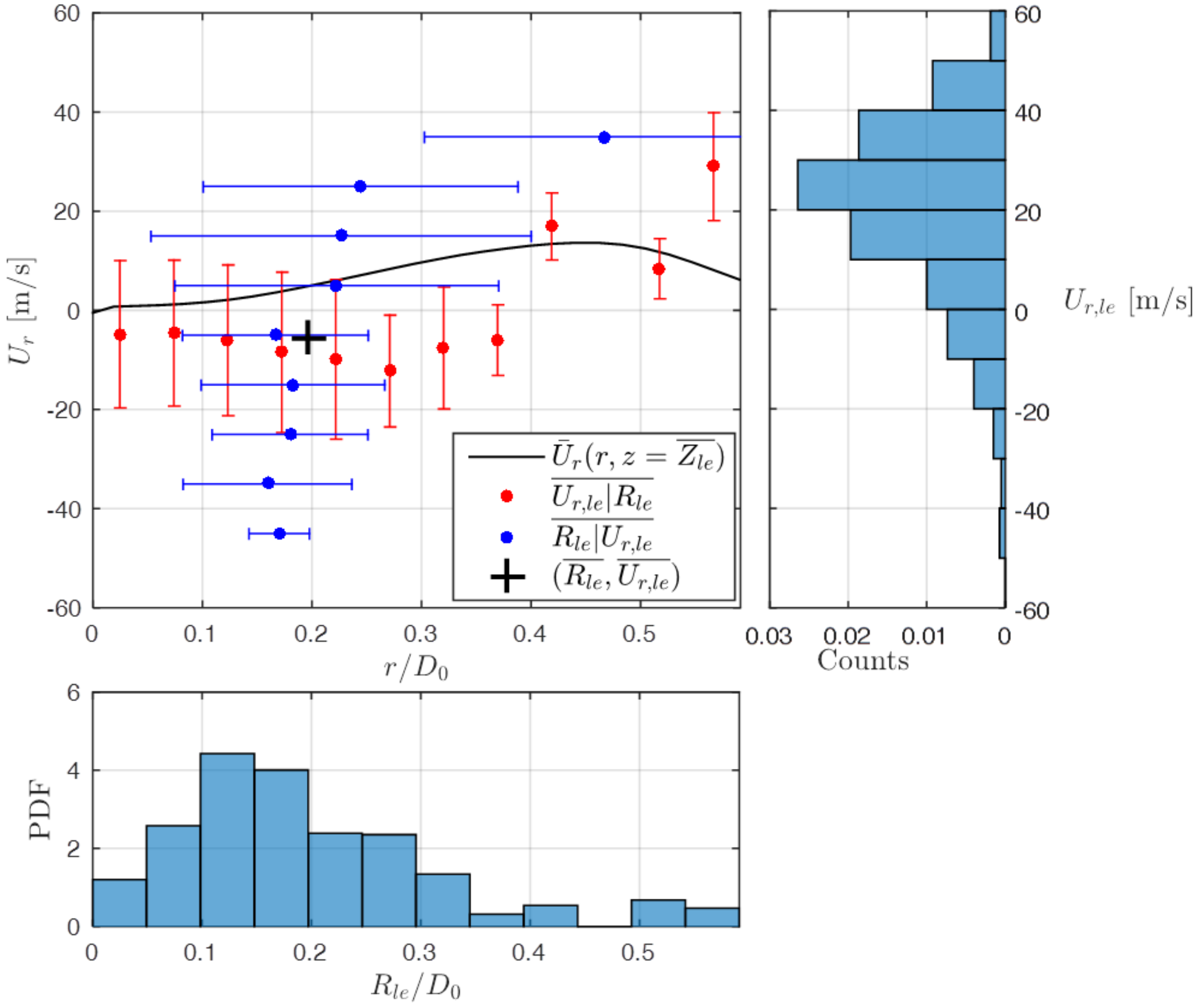

Figure 7.28: Case 2, plot 11, $U_{r,le}$ vs. R_{le}

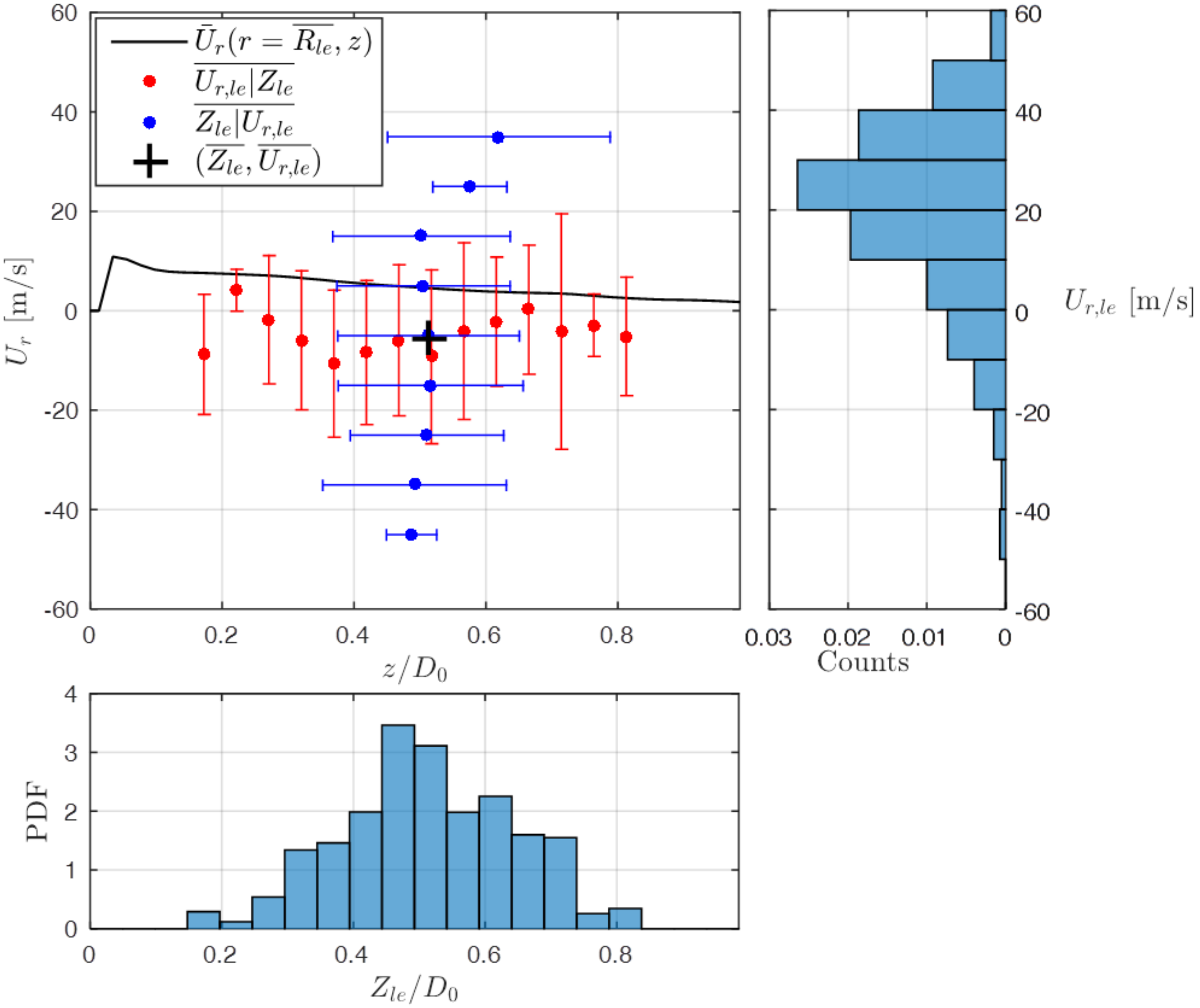

Figure 7.29: Case 2, plot 12, $U_{r,le}$ vs. Z_{le}

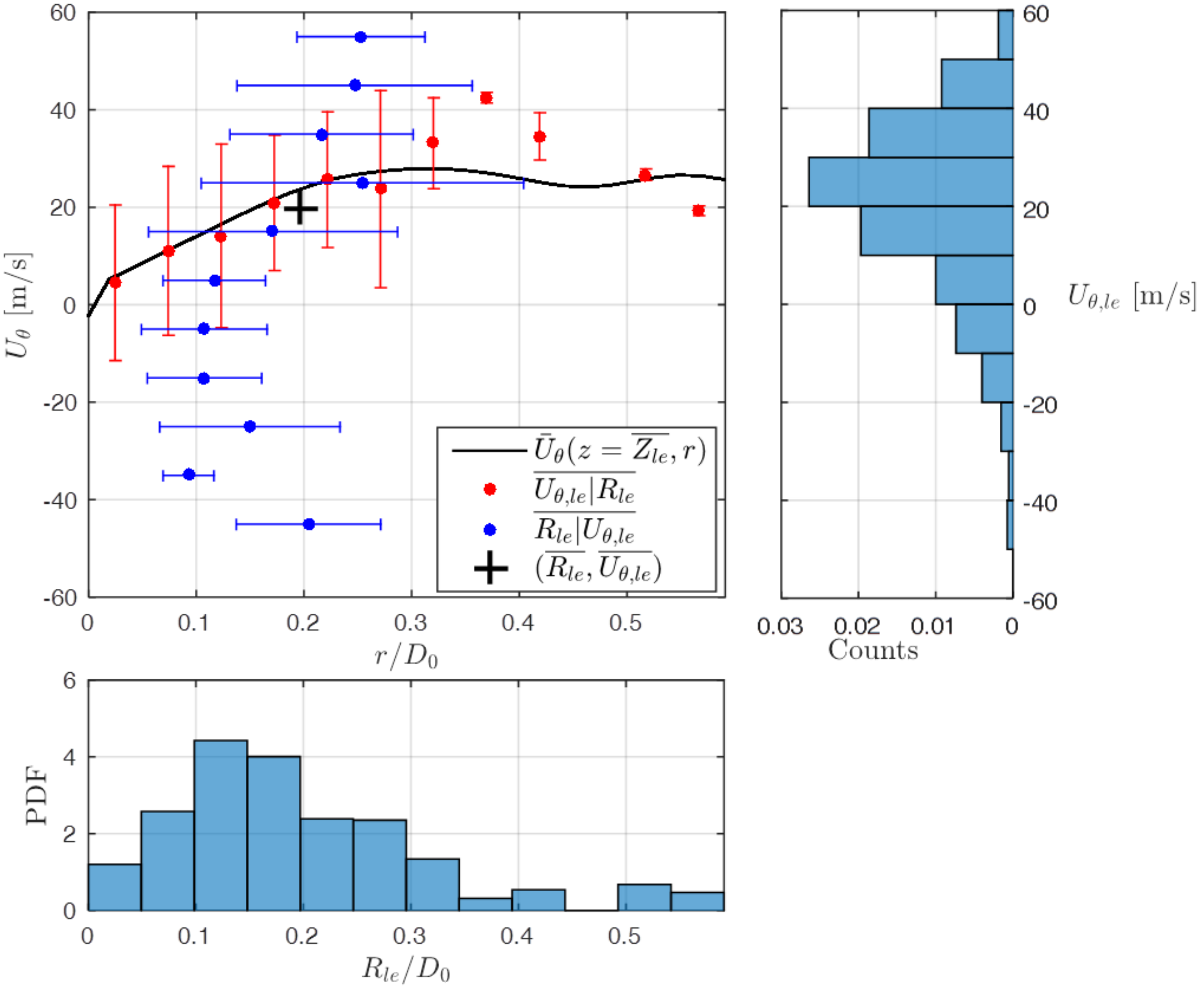

Figure 7.30: Case 2, plot 13, $U_{\theta,le}$ **vs.** R_{le}

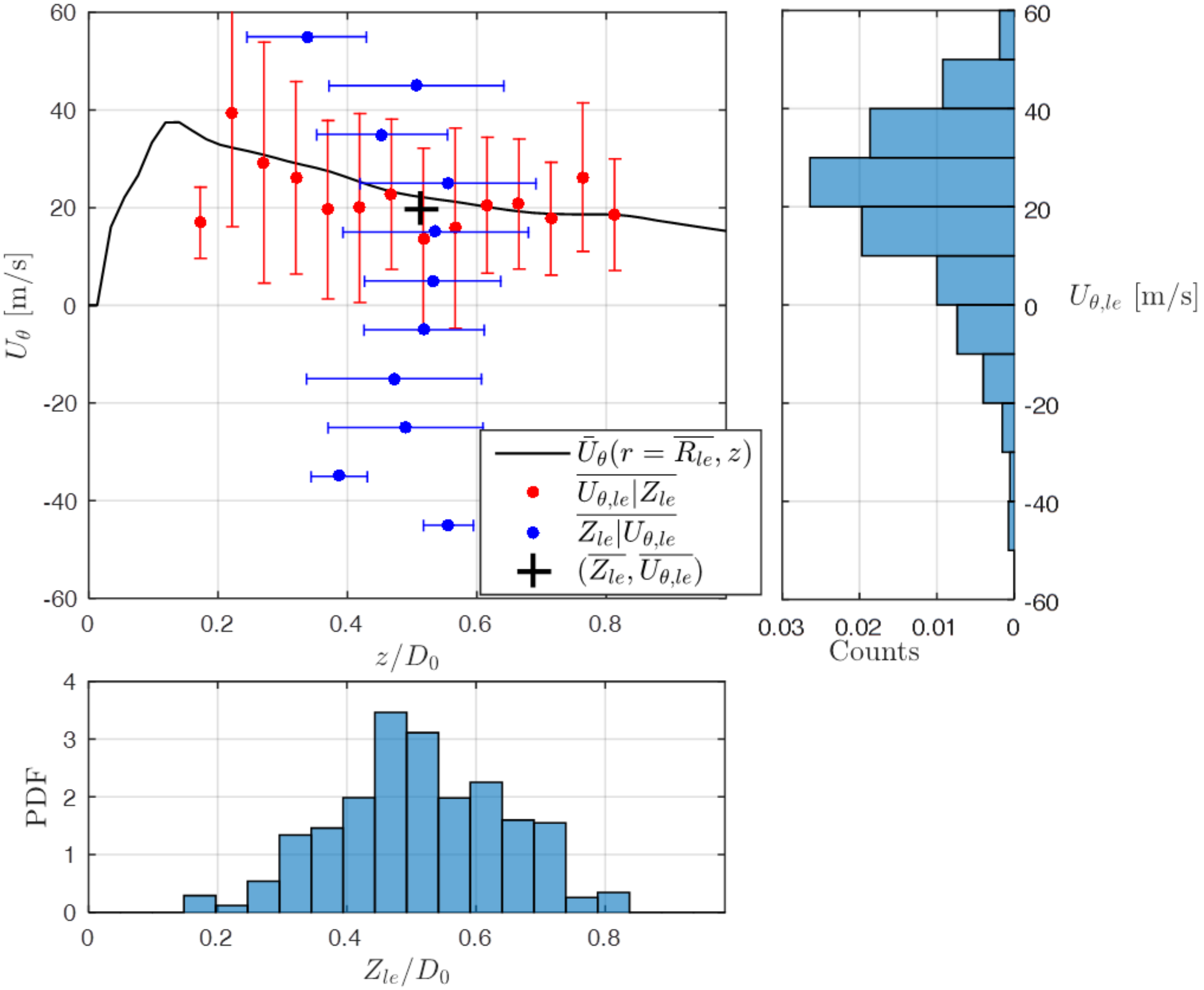

Figure 7.31: Case 2, plot 14, $U_{\theta,le}$ vs. Z_{le}

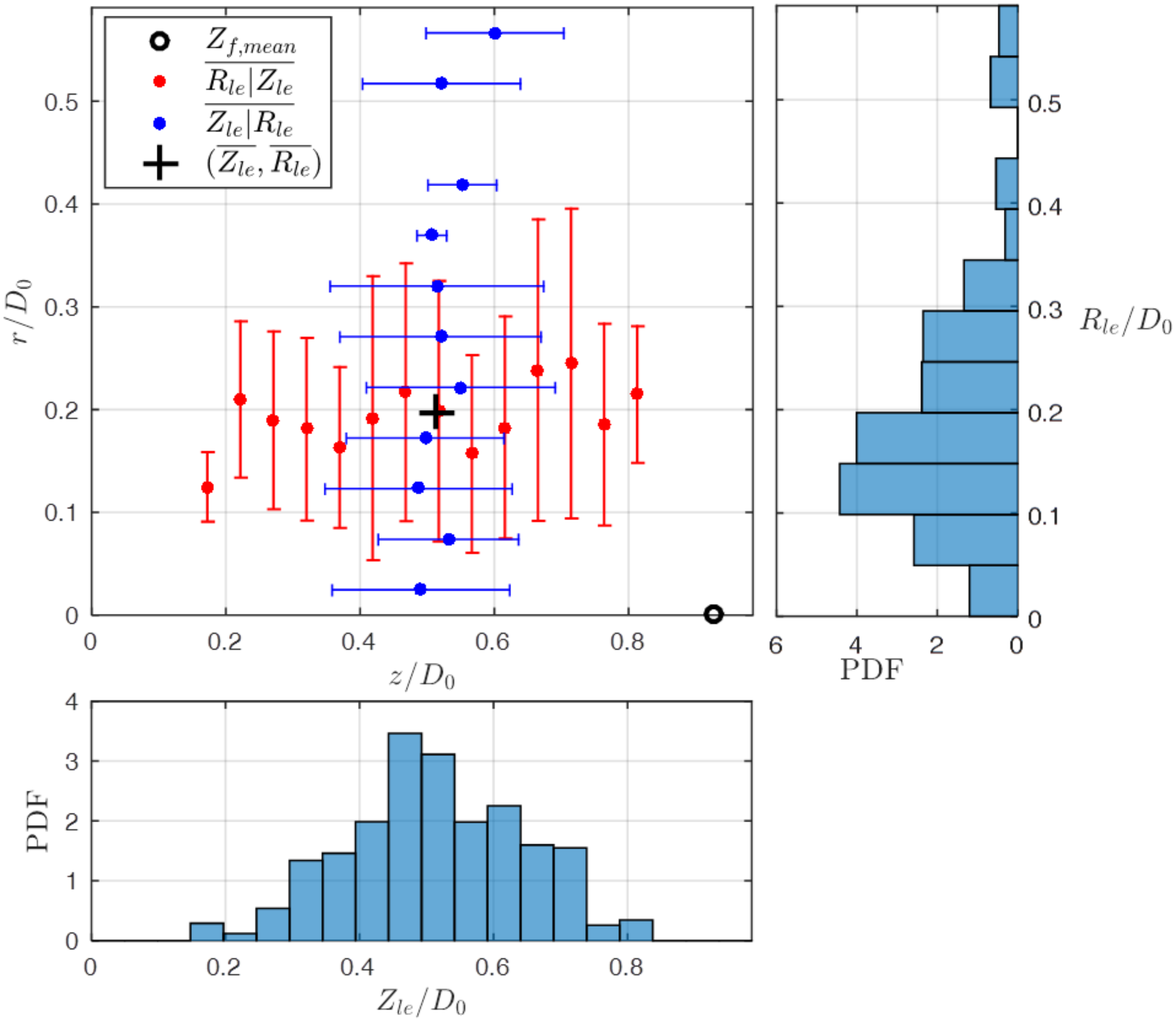

Figure 7.32: Case 2, plot 15, R_{le} **vs.** Z_{le}

APPENDIX B

AERODYNAMICALLY STABILIZED FLAME LEADING EDGE FLOW CHARACTERIZATION ADDITIONAL PLOTS

The following plots first illustrate the flow angle at the flame leading edge, in Figure 8.1, Figure 8.3, and Figure 8.4, with a side, downstream, and top-down view, respectively. Figure 8.1 indicates that in the low stretch case 2, the in-plane flow angle is nominally in the positive axial direction with second most frequent angle pointing in the negative axial direction. This observation is consistent with discussion from Chapter 4.2, and normal flame propagation, and positive flame speed. What's interesting for the high stretch case 1, is that the flow angle is frequently non-zero, suggesting that there is some non-normal flame propagation, which is likely linked to the high measured levels of stretch. The histogram in Figure 8.1 is asymmetric because there are more realizations at the top half of the combustor vs. the bottom half. If the top and bottom halves are viewed separately, as in Figure 8.2, it is easier to see that 45 degrees is the most probable flow angle when the flame stabilizes in positive flow. This 45 degree angle implies that the flame stretch computed using our definition (the negative of the axial velocity gradient) is inflated by a factor of $\sqrt{2}$.

Second, we show the statistics of the flame leading edge passing time, or the time between instances when the leading edge crosses the interrogation plane, in Figure 8.5. In case 1, the 70m/s premixer velocity case, the most frequent passing time is ~ 1ms, corresponding to the ~ 1000Hz PVC frequency observed for this geometry, as the flame follows the precessing flow. In the case 2, the slower 45m/s premixer velocity case, the most frequent passing time is ~ 1.5–2ms, corresponding to a lower PVC rate of ~ 500–670Hz.

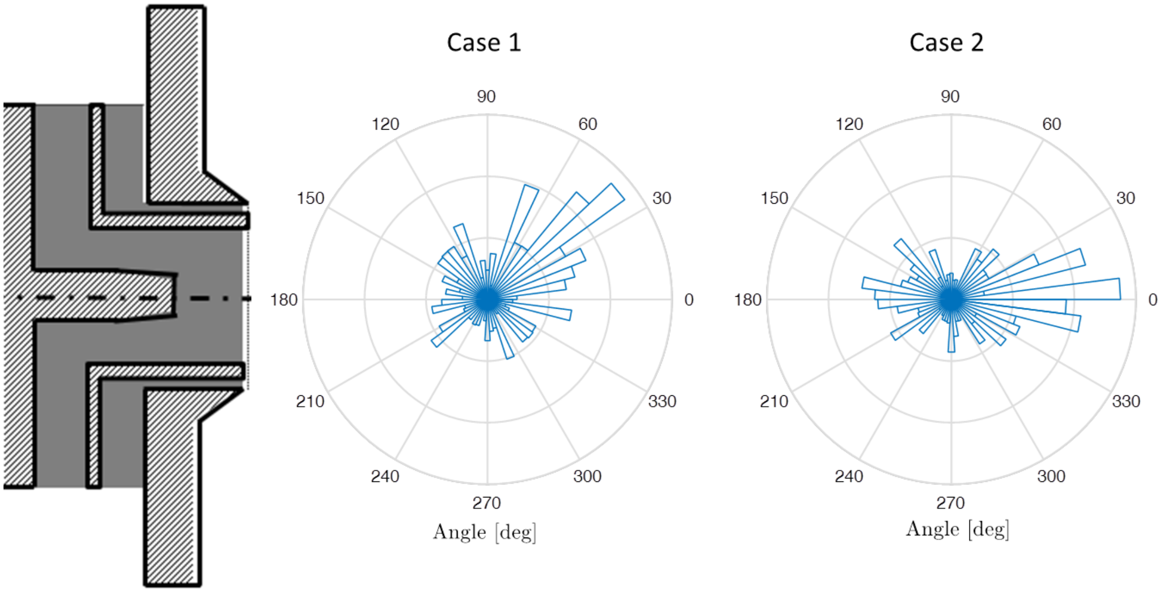

Figure 8.1: Flow angle polar histogram viewed normal to the interrogation plane at the flame leading edge for cases 1 and 2

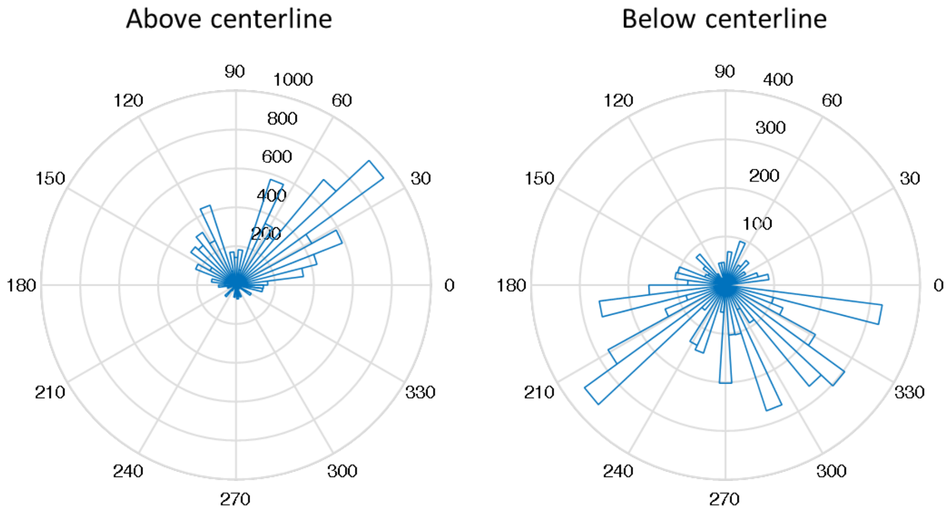

Figure 8.2: Polar histograms of flow angle viewed normal to the interrogation plane at the flame leading edge for case 2, split into realizations above the centerline vs. below the centerline

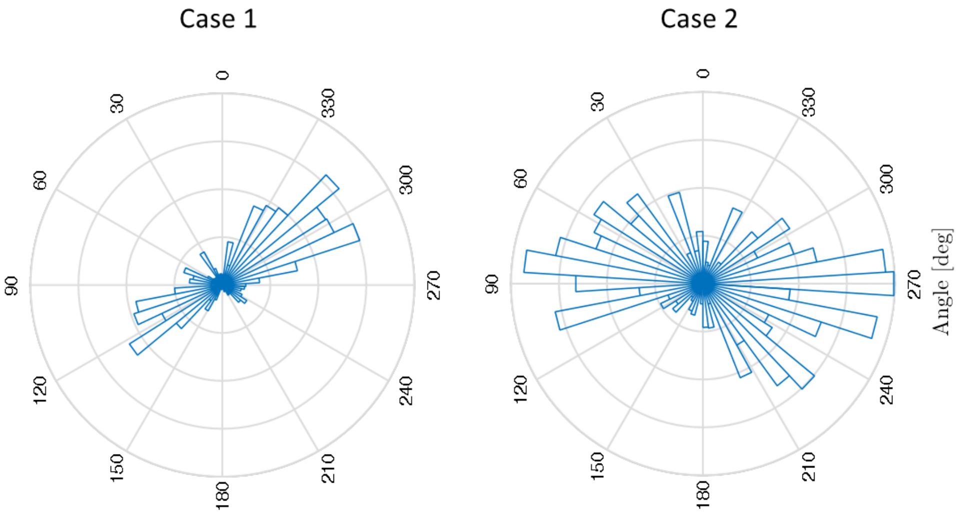

Figure 8.3: Flow angle polar histogram viewed in the downstream (*z*-direction) at the flame leading edge for cases 1 and 2

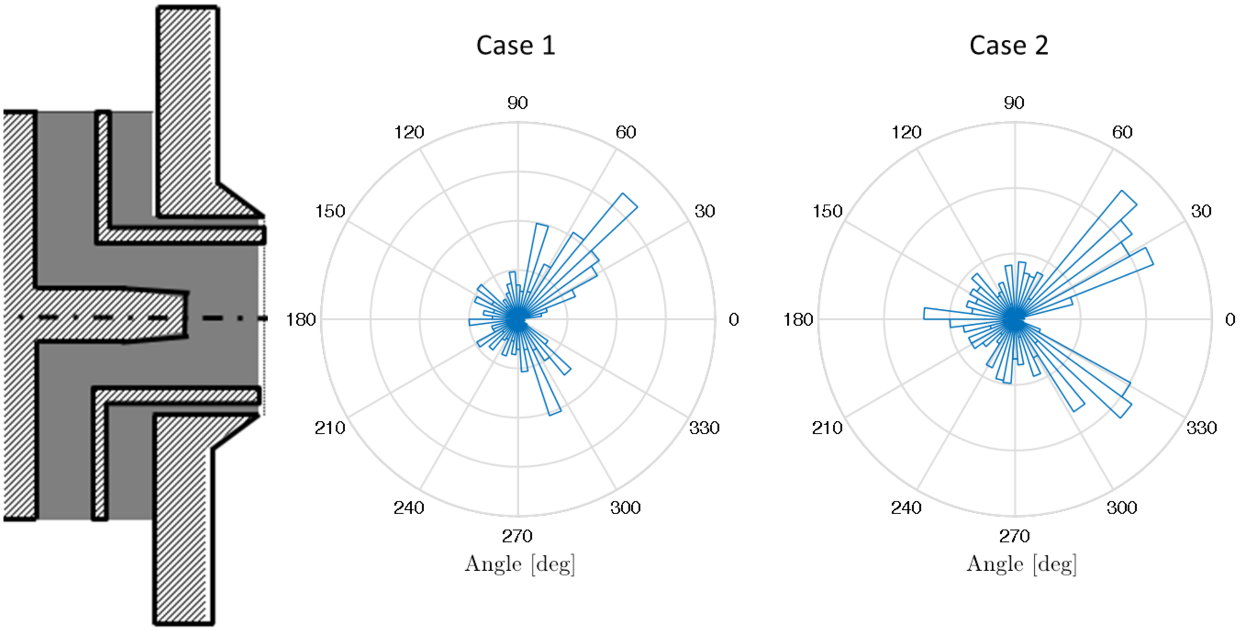

Figure 8.4: Flow angle polar histogram viewed top-down, tangential to the interrogation plane at the flame leading edge for cases 1 and 2

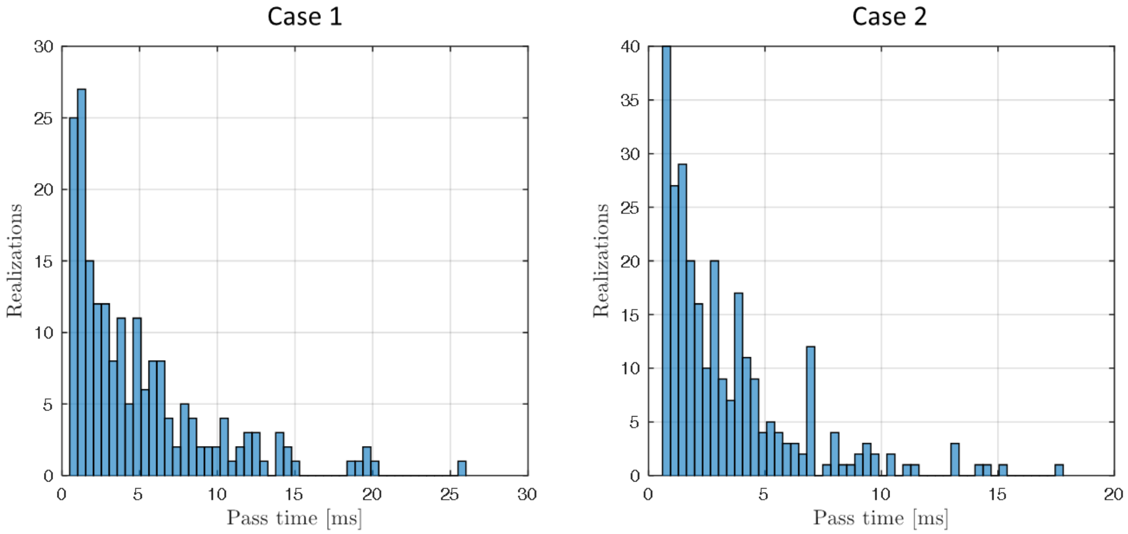

Figure 8.5: Histogram of the time between instances when the flame leading edge crosses the interrogation plane for cases 1 and 2

REFERENCES

[1] Ko, N.W.M., W.T. Chan, Similarity in the Initial Region of Annular Jets: Three Configurations, Fluid Mech. 84 (4) (1978) 641-656.

[2] Chan, W.T., N.W.M. Ko, Coherent Structures in the Outer Mixing Region of Annular Jets, Fluid Mech. 89 (3) (1978) 515-533.

[3] Ko, N.W.M., W.T. Chan, The Inner Regions of Annular Jets, Fluid Mech. 93 (3) (1979) 549-584.

[4] Ko, N.W.M., K.M. Lam, Flow Structures of a Basic Annular Jet, AIAA 23, No. 8 (August) (1985).

[5] Ko, N.W.M., K.K. Lau, Flow Structures in Initial Region of Two Interacting Parallel Plane Jets, Exp. Therm. Fluid Sci. 2 (1989) 431-449.

[6] Brown, G.L., J.M. Lopez, Axisymmetric Vortex Breakdown. Part 2. Physical Mechanisms, Fluid Mech. 221 (1990) 553-576.

[7] Peckam, D.H., S.A. Atkinson, Preliminary Results of Low Speed Tunnel Tests on a Gothic Wing of Aspect Ratio 1.0, 1957, A.R.C.

[8] Elle, B.J., An Investigation at Low Speed of the Flow near the Apex of Thin Delta Wings with Sharp Leading Edges, 1958, Ministry of Aviation, A.R.C. 1-19.

[9] Elle, B.J., On the Breakdown at High Incidence of the Leading Edge Vortices on Delta Wings, R. Aero. Soc 64 (596) (1960) 491-493.

[10] Hummel, D., P.S. Srinivasan, Vortex Breakdown Effects on the Low-Speed Aerodynamic Characteristics of Slender Delta Wings in Symmetrical Flow, R. Aero. Soc 71 (April) (1966) 319-322.

[11] Peake, D.J., M. Tobak, On Issues Concerning Flow Separation and Vortical Flows in Three Dimensions, AGARD-CP, No. 342, Aerodynamics of vortical type flows in three dimensions, paper 1. 1983.

[12] Escudier, M., Vortex Breakdown: Observations and Explanations, Prog. in Aerospace Sciences 25 (1988) 189-229.

[13] Hall, M.G., Vortex Breakdown, Annual review of fluid mechanics 4 (1) (1972) 195-218.

[14] Leibovich, S., The Structure of Vortex Breakdown, Annu. Rev. Fluid Mech. 10 (1978) 221-246.

[15] Leibovich, S., Vortex Stability and Breakdown: Survey and Extention, AIAA 22 (1984) 1192-1206.

[16] Stuart, J.T., A Critical Review of Vortex Breakdown Theory, Vortex Control and Breakdown Behaviour, Second International Colloquium on Vortical Flows, BBC 1987.

[17] Lucca-Negro, O., T. O'Doherty, Vortex Breakdown: a Review, Progr. Energy and Combust. Sci. 27 (2001) 431-481.

[18] Liang, H., T. Maxworthy, An Experimental Investigation of Swirling Jets, Fluid Mech. 525 (2005) 115-159.

[19] Billant, P., J.M. Chomaz, P. Huerre, Experimental Study of Vortex Breakdown in Swirling Jets, Fluid Mech. 376 (1998) 183-219.

[20] Sarpkaya, T., Turbulent Vortex Breakdown, Phys. Fluids 7 (1995).

[21] Healey, J.J., Inviscid Axisymmetric Absolute Instability of Swirling Jets, Fluid Mech. 613 (2008) 1-33.

[22] Darmofal, D.L., The Role of Vorticity Dynamics in Vortex Breakdown, AIAA (1993).

[23] Rusak, Z., S. Wang, C.H. Whiting, Numerical Computations of Axisymmetric Vortex Breakdown in a Pipe, AIAA (1996) Paper 96-0801.

[24] Wang, S., Z. Rusak, The Dynamics of a Swirling Flow in a Pipe and Transition to Axisymmetric Vortex Breakdown, Fluid Mech. 340 (1997) 177-223.

[25] Rusak, Z., S. Wang, S.H. Whiting, The Evolution of a Perturbed Vortex in a Pipe to Axisymmetric Vortex Breakdown, Fluid Mech. 366 (1998) 211-237.

[26] Sarpkaya, T., On Stationary and Travelling Vortex Breakdowns, Fluid Mech. 45 (3) (1971) 545-459.

[27] Gupta, A.K., D.J. Lilley, N. Syred, Swirl Flows1984, Tunbridge Wells, UK: Abacus Press.

[28] Wicksall, D.M., A.K. Agrawal, R.W. Schefer, J.O. Keller. The Interaction of Flame and Flow Field in a Lean Premixed Swirl-Stabilized Combustor Operated on H2/CH4/Air. Proc. Combust. Inst. (2004).

[29] Lu, X., S. Wang, H. Sung, S. Hsieh, V. Yang, Large Eddy Simulations of Turbulent Swirling Flows Injected into a Dump Chamber, Fluid Mech. 527 (1999) 171-195.

[30] Sheen, H.J., W.J. Chen, S.Y. Jeng, Recirculation Zones of Unconfined and Confined Annular Swirling Jets, AIAA 34 (3) (1996) 572–579.

[31] Emara, A., A. Lacarelle, C. Paschereit, Planar Investigation of Outlet Boundary Conditions Effect on Isothermal Flow Fields of a Swirl-Stabilized Burner, Turbo Expo 2009, ASME.

[32] Faler, J.H., S. Leibovich, An Experimental Map of the Internal Structure of a Vortex Breakdown, Fluid Mech. 86 (02) (1978).

[33] Spall, R.E., T.B. Gatski, R.L. Ash. The Structure and Dynamics of Bubble-Type Vortex Breakdown. R Soc London A. (1990).

[34] Vanierschot, M., E.V.d. Bulck, Influence of Swirl on the Initial Merging Zone of a Turbulent Annular Jet, Phys. Fluids 20 (2008).

[35] Chterev, I., C.W. Foley, D. Foti, S. Kostka, A.W. Caswell, N. Jiang, A. Lynch, D.R. Noble, S. Menon, J.M. Seitzman, T. Lieuwen, Flame and Flow Topologies in an Annular Swirling Flow, Combust. Sci. Tech. 186 (8) (2014) 1041-1074.

[36] Rusak, Z., A.K. Kapila, J.J. Choi, Effect of Combustion on near-Critical Swirling Flow, Combust. Theory Model. 6 (4) (2002) 625-645.

[37] Stein, O., A. Kempf. LES of the Sydney Swirl Fame Series: A Study of Vortex Breakdown in Isothermal and Reacting Fows. Proc. Combust. Inst. (2007).

[38] Lacarelle, A., Faustmann, T., Greenblatt, D., Paschereit, C. O., Lehmann, O., Luchtenburg, D. M., and Noack, B. R., Spatiotemporal Characterization of a Conical Swirler Flow Field Under Strong Forcing, Eng. Gas Turbines Power 131 (2009) 031504.

[39] Paschereit, C.O., P. Flohr, M. Bockholts, W. Polifke, Fluid Dynamic Instabilities in a Swirl Stabilized Burner and their Effect on Heat Release Fluctuations. Flow-Induced Vibration, ed. S. Ziada and T. Staubli2000, Leiden: A a Balkema Publishers. 687-694.

[40] Schimek, S., J.P. Moeck, C.O. Paschereit, An Experimental Investigation of the Nonlinear Response of an Atmospheric Swirl-Stabilized Premixed Flame, Eng. Gas Turbines Power 133 (2011).

[41] Acharya, V., M. Malanoski, M. Aguilar, T. Lieuwen, Dynamics of a Transversely Excited Swirling, Lifted Flame: Flame Response Modeling and Comparison With Experiments, Eng. Gas Turbines Power 136 (5) (2014).

[42] Kang, D.M., F.E.C. Culick, A. Ratner, Combustion Dynamics of a Low-Swirl Combustor, Combust. Flame 151 (3) (2007) 412-425.

[43] Huang, Y., Ratner, A., Experimental Investigation of Thermoacoustic Coupling for Low-Swirl Lean Premixed Flames, Propulsion and Power 25 (2) (2009) 365-373.

[44] Candel, S., D. Durox, T. Schuller, P. Palies, Progress and Challenges in Swirling Flame Dynamics, C. R. Mecanique 340 (2012) 758-768.

[45] Palies, P., D. Durox, T. Schuller, S. Candel, The Combined Dynamics of Swirler and Turbulent Premixed Swirling Flames, Combust. Flame 157 (9) (2010) 1698-1717.

[46] Syred, N., A Review of Oscillation Mechanisms and the Role of the Precessing Vortex Core (PVC) in Swirl Combustion Systems, Progr. Energy and Combust. Sci. 32 (2006) 93-161.

[47] Rodriquez-Martinez, V.M., 2003, Cardiff University.

[48] Fick, W., 1968, Cardiff University.

[49] Froud, D., 1996, University of Wales: Cardiff.

[50] Chanaud, R.C., Observations of Oscillatory Motion in Certain Swirling Flows, Fluid Mech. 21 (01) (1965).

[51] Fick, W., Griffiths, A. J., O'Doherty, T., Visualisation of the precessing vortex core in an unconfined swirling flow, Opt. Diagn. Eng 2 (1) (1997) 19-31.

[52] Syred, N., J.M. Beer, Combustion in Swirling Flows: A Review, Combust. Flame 23 (2) (1974) 143-201.

[53] Syred, N., K.R. Dahmen, The Effect of High Levels of Confinement Upon the Aerodynamics of Swirl Burners, AIAA 2 (1) (1978) 8-15.

[54] Claypole, T.C., 1980, University of Wales.

[55] Claypole, T.C., Coherent Structures in Swirl Generators and Combustors, Symp. Vortex Flows, Winter Annual Meeting 1980, ASME: Chicago, IL.

[56] Ho, C.M., P. Huerre, Perturbed Free Shear Layers, Annu. Rev. Fluid Mech. 16 (1) (1984) 365–422.

[57] Brown, G.L., A. Roshko, On Density Effects and Large Structure in Turbulent Mixing Layers, Fluid Mech. 64 (04) (1974) 775–816.

[58] Stöhr, M., I. Boxx, C.D. Carter, W. Meier, Experimental Study of Vortex-Flame Interaction in a Gas Turbine Model Combustor, Combust. Flame 159 (2012) 2636-2649.

[59] Alekseenko, S.V., P.A. Kuibin, V.L. Okulov, S.I. Shtork, Helical Vortices in Swirl Flow, Fluid Mech. 382 (1999) 195-243.

[60] Cala, C.E., E.C. Fernandes, M.V. Heitor, S.I. Shtork, LDA Analysis of PVC-Central Recirculation Zone Interaction in a Model Vortex Burner, Int. Symp. on Applications of Laser Techniques to Fluid Mechanics 2004: Lisbon, Portugal.

[61] Cala, C.E., Fernandes, E., Heitor, M. V., Shtork, S. I., Coherent structures in unsteady swirling jet flow, Exp Fluids 40 (2) (2006) 267-276.

[62] Brücker, C., Study of Vortex Breakdown by Particle Tracking Velocimetry, Exp. Fluids 14 (1993) 133-139.

[63] Jochmann, P., A. Sinigersky, M. Hehle, O. Schäfer, R. Koch, H.J. Bauer, Numerical Simulation of a Precessing Vortex Breakdown, Int. J. Heat and Fluid Flow 27 (2006) 192-203.

[64] Thumuluru, S.K., T. Lieuwen. Characterization of acoustically forced swirl flame dynamics. Proc. Combust. Inst. (2009).

[65] Zhang, Q., S.J. Shanbhogue, Shreekrishna, T.Lieuwen, J. O'Connor, Strain Characteristics near the Flame Attachment Point in a Swirling Fow, Combust. Sci. Tech. 183 (7) (2011) 665–685.

[66] Durbin, M.D., M.D. Vangsness, D.R. Ballal, V.R. Katta, Study of flame stability in a step swirl combustor, J. Eng. Gas Turbines Power 118 (2) (1996) 308–315.

[67] Kim, D., Lee, J. G., Quay, B. D., Santavicca, D. A., Kim, K., Srinivasan, S., Effect of flame structure on the flame transfer function in a premixed gas turbine combustor, Eng. Gas Turbines Power 132 (2) (2010).

[68] Kim, K.T., Lee, J. G., Lee, H. J., Quay, B. D., Santavicca, D. A., Characterization of forced flame response of swirl-stabilized turbulent lean-premixed flames in a gas turbine combustor, Eng. Gas Turbines Power 132 (4) (2010).

[69] Shanbhogue, S.J., Y. S. Sanusi, S. Taamallah, M. A. Habib, E. M. A. Mokheimer, A. F. Ghoniem, Flame macrostructures, combustion instability and extinction strain scaling in swirl-stabilized premixed CH 4/H 2 combustion, Combust. Flame 163 (2016) 494-507.

[70] Taamallah, S., LaBry, Z. A., Shanbhogue, S. J., Ghoniem, A. F., Thermo-acoustic instabilities in lean premixed swirl-stabilized combustion and their link to acoustically coupled and decoupled flame macrostructures, Proc. Comb. Institute 35 (3) (2015) 3273-3282.

[71] Taamallah, S., LaBry, Z. A., Shanbhogue, S. J., Habib, M. A., Ghoniem, A. F., Correspondence Between "Stable" Flame Macrostructure and Thermo-acoustic Instability in Premixed Swirl-Stabilized Turbulent Combustion, Engineering for Gas Turbines and Power 137 (7) (2015).

[72] Lieuwen, T., V. McDonell, E. Petersen, D. Santavicca, Fuel Flexibility Influences on Premixed Combustor Blowout, Flashback, Autoignition, and Stability, Eng. Gas Turbines Power 130 (1) (2008) 954-961.

[73] Zhang, Q., D.R. Noble, T. Lieuwen, Characterization of Fuel Composition Effects in H2 /CO/CH4 Mixtures Upon Lean Blowout, Eng. Gas Turbines Power 129 (3) (2007) 688.

[74] Plessing, T., C. Kortschik, N. Peters, M.S. Mansour, R.K. Cheng, Measurements of the Turbulent Burning Velocity and the Structure of Premixed Flames on a Low-Swirl Burner, Int. Symp. on Combustion 2000 359-366.

[75] Marshall, A., P. Venkateswaran, J. Seitzman, T. Lieuwen, Measurements of Leading Point Conditioned Statistics of High Hydrogen Content Fuels, Int. Symp. on Combustion 2013.

[76] Marshall, A., J. Lundrigan, P. Venkateswaran, J. Seitzman, T. Lieuwen, Fuel Effects on Leading Point Curvature Statistics of High Hydrogen Content Fuels, Int. Symp. on Combustion 2014.

[77] Marshall, A., J. Lundrigan, P. Venkateswaran, J. Seitzman, T. Lieuwen, Measurements of Stretch Statistics at Flame Leading Points for High Hidrogen Content Fuels, Turbo Expo 2014, ASME: Düsseldorf, Germany.

[78] Feikema, D., R.H. Chen, J.F. Driscoll, Enhancement of Flame Blowout Limits by the Use of Swirl Combust. Flame 80 (2) (1990) 183-195.

[79] Thumuluru, S.K., Lieuwen, T., Characterization of Acoustically Forced Swirl Flame Dynamics, Proc. Combust. Inst. 32 (2) (2009) 2893-2900.

[80] Durbin, M.D., M.D. Vangness, D.R. Ballal, V.R. Katta, Study of Flame Stability in a Step Swirl Combustor, Eng. Gas Turbines Power 118 (2) (1996).

[81] Malanoski, M., M. Aguilar, V. Acharya, T. Lieuwen, Dynamics of a Transversely Excited Swirling, Lifted Flame Part I: Experiments and Data Analysis, Turbo Expo 2013, ASME: San Antonio, TX.

[82] Biagioli, F., F. Güthe, B. Schuermans, Combustion Dynamics Linked to Flame Behaviour in a Partially Premixed Swirled Industrial Burner, Exp. Therm. Fluid Sci. 32 (7) (2008) 1344-1353.

[83] Schmitt, P., Poinsot, T., Schuermans, B., Geigle, K. P., Large-eddy simulation and experimental study of heat transfer, nitric oxide emissions and combustion instability in a swirled turbulent high-pressure burner, Fluid Mech. 570 (2007) 17-46.

[84] Janus, B., A. Dreizler, J. Janicka, Experimental Study on Stabilization of Lifted Swirl Flames in a Model GT Combustor, Flow, Turbulence and Combustion 75 (1-4) (2005) 293-315.

[85] Escudier, M.P., J.J. Keller, Recirculation in Swirling Flow - A Manifestation of Vortex Breakdown, AIAA 23 (1) (1985) 111-116.

[86] Huang, R.F., F.C. Tsai, Observations of Swirling Flows Behind Circular Disks, AIAA 39 (6) (2001).

[87] Syred, N., T.C. Claypole, A.C. Styles, The Role of Centrifugal Force Fields in the Stabilization of Swirling Flames, Energy 6 (5) (1982) 344-345.

[88] Najim, S.E., An Aerodynamic Study of Cyclone Combustion with Gaseous Fuels, 1979, University of wales.

[89] Law, C.K., Combustion Physics2006, New York: Cambridge University Press.

[90] Law, C.K., C.J. Sung, Structure, Aerodynamics, and Geometry of Premixed Flamelets, Progr. Energy and Combust. Sci. 26 (4) (2000) 459-505.

[91] Lewis, G.D. Combustion in a Centrifugal-Force Field. Int. Symp. on Combustion. (1971). The Combustion Institute.

[92] Lewis, G.D. Centrifugal-Force Effects on Combustion. Int. Symp. on Combustion. (1973). The Combustion Institute.

[93] Foley, C.W., I. Chterev, J. Seitzman, T. Lieuwen, High Resolution PIV and CH-PLIF Measurements and Analysis of a Shear Layer Stabilized Flame, Turbo Expo 2015, ASME: Montreal, Canada.

[94] Shanbhogue, S.J., S. Husain, T. Lieuwen, Lean Blowoff of Bluff Body Stabilized Flames: Scaling and Dynamics, Progr. Energy and Combust. Sci. 35 (2009) 98-120.

[95] Chaudhuri, S., Kostka, S., Renfro, M. W., Cetegen, B. M., Blowoff dynamics of bluff body stabilized turbulent premixed flames, Combust. Flame 157 (4) (2010) 790-802.

[96] Chaudhuri, S., Kostka, S., Tuttle, S. G., Renfro, M. W., Cetegen, B. M. , Blowoff mechanism of two dimensional bluff-body stabilized turbulent premixed flames in a prototypical combustor, Combust. Flame 158 (7) (2011) 1358-1371.

[97] Chaudhuri, S., Kostka, S., Renfro, M. W., Cetegen, B. M., Blowoff mechanism of harmonically forced bluff body stabilized turbulent premixed flames, Combust. Flame 159 (2) (2012) 638-640.

[98] Tuttle, S.G., Chaudhuri, S., Kostka, S., Kopp-Vaughan, K. M., Jensen, T. R., Cetegen, B. M., Renfro, M. W., Time-resolved blowoff transition measurements for two-dimensional bluff body-stabilized flames in vitiated flow, Combust. Flame 159 (1) (2012) 291-305.

[99] Petersson, P., J. Olofsson, C. Brackman, H. Seyfried, J. Zetterberg, M. Richter, A. Dreizler, Simultaneous PIV/OH-PLIF, Rayleigh Thermometry/OH-PLIF and Stereo PIV Measurements in a Low-Swirl Flame, Applied Optics 49 (19) (2007) 3928-3936.

[100] Hult, J., U. Meier, W. Meier, A. Harvey, C.F. Kaminski. Experimental Analysis of Local Flame Extinction in a Turbulent Jet Diffusion Flame by High Repetition 2-D Laser Techniques and Multi-Scalar Measurements. Proc. Combust. Inst. (2005).

[101] Steinberg, A.M., J.F. Driscoll, S.L. Ceccio, Measurements of Turbulent Premixed Flame Dynamics Using Cinema Stereoscopic PIV, Exp. Fluids 44 (6) (2008) 985-999.

[102] Arndt, C., A. Steinberg, I. Boxx, W. Meier, M. Aigner, C. Carter, Flow-Field and Flame Dynamics of a Gas Turbine Model Combustor During Transition Between Thermo-Acoustically Stable and Unstable States, Turbo Expo 2010, ASME: Glasgow, UK.

[103] Steinberg, A., I. Boxx, M. Stöhr, W. Meier, C. Carter, Effects of Flow Structure Dynamics on Thermoacoustic Instabilities in Swirl-Stabilized Combustion, AIAA 50 (4) (2012).

[104] Upatnieks, A., J.F. Driscoll, S.L. Ceccio. Cinema Particle Imaging Velocimetry Time History of the Propagation Velocity of the Base of a Lifted Turbulent Jet Flame. Proc. Combust. Inst. (2002).

[105] Tanahashi, M., S. Murakami, G.M. Choi, Y. Fukuchi, T. Miyauchi. Simultaneous CH–OH PLIF and Stereoscopic PIV Measurements of Turbulent Premixed Flames. Proc. Combust. Inst. (2005).

[106] Shimura, M., T. Ueda, G.M. Choi, M. Tanahashi, T. Miyauchi. Simultaneous Dual-Plane CH PLIF, Single-Plane OH PLIF and Dual-Plane Stereoscopic PIV Measurements in Methane-Air Turbulent Premixed Flames. Proc. Combust. Inst. (2011).

[107] Böhm, B., Heeger, C., Boxx, I., Meier, W., Dreizler, A., Time-resolved conditional flow field statistics in extinguishing turbulent opposed jet flames using simultaneous highspeed PIV/OH-PLIF, Proc. Comb. Institute 32 (2) (2009) 1647-1654.

[108] Sadanandan, R., Stöhr, M., Meier, W., Simultaneous OH-PLIF and PIV measurements in a gas turbine model combustor, Applied Physics B 90 (3) (2008) 609-618.

[109] Coriton, B., Steinberg, A. M., Frank, J. H., High-speed tomographic PIV and OH PLIF measurements in turbulent reactive flows, Exp. Fluids 55 (6) (2014) 1743.

[110] Steinberg, A.M., Boxx, I., Arndt, C. M., Frank, J. H., Meier, W., Experimental study of flame-hole reignition mechanisms in a turbulent non-premixed jet flame using sustained multi-kHz PIV and crossed-plane OH PLIF, Proc. Comb. Institute 33 (1) (2011) 1663-1672.

[111] Chong, C.T., S. Hochgreb, Spray Flame Study Using a Model Gas Turbine Swirl Burner, Applied Mechanics and Materials 316 (2013) 17-22.

[112] Chong, C.T., S. Hochgreb, Spray Flame Structure of Rapeseed Biodiesel and Jet-A1 Fuel, Fuel 115 (2014) 551-558.

[113] Schroll, M., J. Klinner, L. Lange, C. Willert, Particle Image Velocimetry of Highly Luminescent, Pressurized Combustion Flows of Aero Engine Combustors, Int. Symp. on Particle Image Velocimetry 2013: Delft, The Netherlands.

[114] Meier, U., J. Heinze, E. Magens, M. Schroll, C. Hassa, S. Bake, T. Doerr, Optically Accessible Multisector Combustor: Application and Challenges of Laser Techniques at Realistic Operating Conditions, Turbo Expo 2015, ASME: Montreal, Canada.

[115] Slabaugh, C., A.C. Pratt, R.P. Lucht, Simultaneous 5 kHz OH-PLIF/PIV for the study of turbulent combustion at engine conditions, Applied Physics B 118 (1) (2015) 109-130.

[116] Slabaugh, C., I. Boxx, S. Werner, R.P. Lucht, W. Meier, Structure and Dynamics of Premixed Swirl Flames at Elevated Power Density, AIAA 54 (3) (2016) 946-961.

[117] Allen, M.G., K.R. McMagnus, D.M. Sonnenfroh, P.H. Paul, Planar Laser-Induced-Fluorescence Imaging Measurements of OH and Hydrocarbon Fuel Fragments in High-Pressure Spray-Flame Combustion, Applied Optics 34 (27) (1995) 6287.

[118] Roditcheva, O.V., X.S. Bai, Pressure Effect on Soot Formation in Turbulent Diffusion Flames, Chemosphere 42 (5) (2001) 811-821.

[119] Zhang, Z., Q.A. Ezekoye, Soot Production Rate Calculations at Elevated Pressure in a Methane-Air Jet Diffusion Flame, Combust. Sci. Tech. 137 (1-6) (1998) 323-346.

[120] Frank, J.H., M.F. Miller, M.G. Allen, Imaging of Laser-Induced Fluorescence in a High-Pressure Combustor, AIAA Paper 99-0773. 1999.

[121] Locke, R.J., Y.R. Hicks, R.C. Anderson, K.A. Ockunzzi, OH Imaging in a Lean Burning High-Pressure Combustor, AIAA 34 (3) (1996) 622-624.

[122] Hicks, Y.R., R.J. Locke, R.C. Anderson, Optical measurement and visualization in high-pressure high-temperature aviation gas turbine combustors, Symp. Applied Photonics 2000, Int. Society Optics and Photonics.

[123] Skeen, S.A., Manin, J. and Pickett, L. M., Simultaneous formaldehyde PLIF and high-speed schlieren imaging for ignition visualization in high-pressure spray flames, Proc. Comb. Institute 35 (3) (2015) 3167-3174.

[124] Lantz, A., R. Collin, J. Sjöholm, Z.S. Li, P. Petersson, M. Aldén, High-Speed Fuel/Hydroxyl Radical Imaging in a Gas Turbine Pilot Burner, AIAA 50 (4) (2012) 971-975.

[125] Hult, J., M. Richter, J. Nygren, M. Aldén, A. Hultqvist, M. Christensen, B. Johansson, Application of a High-Repetition-Rate Laser Diagnostic System for Single-Cycle-Resolved Imaging in Internal Combustion Engines, Applied Optics 41 (24) (2002) 5002-5014.

[126] Müller, S.H.R., B. Böhm, M. Gleißner, S. Arndt, A. Dreizler, Analysis of the Temporal Flame Kernel Development in an Optically Accessible IC Engine Using High-Speed OH-PLIF, Applied Physics B 100 (3) (2010) 447-452.

[127] Peterson, B., V. Sick, High-speed flow and fuel imaging study of available spark energy in a spray-guided direct-injection engine and implications on misfires, Int. J. Engine Research 11 (5) (2010) 313-329.

[128] Seitzman, J.M., R.K. Hanson, Comparison of Excitation Techniques for Quantitative Fluorescence Imaging of Reacting Flows, AIAA 31 (3) (1993) 513-519.

[129] Battles, B.E., R.K. Hanson, Laser-Induced Fluorescence Measurements of NO and OH Mole Fraction in Fuel-Lean, High-Pressure (1–10 atm) Methane Flames: Fluorescence Modeling and Experimental Validation, Quantitative Spectroscopy and Radiative Transfer 54 (3) (1995) 521-537.

[130] Kobayashi, H., Y. Oyachi, K. Maruta, LIF Measurements of Turbulent Premixed Flames in a High Pressure Environment, Joint Thermal Engineering Conference 1999, ASME/JSME.

[131] Singla, G., P. Scouflaire, C. Rolon, S. Candel, Planar Laser-Induced Fluorescence of OH in High-Pressure Cryogenic LOx/GH 2 Jet Flames, Combust. Flame 144 (1) (2006) 151-169.

[132] Jiang, N., Patton, R. A., Lempert, W. R., Sutton, J. A., Development of high-repetition rate CH PLIF imaging in turbulent nonpremixed flames, Proc. Comb. Institute 33 (1) (2011) 767-774.

[133] Slipchenko, M.N., Miller, J. D., Roy, S., Gord, J. R., Meyer, T. R., All-diode-pumped quasi-continuous burst-mode laser for extended high-speed planar imaging, Optics express 21 (1) (2013) 681-689.

[134] Miller, J.D., Slipchenko, M., Meyer, T. R., Jiang, N., Lempert, W. R., Gord, J. R., Ultrahigh-frame-rate OH fluorescence imaging in turbulent flames using a burst-mode optical parametric oscillator, Optics Letters 34 (9) (2009) 1309-1311.

[135] Chong, C.T., S. Hochgreb, Flow Field of a Model Gas Turbine Swirl Burner, Advanced Materials Research 622 (2013) 1119-1124.

[136] Steinberg, A.M., Arndt, C. M., Meier, W., Parametric study of vortex structures and their dynamics in swirl-stabilized combustion, Proc. Comb. Institute 34 (2) (2013) 3117-3125.

[137] Roy, S., Hua, J. C., Barnhill, W., Gunaratne, G. H., Gord, J. R., Deconvolution of reacting-flow dynamics using proper orthogonal and dynamic mode decompositions, Physical Review E 91 (1) (2015).

[138] S. Roy, T.Y., N. Jiang, G. Gunaratne, I. Chterev, B. Emerson, T. Lieuwen, A. W. Caswell, and J. R. Gord, Dynamics of Robust Structures in Turbulent Swirling Flows, J. Fluid Mech. (2017).

[139] Joshi, N.D., Epstein, M. J., Durlak, S., Marakovits, S., Sabla, P. E. , Development of a fuel air premixer for aero-derivative dry low emissions combustors, Int. Gas Turbine and Aeroengine Congress and Exposition 1994, ASME.

[140] Kim, J.C., Sung, H. G., Min, D. K., Yang, V., Large Eddy Simulation of the Turbulent Flowfield in a Swirl Stabilized Annular Combustor, ASM 2009, AIAA 645.

[141] Mongia, H.C., M. Al-Roub, A. Danis, D. Elliott-Lewis, S. M. Jeng, A. Johnson, V. G. McDonell, G. S. Samuelsen, S. Vise., Swirl cup modeling part 1, AIAA Paper 3576 (2001).

[142] Scheiman, J., J.D. Brooks, Comparison of experimental and theoretical turbulence reduction from screens, honeycomb, and honeycomb-screen combinations, J. Aircraft 18 (8) (1981) 638-643.

[143] Rosfjord, T.J., J.M. Cohen, Air and Spray Patterns Produced by Gas Turbine High-Shear Nozzle Swirler Assemblies, ASM 1990, AIAA: Reno, Nevada.

[144] Cohen, J.M., T.J. Rosfjord. Influences on the Uniformity of Sprays Produced by gas Turbine High Shear Nozzle/Swirler Assemblies. JPC. (1990). Orlando, FL.

[145] Cohen, J.M., T.J. Rosfjord, Influences on the Sprays Formed by High-Shear Fuel Nozzle/Swirler Assemblies, Propulsion and Power 9 (1) (1993) 16-27.

[146] Li, X., M.C. Soteriou, W. Kim, J.M. Cohen, High Fidelity Simulation of the Spray Generated by a Realistic Swirling Flow Injector, Eng. Gas Turbines Power 136 (2014).

[147] Li, X., M.C. Soteriou, High-Fidelity Simulation of Fuel Atomization in a Realistic Swirling Flow Injector, Atomization and Sprays 23 (11) (2013) 1049-1078.

[148] Colket, M., J. Heyne, M. Rumizen, M. Gupta, A. Jardines, T. Edwards, W.M. Roquemore, G. Andac, R. Boehm, J. Zelina, J. Lovett, J. Condevaux, S. Bornstein, N. Rizk, D. Turner, C. Graves, M.S. Anand, R. Williams, F. Xu, J. Tishkoff, C. Li, J. Moder, R. Anthenien, D. Friend, P.Chu, R. Kamin, P. Serino, M. Domen, C.M. Kweon, V. Sankaran, J. Cohen, W. Chishty, An Overview of the National Jet Fuels Combustion Program, SciTech 2016, AIAA: San Diego, California.

[149] Mei, R., Velocity Fidelity of Flow Tracer Particles, Exp. Fluids 22 (1996) 1-13.

[150] Tomasi, C., R. Manduchi, Bilateral filtering for gray and color images, 6th International Conference on Computer Vision 1998, IEEE 839-846.

[151] Steinberg, A.M., Boxx, I., Stöhr, M., Carter, C. D., Meier, W., Flow–flame interactions causing acoustically coupled heat release fluctuations in a thermo-acoustically unstable gas turbine model combustor, Combust. Flame 157 (12) (2010) 2250-2266.

[152] Boxx, I., Slabaugh, C., Kutne, P., Lucht, R. P., Meier, W., 3kHz PIV/OH-PLIF measurements in a gas turbine combustor at elevated pressure, Proc. Comb. Institute 35 (3) (2015) 3793-3802.

[153] Wellander, R., Richter, M., Aldén, M., Time-resolved (kHz) 3D imaging of OH PLIF in a flame, Exp Fluids 55 (6) (2014) 1764.

[154] Pope, S.B., Turbulent Flows2000: Cambridge: Cambridge University Press.

[155] Marshall, A., Turbulent Flame Propagation Characteristics of High Hydrogen Content Fuels, Mechanical Engineering 2015, Georgia Institute of Technology.

[156] Hawkes, E.R., R. Sankaran, J.H. Chen. Estimates of the Three-Dimensional Flame Surface Density and Every Term in its Transport Equation from Two-Dimensional Measurements. Proc. Combust. Inst. (2011). Combustion Institute.

[157] Kerl, J., C. Lawn, F. Beyrau, Three-Dimensional Flame Displacement Speed and Flame Front Curvature Measurements Using Quad-Plane PIV, Combust. Flame (2013).

[158] Gashi, S., J. Hult, K.W. Jenkins, N. Chakraborty, S. Cant, C.F. Kaminski. Curvature and Wrinkling of Premixed Flame Kernels Comparisons of OH-PLIF and DNS Data(2005).

[159] Santhosh, R., A. Miglani, S. Basu, Transition in Vortex Breakdown Modes in a Coaxial Isothermal Unconfined Swirling Jet, Phys. Fluids 26 (2014).

[160] Santhosh, R., A. Miglani, S. Basu, Transition and Acoustic Response of Recirculation Structures in an Unconfined Co-Axial Isothermal Swirling Flow, Phys. Fluids 25 (2013).

[161] Bendat, J.S., A.G. Piersol, Random Data: Analysis and Measurement Procedures. 4th ed2010: Wiley.

[162] Sankaran, R., H.G. Im. Dynamic Flammability Limits of Methane/Air Premixed Flames with Mixture Composition Fluctuations. Proc. Combust. Inst. (2002).

[163] Im, H.G., J.H. Chen. Effects of Flow Transients on the Burning Velocity of Laminar Hydrogen/Air Premixed Flames. Proc. Combust. Inst. (2000).

[164] Korusoy, E., J. Whitelaw, Extinction and Relight in Opposed Flames, Exp. Fluids 33 (1) (2002) 75-89.

[165] Luff, D., E. Korusoy, P. Lindstedt, J.H. Whitelaw, Counterflow Flames of Air and Methane, Propane and Ethylene, with and Without Periodic Forcing, Exp. Fluids 35 (6) (2003) 618-626.

[166] Lieuwen, T.C., Unsteady Combustor Physics2012, New York, NY: Cambridge Univ. Press.